

CATALYTIC CO₂ HYDROGENATION TO CO AND METHANOL

by

Chen-Yu Chou

A dissertation submitted to the Faculty of the University of Delaware in partial fulfillment of the requirements for the degree of Doctor of Philosophy in Chemical Engineering

Spring 2019

© 2019 Chen-Yu Chou
All Rights Reserved

CATALYTIC CO₂ HYDROGENATION TO CO AND METHANOL

by

Chen-Yu Chou

Approved: _____
Eric M. Furst, Ph.D.
Chair of the Department of Chemical and Biomolecular Engineering

Approved: _____
Levi T. Thompson, Ph.D.
Dean of the College of Engineering

Approved: _____
Douglas J. Doren, Ph.D.
Interim Vice Provost for Graduate and Professional Education

I certify that I have read this dissertation and that in my opinion it meets the academic and professional standard required by the University as a dissertation for the degree of Doctor of Philosophy.

Signed:

Raul F. Lobo, Ph.D.
Professor in charge of dissertation

I certify that I have read this dissertation and that in my opinion it meets the academic and professional standard required by the University as a dissertation for the degree of Doctor of Philosophy.

Signed:

Douglas J. Buttrey, Ph.D.
Member of dissertation committee

I certify that I have read this dissertation and that in my opinion it meets the academic and professional standard required by the University as a dissertation for the degree of Doctor of Philosophy.

Signed:

Terry G. Dubois, Ph.D.
Member of dissertation committee

I certify that I have read this dissertation and that in my opinion it meets the academic and professional standard required by the University as a dissertation for the degree of Doctor of Philosophy.

Signed:

Michael T. Klein, Sc.D.
Member of dissertation committee

I certify that I have read this dissertation and that in my opinion it meets the academic and professional standard required by the University as a dissertation for the degree of Doctor of Philosophy.

Signed:

Bingjun Xu, Ph.D.
Member of dissertation committee

ACKNOWLEDGMENTS

I have received enormous support for helping me to complete this dissertation. There are a lot of people I would like to acknowledge. First, I would like to express my greatest attitude to my advisor, Dr. Raul Lobo, for giving me the opportunity to conduct research in this lovely group, and for all the continuous support and great guidance. He is not only a great advisor, but also a great person to work with. I have learned so much from him in many areas. I know that all the inspiration from him will turn into something great in the future, and the experience here in his group will always be helpful. I am extremely grateful and appreciate all the supports he gave me during my PhD program at University of Delaware.

I am honored to work with Dr. Terry Dubois on a project funded by U.S. Army. Dr. Dubois gave us a lot of useful information and feedback on tackling the practical problem. I really enjoyed the meetings with him. I would like to acknowledge U.S. Army for funding the research that led to the production of this thesis. I would also like to thank Dr. Douglas Buttrey, Dr. Michael Klein, Dr. Bingjun Xu for kindly agreeing to be on my thesis committee and helping to improve this thesis.

I would also like to thank all members of Dr. Lobo's research group who have been at the University of Delaware throughout the years: Dr. Jason Loiland, Dr. Trong Pham, Dr. Bahar Ipek, Dr. Eyas Mahmoud, Dr. Jelvehnaz Mirzababaei, Dr. Efi Vasileiadou, Dr. Molly Koehle, Dr. Edward Schreiner, Dr. Huibo Sheng, Dr. Hannah Nguyen, Dr. Young Jin Kim, Dr. Erisa Saraci, Dr. Ting Jiang, Dr. Shoucheng Du,

Muyuan Li, Mark LaFollette, Jason Lee, Eric Steinman, Hsuan-Lan Wang. I would like to thank all the other colleagues in Colburn lab and ISE lab who gave me so much support. It has been a pleasure to work with you.

I would like to thank the support staff within the Department of Chemical and Biomolecular Engineering at the University of Delaware. Alan Price, Neilsen Garrett, and Weihua Deng have been so helpful in safety and instrumental set up. Rechilda Alba, Mary Walsh, Kathleen Young, and Cheryl Davis-Robinson have been supportive in all the operations in Colburn throughout the years.

I would like to thank my family and friends for their continued support over the years. I would like to dedicate this work to Sophie Liao, my greatest supporter through my roughest time, and have always been by my side. Without your love and encouragement, I could not have completed the thesis.

TABLE OF CONTENTS

LIST OF TABLES	x
LIST OF FIGURES	xii
LIST OF SCHEMES	xii
ABSTRACT	xix

Chapter

1	INTRODUCTION	1
1.1	CO ₂ Emission and Utilization	1
1.2	CO Synthesis via Reverse Water-Gas Shift (RWGS) Reaction	5
1.3	Methanol Synthesis	8
1.3.1	Methanol production in industry	8
1.3.2	Recent advances in hydrogenation of CO ₂ to methanol	12
1.3.3	Mechanism	13
1.4	Scope of Dissertation.....	15
2	EXPERIMENTAL METHODS	19
2.1	Catalyst Synthesis.....	19
2.1.1	Wet impregnation	19
2.1.2	Dry Impregnation	21
2.1.3	Co-precipitation method	21
2.2	Characterization Techniques and Spectroscopies	21
2.2.1	Powder X-ray Diffraction (XRD).....	22
2.2.2	X-ray Photoelectron Spectroscopy (XPS)	23
2.2.3	Scanning Electron Microscopy (SEM) and Energy Dispersive X-ray (EDX) Spectroscopy	25
2.2.4	Temperature-programmed Reduction/Oxidation/Desorption (TPR/TPO/TPD).....	26
2.3	Catalyst Evaluation and Kinetic Studies	29

2.3.1	Flow-reactor Setup for Catalysts Evaluation.....	29
2.3.2	Chromatography and Mass Spectrometry	31
3	REVERSE WATER-GAS SHIFT IRON CATALYST DERIVED FROM MAGNETITE.....	33
3.1	Introduction	33
3.2	Materials and Methods	36
3.2.1	Materials	36
3.2.2	Reactor setup for kinetics and gas-switching experiments.....	37
3.2.3	Catalyst Characterization.....	37
3.2.4	Measurement of product formation rates and reaction rates with gas-switching or isotopic experiments	39
3.3	Results and Discussion	43
3.4	Conclusions	68
4	DIRECT CONVERSION OF CO ₂ INTO METHANOL OVER PROMOTED INDIUM-BASED CATALYSTS.....	70
4.1	Introduction	70
4.2	Experimental.....	74
4.2.1	Catalyst preparation.....	74
4.2.2	Catalyst Characterization.....	74
4.2.3	Reactor setup and catalytic activity.....	76
4.3	Results and Discussion	79
4.4	Conclusions	107
5	HIGHLY SELECTIVE CONVERSION OF CO ₂ INTO METHANOL OVER COBALT-INDIUM BIMETAL OXIDES CATALYSTS	108
5.1	Introduction	108
5.2	Materials and Methods	110
5.2.1	Catalyst preparation.....	110
5.2.2	Catalyst Characterization.....	111
5.2.3	Reactor setup and catalytic activity.....	113
5.3	Results and Discussion	114
5.4	Conclusions	135

6	COMPARISON OF DIFFERENT CATALYSTS BY SIMULATION OF CO ₂ TO METHANOL PRODUCTION PROCESS VIA ASPEN PLUS	137
6.1	Introduction	137
6.2	Methods	138
6.3	Results and Discussion	140
6.3.1	Methanol synthesis process under equilibrium condition	140
6.3.2	Methanol synthesis process over conventional catalyst and selective catalysts using RStoic reactor	144
6.4	Conclusions	150
7	CONCLUSIONS AND RECOMMENDATIONS	151
7.1	Dissertation Summary	151
7.2	Recommendations for future work	154
7.2.1	Further improvements on In ₂ O ₃ catalyst for methanol synthesis	154
7.2.2	Further improvements on bimetal oxide catalysts for methanol synthesis	155
7.2.3	Conversion of methanol to other value-added products	157
	REFERENCES	158
Appendix		
A	STREAM RESULTS FROM ASPEN PLUS SIMULATION	175
B	REPRINT PERMISSION LETTERS	186

LIST OF TABLES

Table 3.1 Measured reaction orders with respect to CO ₂ and H ₂ , and measured activation energies (E_{meas}) over Fe ₃ O ₄ . Reaction conditions: 100 mg Fe ₃ O ₄ , $F_{\text{tot}} = 75$ sccm, $T = 723$ K.	47
Table 3.2 XPS peak fittings for Fe 2p _{3/2} spectra for Fe ₃ O ₄ and post-reaction Fe ₃ O ₄ ...	54
Table 3.3 Estimated initial rates of CO production after gas switches from H ₂ to CO ₂ and from CO ₂ to H ₂ during gas-switching experiment on Fe ₃ O ₄ in Figure 3.7.....	61
Table 3.4 Fitted initial slopes and area of H ₂ O in H ₂ /CO ₂ switching experiment with different He purging time in Figure 3.11	68
Table 4.1 Comparison of various catalysts for CO ₂ hydrogenation to methanol.	72
Table 4.2 Physical properties of In ₂ O ₃ /ZrO ₂ and promoted catalysts determined by N ₂ adsorption, XRF, and XPS.....	84
Table 5.1 Metallic concentrations in molar (mol) or weight (Wt) percentages of 2Co-1In/ZrO ₂ and 1Co-2In/ZrO ₂ determined by EDX, XPS, and XRF.	117
Table 5.2 Metallic concentration molar (mol) or weight (Wt) percentages of In ₂ O ₃ /ZrO ₂ and Co ₃ O ₄ /ZrO ₂ determined by XRF.....	117
Table 5.3 Catalytic activities of Co ₃ O ₄ /ZrO ₂ at the temperatures between 528 K and 573 K under 40 bar.	130
Table 5.4 CO ₂ desorption temperature and amount of CO ₂ desorption for spent of In ₂ O ₃ /ZrO ₂ and spent 2Co-1In/ZrO ₂ from the deconvolution of TPD profiles as shown in Figure 5.8.	135
Table 6.1 Simulation results for the methanol process under (i) Equilibrium condition and (ii) Equilibrium without CO as product at 543 K, 60 bar with RGibbs reactor in Aspen Plus.	143

Table 6.2 Cost analysis for case (i): equilibrium reaction in RGibbs reactor and case (ii): equilibrium reaction without CO production in RGibbs reactor.....	144
Table A1 Stream results in section 6.3.1 using RGibbs reactor with CO as byproduct at 543 K and 60 bar.	176
Table A2 Stream results in section 6.3.1 using RGibbs reactor without CO as byproduct at 543 K and 60 bar	178
Table A3 Stream results in section 6.3.2 using RStoic reactor over CZA catalyst at 543 K and 40 bar.	180
Table A4 Stream results in section 6.3.2 using RStoic reactor over 3La10In/ZrO ₂ catalyst at 543 K and 40 bar.	182
Table A5 Stream results in section 6.3.2 using RStoic reactor over 1Co-2In/ZrO ₂ catalyst at 543 K and 40 bar.	184

LIST OF FIGURES

- Figure 1.1** Monthly mean atmospheric carbon dioxide in parts per million (ppm) at Mauna Loa Observatory, Hawaii. The carbon dioxide data (red curve), measured as the mole fraction in dry air. The black curve represents the seasonally corrected data. Source: National Oceanic & Atmospheric Administration (NOAA) [3]. 2
- Figure 1.2** Schematic illustration of the variety of potential uses for carbon dioxide after it has been captured (modified from the report of National Academies Press [1])..... 3
- Figure 1.3** Schematic of the intensified RWGS-chemical looping process [27]. Reprinted and modified with permission from Y.A. Daza, R.A. Kent, M.M. Yung, J.N. Kuhn, Industrial and Engineering Chemistry Research. 53 (2014) 5828–5837. Copyright © 2014 American Chemical Society..... 7
- Figure 1.4** Equilibrium CO₂ conversion and methanol selectivity at different temperatures with initial H₂/CO₂ = 3 and at (a) 10 bar, (b) 30 bar, (c) 100 bar, (d) 200 bar, (e) 300 bar, (f) 400 bar, and (g) 500 bar. This figure is reprinted with permission from ref. [31] (<https://pubs.acs.org/doi/abs/10.1021/acs.chemrev.6b00816>, further permissions related to the material excerpted should be directed to the ACS). Copyright © 2017 American Chemical Society. 10
- Figure 1.5** Possible reaction pathways of CO₂ hydrogenation to CO, CH₃OH, and CH₄. *(X) indicates adsorbed species [54] Reprinted with permission from S. Kattel, P. Liu, J.G. Chen, J. Am. Chem. Soc. 139 (2017) 9739–9754. Copyright © 2017 American Chemical Society..... 14
- Figure 2.1** Illustration of wet impregnation method in synthesizing In₂O₃/ZrO₂ catalyst used in direct conversion of CO₂ to methanol. 20
- Figure 2.2** Illustration of the beams diffracted by two different layers. 22

Figure 2.3 TPR _{H2} profiles for: (1) goethite; (2) ferrihydrite; (3) hematite; (4) magnetite; (5) wustite; heating rate 1.07°C/min [60] Reprinted and modified with permission from W.K. Jozwiak, E. Kaczmarek, T.P. Maniecki, W. Ignaczak, W. Maniukiewicz, <i>Appl. Catal. A Gen.</i> 326 (2007) 17–27. Copyright © 2007 Elsevier.....	27
Figure 2.4 TPR _{H2} profiles obtained by mass spectrometer for fresh magnetite (reduction conditions: Fe ₃ O ₄ 50mg; F _{tot} = 64 sccm; ramped from room temperature to 800 °C with 17.4% H ₂ and He mixture gas; total molar flow rate of H ₂ = 4.91x10 ⁻⁴ mol/min).....	27
Figure 2.5 Process flow diagram of the experimental setup used for high pressure experiments	30
Figure 3.1 CO formation rates and their turnover frequencies (T.O.F.) on Fe ₃ O ₄ at partial pressures of CO ₂ and H ₂ indicated in the legend. Other reaction conditions: P _{tot} = 1 bar, T = 753 K, F _{tot.} = 75 sccm, GHSV = 4.5×10 ⁴ cm ³ h ⁻¹ g _{cat.} ⁻¹	44
Figure 3.2 XRD pattern of Fe ₃ O ₄ after the reduction in H ₂	45
Figure 3.3 (a) H ₂ consumption (%) of reduction period during the pretreatment following the temperature-programmed reduction (TPR) of 100 mg Fe ₃ O ₄ . (b) TPR curve of post-reaction Fe ₃ O ₄ sample.	49
Figure 3.4 XRD patterns of fresh Fe ₃ O ₄ (down) and post-reaction Fe ₃ O ₄ (up); inset is the magnification of post-reaction Fe ₃ O ₄ from 44° to 45.5°.....	51
Figure 3.5 XPS Fe 2p _{3/2} spectra of Fe ₃ O ₄ and post-reaction Fe ₃ O ₄ . The curves under the fitted envelope and above the background are contributions of estimated components from peak fitting.....	53
Figure 3.6 (a) CO formation rate on 100 mg Fe ₃ C. Reaction conditions: F _{tot} = 75 sccm; the reactor was ramped to 753K with P _{H2} = 15kPa and He as remainder. No further reduction was applied after the ramping. During the reaction, T = 753K, P _{tot} = 1 bar, P _{H2} = P _{CO2} = 15kPa. (b) CO formation rate on 100 mg Fe ₃ C. The temperature was directly ramping from room temperature to 773K as shown in the figure with P _{tot} = 1 bar, P _{H2} = P _{CO2} = 15kPa, the remainder is He.	56

Figure 3.7 Ion current at $m/z = 18$ (H_2O) and 28 (CO) during H_2/CO_2 switching experiments on Fe_3O_4 . Arrows with a label indicate a change in gas composition to the indicated gas. The catalyst first was reduced in flowing H_2 for 2 h, following the reaction in H_2 and CO_2 for 2 h, and H_2/He in 20 min before the first admission of CO_2 . Reaction conditions: $T = 773$ K, $F_{\text{He}} = 36$ sccm, F_{H_2} or $F_{\text{CO}_2} = 4$ sccm	60
Figure 3.8 Ion current at $m/z = 18$ (H_2O), 28 (CO), and 44 (CO_2) during H_2/CO_2 switching experiments on Fe_3O_4 . Arrows with a label indicate a change in gas composition to the indicated gas. Reaction conditions: $T = 773$ K, $F_{\text{He}} = 36$ sccm, F_{H_2} or $F_{\text{CO}_2} = 4$ sccm. The figure is a modification of Figure 3.7	62
Figure 3.9 Ion current at $m/z = 28$ (CO) and 30 (C^{18}O) during $\text{CO}_2/\text{C}^{18}\text{O}_2$ switching experiments on Fe_3O_4 (100 mg). Labels in each region indicate a change in gas composition. A standard pretreatment (reduced in flowing H_2 for 2 h) and RWGS reaction (>2 h) had been done before the switching experiment. Switching experiment conditions: $T = 753$ K, $F_{\text{tot}} = 40$ sccm, $F_{\text{H}_2} = 4$ sccm, F_{CO_2} or $F_{\text{C}^{18}\text{O}_2} = 4$ sccm	64
Figure 3.10 Ion current at $m/z = 2$ (H_2), 3 (HD), 4 (D_2), and 28 (CO) during flow of 7.5 kPa $\text{H}_2 + 7.5$ kPa $\text{D}_2 + 15$ kPa CO_2 and 7.5 kPa $\text{H}_2 + 15$ kPa CO_2 on Fe_3O_4 . Reaction conditions: $T = 753$ K, $F_{\text{tot}} = 75$ sccm.	65
Figure 3.11 (a) Ion current at $m/z = 28$ (CO) and $m/z = 18$ (H_2O) during H_2/CO_2 switching experiments on Fe_3O_4 . Arrows with a label indicate a change in gas composition to the indicated gas. The catalysts were in flowing H_2 for 2 h followed by the reaction in CO_2+H_2 for 2 h before the first admission of H_2 (relative time: 31 min) and CO_2 (relative time: 46 min). Reaction conditions: $T = 753$ K, $F_{\text{tot}} = 75$ sccm, P_{H_2} or $P_{\text{CO}_2} = 15$ kPa. (b) is the modification of (a).	67
Figure 4.1 SEM images of (a) $\text{In}_2\text{O}_3/\text{ZrO}_2$, (b) $1.5\text{Y}9\text{In}/\text{ZrO}_2$, and (c) $3\text{La}10\text{In}/\text{ZrO}_2$	81
Figure 4.2 Pore size distribution of $\text{In}_2\text{O}_3/\text{ZrO}_2$, $2\text{Y}8\text{In}/\text{ZrO}_2$, and $3\text{La}10\text{In}/\text{ZrO}_2$	82
Figure 4.3 XRD patterns of ZrO_2 , In_2O_3 , $\text{In}_2\text{O}_3/\text{ZrO}_2$, $1.5\text{Y}9\text{In}/\text{ZrO}_2$, and $3\text{La}10\text{In}/\text{ZrO}_2$	86
Figure 4.4 XPS spectra of Y 3d in $2\text{Y}8\text{In}/\text{ZrO}_2$ and La 3d _{5/2} in $3\text{La}10\text{In}/\text{ZrO}_2$ after calcined in air at 573 K for 3h.	87

Figure 4.5 SEM-EDX layered images of (a) In ₂ O ₃ /ZrO ₂ , (b) 2Y8In/ZrO ₂ , and (c) 3La10In/ZrO ₂	88
Figure 4.6 H ₂ -TPR profiles of In ₂ O ₃ /ZrO ₂ , 1.5Y9In/ZrO ₂ , 2Y8In/ZrO ₂ , 3Y8In/ZrO ₂ , and 3La10In/ZrO ₂	89
Figure 4.7 H ₂ -TPR profiles of unsupported In ₂ O ₃ and In ₂ O ₃ /ZrO ₂	90
Figure 4.8 CO ₂ -TPD profiles of In ₂ O ₃ /ZrO ₂ , 2Y8In/ZrO ₂ , and 3La10In/ZrO ₂ after He treatment at 573 K for 1 h.	92
Figure 4.9 XPS spectra of O1s in In ₂ O ₃ /ZrO ₂ , 2Y8In/ZrO ₂ , and 3La10In/ZrO ₂ after calcined in air at 573 K for 3h. The [O _{defect}] is defined as: [O _{defect}] = (Area of O _{defect})/(Area of O _{defect} + Area of O _{lattice}).	94
Figure 4.10 (a) CO ₂ conversion, (b) selectivity to methanol, (c) methanol formation rate, and (d) CO formation rate versus temperature over In ₂ O ₃ /ZrO ₂ , 1.5Y9In/ZrO ₂ , 2Y8In/ZrO ₂ , 3Y8In/ZrO ₂ , and 3La10In/ZrO ₂ . (e) Methanol selectivity versus CO ₂ conversion over the catalysts mentioned above.	97
Figure 4.11 Arrhenius plot of methanol formation from CO ₂ hydrogenation at 40 bar and 528 – 573 K over In ₂ O ₃ /ZrO ₂ , 1.5Y9In/ZrO ₂ , 2Y8In/ZrO ₂ , 3Y8In/ZrO ₂ , and 3La10In/ZrO ₂	99
Figure 4.12 Methanol formation rate normalized by mole percent of surface In (n% _{In, surface}) versus temperature over In ₂ O ₃ /ZrO ₂ , 1.5Y9In/ZrO ₂ , 2Y8In/ZrO ₂ , 3Y8In/ZrO ₂ , and 3La10In/ZrO ₂ . n% _{In, surface} was derived from XPS spectra for each sample.	100
Figure 4.13 Reaction orders of (a) H ₂ and (b) CO ₂ for methanol synthesis at 573 K over 2Y8In/ZrO ₂ catalyst.	101
Figure 4.14 Methanol formation rate over 2Y8In/ZrO ₂ as a function of CO concentration in CO and CO ₂ mixture gas feed at 573 K and 543 K. Blue square with the cross indicates the methanol formation rate measured after the CO co-feeding experiment at 573 K to quantify for any change of activity due to deactivation. Reaction conditions: P _{tot.} = 40 bar, SV = 52000 cm ³ h ⁻¹ g _{cat.} ⁻¹ . For R = 0, H ₂ :CO ₂ :He =80:20:30 (in sccm). The flow of He was stepwise reduced to admit progressively higher amounts of CO.	104
Figure 4.15 CO-TPD on partially reduced (473K, 20% H ₂ /He) 2Y8In/ZrO ₂ catalyst. CO signal in blank test was ~1.1×10 ⁻⁸ A.	105

Figure 4.16 Schematic illustration of the possible initial steps of CO ₂ hydrogenation on In ₂ O ₃ . (a) The formation of formate intermediate (HCOO*). The blank square is the oxygen vacancy. (b) The formation of HOCO* on In ₂ O ₃ . (c) The formation of HOCO* affected by yttrium or lanthanum oxides. E _{a,b} and E _{a,c} denote the activation energy of step (b) and (c), respectively.	106
Figure 5.1 SEM images of 2Co-1In/ZrO ₂ in the magnification of 10000 (a1) and 20000 (a2); 1Co-2In/ZrO ₂ in the magnification of 10000 (b1) and 20000 (b2).	116
Figure 5.2 XRD patterns of Co ₃ O ₄ /ZrO ₂ , 1Co-2In/ZrO ₂ , 2Co-1In/ZrO ₂ , and spent 2Co-1In/ZrO ₂	119
Figure 5.3 (a) XPS Co 2p spectra of 2Co-1In/ZrO ₂ and spent 2Co-1In/ZrO ₂ . (b) XPS In 3d spectra of In ₂ O ₃ /ZrO ₂ and 2Co-1In/ZrO ₂ after the calcination at 573 K in air.	122
Figure 5.4 Deconvolution of the core-level O 1s XPS spectrum of 2Co-1In/ZrO ₂ and spent 2Co-1In/ZrO ₂	124
Figure 5.5 Methanol formation rate and methanol selectivity versus time on stream over (a) 2Co-1In/ZrO ₂ and (b) 1Co-2In/ZrO ₂ catalysts. Vertical dashed lines separate different temperature zone during the reaction...	127
Figure 5.6 Comparison of methanol selectivity and CO ₂ conversion versus temperature over 2Co-1In/ZrO ₂ and In ₂ O ₃ /ZrO ₂ catalysts.	128
Figure 5.7 TPR profiles of 2Co-1In/ZrO ₂ Co ₃ O ₄ /ZrO ₂ , and In ₂ O ₃ /ZrO ₂	132
Figure 5.8 CO ₂ -TPD profiles of In ₂ O ₃ /ZrO ₂ , 2Co-1In/ZrO ₂ after reaction at 573-543 K for 18 h.	133
Figure 6.1 Flowsheet of CO ₂ hydrogenation to methanol process using RGibbs reactor at equilibrium (T = 543 K, P = 60 bar).	141
Figure 6.2 Flowsheet of CO ₂ hydrogenation to methanol process simulated by Aspen Plus.	147
Figure 6.3 Methanol productivity (%) simulated from Aspen Plus over Cu/Zn/Al ₂ O ₃ , 3La10In/ZrO ₂ , and 1Co-2In/ZrO ₂ catalysts at 543 K and 40 bar.	148

Figure 6.4 Net energy consumption (KJ/Kg) simulated from Aspen Plus over Cu/Zn/Al₂O₃, 3La10In/ZrO₂, and 1Co-2In/ZrO₂ catalysts at 543 K and 40 bar. 148

Figure 6.5 Methanol productivity (%) and net energy consumption versus CO₂ conversion at the methanol selectivity of 90% at 543 K and 40 bar simulated from Aspen Plus..... 149

LIST OF SCHEMES

Scheme 1.1 Hydrogen via steam reforming of methane and WGS reactions forms CO ₂ as co-product	4
Scheme 3.1 Redox reaction pathway for CO formation	63

ABSTRACT

The catalytic CO₂ hydrogenation for carbon monoxide or methanol production has attracted significant attention recently as a strategy of introducing green H₂ into the fuel economy and recycling carbon dioxide as a chemical feedstock. In the past decades, research into catalysts for this reaction has primarily centered on Cu-based materials supported on Al₂O₃, specially for the hydrogenation of synthesis gas to methanol. However, Cu-based materials show limited selectivity to methanol and limited stability. The aim of the research conducted in this thesis is to increase the energy efficiency of carbon-based technology by developing stable, selective, and efficient catalyst for catalytic CO₂ hydrogenation process.

The primary goal of the research described in first part of this dissertation (Chapters 3) has been develop an efficient, inexpensive and selective catalyst with good stability for the conversion of CO₂ and H₂ to CO, the so-called reverse water-gas shift (RWGS) reaction. The RWGS reaction is, fundamentally and practically, an essential reaction for sustainability because of the versatility of CO as a chemical intermediate and the simplest product for CO₂ utilization. The catalytic properties of unsupported iron oxides, specifically magnetite (Fe₃O₄), were investigated at temperatures between 723 K and 773 K and atmospheric pressure. This catalyst exhibited fast catalytic CO formation rate (35.1 mmol h⁻¹ g_{cat.}⁻¹), high turnover frequency (0.180 s⁻¹), high CO selectivity (>99%), and high stability (753K, 45000 cm³h⁻¹g_{cat.}⁻¹) under 1:1 H₂ to CO₂ ratio. Reaction rates over Fe₃O₄ catalyst displayed a strong dependence on H₂ partial pressure (reaction order of ~0.8) and a weaker

dependence on CO₂ partial pressure (reaction order of 0.33) under equimolar flow of both reactants. X-ray powder diffraction patterns and XPS spectra reveal that the bulk composition and structure of the post-reaction catalyst was formed mostly of metallic Fe and Fe₃C while the surface contained Fe²⁺, Fe³⁺, metallic Fe, and Fe₃C. Catalytic tests using pure Fe₃C (iron carbide) suggest that Fe₃C is not an effective catalyst for this reaction at the conditions investigated. Gas-switching experiments (CO₂ or H₂) indicated that a redox mechanism is the predominant reaction pathway.

The second part of this dissertation (Chapters 4-6) investigates the catalytic CO₂ hydrogenation to methanol and the impact of a highly selective catalysts on the methanol synthesis *process*. Supported indium oxide catalysts (Chapter 4) are investigated for the CO₂ hydrogenation to methanol at a total pressure of 40 bar (528-573K) using a laboratory flow reactor. Surface reducibility, optical spectral characteristics, and catalytic rates and selectivity were correlated to catalyst composition. Promoted catalysts, especially Yttrium or Lanthanum-promoted indium oxide, require higher temperatures (H₂-TPR) for surface reduction and display higher CO₂ desorption temperatures (CO₂-TPD). The promoted samples also have higher methanol selectivity (about 20%) compared to the non-promoted catalyst, while methanol formation rates (0.330-0.420 g_{MeOH} g_{cat.}⁻¹ h⁻¹ at 573 K) remain close to the non-promoted catalyst. From 528 K to 558 K, methanol selectivity was over 80 %, over all the promoted catalysts, and nearly 100% selectivity was observed at the low temperature range (~528 K) investigated. The reaction kinetics of Y-promoted catalyst and the results of CO co-feeding experiments suggest that the formate pathway is the likely reaction mechanism for methanol formation.

In Chapter 5, a novel supported bimetallic oxide, Co-In catalyst supported on ZrO_2 (Co-In/ ZrO_2), was identified as an excellent catalyst for direct conversion of CO_2 to methanol with high selectivity (>99%) under industrially relevant conditions (528 K-543 K, 40 bar). The evaluation of Co-In/ ZrO_2 catalyst over 40 h on stream showed outstanding stability without deactivation. The characterization investigations and catalytic behavior of Co-In/ ZrO_2 show that this hybrid oxide system is a promising alternative for Cu-based materials.

Chapter 6 demonstrates the importance of implementing highly selective catalysts into the process of methanol synthesis by simulations using of Aspen Plus. The first section compares the difference of highly selective reaction of CO_2 hydrogenation (methanol and water are the only two products) with the common CO_2 hydrogenation (CO, methanol, and water are formed along with the competing reverse water-gas shift reaction) under equilibrium condition at 60 bar, 543 K. The second scenario compares three different catalysts such as conventional Cu/Zn/ Al_2O_3 , La-In/ ZrO_2 (Ch4), and Co-In/ ZrO_2 (Ch5) with various conversion and selectivity. The lower net energy consumptions and higher productivity of methanol shown using the Aspen Plus process simulation software over our catalysts demonstrate the value and potential impact of using selective catalysts in the methanol synthesis process.

Chapter 1

INTRODUCTION

1.1 CO₂ Emission and Utilization

Modern societies have recognized the hazard of greenhouse gases (GHG) as atmospheric concentrations of CO₂ continue to rise. Globally, human activities release approximately 35,000 Tg (tetra gram, million metric tons [MMT]) of carbon dioxide into the atmosphere each year as recently reported by The National Academies Press [1]. Negative effects such as climate change and ocean acidification could cause irreversible and harmful effects to our society.

Figure 1.1 shows the trend of continuing rise in atmospheric CO₂ concentration (exceeding 400 ppm in 2016) [2][3]; there is, thus, an urgent need to mitigate CO₂ emissions. At present, CO₂ can be reduced in three ways: control of CO₂ emissions, CO₂ capture and storage, and chemical conversion and utilization of CO₂. Though the research and development of new emission-free energy sources must be the long-term goal, efficient CO₂ capture and storage/recycling technologies remain very important strategies to control the level of CO₂ concentration. More recent emphasis has been placed on the potential synergy of carbon capture and utilization of large outflows of carbon dioxide (see Figure 1.2). After CO₂ is captured, utilizing CO₂ in a catalytic process to produce value-added chemicals and fuels is more desirable than sequestration because the net amount of CO₂ mitigated by conversion with renewable energy is 20-40 times greater than sequestration over a 20 year span [4][5]. Therefore,

chemical conversion of CO₂ is one of the most promising areas of catalyst development.

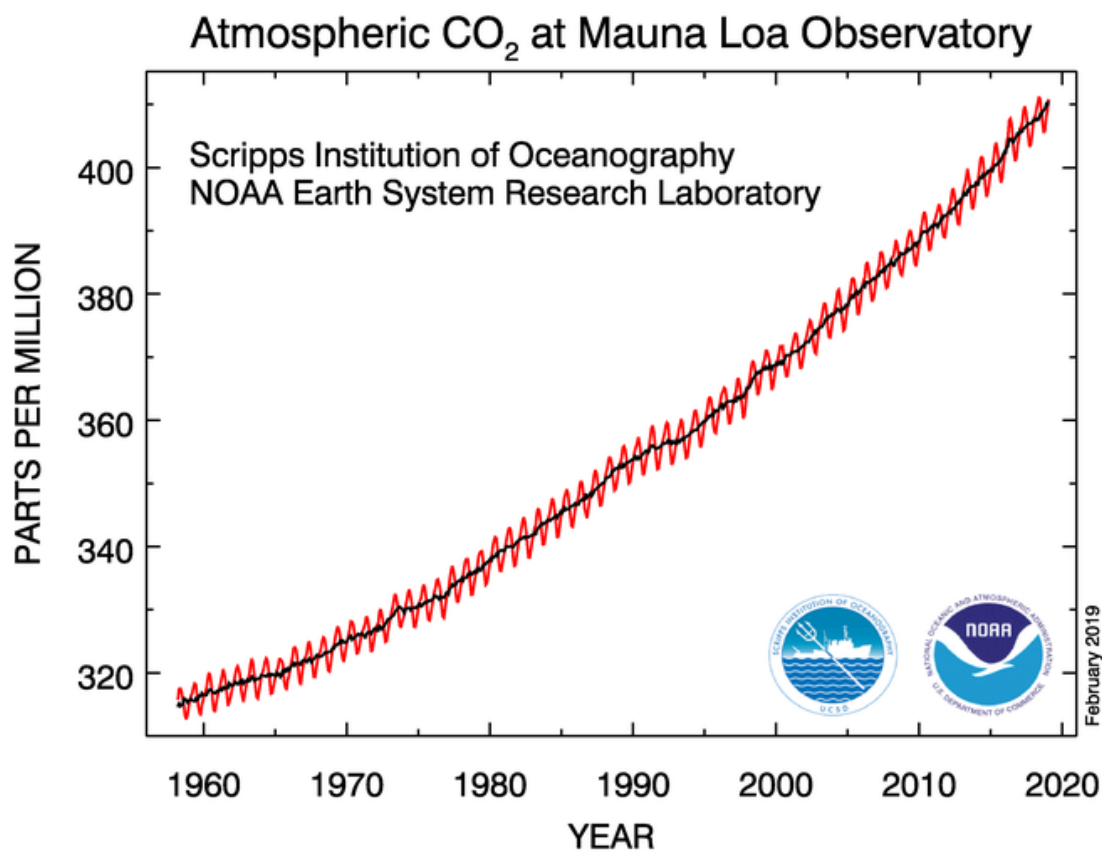


Figure 1.1 Monthly mean atmospheric carbon dioxide in parts per million (ppm) at Mauna Loa Observatory, Hawaii. The carbon dioxide data (red curve), measured as the mole fraction in dry air. The black curve represents the seasonally corrected data. Source: National Oceanic & Atmospheric Administration (NOAA) [3].

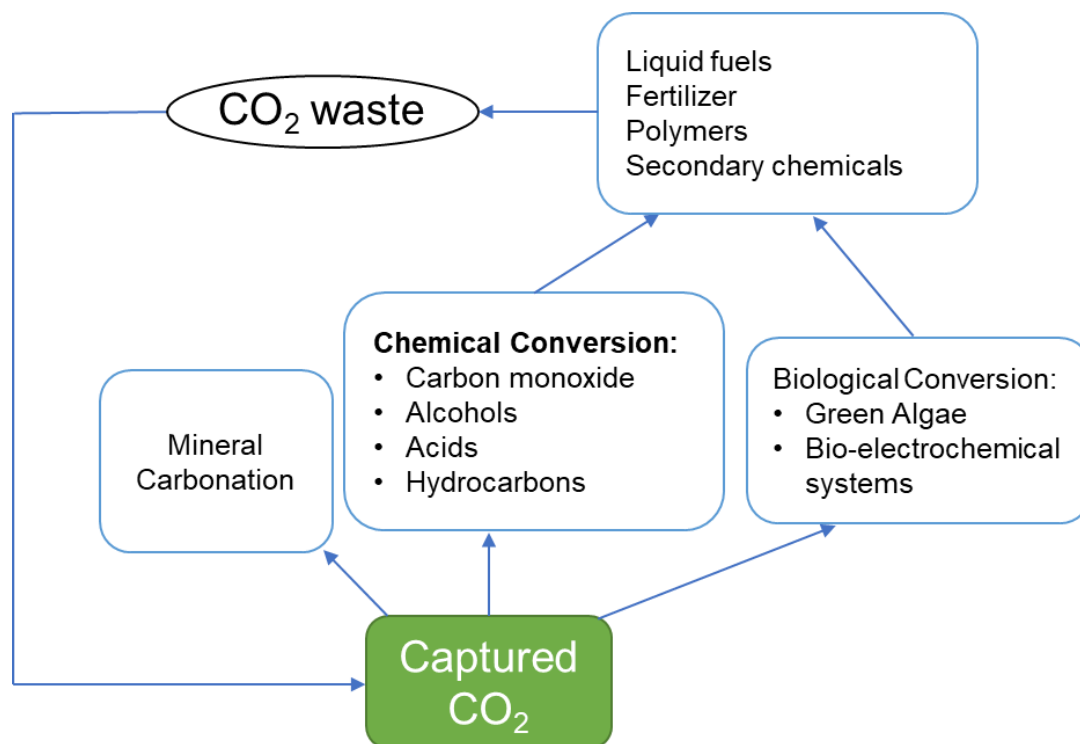
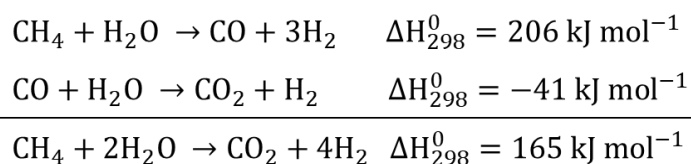


Figure 1.2 Schematic illustration of the variety of potential uses for carbon dioxide after it has been captured (modified from the report of National Academies Press [1])

A strategy for the conversion of CO₂ into valuable chemicals or fuels is its catalytic hydrogenation using molecular hydrogen since the carbon in CO₂ is in its highest oxidation state (+4). The catalytic CO₂ hydrogenation has been widely studied for the synthesis of carbon monoxide (CO, from Reverse Water-Gas Shift Reaction) [6–8], methane (CH₄, methanation for Power-To-Gas process) [9], C₂₊ hydrocarbons (Fischer-Tropsch-like processes) [10–14], methanol [15–18], higher alcohols [19], and dimethyl ether (DME) [20]. To contribute meaningfully to a reduction in carbon dioxide emissions, a sustainable process must use ingredients that themselves do not

produce CO₂ as a byproduct of their manufacture. Although there are various hydrogen resources available, fossil fuels still act as the main feedstock (96%) for H₂ production. Currently, hydrogen gas is primarily produced by the steam reforming of natural gas (mainly methane), plus the water-gas shift reaction (WGS); these reactions form, at a minimum, one mole of CO₂ for each four hydrogen molecules generated (Scheme 1.1), in addition to the carbon dioxide generated to provide the heat needed by the endothermic methane steam reforming reaction.



Scheme 1.1 Hydrogen via steam reforming of methane and WGS reactions forms CO₂ as co-product

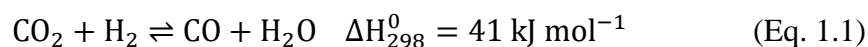
Hence, it is very important to introduce renewable energy such as wind, solar, and geothermal energy into this circular economy, leading to more sustainable habitat than the current use-and-discard linear economy. For instance, solar energy can be used in electrolysis for water-splitting and produce hydrogen. In this context, progress in energy-efficient catalytic CO₂ conversion using renewable energy could reduce both greenhouse-gas emissions and dependence on nonrenewable resources.

In the following sections, we discuss the synthesis of CO and methanol from CO₂ hydrogenation, recent development in methanol synthesis catalyst, the current understanding of technology, and existing challenges we need to overcome. In the last

section of this chapter, we then summarize the scope of this dissertation and describe the objectives of each project.

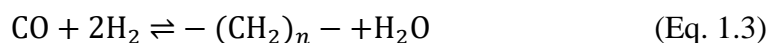
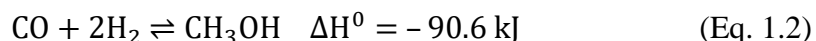
1.2 CO Synthesis via Reverse Water-Gas Shift (RWGS) Reaction

To efficiently utilize CO₂ emissions as feedstock, one critical reaction in the conversion of CO₂ by hydrogenation is the reverse water-gas shift (RWGS) reaction, which is the reaction of CO₂ with H₂ to form CO and H₂O.



The RWGS reaction is endothermic and conversion of CO₂ is favored by high reaction temperature based on Le Chatelier's principle. Therefore, to reach high CO₂ conversion (~50 %), the RWGS reaction commonly operates at high temperature (500°C). Over several decades, the RWGS reaction has attracted only little attention due to limited demand, while WGS reaction has been studied intensively to adjust the H₂/CO ratio in the synthesis gas. In industry-scale application, the WGS reaction is carried out in two-stage reactors connected in series; the first reactor is operated at “high temperature” (623-723 K) and uses Fe_xO_y-based catalysts with various promoters (Pt, Cu, Ag, Ba, K, Cr, etc.) and supports (Cr₂O₃, CeO₂-ZrO₂, MnO) [21,22]. The second stage is the low-temperature shift (LTS) reaction (463–523 K) with Cu/ZnO-based catalysts [23]. For more than 60 year, the Fe₂O₃/Cr₂O₃ catalyst is a well-known commercial catalyst for the application of WGS reaction in high temperature regime, which is a more promising material for the RWGS reaction since high temperature is more favorable to achieve high CO₂ conversion.

CO produced by RWGS reaction offers high flexibility and plays an important role as a chemical intermediate in CO₂ utilization because CO can be used in both methanol synthesis (Eq. 1.2) and downstream Fischer–Tropsch (FT) (Eq. 1.3) for chemicals and fuels.



The two-step approach using RWGS for methanol synthesis has been proposed and developed on a pilot plant scale by The Carbon Dioxide Reduction and Sequestration (CDRS) R&D Center in South Korea. This approach is the so-called CAMERE (Carbon dioxide hydrogenation to form Methanol via a Reverse-water-gas-shift reaction) process [24,25]. In this process, carbon dioxide is converted to CO and H₂O by the RWGS reaction and then, the product (CO/CO₂/H₂) is fed to the methanol reactor after removing the water. The advantage of this approach is the higher catalyst productivity. The removal of water after first step also prevents the catalyst from the water inhibition in the second step of methanol synthesis.

RWGS has attracted attention recently because of results from the potential impact of a novel chemical-looping process [26,27], as shown in Figure 1.3. First, H₂ is used to reduce the metal oxide. CO is formed when CO₂ comes in and serves as an oxidant of the solid, returning the metal oxide to an oxidized state. A metal oxide can be viewed as an oxygen carrier in this process. One of the main advantages of an intensified RWGS-chemical looping process is the elimination of the methanation of

CO₂ because the H₂/H₂O and CO/CO₂ flows are separated which also drives the equilibrium towards the products.

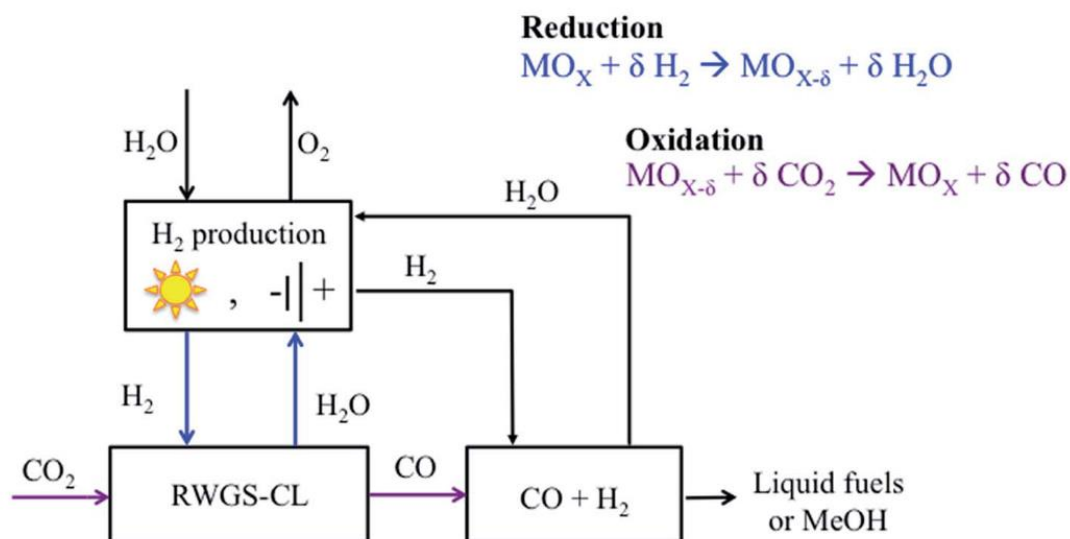


Figure 1.3 Schematic of the intensified RWGS-chemical looping process [27]. Reprinted and modified with permission from Y.A. Daza, R.A. Kent, M.M. Yung, J.N. Kuhn, *Industrial and Engineering Chemistry Research*. 53 (2014) 5828–5837. Copyright © 2014 American Chemical Society.

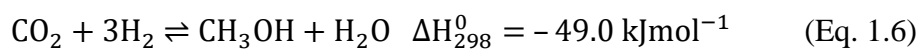
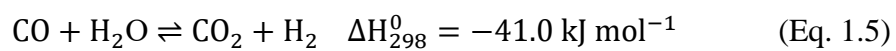
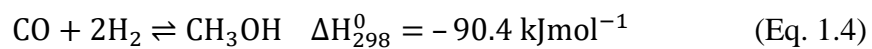
The above discussion indicates that it is worthy to develop more efficient and stable catalyst for RWGS reaction in industrially feasible process because of its crucial role in CO₂ utilization. A more detailed review in catalysts (especially Fe oxide-based catalysts), current technology, and challenges in RWGS reaction is discussed in Chapter 3.

1.3 Methanol Synthesis

1.3.1 Methanol production in industry

Methanol, the fifth largest commodity chemical produced in the world, can be stored and transported safely, is now regarded as a novel and alternative fuel resource and energy storage medium. It is very valuable and versatile in the chemical production chain as feedstocks to produce formaldehyde (36%), methyl tertiary-butyl ether/tertiary-amylmethylether (MTBE/TAME; 13%), and acetic acid (9%). In addition, olefins can also be produced via the methanol to olefins/propene (MTO/ MTP) process [28]. Methanol demand is also growing. In 1985 the methanol production was 12.4 million tons, reached 85 million tons in 2016, and approximately 80–90 million tons in 2018 [29]. The installed production capacity of methanol is around 110 million tons per year (MT/y), while the requirement for methanol in 2023 is forecasted to exceed 110 MT/y and is expected to outgrow the production capacity [30]. Methanol typically is synthesized from syngas ($H_2 + CO$) obtained directly from steam reforming, partial combustion, gasification (in the case of production from coal), which are all fossil fuel carbon sources. The first industrial plant was built by BASF in 1920s. In this process, ZnO/Cr_2O_3 , developed by Alwin Mittasch, was used as catalyst. The reaction was operated at 573-673 K and 200-300 bar. Lower temperatures and high pressures favor the conversion to methanol (Eq. 1.4 and Eq. 1.6). Thermodynamic studies from Álvarez *et. al.* (Figure 1.4) show that at 543 K (270 °C) and $H_2: CO_2$ ratios of 3:1, equilibrium conversion increases from 18%, to 23% to 38% as the pressure is increased from 10 bar, to 30 bar and to 100 bar. Selectivity is also a strong function of temperatures and pressures. The equilibrium methanol selectivity at 543 K are 5%, 20%, and 80% at the same pressures. Thus, promising methanol catalysts must be not

only active at relatively low temperatures (less than 543 K) but should be stable and highly selective.



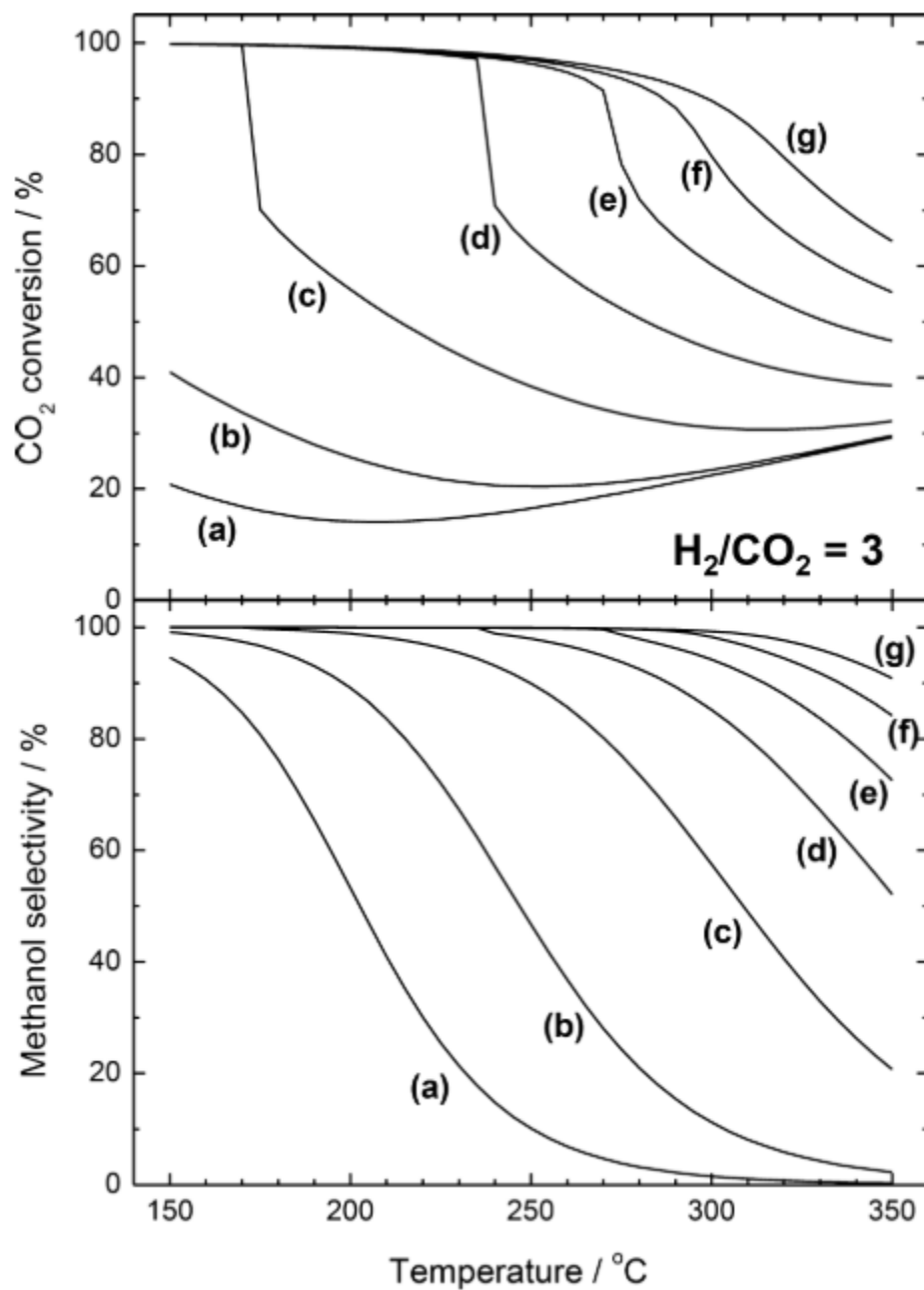


Figure 1.4 Equilibrium CO₂ conversion and methanol selectivity at different temperatures with initial H₂/CO₂ = 3 and at (a) 10 bar, (b) 30 bar, (c) 100 bar, (d) 200 bar, (e) 300 bar, (f) 400 bar, and (g) 500 bar. This figure is reprinted with permission from ref. [31] (<https://pubs.acs.org/doi/abs/10.1021/acs.chemrev.6b00816>, further permissions related to the material excerpted should be directed to the ACS). Copyright © 2017 American Chemical Society.

Today, methanol is produced through heterogeneous catalysis using feed gases of CO, CO₂, and H₂ over a Cu/ZnO/Al₂O₃-based catalyst [16], developed by ICI about half-century ago. These catalysts allow to operate in milder reaction conditions (240–260 °C and 50–100 bar) and are currently the basis for almost all methanol synthesis processes [32]. Main companies such as Südchemie (now Clariant), Haldor-Topsøe, and BASF also commercialize methanol catalysts.

In the context of using renewable energy as the source of H₂, the first contemporary commercial CO₂ to methanol recycling plant is presently being operated in Iceland (also known as George Olah Renewable Methanol Plant) by the Carbon Recycling International (CRI) company [33]. The demonstration plant, with the initial annual capacity of 4500 m³ (10 tons/day) is based on the locally available, inexpensive geothermal energy sources. In 2015, after the expansion, the plant produced around 4000 tons/year and recycled ~5500 tons of CO₂ a year. CRI recently has started the design and construction of a new emissions-to-liquids demonstration plant geared towards producing methanol from captured carbon dioxide (MefCO₂), using surplus electricity from intermittent renewable energy. These examples stress the importance of the colocation of an inexpensive CO₂ source, and the local availability of inexpensive renewable electricity for hydrogen production for the process success.

The success of George Olah Renewable Methanol Plant is a good example of the so-called methanol economy proposed by Dr. Olah [34,35]. The produced methanol, called Vulcanol, is currently mixed with gasoline. Despite these advances, for direct CO₂ hydrogenation to methanol, the conventional Cu/Zn/Al₂O₃-based catalyst still has issues to be overcome, such as selectivity and stability, to obtain a more efficient process. The development of catalyst for direct CO₂ hydrogenation to

methanol is crucial to facilitate the growth and market penetration of a methanol economy (which methanol is used as fuel or source of H₂) and a sustainable cycle of CO₂ utilization. Below, recent advances and challenges of methanol synthesis from CO₂ hydrogenation are briefly introduced.

1.3.2 Recent advances in hydrogenation of CO₂ to methanol

CO₂ hydrogenation to methanol, due to thermodynamics, should be run at the lowest practical temperature to facilitate high conversion. Use of an effective catalyst becomes essential. The typical composition of the commercial Cu/Zn/Al₂O₃ (CZA) catalyst is 50–70 atomic% CuO, 20–50% ZnO, and 5–20% Al₂O₃. The commercialized form of CZA catalyst is 4–6 mm cylindrical pellets with specific surface area of 60–100 m²/g [32]. Activation with dilute hydrogen is needed before the reaction. CZA catalysts typically have low selectivity (around 40% to methanol)—because of the competing reverse WGS reaction—and limited stability, due to sintering of the active phase (Cu) under reaction conditions. Due to the complex nature of reaction network in CO₂ hydrogenation, various products such as CO, hydrocarbons, methanol, and higher alcohols, can be formed. The low selectivity can make the separation of products very expensive in practical applications. The lifetimes of CZA catalyst are about 2 years, with one-third of the total activity loss occurring during the first 1,000 h of operation [32]. Similar to the commercial CZA catalyst, Cu-based materials are common choices for MeOH synthesis from CO₂. Among the Cu-based materials investigated, only a few catalysts such as LaCr_{0.5}Cu_{0.5}O₃ [36], Cu-Ga/ZnO [37], and Cu@ZnO (core-shell) [38] exhibit high selectivity to methanol (88–100%); the long-term stability and scalability of these materials, however, have not been evaluated.

Promoters have also been considered to enhance the catalytic performance for converting CO₂ to methanol. Potassium on Cu/Al₂O₃ stabilize surface intermediates and enhance formate dissociation [39]. Enhanced reducibility of the Cu surface of the Ba promoted catalyst was identified to favor the formates formation on the surface and further hydrogenation to methanol [39]. Lanthanum promoters on Cu/ZrO₂ facilitates formate hydrogenation to methanol and inhibits its dissociation into CO, and thus increases the selectivity [40]. Other investigations have attempted to identify new catalyst formulations (such as Cu/CeO₂ [17], Pd/Ga₂O₃ [41], Pd/CeO₂ [42], and In₂O₃ [43] showing promising catalytic activity for CO₂ hydrogenation to methanol. In₂O₃-based catalysts, particularly, showed excellent selectivity and stability, as demonstrated by DFT model [44,45] and experimental test [43,46], are the main topic in Chapter 4 and are discussed in detail in this thesis.

1.3.3 Mechanism

Although the Cu-based catalysts have been used for decades, different reaction intermediates and reaction mechanism are still under debate [47]. Various hypotheses for identifying active sites and reaction mechanism are presented in multiple reports [48–53], regarding the intermediates and precursors of methanol formation. In 2012, a seminal report from Behrens *et al.* elucidated detailed elementary steps and the role of the multi-component catalyst material Cu/ZnO/Al₂O₃ in the hydrogenation of CO and CO₂ to methanol [16]. The active site consists of Cu steps decorated with Zn atoms, all stabilized by a series of well-defined bulk defects and surface species. The seemingly simple overall transformation of CO or CO₂ and H₂ to methanol passes through a series of bond cleavage and bond forming processes involving the intermediates HCOO, HCO, HCOOH, H₂COOH, H₂CO, and CH₃O on the catalyst surface.

Possible reaction pathways of CO₂ hydrogenation to CO, CH₃OH, and CH₄ are summarized in Figure 1.5 which includes RWGS +CO hydro pathway, direct C-O bond cleavage, and formate pathway. In CO₂ hydrogenation, multiple products can be formed, and many intermediates have been proposed and identified by in-situ methods such as in-situ FTIR, in-situ Raman spectroscopy, and AP-XPS.

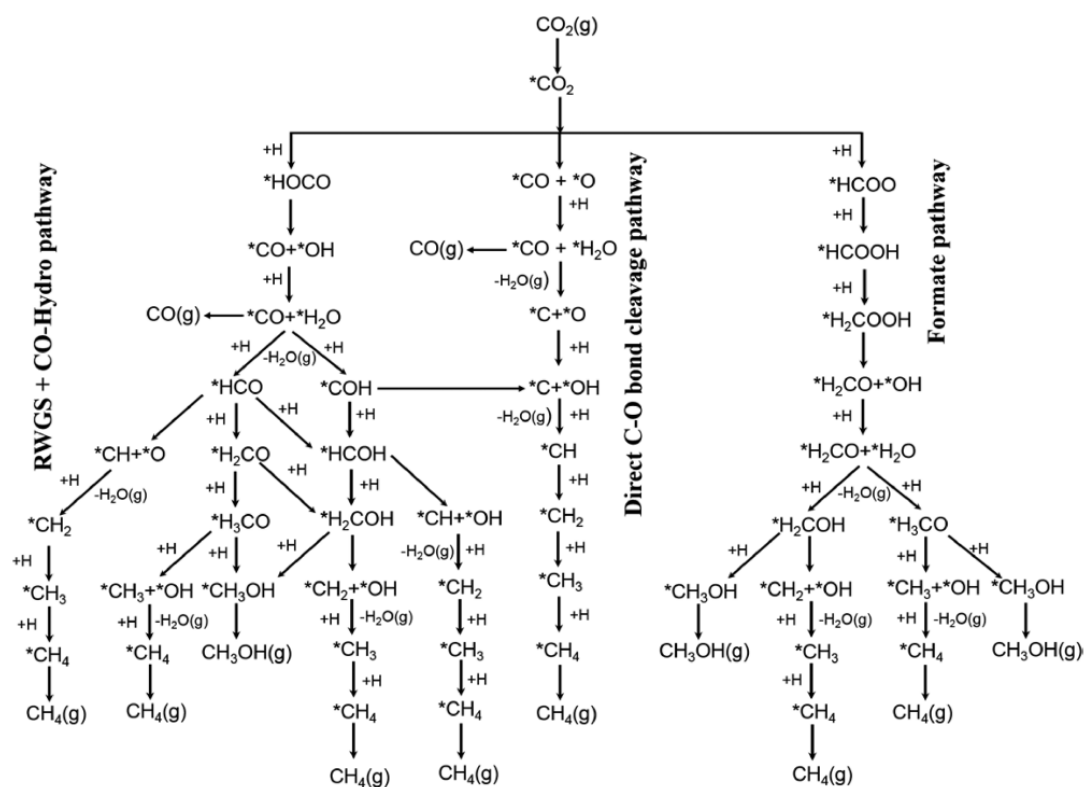


Figure 1.5 Possible reaction pathways of CO₂ hydrogenation to CO, CH₃OH, and CH₄. *(X) indicates adsorbed species [54] Reprinted with permission from S. Kattel, P. Liu, J.G. Chen, J. Am. Chem. Soc. 139 (2017) 9739–9754. Copyright © 2017 American Chemical Society.

Mechanistic studies are primarily focused on the CZA catalysts due to its extensive use in industry. A few investigations of the mechanism just started in other promising In_2O_3 catalyst. In 2018, Frei *et. al.* [55], following a previous report of highly selective indium oxide catalyst in 2016 by Martin *et. al.* [46], outlined two paths of CO_2 hydrogenation to methanol on In_2O_3 surface. It indicated that the most energetically favored path to methanol comprises three consecutive additions of hydrides and protons and features CH_2OOH and $\text{CH}_2(\text{OH})_2$ derived from HCOO (formate pathway) as intermediates. But more investigations are still need in In_2O_3 -base catalysts, including reproducibility, catalyst composition, and the effect of promoters to foster advances in potential large-scale methanol synthesis from CO_2 .

In summary, methanol economy is one of the possible solutions to the energy challenges that we face in the near future as it may be produced from renewable resources and has an energy density (15.6MJ/liter, compared with 33 MJ/liter for gasoline) that permits long-distance transport. Development and understanding of methanol synthesis directly from CO_2 are very active research fields. One of the main challenges is to make a more stable methanol synthesis catalyst to reduce thermal deactivation, and to make the reaction more selective to reduce the cost. As an abundant and renewable C1 feedstock, the catalytic conversion of CO_2 into methanol would be particularly important and thus deserves more attention in both research community and industrial application.

1.4 Scope of Dissertation

This thesis focuses on the development of highly selective catalytic materials and pathways for CO_2 hydrogenation into value-added chemicals. In this dissertation, two CO_2 hydrogenation reactions were investigated: catalytic CO_2 to CO via reverse

water-gas shift (RWGS) reaction over magnetite-derived catalyst and direct conversion of CO₂ to methanol (CH₃OH) over indium oxide-based catalyst supported on zirconia (ZrO₂).

Chapter 2 introduces background information on catalyst preparation, the materials characterization techniques, analytical methods, and the reactor used to collect and analyze the data presented in this dissertation. Specifically, physical and chemical characterization techniques, spectroscopic techniques, and an experimental set-up for catalysts evaluation are described in the chapter. Detailed synthesis processes and experimental design for certain experiments can be found in Chapter 3-5.

Chapter 3 presents my investigation of the RWGS reaction over unsupported catalyst derived from magnetite. As Fe-oxides are commonly used as catalysts in Fischer-Tropsch (FT) process, our results demonstrate highly selective (>99%), stable, and efficient iron oxide-derived catalysts in RWGS reaction to produce CO from CO₂ at temperatures between 723 K and 773 K under 1 atm. Gas-switching experiment suggests the redox mechanism is the dominant reaction pathway. I show that the catalyst was first reduced to metallic iron and remained partially oxidized during the reaction under CO₂/H₂ gas flow.

Chapter 4 presents the catalyst development of direct conversion of CO₂ to methanol. Catalytic behavior regarding reaction rate, CO₂ conversion, methanol selectivity on In₂O₃-based catalyst supported on ZrO₂. Two promoters, yttrium (Y) and lanthanum (La) were incorporated into the catalyst composition to make the catalyst less reducible. Subsequently, highly selective Y-In/ZrO₂ and La-In/ZrO₂ were investigated in more detail. The methanol selectivity can be tuned up to ~100% at

528K and 40 bar compared with the conventional CZA catalyst (~30-40% in selectivity). Reaction kinetics and potential mechanism of the Y-promoted $\text{In}_2\text{O}_3/\text{ZrO}_2$ catalyst were also studied.

Chapter 5 presents a novel catalyst composition for direct CO_2 hydrogenation to methanol with cobalt (Co) and indium mixed metal oxides at the temperatures between 528 K and 573 K and at 40 bar. The Co-In mixed oxide supported on ZrO_2 was synthesized by co-impregnation of cobalt nitrate and indium nitrate on zirconium oxide. The catalyst with Co:In = 2:1 molar ratio ($2\text{Co}-1\text{In}/\text{ZrO}_2$) showed impressive methanol selectivity of more than 99% between 528 K to 558 K. The stability of the catalyst was evaluated over 40h on the stream. No significant deactivation was found at the temperature of 528K, demonstrating a highly promising catalyst for methanol synthesis.

Chapter 6 describes the simulation of methanol synthesis process via Aspen Plus. The aim is to further compare the effect of catalysts with different selectivity, highlighting the impact of selective catalyst on the energy consumption and subsequently, the direct costs of manufacture. Two catalysts were compared: the standard CZA catalyst with 12% of CO_2 conversion and 35% of selectivity and the La-promoted catalyst ($3\text{La}10\text{In}/\text{ZrO}_2$) with 5% of CO_2 conversion and 90% of methanol selectivity. The energy consumption of the promoted catalyst was one third of the conventional CZA catalyst.

Chapter 7 concludes the thesis with an overview of the major findings and accomplishments. In addition, several proposed suggestions for future research are presented on topics related to this thesis work. Proposed fields of research that are

discussed focus on the potential development of catalyst in CO₂ hydrogenation to methanol or further conversion to gasoline, in order to foster the methanol economy.

Chapter 2

EXPERIMENTAL METHODS

This chapter describes experimental methods used throughout the thesis, and essential information to understand and interpret the characterization techniques used in this dissertation. The chapter starts with the methods of synthesizing metal oxide catalyst, followed with the design of flow reactor. The techniques described include temperature-programmed reduction/oxidation/desorption, spectroscopic methods, and the data collection and analyses. The detailed materials synthesis procedures and the characterization experiments can be found in the specific chapters where the materials are prepared.

2.1 Catalyst Synthesis

2.1.1 Wet impregnation

According to a technical report [56] of International Union of Pure and Applied Chemistry, impregnation consists in contacting a solid with a liquid containing the components to be deposited on the surface of the solid. During impregnation numerous processes take place with different rates. In the present dissertation, most catalysts were synthesized following the, so-called, wet impregnation method. An example illustrating this process is shown in Figure 2.1. Typically, a metal precursor (in our example, $\text{In}(\text{NO}_3)_3$) is firstly dissolved in a solvent such as ethanol or DI water. Then the catalyst support (ZrO_2) is added into the solution. If there are more than one metal precursor (such as $\text{Y}(\text{NO}_3)_3$ or $\text{La}(\text{NO}_3)_3$) in

the solution, it is designated co-impregnation. The mixture is then dried or evaporated at given temperature and is then calcined under a specific gas composition. For metal oxide catalysts, the calcination is usually carried out in air and the temperature is chosen to fully oxidize the metal precursor to its oxide form. Before reaction, the catalyst usually needs to be pre-treated either to reduce the metal or produce active sites that are beneficial for the reaction.

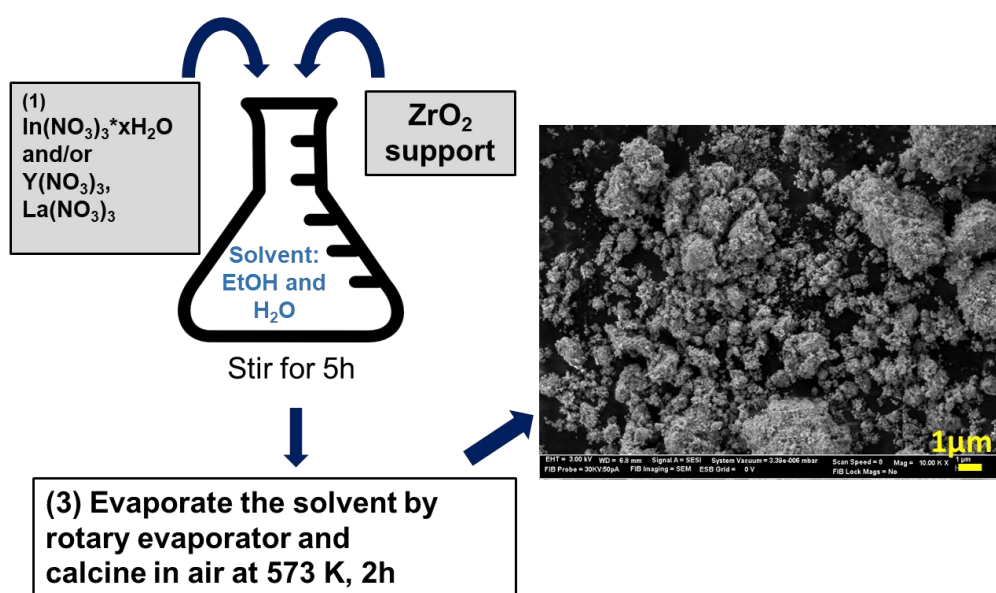


Figure 2.1 Illustration of wet impregnation method in synthesizing $\text{In}_2\text{O}_3/\text{ZrO}_2$ catalyst used in direct conversion of CO_2 to methanol.

2.1.2 Dry Impregnation

Another way to prepare catalysts by impregnation that is widely used in literature is the dry impregnation method. Here, first, the active metal precursor is dissolved in an aqueous or organic solution. Then the metal-containing solution is added to a catalyst support which contains the same total pore volume as the volume of the solution that was added. The mixture is then dried to evaporate the volatile solvent, depositing the metal precursor on the surface of the support material. The method is limited by the solubility of the precursor in the solution. After drying the catalyst is then calcined at the desired temperature. This procedure is also called incipient wetness impregnation (IWI) when the volume of the metal-containing solutions is empirically determined, and the catalyst begins to look wet.

2.1.3 Co-precipitation method

This method is a common way to synthesize nanoparticles. In general, it consists of the precipitation of cation solutions and anion solutions. The precipitate, or slurry, then goes through the so-called nucleation and growth stage. The reaction conditions are carefully controlled by temperature, pH values, aging time, and concentration. After the filtration and calcination, the as-prepared metal oxides can be used as catalyst. This method is used in Chapter 4 for synthesis of the conventional Cu/Zn/Al₂O₃ catalyst used in methanol production as the benchmark of the new In₂O₃/ZrO₂ catalysts.

2.2 Characterization Techniques and Spectroscopies

The following sections summarize critical information to understand the value of the various characterization techniques used in this thesis.

2.2.1 Powder X-ray Diffraction (XRD)

Powder X-ray Diffraction is used in determining the atomic structure of the crystalline materials. It is a technique that can identify the crystalline phases and quantify their unit cell dimensions in a particular sample. Bragg demonstrated in 1912 that the constructive interference from a set of consecutive parallel planes can only occur for certain angles θ , and that angle θ is related to the X-ray wavelength and the interplanar spacing of the material (Figure 2.2). This relation can be written as Bragg's law (Eq. 2.1). Note that the fraction of the X-ray photons that is not scattered passes through to the next layer of atoms, where another portion of the X-rays is scattered.

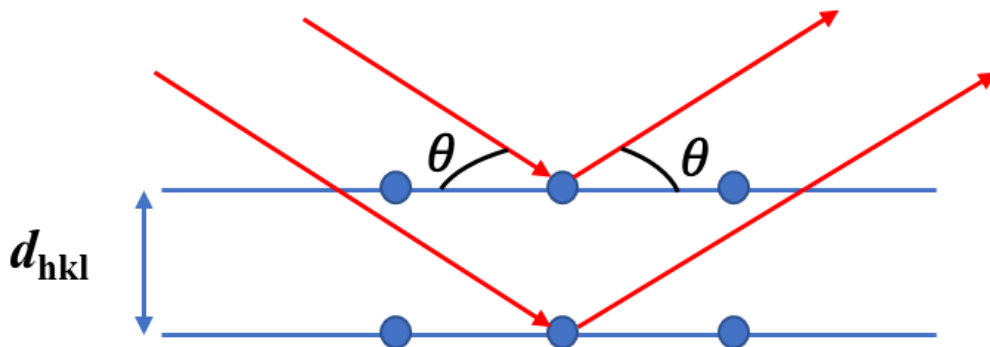


Figure 2.2 Illustration of the beams diffracted by two different layers.

$$2d_{hkl}\sin\theta = n\lambda \quad (\text{Eq. 2.1})$$

where θ is the angle of incidence of the X-ray, n is an integer, λ is the wavelength, and d_{hkl} is the spacing between atomic layers. The typical wavelengths selected for XRD will be in the range of 0.1 Å to 25 Å in order to be on the same scale

as the distance between atomic planes in the sample (d_{hkl}). XRD was extensively used in this thesis to characterize the structure of the catalysts in this thesis. For example, the crystalline phases of iron oxides phases before and after the RWGS reaction were obtained through XRD (Chapter 3). To understand if the Y and La promoters form isolated crystallites in the catalysts, XRD spectra of unpromoted $\text{In}_2\text{O}_3/\text{ZrO}_2$ and promoted $\text{In}_2\text{O}_3/\text{ZrO}_2$ catalysts were obtained and compared (Chapter 4). The new bimetal oxide catalyst, Co-In/ZrO₂, was characterized and cobalt oxide crystallite was identified in the bulk structure.

2.2.2 X-ray Photoelectron Spectroscopy (XPS)

XPS is a surface-sensitive technique (<~10 nm of the surface) useful to quantify the surface composition, chemical state, and electronic state of the elements in the material. The principle of XPS is originated from the photoelectric effect proposed by Einstein and the photoemission used as an analytical tool was proposed by Kai Siegbahn [57]. In brief, when an atom or molecule absorbs a photon, an electron can be ejected. The kinetic energy (K.E.) of the ejected electron depends upon the photon energy ($h\nu$) and the binding energy (B.E.) of the electron, i.e., the energy required to remove the electron from the surface. XPS is a quantitative technique in the sense that the number of electrons recorded for a given transition is proportional to the number of atoms at the surface. A relation between $h\nu$, K.E., and B.E. can be expressed as Eq. 2.2:

$$h\nu = \text{K. E.} + \text{B. E.} + \phi \quad (\text{Eq. 2.2})$$

where ϕ is a work function of specimen, in the case of a solid. The value of binding energy and chemical shift (difference from the elemental state) are utilized for

identification of an element and estimation of its chemical bonding state in the specimen [58].

A few handbooks and database are recommended to familiarize the technique and peak fitting, such as CasaXPS: 2.3.15 Introduction to XPS and AES, NIST X-ray Photoelectron Spectroscopy Database. There are two software packages that are used for fitting XPS spectra in this thesis. One is *CasaXPS*, which numerous universities in the world, including University of Delaware, are holding site academic licenses for it. The other software package is *Avantage*TM, from *Thermo Scientific*TM, which comes with the instrument from Thermo Scientific. Both packages can be used for peak deconvolution, but *Avantage*TM is recommended if the data is acquired from Thermo Scientific instrument. It offers more customized options when it comes to data analysis, and the user interface is friendlier. For example, the background function of a XPS spectra in CasaXPS can be Shirley, Tougaard, and Linear, whereas *Avantage* gives more options in background deduction including their own “Smart” function. The copy-paste function from spectra to excel spreadsheet in *Avantage*TM also makes the analyses easier. XPS spectra were obtained to analyze the surface composition in Chapter 3 for iron oxide catalysts, and chapter 4 and 5 for surface composition of indium-based catalysts and for identifying the oxygen near defects. XPS is a powerful technique that reveals a lot of information on the surface; however, there are some weaknesses. The fitting of the spectra sometimes can be tricky when the peak is not prominent or when the signal to noise ratio is low, leading to an erroneous result. Researchers must be cautious (e.g., applying the constraint of the fitting in FWHM or peak locations) and apply chemistry knowledge on peak-fitting. Ex-situ XPS also encounters the effects of exposure to the atmosphere during the sample transportation.

2.2.3 Scanning Electron Microscopy (SEM) and Energy Dispersive X-ray (EDX) Spectroscopy

The scanning electron microscope (SEM) allows for the morphology of solid materials to be observed and characterized at the nanoscale. SEM technique commonly offers the image on the nanometer (nm) to micrometer (μm) scale. Topographical images in a SEM are formed from back-scattered primary or low-energy secondary electrons. With non-crystalline catalysts, SEM is especially useful for examining the distribution and sizes of mesopores. To obtain images that are representative, more than one spot of the sample should be checked and acquired in several magnifications.

SEM can be coupled by X-ray analysis, a technique known as SEM with energy dispersive X-ray spectroscopy (EDX). In general, X-rays are emitted from the sample during the bombardment with the electron beam and can be measured by an energy-dispersive spectrometer. Quantitative elemental composition can be obtained in EDX because X-ray energies are characteristic of specific atoms. However, the accuracy is not very high. During the analysis, one should be careful to check if the characteristic peaks of the element in the dispersive spectra overlap with each other to prevent from the erroneous report. EDX is usually known as semi-quantitative analysis in chemical composition and should be used as supportive information for the elements. EDX was used to confirm that the metal precursor could be found in the catalyst and also to compare with the nominal metallic concentration of the catalyst (The analyses are shown in Chapter 4 for the identification of Y and La in indium oxide and Chapter 5 for the identification of both cobalt and indium in the catalysts).

2.2.4 Temperature-programmed Reduction/Oxidation/Desorption (TPR/TPO/TPD)

TPR and TPO are techniques for catalyst characterization. TPR and TPO mainly give information about the degree of reduction or oxidation of active sites in heterogeneous catalysts. The apparatus consists of a reactor with temperature controller, gas mass flow controllers to provide a mixture of gases of a given reducing gas (or oxidizing gas for TPO) and a carrier gas, and a TCD (thermal conductivity detector) or mass spectrometer to detect the gas flow composition after the reaction.

The TPR procedure involves reduction of the catalyst in a reducing gas mixture of known concentration; the temperature is raised linearly at certain ramping rate while monitoring the reduction. Hydrogen consumption is measured by TCD, which can be calibrated by the reduction of pure metal oxides (*e.g.* Fe₂O₃, Co₃O₄, CuO, NiO) [59]. Oxygen consumption can be calibrated by the oxidation of pure metallic Co. Molecular sieves are used to avoid interference of the measured signal with water, which is normally formed by metal reduction and precursor decomposition. The TPO procedure is similar to the procedure for TPR, but instead of using a reducing agent, an oxidizing agent, such as O₂, is applied in the gas mixture. Heat pretreatment is generally used before conducting the reduction or oxidation to remove the surface contamination and water vapor in the pores of the catalyst. Typical TPR profiles of iron oxides [60] are shown in

Figure 2.3, demonstrating that TPR illustrates different reducibility of various iron oxides. The TPR profile obtained from mass spectrometry is also presented below in Figure 2.4 to demonstrate the H₂ consumption percentage from total H₂ flow.

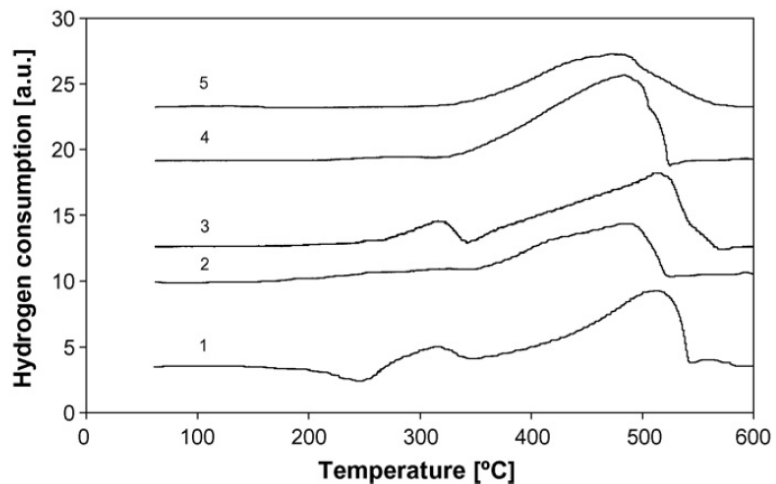


Figure 2.3 TPR_{H₂} profiles for: (1) goethite; (2) ferrihydrite; (3) hematite; (4) magnetite; (5) wustite; heating rate 1.07°C/min [60] Reprinted and modified with permission from W.K. Jozwiak, E. Kaczmarek, T.P. Maniecki, W. Ignaczak, W. Maniukiewicz, *Appl. Catal. A Gen.* 326 (2007) 17–27. Copyright © 2007 Elsevier.

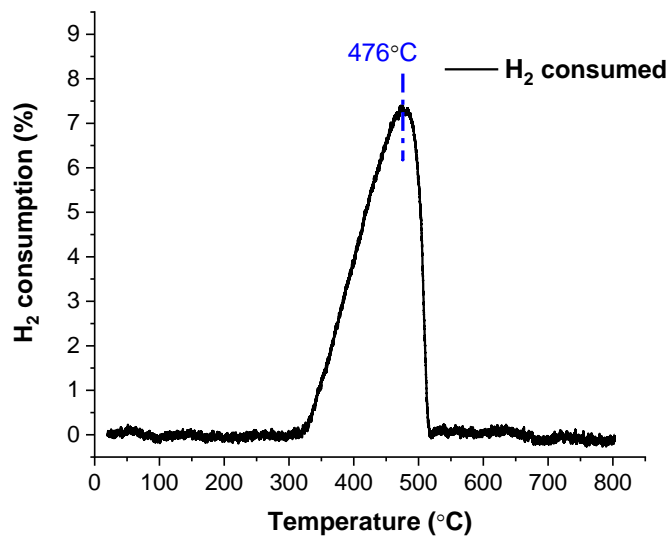


Figure 2.4 TPR_{H₂} profiles obtained by mass spectrometer for fresh magnetite (reduction conditions: Fe₃O₄ 50mg; F_{tot} = 64 sccm; ramped from room temperature to 800 °C with 17.4% H₂ and He mixture gas; total molar flow rate of H₂ = 4.91x10⁻⁴ mol/min)

Analysis of the TPD traces provides a wealth of information including number of adsorption sites, the degree of dispersion, surface desorption temperature, rate of desorption, kinetic order of desorption, and the energy of desorption. During TPD, the pre-treated sample reacts in an environment of increasing temperature with constant ramping rate, while it is purged by an inert gas such as helium, argon or nitrogen. The sample surface desorbs the gas that has been previously chemisorbed, and a TCD or mass spectrometer monitors the process. The Langmuir adsorption model may be used as well for the TPD spectra interpretation as it describes both gas adsorption and desorption in the two cases of associative and dissociative adsorption [61].

Typically, TPD runs with a linear heating ramp, and in this case the temperature profile can be written as

$$T(t) = T_0 + \beta t \quad (\text{Eq. 2.3})$$

where T = temperature, β = heating rate, t = time

The rate of desorption can be written as follows.

$$-\frac{d\theta}{dt} = k_d \theta^m \quad (\text{Eq. 2.4})$$

where θ = surface coverage, k_d = desorption rate constant, and m = desorption order

Applying a linear ramping rate, $\beta = \frac{dT}{dt}$ gives the equation

$$-\frac{d\theta}{dT} = \frac{k_d}{\beta} \theta^m \quad (\text{Eq. 2.5})$$

If the adsorption is an activated process, it obeys the Arrhenius equation, and we can plug k_d from the Arrhenius equation, which gives the Polanyi-Wigner equation [62].

$$-\frac{d\theta}{dT} = \frac{A}{\beta} \theta^m \exp\left(\frac{-E_d}{RT}\right) \quad (\text{Eq. 2.6})$$

With the Polanyi-Wigner equation, one can determine the desorption order by fitting the experimental data to the different orders of the desorption profiles.

TPD is a technique that provides much useful information, but it has a number of limitations. First, TPD is destructive on samples; secondly, there is no way to “see” what is on the surface but just what comes off the surface. In addition, the binding sites, structures, and absolute coverage cannot be identified by TPD itself.

2.3 Catalyst Evaluation and Kinetic Studies

The catalyst evaluation including CO₂ conversion, product selectivity, and kinetic studies, were conducted by setting up a in-house built, packed-bed microreactor flow system connected with online chromatography or mass spectrometry.

2.3.1 Flow-reactor Setup for Catalysts Evaluation

An example of the reactor system configuration used in this thesis is presented in Figure 2.5. In this specific case, this setup was designed for high pressure CO₂ hydrogenation to methanol (Chapter 4).

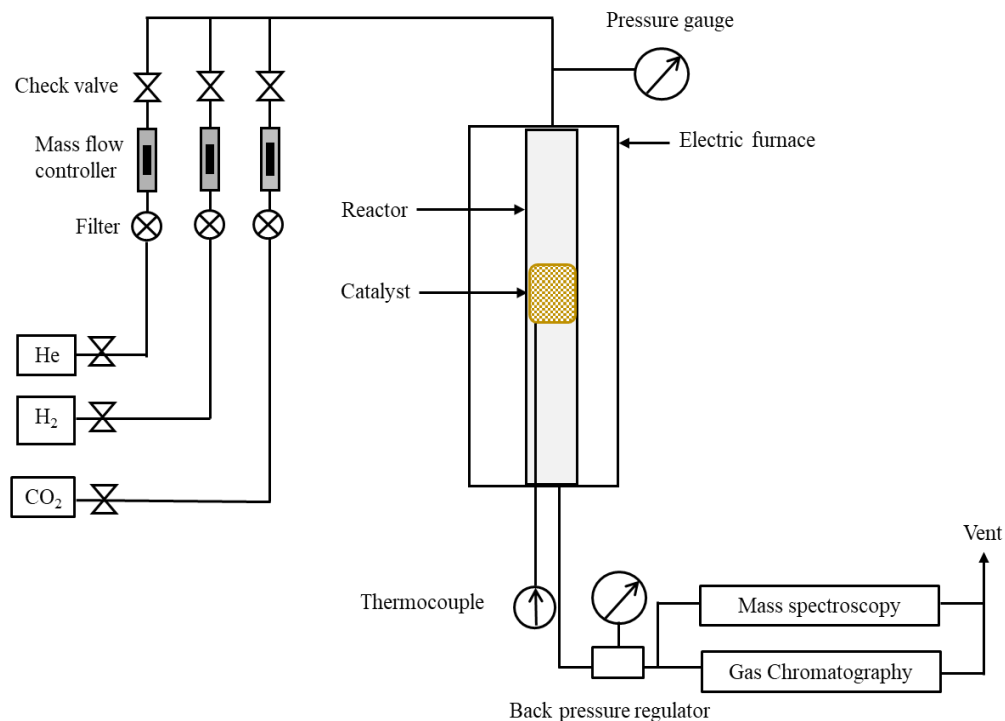


Figure 2.5 Process flow diagram of the experimental setup used for high pressure experiments

Another setup for RWGS reaction under atmospheric pressure (Chapter 3) is similar to the system shown in Figure 2.5. The key difference is that instead of using stainless-steel reactor, a quartz tube reactor was used instead. The system had no backpressure regulator neither. Multiple gases can be fed into the vertically-positioned flow reactor, while the catalyst is supported between two layers of quartz wools inside the reactor tube. The reactor was heated by a tubular furnace connected with a PID controller, and all the heated parts were controlled at the same temperature to ensure an isothermal condition. A pressure relief valve was installed to prevent the system from over pressurization. Finally, the products are collected and analyzed with an

online GC equipped with TCD and/or FID. The sealing, safety, and thermodynamics of the high-pressure reactor system need extra consideration to achieve a safe and reliable evaluation of catalysts. For example, before the construction of the system, strength and chemical compatibility of the materials must be reviewed according to the reactants and potential products. The thermodynamics of the reaction were investigated as well. To avoid methanol product condensation, all lines should be heated at least to 423 K under high pressure. The leak test and maintenance of fitting parts and filters should be done regularly. All the operation involving gas feed must always be in the hood with hazardous gas detector.

2.3.2 Chromatography and Mass Spectrometry

Chromatography is an analytical technique used to separate and quantify chemical compounds in a gas or liquid sample, or in a feed stream if equipped with an on-line sampling device. In the experimental setup I used in this thesis, the feed stream is the effluent of the reactor and a gas chromatograph (GC) is used for analysis. Two types of GC instruments were used in this thesis. One is the Agilent 7890A (chapter 3), the other is Agilent MicroGC490 (Chapter 4). Both GC serve the same purpose but 7890A was equipped with both TCD and FID, while MicroGC490, equipped with several TCDs, consists of three different channels with different columns to separate permanent gas, hydrocarbons, and alcohols, respectively. The MicroGC is a compact module, which is portable, accurate, and fast in response time. Therefore, it is preferably used in the scenario that needs fast sampling (e.g. 1 point every 2 min). The disadvantage of MicroGC is that the built-in parts of the instrument are harder to replace, and it is very difficult to do it without sending it back to the factory. The software used to analyze the chromatograph were Chemstation (for 7890A) and

EZchrom (for MicroGC490) were provided by Agilent. The calibration of GCs was done by standard calibration gases obtained from Matheson and Sigma-Aldrich.

Mass spectrometry (MS) uses electrons to break apart molecules and measures mass to charge ratios of the fragments formed. Hard ionization causes extensive fragmentation of the parent molecule. The resulting fragmentation pattern can be compared with the database (NIST) for identification of the parent molecules. It has several modes of operation. One can specify, for example, certain range of m/z to screen for possible molecules in the effluent. The change in concentration of known molecules in the effluent can also be monitored by selecting various m/z ratios. Mass spectrometry is commonly paired with gas chromatography, where GC provides separation and quantification and MS provides identification of the compound. In the evaluation of catalytic performance, GC is normally the major way to quantify the concentrations of products, e.g. methanol and CO, in effluent in this thesis (see Chapter 3-5) The selectivity can thus be determined by the product distribution and CO₂ conversion can be obtained by calculating the change of CO₂ concentration during the reaction.

This chapter summarizes the experimental methods and the important techniques used in this thesis. In the following chapters from chapter 3 to chapter 5, we present the catalyst development and evaluation for CO₂ hydrogenation into CO or methanol, along with some discussions about the reaction pathways.

Chapter 3

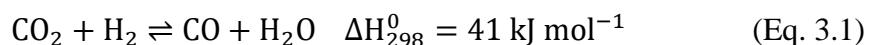
REVERSE WATER-GAS SHIFT IRON CATALYST DERIVED FROM MAGNETITE

3.1 Introduction

Today's anthropogenic emissions of carbon dioxide to the atmosphere amount to about 35,000 Tg per year and the greenhouse effect of these accumulated emissions has been recognized as an alarming hazard to the well-being of modern societies. Although multiple approaches have been considered to mitigate these emissions, recently more emphasis has been placed on the potential synergy of carbon capture and utilization of these large outflows of carbon dioxide. Among several possibilities, a recent National Academies of Science and Engineering report [1] on CO₂ waste gas utilization highlights the conversion of CO₂ by hydrogenation into CO and water — the reverse water-gas shift (RWGS) reaction (Eq 3.1) — as critical and points to the need for improved catalysts with high stability and durability.

The RWGS reaction can be part of a two-step hydrogenation process for the conversion of CO₂ to valuable products. First, CO₂ is reduced to CO via the RWGS reaction and second CO can be converted to either hydrocarbons via the Fischer-Tropsch (FT) process or methanol via CAMERE (CARbon dioxide hydrogenation to form MEthanol via a REverse WGS reaction) process [25]. The RWGS reaction is an

endothermic reaction ($\Delta H^{\circ}_{298\text{ K}} = 41.2\text{ kJ mol}^{-1}$) and thus is thermodynamically favorable at higher temperatures.



Noble metals such as Pt [63–65] and Pd [66,67], and other various metals such as Cu [68–71], Ni [8,72], and Fe [73] supported on oxides were reported to be active to the production of CO. Among them, Cu-based materials have been widely studied, and thus have also been investigated in many instances for the RWGS reaction. For example, Cu-Ni/Al₂O₃ [74], Cu/ZnO [75], Cu-Zn/Al₂O₃[75], and Cu/SiO₂ promoted with potassium [76] have all shown good RWGS activity. However, Cu materials tend to deactivate by sintering at high temperatures ($T > 773\text{ K}$), which are required for high RWGS activity. For high temperature applications, iron can be added as a thermal stabilizer: Chen et al. [70] showed that adding small amounts of iron to 10% Cu/SiO₂ resulted in stable RWGS activity for 120 h at 873 K and atmospheric pressure, while non-promoted 10% Cu/SiO₂ deactivated rapidly.

Iron oxides (Fe_xO_y) are often used industrially for FT synthesis (473 K-623 K, 1 MPa) [77,78] and high-temperature (623 K- 723 K) WGS reaction [23,79,80]. In FT synthesis, alkalized iron-based catalysts are combined with Cu for reduction promotion. Schulz *et. al.*[77] [81] showed that the working FT catalysts contain several iron carbide phases and elemental carbon formed after the hydrogen reduction period. Iron oxides and the metallic iron are still present in the catalyst composition, but iron carbide phases are identified as active sites [81]. The RWGS and WGS reactions are often carried out in conjunction with FT synthesis at higher temperature

regime on iron catalysts, and iron oxide or oxidic amorphous iron phases is known as the active phase for WGS and RWGS [82][22][83].

Extensive research on iron-based catalysts has been reported mainly on the WGS reaction over decades[23]. Chromium is a structural promoter that helps prevent the iron from sintering at high temperature. A more recent survey on Cr-free Fe-based WGS catalysts shows the current strong interest in this topic [21]. However, the studies on RWGS reaction over iron-based catalysts are much less frequent. Fishman *et. al.* [84] synthesized hematite nanosheets to obtain 28% CO₂ conversion at 783 K, and hematite nanowires to obtain 50% CO₂ conversion at a very high temperature of 1023 K. Hematite was reduced to magnetite during the reaction. The catalytic behavior over time on stream and the stability of the CO production were however, not investigated. Fe nanoparticles have also shown good stability and activity (35% CO₂ conversion, >85% CO selectivity) in RWGS by Kim *et. al.* [85], yet no kinetic parameters were determined and the mechanism was not discussed.

Two principal mechanisms of the WGS (or RWGS) reaction have been investigated extensively: the “redox mechanism” and the “associative” mechanism [47,86]. Different catalysts may lead to different reaction pathway. The redox mechanism was suggested to be active for the WGS reaction over iron catalysts promoted with chromium [87]. A distinguishing feature of the redox mechanism is that products can be generated in the absence of both reactants. The catalyst is first reduced by the adsorbed H₂ and is subsequently oxidized by CO₂ (in RWGS) or H₂O (in WGS). The associative mechanism was proposed to be dominant in WGS reaction over iron oxide catalysts [88]. In this mechanism, both reactants are adsorbed on the catalyst surface at the same time to create products. Several carbon-containing

intermediates, including formate, carbonate, carbonyl, and carboxyl species, have been proposed. In a previous report in alumina-supported iron catalysts [73] we showed that, the redox mechanism is the only pathway for RWGS over Fe/ γ -Al₂O₃, and the predominant pathway over Fe-K/ γ -Al₂O₃. The addition of the potassium promoter activates a secondary pathway for CO formation, which is probably the associative pathway.

In the present report, unsupported Fe₃O₄-derived catalyst is identified as a highly active, selective, and stable catalyst for the reverse water-gas shift reaction at temperatures between 723 K and 753 K. The characterization of surface composition, bulk properties, and the evaluation of CO production specific rate showed that the working catalyst is constructed during the H₂-activation and the period of reaction conditions. Quantitative gas-switching experiments in combination with isotopic switching experiments allowed the redox and associative reaction pathway to be differentiated. The catalysts appear to be highly stable under the reaction conditions investigated.

3.2 Materials and Methods

3.2.1 Materials

Magnetite (Fe₃O₄, Aldrich, 99.99%) was pressed and sieved to obtain particle sizes within the range of 250-425 μ m. Iron carbide (Fe₃C, American Element, 99.5%) was ball-milled, pressed, and sieved within the range of 250-425 μ m. The gases used were CO₂ (Keen, Grade 5.0), H₂ (Matheson, UHP), Helium (Keen, Grade 5.0), C¹⁸O₂ (Sigma-Aldrich, 95 atom% ¹⁸O), and D₂ (Cambridge Isotopes, 99.6% gas purity, 99.8% isotope purity).

3.2.2 Reactor setup for kinetics and gas-switching experiments

The reaction rates and other kinetic parameters were measured using a packed-bed microreactor operated in a down-flow mode at atmospheric pressure. The catalyst particles were supported on a plug of quartz wool within a 7 mm I.D. quartz tube reactor. The quartz tube was positioned inside an Omega, CRFC-26/120-A ceramic radiant full cylinder heater. The temperature was controlled by an Omega CN/74000 temperature controller using the input from a K-type, 1/16 in. diameter thermocouple (Omega) placed around the outside of the quartz tube at the center of the catalyst bed. Gas flows were controlled by mass flow controllers (Brooks Instruments) through the reactor or the other instruments. Gas transfer lines were heated to a temperature above 373 K at all times to avoid water condensation. The composition of the effluent stream was analyzed online by a gas chromatograph (GC, Agilent, 7890A) during continuous flow experiments or by a mass spectrometer (MS, Pfeiffer, GSD320) during gas-switching experiments or isotopic experiments. The GC was equipped with both a thermal conductivity detector (TCD) and a flame-ionization detector (FID). The TCD was used to quantify CO₂, CO, and H₂ concentrations while the FID was used to quantify hydrocarbon concentrations. An Agilent, 2 mm ID × 12 ft Hayesep Q column was used in the GC to separate products quantified with the TCD, and an Agilent, 0.32 mm ID × 30 m HP-Plot Q column was used to separate products quantified with the FID.

3.2.3 Catalyst Characterization

Temperature-programmed reduction (TPR) was performed by using a MS including the reduction period (773 K, P_{tot} = 1 bar, P_{H₂} = 15 kPa in He for 2h), and then the temperature was ramped up to 1073 K. The ramping rate of each step was 5 K

min⁻¹. Another TPR experiment was performed after the RWGS reaction (553K, P_{tot} = 1 bar, GHSV = 4.5×10⁴ cm³ h⁻¹ g_{cat.}⁻¹, P_{CO₂} = P_{H₂} = 15 kPa with He as an inert balance gas). The post-reaction sample was cooled down to room temperature in He flow inside the microreactor. The TPR was then continued in 15 kPa H₂ and 86.3 kPa He from room temperature to 1073 K at the rate of 5 K min⁻¹. The H₂ consumption was converted from the ion current (m/z = 2) after the calibration of the H₂ signal each time before the experiment using a mass spectrometer.

X-Ray Diffraction (XRD) patterns of catalyst powders were collected at room temperature on a Bruker diffractometer using Cu K α radiation ($\lambda = 1.5418 \text{ \AA}$). Measurements were taken over the range of $5^\circ < 2\theta < 70^\circ$ with a step size of 0.02° before and after the RWGS reaction. X-ray photoelectron spectroscopy (XPS) measurements were performed on a K-alpha Thermo Fisher Scientific spectrometer using monochromated Al K α X-ray source. The measurements of iron oxide samples (pre- and post-reaction) were done with a spot size of 50 μm at ambient temperature and a chamber pressure of $\sim 10^{-7}$ mbar. A flood gun was used for charge compensation. All the spectra measured were calibrated by setting the reference binding energy of carbon 1s at 284.8 eV. The spectra were analyzed by Avantage[®] commercial software. For the fitting, each component consists of a linear combination of Gaussian and Lorentzian product functions, and the full width at half maximum (FWHM) and differences in binding energy of the same species between the Fe2p_{3/2} and Fe2p_{1/2} scan were kept constant. SMART background in Avantage[®] was used over the region to define the peaks.

3.2.4 Measurement of product formation rates and reaction rates with gas-switching or isotopic experiments

Most of the procedures in the measurement of the reaction rates, gas-switching, or isotopic experiments are identical to the ones described in our previous report [89]. Fe₃O₄ samples were pretreated before all experiments in the by increasing the reactor temperature at a rate of 5 K min⁻¹ to 773 K under a gas flow of 15 kPa H₂. After the pretreatment at 773 K for 2 h, the temperature was lowered to the initial reaction temperature of 753K. During the measurement of the reaction rates, the partial pressures of the reactants were P_{CO2} = P_{H2} = 15 kPa. A constant total flow rate of 75 cm³ min⁻¹ (sccm) was maintained with He as an inert balance gas.

Gas hourly space velocity (GHSV) in cm³ h⁻¹ g_{cat.}⁻¹ was calculated according to the equation below:

$$GHSV = \frac{F_{tot}}{m_{cat.}} \quad (\text{Eq. 3.2})$$

where $m_{cat.}$ is the mass of the catalyst.

CO₂ and H₂ reaction orders were measured by independently varying the inlet CO₂ and H₂ partial pressures. The total pressure remained at 1 bar. The activation energy was estimated by using the Arrhenius plot with the temperature varied between 723K and 773K while monitoring the CO formation rate.

Rates of CO formation were calculated assuming differential reactor operation according to Eq. 3.3:

$$r_{CO} = \frac{\dot{V}\Delta C_{CO}}{m_{cat.}} \quad (\text{Eq. 3.3})$$

where \dot{V} is the total volumetric flow rate, ΔC_{CO} is the change in CO concentration. Measured reaction rates are the net rate of the forward and reverse reactions; therefore, the observed rate must be transformed into the reaction rate for the forward reaction by using Eq. 3.4, Eq. 3.5, and Eq. 3.6. The equilibrium constant (K_C) is low (< 1) for the RWGS at the temperatures investigated, although the reverse reaction had a negligible contribution to the observed rates because of the low conversion ($< 12\%$) under conditions at which the reactor was operated. Note that C_o (Eq. 3.6) represents the standard state (1 mol L^{-1}) and equals 1 since the reaction is equimolar.

$$r_{obs.} = r_+ - r_- = r_+(1 - \eta) \quad (\text{Eq. 3.4})$$

$$\eta = \frac{[CO][H_2O]}{K_C[CO_2][H_2]} \quad (\text{Eq. 3.5})$$

$$K_C = \left(\prod_i C_{i_{eq.}}^\nu \right) \frac{1}{C_o} \quad (\text{Eq. 3.6})$$

Experiments were also conducted to *i*) determine reaction rates in excess (i.e. non-equimolar) CO_2 or H_2 , and *ii*) determine apparent kinetic parameters. In the first case, CO_2 and H_2 were fed with the catalyst— Fe_3O_4 (100 mg)—held at a temperature of 753 K. The initial partial pressure of both CO_2 and H_2 was 15 kPa. After a period of 16 h, the partial pressure of CO_2 was increased to 60 kPa, while the partial pressure of H_2 was held at 15 kPa. After another period of 2 h, the partial pressure of CO_2 was decreased to 15 kPa and the partial pressure of H_2 was increased to 60 kPa. Finally, both partial pressures were returned to 15 kPa. CO_2 conversion was quantified under the same conditions.

For the second case, apparent kinetic parameters (activation energy and reaction orders) were determined with near equimolar concentrations of CO₂ and H₂ on Fe₃O₄, and under large H₂ excess on Fe₃O₄ as well. With near equimolar concentrations of CO₂ and H₂, the reaction was first performed for 15-16 h at a temperature of 753 K with reactant partial pressures of 15 kPa. The temperature was then lowered in 10 K increments to 723 K, with 5-6 GC injections (a period of about 60 min) taken at each temperature. After the period at 723 K, the CO₂ partial pressure was reduced to 10 kPa and increased in 2.5 kPa increments to a final partial pressure of 20 kPa. Finally, the CO₂ partial pressure was returned to 15 kPa and the H₂ partial pressure was lowered to 10 kPa and increased in 2.5 kPa increments. The basic outline of experiments conducted with excess H₂ was the same as that used for near equimolar reactant concentrations (see also our previous report) [89]. Reactant partial pressures during the initial period were 90 kPa H₂ and 10 kPa CO₂. During the variable CO₂ partial pressure period, the H₂ partial pressure was 85 kPa and the CO₂ partial pressure was varied between 5 and 12.5 kPa in 2.5 kPa increments. To investigate the effect of H₂ partial pressure, the CO₂ partial pressure was kept at 10 kPa and the H₂ partial pressure was varied between 70-90 kPa in 5 kPa increments.

The measurement of the CO formation rate over Fe₃C has been performed in two different manners. First, the temperature of 100 mg Fe₃C was ramped under a flow of H₂ (15 kPa) and He at the rate of 5 K min⁻¹ up to 753 K. 15 kPa CO₂ was then added into the flow while monitoring the CO formation rate. The second part of the Fe₃C activity test was done by ramping the temperature to 573 K, 623 K, 673 K, 723 K, and cooling back to 673 K again at the rate of 5 K min⁻¹ under the flow of H₂ (15

kPa), CO₂ (15 kPa), and He (remainder). Each temperature was held for 80 min respectively for GC injection.

Gas-switching experiments were done by measuring CO formation rates while alternating between CO₂ and H₂ gas flows. Catalysts were pretreated as described above, after pretreatment, CO₂ was added into the reactor to proceed RWGS reaction for 2 h. After the reaction, the gas flow rates were changed to 36 sccm helium and 4 sccm H₂. After 20 min, H₂ flow was stopped and was replaced by 4 sccm of CO₂. After 20 min, CO₂ in the gas stream was replaced by H₂. This CO₂→H₂ sequence was repeated three times. The reactor was then purged with helium for 20 min before CO₂ was readmitted to the gas stream. After 20 min, the reactor was again purged with helium before H₂ was readmitted to the gas stream. All sequences with a given gas composition lasted for 20 min, and the temperature of the reactor was 773 K throughout the duration of the gas switching portion of the experiment.

Additional gas-switching experiments involving purge times of varying length with an inert gas were carried out at 753 K. Following the same pretreatment and the reaction in 15 kPa H₂ and 15 kPa for 2 h at 773 K, 15 kPa H₂ was admitted to the reactor. After 15 min, H₂ was replaced by 15 kPa CO₂ for 15 min, and CO₂ was then replaced by H₂ for another 15 min. Then, the reactor was purged with helium for 5 min. This sequence (CO₂ → H₂ → He) was repeated several times, but each time the length of the inert purge was increased by 5 min.

An isotopic experiment for CO formation rate was monitored by MS on Fe₃O₄ (100 mg) while alternating between CO₂ (4 sccm) and C¹⁸O₂ (4 sccm) after the RWGS reaction for 2 h. The temperature was kept at 753 K. The total flow rate was 40 sccm with H₂ maintained at 4 sccm. The kinetic isotope effect (KIE) of H₂/D₂ was

investigated on Fe₃O₄ (100 mg) for various H₂:CO₂ ratio. After pretreatment, the reaction began at a temperature of 753 K with CO₂ and H₂ partial pressures of 15 kPa. After 16 h, the temperature was lowered to 723 K and, after 1.5 h, H₂ in the feed was replaced by D₂.

3.3 Results and Discussion

The catalytic CO formation rates on Fe₃O₄ catalyst with various H₂ to CO₂ ratios (Figure 3.1) show that after an induction period of ~120 min, the catalyst produced CO at a steady rate of 35.1 mmol h⁻¹ g_{cat.}⁻¹ at 753 K with 12.5% CO₂ conversion. The selectivity to CO was greater than 99% under equimolar CO₂ and H₂. After 950 min, the partial pressure of CO₂ was raised to 60 kPa while the partial pressure of H₂ was kept constant. The rate increased to 54.6 mmol h⁻¹ g_{cat.}⁻¹ with 4.4% CO₂ conversion. Deactivation also occurred during this period: starting at a deactivation rate of 3.71 mmol h⁻¹ g_{cat.}⁻¹ per h, this rate gradually decreased to 0.23 mmol h⁻¹ g_{cat.}⁻¹ per h. When the partial pressure of H₂ was 60 kPa and CO₂ was switched back to 15 kPa, CO formation rate increased first to 91.3 mmol h⁻¹ g_{cat.}⁻¹ and gradually stabilized to a value of 95.3 mmol h⁻¹ g_{cat.}⁻¹ with 33.7% CO₂ conversion. The final rate of the catalyst reactivation was about 0.50 mmol h⁻¹ g_{cat.}⁻¹ per h.

With a higher 60 kPa of H₂ and 15 kPa of CO₂ in the feed, small amount of CH₄ — the only side product—was produced at the rate of 1.35 mmol h⁻¹ g_{cat.}⁻¹, reducing the CO selectivity from near 100% to 98.6%. Methane production implies that C-H bond formation is facilitated at higher partial pressure of H₂. There was no further C-C chain growth under this reaction condition, indicating the FT synthesis was not active over the working catalyst. The effect of H₂ on CO formation rate was much higher than the effect of CO₂, implying a higher reaction order on H₂ than CO₂.

The catalyst showed, overall, high stability and the final reactivation rate in excess H₂ was higher than the deactivation rate under excess CO₂ condition; this result makes this Fe₃O₄ catalyst attractive.

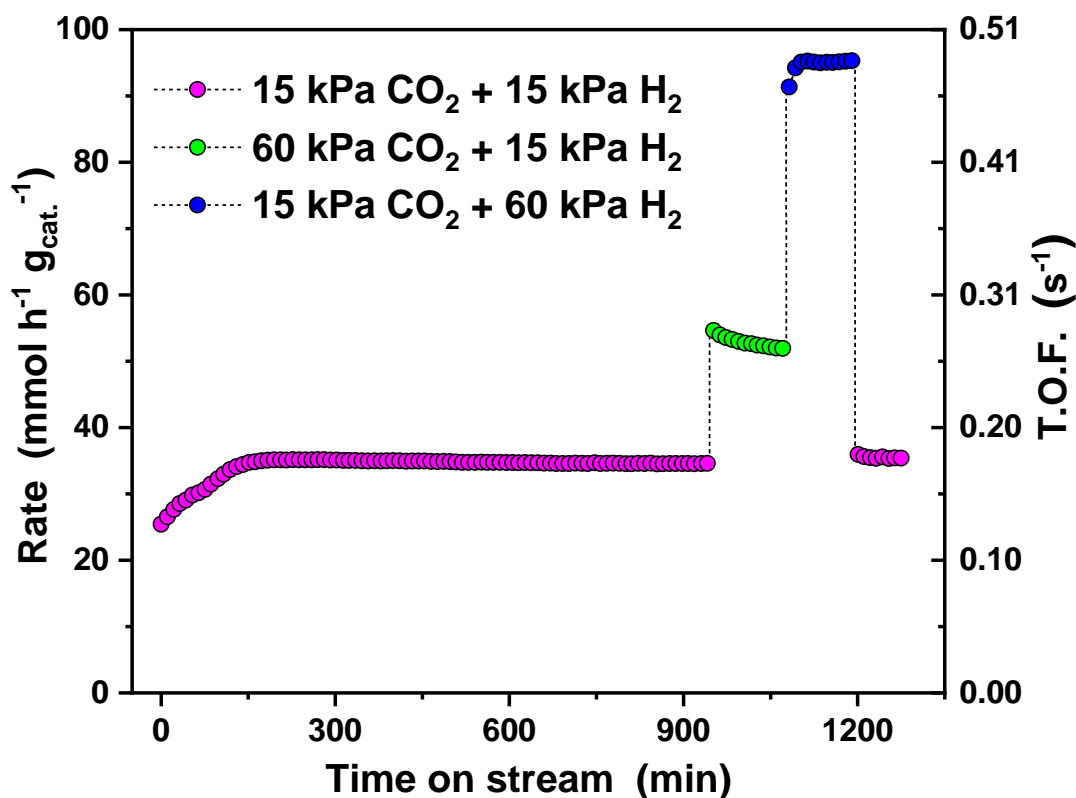


Figure 3.1 CO formation rates and their turnover frequencies (T.O.F.) on Fe₃O₄ at partial pressures of CO₂ and H₂ indicated in the legend. Other reaction conditions: P_{tot} = 1 bar, T = 753 K, F_{tot.} = 75 sccm, GHSV = 4.5×10⁴ cm³ h⁻¹ g_{cat.}⁻¹.

The activation of catalyst was done by a pretreatment under reducing conditions (H₂ gas). The bulk structure of the catalyst after the pretreatment can be identified. Based on the body-centered cubic (BCC) structure of α -Fe (JCPDS PDF 00-006-0696) after the pretreatment (Figure 3.2), the surface density of Fe atoms on

the Fe(110) surface can be calculated as 1.297×10^{19} Fe atoms m^{-2} . Assuming all Fe atoms on Fe(110) were active sites, the observed CO formation rates can be converted to turnover frequency (TOF). This is reported in Figure 3.1 based on the measured CO formation rates, atomic surface density, and BET surface area ($2.52 \text{ m}^2/\text{g}$ for Fe_3O_4) of the pristine catalyst. The turnover frequency of this catalyst under equimolar condition was as high as 0.18 s^{-1} ($P_{\text{tot}} = 1 \text{ bar}$, $T = 753 \text{ K}$, $F_{\text{tot.}} = 75 \text{ sccm}$, $\text{GHSV} = 4.5 \times 10^4 \text{ cm}^3 \text{ h}^{-1} \text{ g}_{\text{cat.}}^{-1}$).

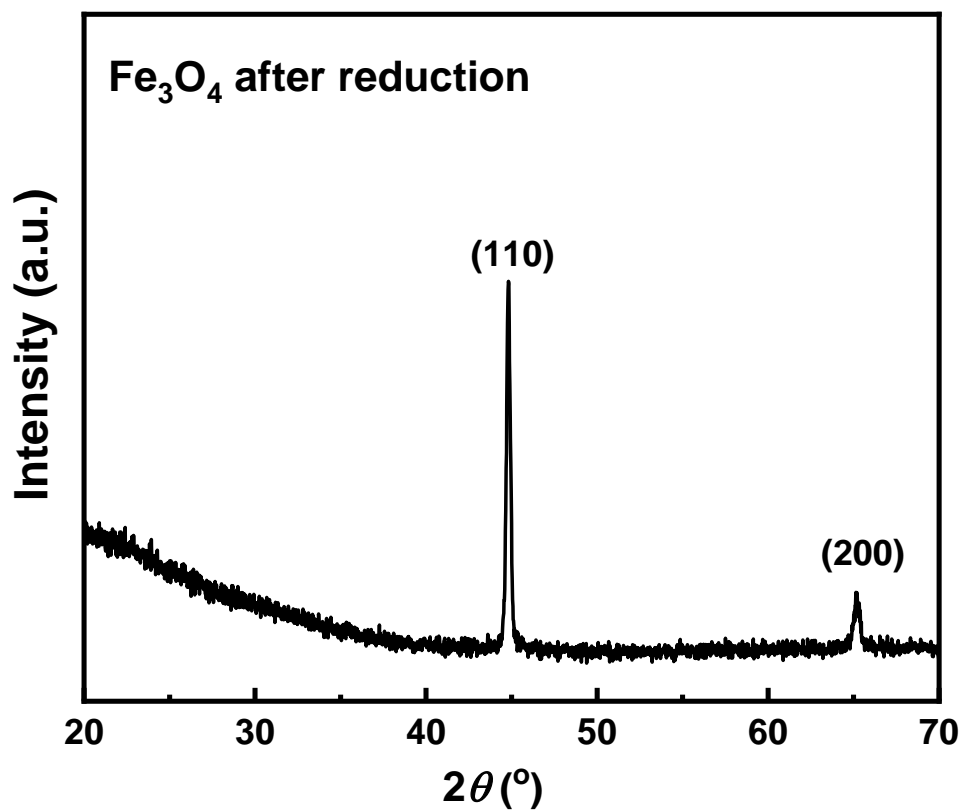


Figure 3.2 XRD pattern of Fe_3O_4 after the reduction in H_2 .

The stable reaction rates observed after the initial break-in period at 753 K allow for the determination of kinetic parameters without having to model deactivation profiles. The kinetic parameters including reaction orders with respect to CO₂ and H₂, and measured activation energies (E_{meas}) over Fe₃O₄ under near equimolar CO₂ and H₂ (~1:1), and in H₂ excess (2:1, 4:1, and 9:1)—see Table 3.1 — indicate that CO formation rates have a higher dependence on H₂ partial pressure (order of ~0.8) than CO₂ partial pressure (order of ~0.33) under equimolar composition. In general, rate orders depend on reaction conditions: increasing the H₂ partial pressure increased the order on CO₂ to 0.39 and decreased the rate order on H₂ to 0.72. At a ratio of H₂:CO₂ near 4:1 ratio, the reaction orders still showed the same trend: an increasing dependence on CO₂ (order of 0.43) and decreasing dependence on H₂ (order of 0.31). In a high excess of H₂ (H₂:CO₂ = ~9:1), the reaction rate over Fe₃O₄ was of order 1.30 with respect to CO₂ and was independent of H₂ pressure. The activation energies (E_{meas}) also depend on the H₂:CO₂ partial pressure ratios, that is, different reaction pathways may occur under these conditions. Similar reaction orders were also observed by Ginés et al.[90] in the same regime of $\frac{P_{\text{H}_2}}{P_{\text{CO}_2}} < 3$ (CO₂ order ≈ 0.3 , H₂ order ≈ 0.8) on CuO/ZnO/Al₂O₃ catalyst, and by Kim et al.[63] on Pt/Al₂O₃ catalysts (CO₂ order = 0.32, H₂ order = 0.70). It was also suggested by Ginés et al. [90] that different reaction pathways should be existed for $\frac{P_{\text{H}_2}}{P_{\text{CO}_2}} < 3$ and $\frac{P_{\text{H}_2}}{P_{\text{CO}_2}} > 3$ regions.

Table 3.1 Measured reaction orders with respect to CO₂ and H₂, and measured activation energies (E_{meas}) over Fe₃O₄. Reaction conditions: 100 mg Fe₃O₄, F_{tot}= 75 sccm, T = 723 K.

P _{H2} (kPa)	P _{CO2} (kPa)	P _{H2} : P _{CO2}	Reaction order in CO ₂	Reaction order in H ₂	E _{meas} (kJ/mol)
15	10-20	~ 1:1	0.33	-	28.9±0.9
10-20	15		-	0.79	
30	10-20	~ 2:1	0.39	-	27.1±0.5
25-35	15		-	0.72	
40	5-12.5	~ 4:1	0.43	-	34.2±1.9
35-45	10		-	0.31	
85	5-12.5	~ 9:1	1.30	-	39.0±3.4
70-90	10		-	0	

Figure 3.3 presents the temperature-programmed reduction (TPR) profiles of (a) the fresh Fe₃O₄ sample and (b) the post-reaction Fe₃O₄ sample. In Figure 3.3 (a), the fresh Fe₃O₄ was heated to 753 K in a hydrogen atmosphere, kept for 2 h at these conditions, and then heated to 1073 K at the rate of 5 K/min. The small peak observed in the TPR trace at about 563 K is assigned to an impurity of hematite present in the initial sample of magnetite (Fe₃O₄) but not detected in XRD pattern, as shown in the report by Jozwiak *et. al.* [60]. The following broader and asymmetric peak suggests a two-step reduction process that has been previously postulated in literature [91], as the following: (1) $Fe_3O_4 \xrightarrow{H_2} FeO$ and (2) $FeO \xrightarrow{H_2} Fe^0$. These two steps can be deconvoluted into two peaks located at ~ 688 K and 773 K in the TPR traces. After the

2 h reduction period at 773 K, there are no further H₂ consumption at higher temperatures. That is, the sample, after the reduction pretreatment used in our activation protocol, has been converted into metallic iron. This result is also consistent with the XRD pattern in Figure 3.2, which shows that α -Fe was the crystal formed after the reduction pretreatment of Fe₃O₄ sample in the microreactor.

As soon as CO₂ was fed into the reactor, the surface of the catalyst was partially oxidized. This is known from the results of Figure 3.3(b) that illustrates the presence of two significant peaks in the TPR profile for the post-reaction catalysts (at 630 K and 780 K, respectively). The location of these two predominant peaks shows good agreement with the results of Figure 3.3(a) and results reported elsewhere [60][92]. There is at least a two-step reduction at ~630 K and 780 K, implying the coexistence of different oxidation states of iron on the post-reaction sample due to the partial oxidation from CO₂. For this post-reaction sample, H₂ concentration in the effluent stream decreased by only a small amount (less than 1%), suggesting that the consumption of the H₂ feed would not affect the reduction rate during the TPR reaction.

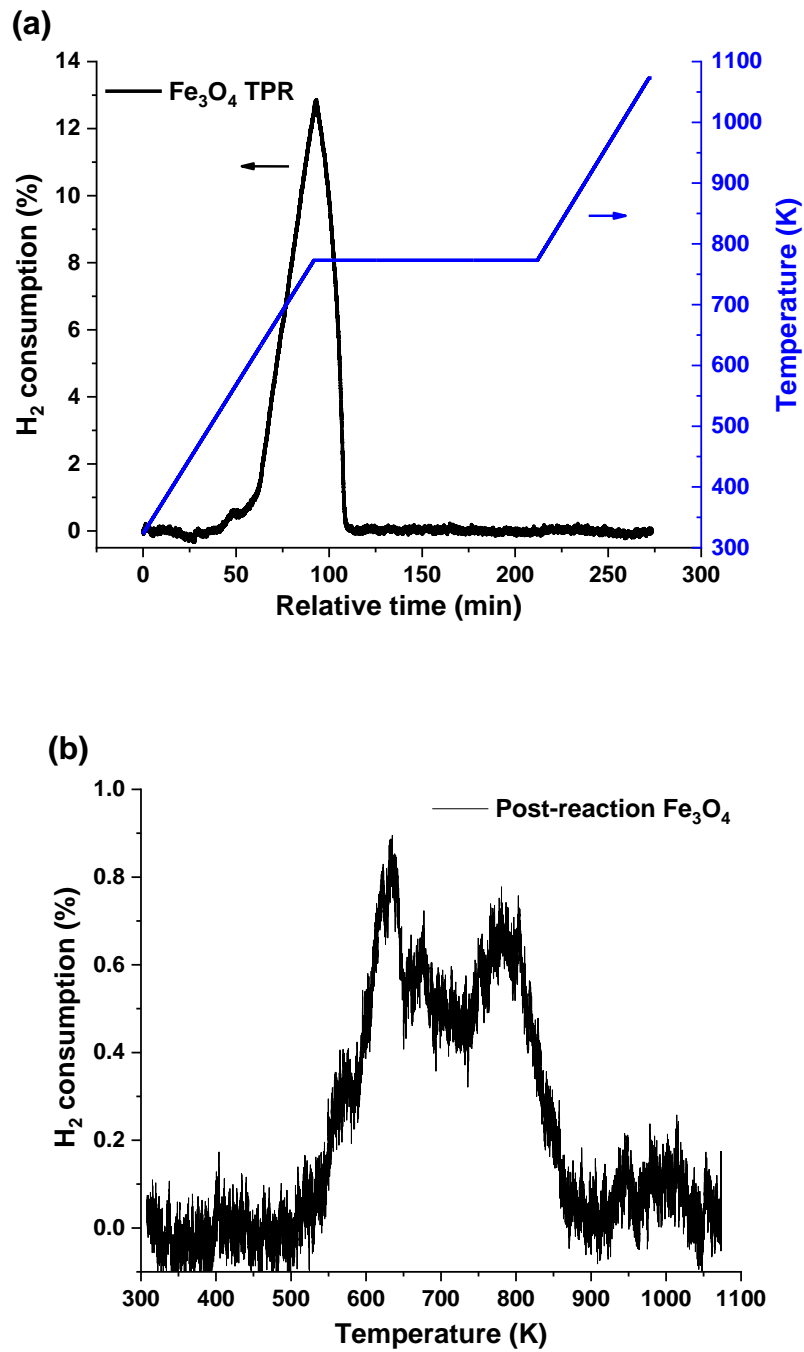


Figure 3.3 (a) H_2 consumption (%) of reduction period during the pretreatment following the temperature-programmed reduction (TPR) of 100 mg Fe_3O_4 . (b) TPR curve of post-reaction Fe_3O_4 sample.

Figure 3.4 displays the diffraction pattern of fresh Fe₃O₄ and the catalyst after the RWGS reaction (post-reaction Fe₃O₄). The 2θ degree peak position in fresh Fe₃O₄ were 30.15°, 35.45°, 37.15°, 43.15°, 53.50°, 56.95°, and 62.55°, which are all consistent with magnetite (JCPDS PDF 01-071-6336). The post-reaction Fe₃O₄ shows a very different XRD pattern: this pattern was composed of metallic iron (α-Fe, 44.67°, shown in the inset of Figure 3.4), iron carbide (Fe₃C), and a small peak of FeO_x (35.47°). Iron oxides can be converted directly into carbides in a reducing and carburizing atmosphere [93], and the carbon source of the Fe₃C production can be either from impurities in the fresh Fe₃O₄ sample or due to reaction with the product CO, after the RWGS reaction as indicated by Eq. 3.7 [94]:



The bulk composition of the catalyst after the reaction is also consistent with the TPR results in Figure 3.3 (a) and (b). During TPR, the amount of H₂ consumption of magnetite relative to the amount of H₂ consumption after the reaction was 12:1, therefore the iron species in the catalyst has been changed into a more reduced chemical state after the pretreatment and RWGS reaction. The reduction was mainly caused by the pretreatment, while the following CO₂/H₂ reaction shifted the metallic iron back to a slightly more oxidized state; a combination of iron carbide, metallic iron, and some iron oxides.

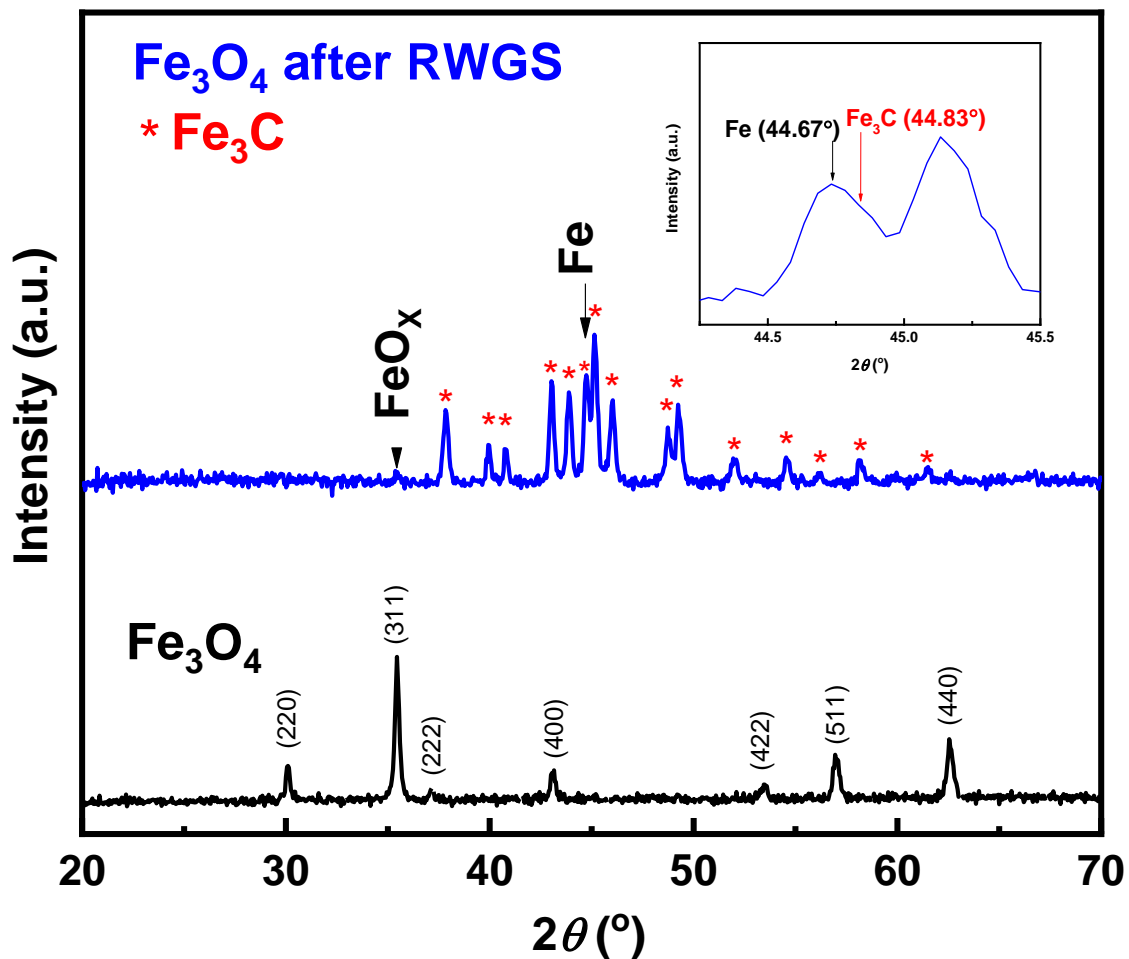


Figure 3.4 XRD patterns of fresh Fe₃O₄ (down) and post-reaction Fe₃O₄ (up); inset is the magnification of post-reaction Fe₃O₄ from 44° to 45.5°.

Besides bulk property information obtained from XRD, XPS analyses were conducted to characterize the surface composition of the initial fresh Fe₃O₄ and the change of the catalyst after the RWGS reaction. Figure 3.5 shows the XPS spectra, peak deconvolutions, and the fitting envelopes for the Fe 2p_{3/2} spectra of Fe₃O₄ and post-reaction Fe₃O₄. Atomic percent contributions are calculated from the fitted peaks

of Fe 2p_{3/2} due to its larger intensity (Area of Fe 2p_{3/2}: Fe 2p_{1/2}= 2:1). The Fe 2p_{3/2} spectra were fitted over the range of 705-722 eV. The spectra between 716-722 eV were not shown in the figure for clarity. In this range, there were only small Fe³⁺ satellite peaks located at 719.2 eV and 719.4 eV for both the fresh and post-reaction Fe₃O₄ samples, respectively, although the area of the satellite peaks was still included in the corresponding components when calculating the relative atomic percentage. The fits, including the binding energy, full width at half maximum (FWHM), and the relative iron composition are summarized in Table 3.2. The fitted XPS spectrum of fresh Fe₃O₄ was composed of doublets for Fe²⁺ at 709.8 eV and Fe³⁺ at 711.3 eV. Fe₃O₄ has an inverse spinel structure which can be written as Fe³⁺_{TET}[Fe²⁺Fe³⁺]_{OCT}O₄, with one Fe³⁺ on a tetrahedral site, and Fe²⁺ and the other Fe³⁺ distributed on octahedral sites. Therefore, the theoretical relative composition of Fe²⁺/Fe³⁺ is 0.5, which is close to the area fitted and the calculated relative composition in our fresh Fe₃O₄ (Fe²⁺: Fe³⁺ = 34.8/65.2 =0.53). The Fe³⁺ peak has a larger FWHM than Fe²⁺. This is as expected because the electronic configuration of Fe²⁺ is 3d⁶ while that of Fe³⁺ is 3d⁵, that is, Fe²⁺ will have a longer life time compared to Fe³⁺; and therefore the FWHM of the Fe²⁺ peak should be smaller than the Fe³⁺ peak [95]. Additionally, the Fe³⁺ peaks can be attributed to two different structures, octahedral Fe³⁺ and tetrahedral Fe³⁺, a factor that will also lead to a broader Fe³⁺ peaks.

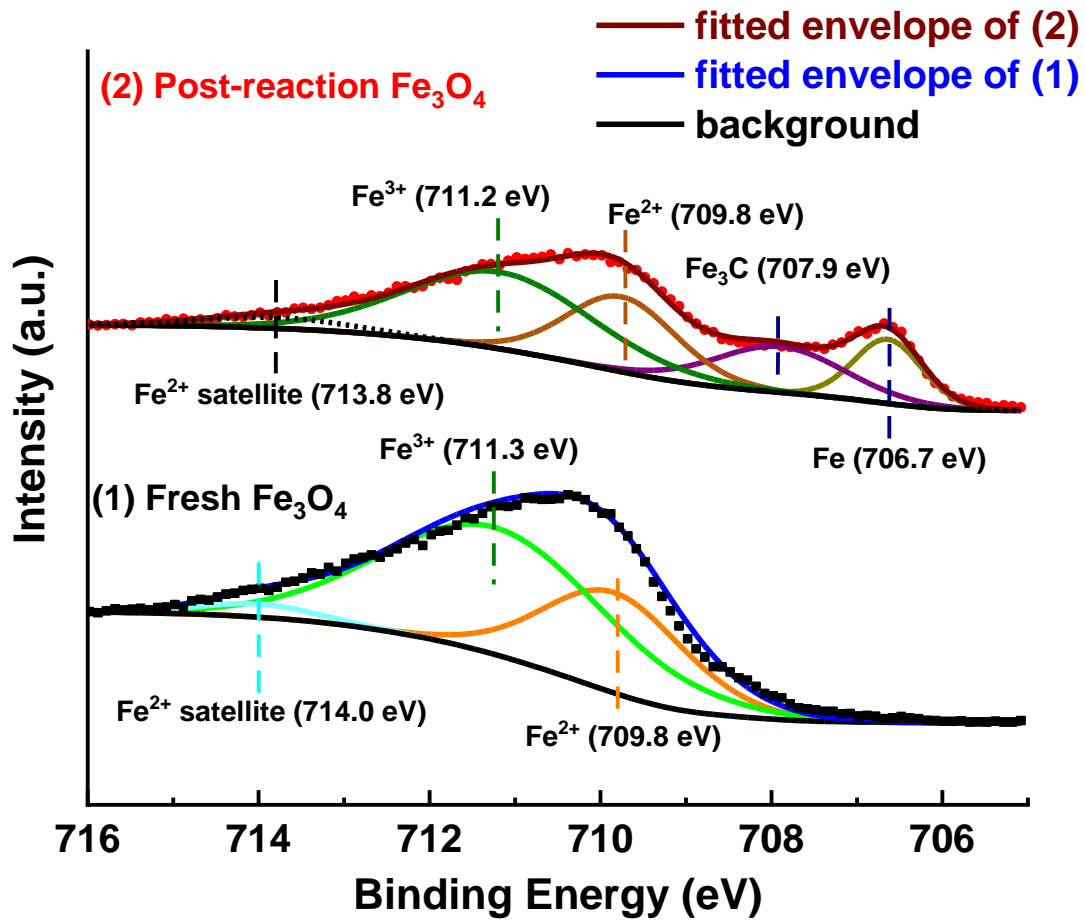


Figure 3.5 XPS Fe 2p_{3/2} spectra of Fe₃O₄ and post-reaction Fe₃O₄. The curves under the fitted envelope and above the background are contributions of estimated components from peak fitting.

After the RWGS reaction, the spectrum was fitted using four different components correspond to metallic Fe (706.7 eV), Fe₃C (707.9 eV), Fe²⁺ (709.8 eV), and Fe³⁺ (711.2 eV). The peak location of Fe²⁺ and Fe³⁺ were the same or very close to the fresh sample, indicating that there was only a small surface charging effect with

the flood gun on. The binding energies of the components are in agreement with literature results [93,95–97]. In terms of the atomic percentages, the overall peak area was re-allocated to a more reduced regime after the RWGS reaction. The Fe²⁺ decreased from 34.8% to 27.5%, the Fe³⁺ decreased from 65.2% to 43.9%, while there were two components formed: Fe (12.2%) and Fe₃C (16.4%). The shift of the spectra was due to the H₂ reduction pretreatment before operating the RWGS reaction, and the flow of H₂/CO₂ reactants through the system would balance each other to make the catalyst partially oxidized or reduced. Though the sample surface could be oxidized by the air during the transportation from the reactor to the XPS analysis chamber, the result from XPS still can confirm the reduction of the surface during the reaction since new crystal structures such as Fe and Fe₃C are detected by XRD.

Table 3.2 XPS peak fittings for Fe 2p_{3/2} spectra for Fe₃O₄ and post-reaction Fe₃O₄.

Sample	Peak Deconvolution	Binding Energy (eV)	FWHM (eV)	Atomic %
Fe ₃ O ₄	Fe ³⁺	711.3	3.08	65.2
	Fe ²⁺	709.8	1.95	34.8
post-reaction Fe ₃ O ₄	Fe ³⁺	711.2	2.58	43.9
	Fe ²⁺	709.8	1.51	27.5
	Fe ₃ C	707.9	1.78	16.4
	Metallic Fe	706.7	0.94	12.2

The XPS analyses indicate that the active catalyst consisted of a mixture of metallic Fe, Fe₃C, Fe²⁺, and Fe³⁺; however, it cannot establish the relative contributions of these components to the observed rate of RWGS reaction. To determine if the iron carbide formed in our reaction can catalyze the RWGS reaction, reaction rates over pure Fe₃C were measured (Figure 3.6). In Figure 3.6(a), Fe₃C showed an initial CO formation rate of 26.0 mmol h⁻¹ g⁻¹ but dropped 48% to near 13.5 mmol h⁻¹ g⁻¹ in 10 min and then further down to 5.7 mmol h⁻¹ g⁻¹ in 160 min at 753 K. This is clearly different from the properties of the Fe₃O₄-derived catalyst in Figure 3.1, since the Fe₃O₄-derived catalyst displayed high stability for at least 1300 min. To evaluate the fast deactivation shown in Figure 3.6(a) and remove the initial reduction effect during the ramping by hydrogen, another measurement was carried out with respect to temperature, (see Figure 3.6(b)). This experiment was conducted flowing a CO₂/H₂/He gas mixture in the same relative concentration used in the standard activity test during the ramping procedure from room temperature to 773 K. At 573 K, the material did not catalyze the formation of CO; however, when the temperature was increased to 623 K, the catalyst immediately showed catalytic rates in the range of 2.60 mmol h⁻¹ g⁻¹ to 2.99 mmol h⁻¹ g⁻¹. After 1 h of the reaction, the rate did not decrease significantly at this moderate temperature. The CO formation rates were 6.60 mmol h⁻¹ g⁻¹, 9.80 mmol h⁻¹ g⁻¹, and 9.16 mmol h⁻¹ g⁻¹, as temperature was increased to 673 K, 723 K, and 773 K, respectively. The formation rate at 773 K, was not higher than that at the lower temperature because of rapid deactivation at this temperature. Faster deactivation rates were observed at higher temperatures: the average deactivation rates 1.36 mmol h⁻¹ g⁻¹ per h, 2.57 mmol h⁻¹ g⁻¹ per h, and 3.50 mmol h⁻¹ g⁻¹ per h.

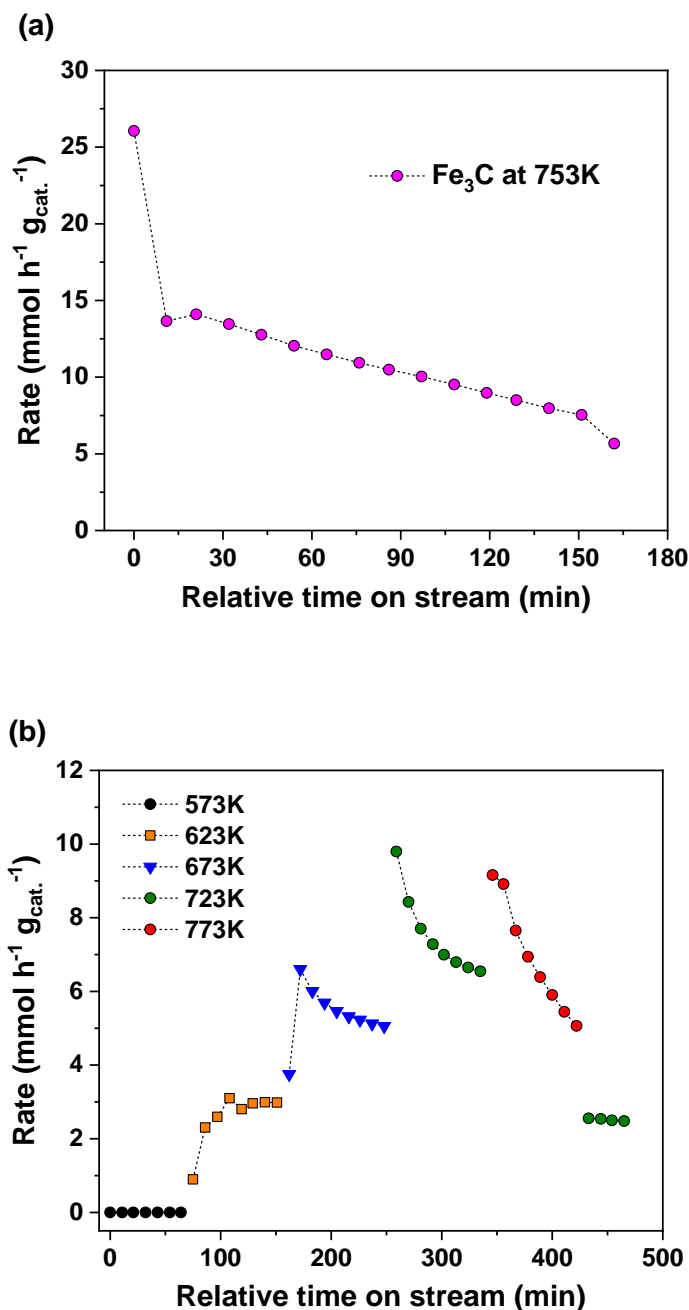
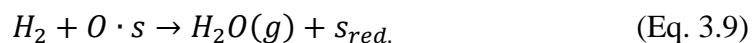
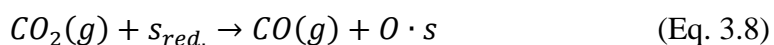


Figure 3.6 (a) CO formation rate on 100 mg Fe₃C. Reaction conditions: $F_{\text{tot}} = 75$ sccm; the reactor was ramped to 753K with $P_{\text{H}_2} = 15\text{kPa}$ and He as remainder. No further reduction was applied after the ramping. During the reaction, $T = 753\text{K}$, $P_{\text{tot}} = 1$ bar, $P_{\text{H}_2} = P_{\text{CO}_2} = 15\text{kPa}$. (b) CO formation rate on 100 mg Fe₃C. The temperature was directly ramping from room temperature to 773K as shown in the figure with $P_{\text{tot}} = 1$ bar, $P_{\text{H}_2} = P_{\text{CO}_2} = 15\text{kPa}$, the remainder is He.

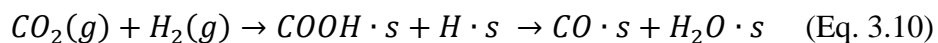
After reacting at 773 K, the temperature was reduced to 723 K to monitor the reaction rate and compare to the previous value. Much lower rates ($2.55 \text{ mmol h}^{-1} \text{ g}^{-1}$) were observed than in the previous measurement at the same temperature (723 K), that is, there was an irreversible change in the catalyst structure or composition. At higher temperatures, the reverse reaction of , where Fe_3C reacts with CO_2 and forms Fe and CO, is more favorable than the Fe_3C formation [94]. Therefore, the initial CO formation rate was probably due to the formation of CO from decomposition but was quickly dropped since it is harder to convert the metallic iron back to Fe_3C at higher temperatures. The iron carbide catalyst only showed steady CO production at 623K. This explains why the deactivation at 723 K over Fe_3C is very different from the steady-state magnetite catalyst reported in Figure 3.1, which showed very stable CO formation rate at 753 K. This observation suggests that the operating temperature of RWGS in this study was not an environment which gave iron carbide to be stably reactive in CO production. In addition, the iron carbide (Fe_5C_2 or Fe_3C) is normally considered to be the active phase of iron for hydrocarbon production [98,99], and iron oxide is the active phase for WGS and RWGS [22]. Several reports have suggested that the stability of the iron catalyst in either FT synthesis [100] or RWGS [85] can be related to an iron carbide layer. Davis [100] suggested that catalyst composition and reaction condition will define the existence of pseudo-equilibrium layer of iron carbide to ensure a very slow deactivation condition. Kim *et. al.* [85] concluded that the stability of the catalyst could have originated from migration of C and O into the catalyst bulk forming iron oxide and iron carbide, which likely prevented the nanoparticles on the surface from agglomerating. Based on the XPS results and Fe_3C

catalytic tests, the iron carbide of the working catalyst is less likely to be the main active site for CO production but is an important species to provide stability in the overall catalytic performance.

Gas-switching experiments, in which H₂ and CO₂ are flown on and off, were used to distinguish and quantify contributions from redox and associative reaction pathways [63,73,101]. In the simplest form of the redox mechanism, gas-phase CO₂ adsorbs on a reduced site to form CO and an oxidized site (Eq. 3.8), which can then be reduced by gas phase H₂ to reform the reduced site (Eq. 3.9). The simplest redox cycle can be described as follows:



A simplified associative pathway can be described generally by Eq. 3.10. CO₂ and H₂ adsorb on the catalyst surface to form a carbon-containing intermediate (i.e. formate, carbonate, or bicarbonate), which then decomposes in the presence of H₂ to form CO and H₂O.



CO and H₂O were the main products formed during gas-switching experiment (Figure 3.7). In the first three cycles, CO was formed when switching from H₂ to CO₂, and a very small amount of CO was formed when switching from CO₂ to H₂ at 30 min, 70 min, and 110 min, respectively. When the catalyst was purged 20 min with helium

before switching from CO₂ to H₂, CO was not formed, and H₂O was produced at 195 min. Water was formed when switching from H₂ to CO₂ and when switching from CO₂ to H₂. After flowing H₂ and purging the reactor with He for 20 min, only a negligible amount of H₂O was formed upon the admission of CO₂ (at 150 min).

In Figure 3.7, the fact that CO was formed when the reduced form of Fe₃O₄ catalyst was contacted with CO₂, even after the purge with He to decrease the concentration of any surface H₂, is evidence of a redox pathway. During the first 125 min of gas-switching experiments, H₂O was produced during flows of only CO₂ or only H₂. This differs from what is expected in the traditional redox cycle, in which H₂O is only produced during the H₂ feeding period (see Eq.3.9) However, after flowing H₂ and purging the reactor with He for 20 min, the admission of CO₂ only produced negligible amounts of water.

Table 3.3 summarizes the estimated initial rates of CO production on Fe₃O₄ catalyst during each segment of the gas-switching experiments. The CO production rates were calculated from the initial slopes of the concentration *vs.* time data in Figure 3.7, essentially modeling the system as a batch reactor (Eq. 3.11)

$$\frac{dC_A}{dt} = r_A \quad (\text{Eq. 3.11})$$

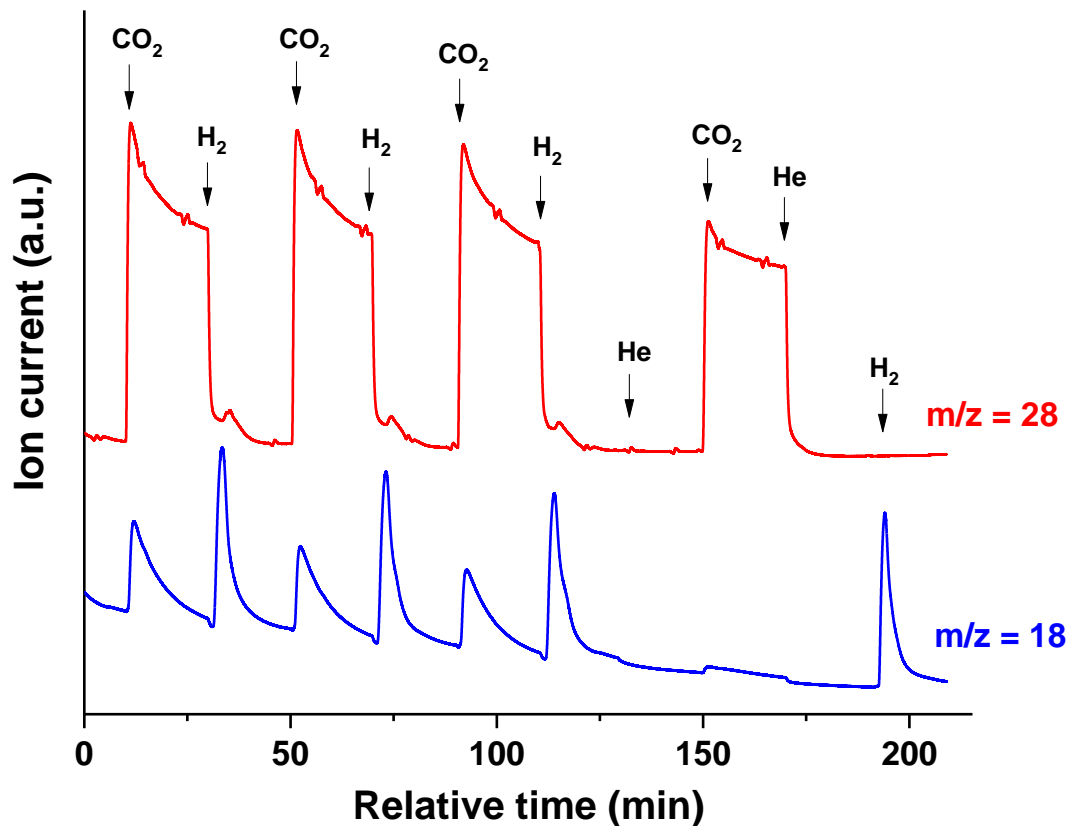


Figure 3.7 Ion current at $m/z = 18$ (H_2O) and 28 (CO) during H_2/CO_2 switching experiments on Fe_3O_4 . Arrows with a label indicate a change in gas composition to the indicated gas. The catalyst first was reduced in flowing H_2 for 2 h, following the reaction in H_2 and CO_2 for 2 h, and H_2/He in 20 min before the first admission of CO_2 . Reaction conditions: $T = 773$ K, $F_{\text{He}} = 36$ sccm, F_{H_2} or $F_{\text{CO}_2} = 4$ sccm

Table 3.3 Estimated initial rates of CO production after gas switches from H₂ to CO₂ and from CO₂ to H₂ during gas-switching experiment on Fe₃O₄ in Figure 3.7

Period	Rate after H ₂ to CO ₂ gas switch (μmol L ⁻¹ s ⁻¹ g _{cat.} ⁻¹)	Rate after CO ₂ to H ₂ gas switch (μmol L ⁻¹ s ⁻¹ g _{cat.} ⁻¹)	(H ₂ to CO ₂ rate)/(CO ₂ to H ₂ rate) ratio
1st CO ₂	2.78	1.64	1.70
2nd CO ₂	2.98	1.00	2.98
3rd CO ₂	2.74	0.91	3.01
4th CO ₂ (after He purge)	1.94	0	-

It is observed (Table 3.3) that the rate after switch from H₂ to CO₂ fluctuated between 2.74 μmol L⁻¹ s⁻¹ g_{cat.}⁻¹ and 2.98 μmol L⁻¹ s⁻¹ g_{cat.}⁻¹ in the first 3 periods of CO₂ admission, and it decreased after He purge. The rate after switch from CO₂ to H₂ decreased in the first three periods, and it was zero (with no CO produced) during the last admission of CO₂ after the He purge. The decrease of the CO initial rate after CO₂ to H₂ switch, especially when equal to zero after the purge, raises doubts about the existence of residual CO₂ during the first three admissions of H₂ in the switching experiment. As a control, when the gas was switched from CO₂ to H₂, the CO₂ gas did not exit from the surface very quickly (see Figure 3.8). Therefore, a small amount of CO can be produced by the residual CO₂ with the available reduced sites; evidence of this interpretation in the detection of very small peaks after the H₂ admissions (Figure 3.7). The negligible CO production (relative time = 34 min, 74 min, and 114 min) after the H₂ admissions should not be considered evidence of the associative mechanism. In summary, CO formation upon switching from H₂ to CO₂ is evidence consistent with the redox mechanism, while the small contribution of CO production

upon switching from CO₂ to H₂ was suppressed by the confirmation of Helium purge. Thus, from the view of gas-switching experiment, only the redox pathway is active on our Fe₃O₄-derived catalyst.

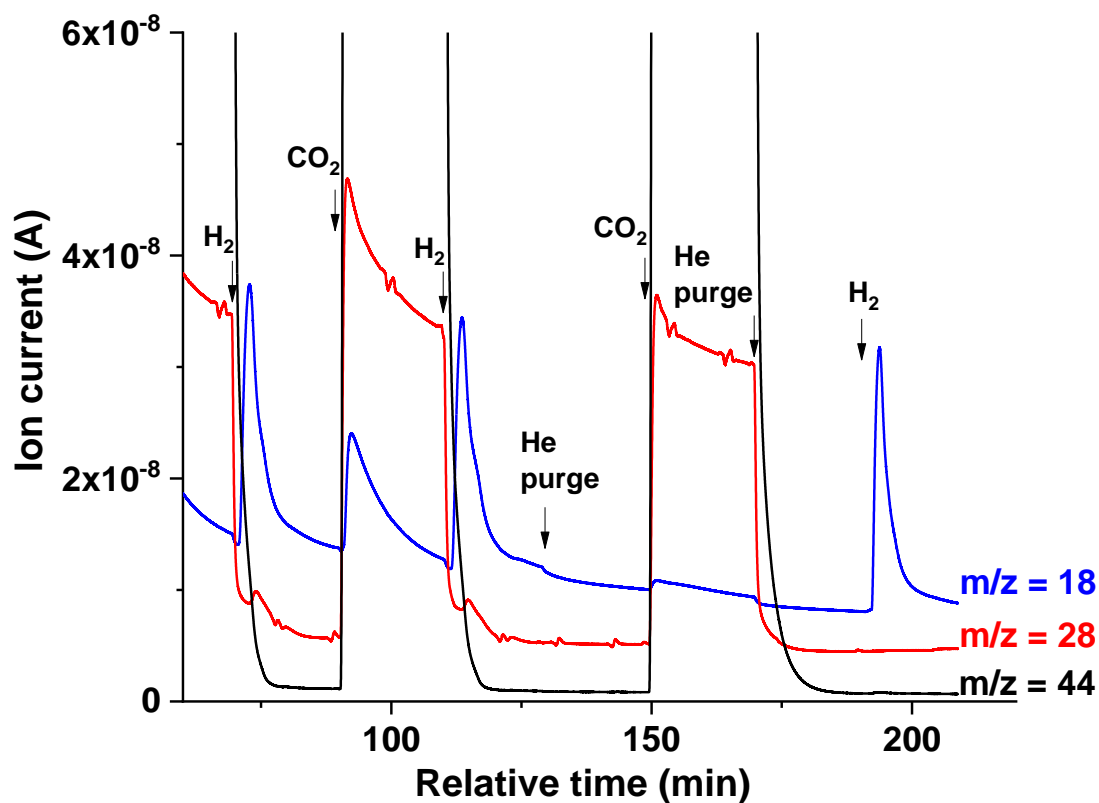
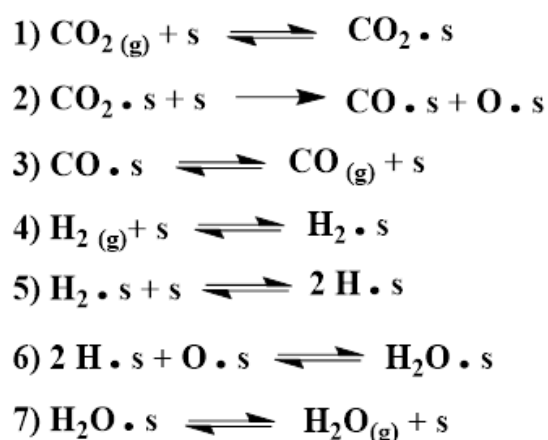


Figure 3.8 Ion current at $m/z = 18$ (H₂O), 28 (CO), and 44 (CO₂) during H₂/CO₂ switching experiments on Fe₃O₄. Arrows with a label indicate a change in gas composition to the indicated gas. Reaction conditions: $T = 773$ K, $F_{\text{He}} = 36$ sccm, F_{H_2} or $F_{\text{CO}_2} = 4$ sccm. The figure is a modification of Figure 3.7

Isotopic experiments were conducted to gain insight into the mechanism of the reaction. The isotopic C¹⁸O₂ to CO₂ switching experiment is shown in Figure 3.9. Here it can be seen that C¹⁸O (m/z = 30) formed and CO (m/z = 28) decreased when the gas (CO₂/H₂) was switched to C¹⁸O₂/H₂. CO can be only formed from CO₂ and not from the lattice oxygen. The gas-switching experiments with CO₂ and H₂ led us to conclude that a redox pathway is active on Fe₃O₄-derived catalyst. A model that can present a redox reaction pathway for this catalyst is given in Scheme 3.1. It includes the adsorption of both the reactants, CO₂ and H₂. In surface redox mechanism, the dissociation of CO₂ at the catalyst surface (step 2 in Scheme 3.1) is known to be the RDS [47,90,102]. Evidence for H₂ dissociation (step 5 in Scheme 3.1) was observed when H₂/D₂ mixtures were fed to the catalyst in the presence of CO₂ (see Figure 3.10). HD formation was observed to occur quickly, since the amount of CO₂ to CO conversion decreased on the same time scale when switching the concentration from H₂/D₂ (7.5kPa/7.5kPa) to H₂ (7.5 kPa), indicating that H₂ dissociation is reversible and not rate limiting.



Scheme 3.1 Redox reaction pathway for CO formation

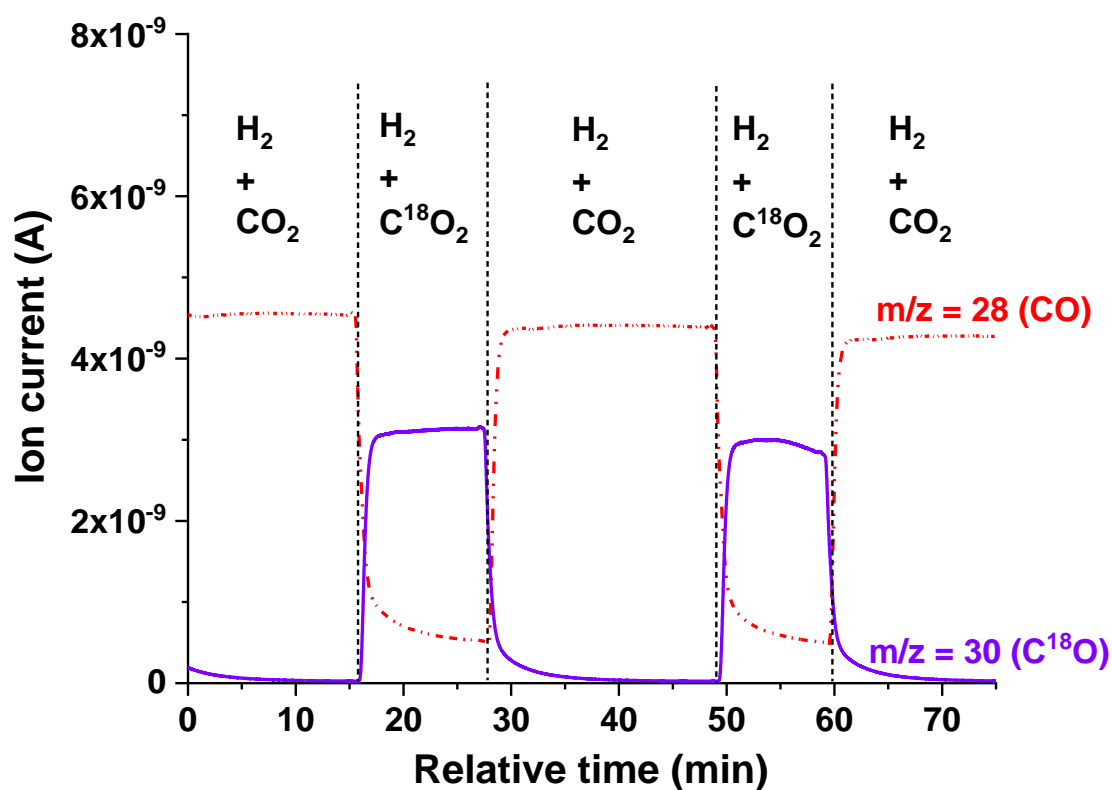


Figure 3.9 Ion current at $m/z = 28$ (CO) and 30 ($C^{18}O$) during $CO_2/C^{18}O_2$ switching experiments on Fe_3O_4 (100 mg). Labels in each region indicate a change in gas composition. A standard pretreatment (reduced in flowing H_2 for 2 h) and RWGS reaction (>2 h) had been done before the switching experiment. Switching experiment conditions: $T = 753$ K, $F_{tot} = 40$ sccm, $F_{H_2} = 4$ sccm, F_{CO_2} or $F_{C^{18}O_2} = 4$ sccm.

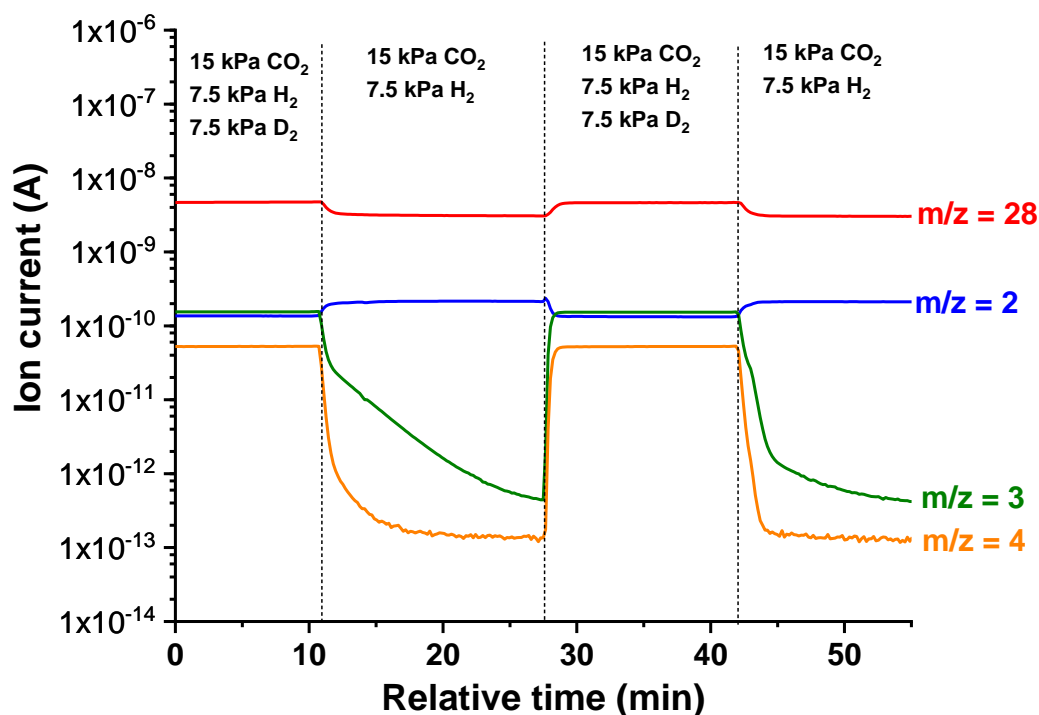


Figure 3.10 Ion current at $m/z = 2$ (H_2), 3 (HD), 4 (D_2), and 28 (CO) during flow of 7.5 kPa H_2 + 7.5 kPa D_2 + 15 kPa CO_2 and 7.5 kPa H_2 + 15 kPa CO_2 on Fe_3O_4 . Reaction conditions: $T = 753 \text{ K}$, $F_{\text{tot}} = 75 \text{ sccm}$.

An additional gas switching experiment was conducted to elaborate the H_2O production (Figure 3.11). The amount of H_2O produced during H_2 flow periods was consistent between each cycle (Figure 3.11 (a)), that is, the adsorbed O·s species formed upon CO_2 reduction are stable at these reaction conditions. However, the amount of H_2O produced during the period of CO_2 flow decreased as the purge time in helium increased. After only a 5 min purge, the amount of H_2O produced during the period of CO_2 flow was much greater than that produced following a 20 min purge in helium, and the rate fitted from the initial slope of this region dropped dramatically

(see Table 3.4). This suggests that H* atoms from the catalyst surface appeared to desorb (as H₂) during the He purge. This was a slow process because even following a 20 min purge, there were enough H* atoms on the sample to form small amounts of H₂O when CO₂ was administered. The above experiment further supports that redox mechanism should be the dominant reaction pathway for this Fe₃O₄-derived catalyst during the CO₂ hydrogenation at our reaction conditions.

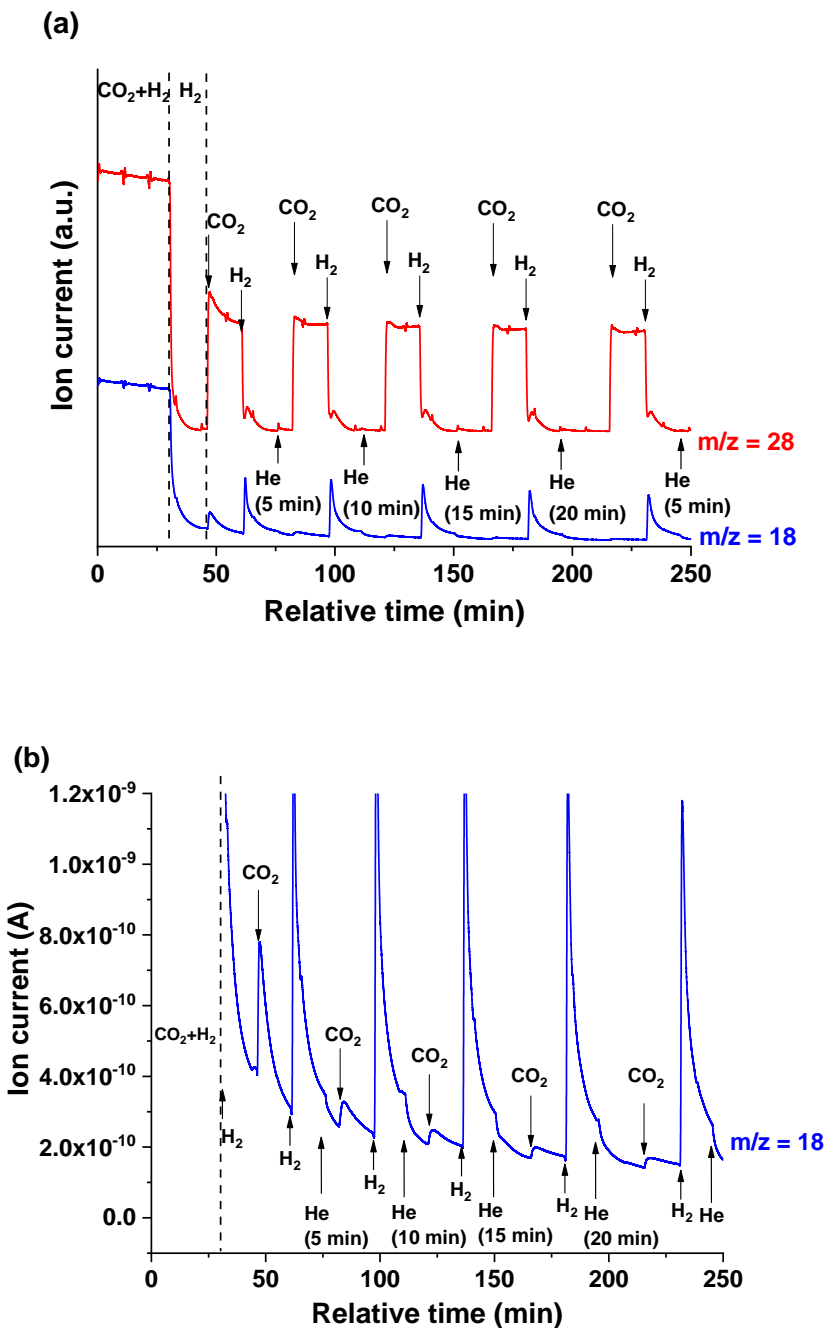


Figure 3.11 (a) Ion current at $m/z = 28$ (CO) and $m/z = 18$ (H_2O) during H_2/CO_2 switching experiments on Fe_3O_4 . Arrows with a label indicate a change in gas composition to the indicated gas. The catalysts were in flowing H_2 for 2 h followed by the reaction in $\text{CO}_2 + \text{H}_2$ for 2 h before the first admission of H_2 (relative time: 31 min) and CO_2 (relative time: 46 min). Reaction conditions: $T = 753$ K, $F_{\text{tot}} = 75$ sccm, P_{H_2} or $P_{\text{CO}_2} = 15$ kPa. (b) is the modification of (a).

Table 3.4 Fitted initial slopes and area of H₂O in H₂/CO₂ switching experiment with different He purging time in Figure 3.11

Period	Magnitude of H ₂ O Initial Slope (10 ⁻¹¹ A min ⁻¹)	H ₂ O Area (10 ⁻⁹ A min)
1st CO ₂	6.46	1.71
2nd CO ₂ (after 5 min purge)	0.70	0.47
3rd CO ₂ (after 10 min purge)	0.38	0.33
4th CO ₂ (after 15 min purge)	0.19	0.29
5th CO ₂ (after 20 min purge)	0.11	0.22

3.4 Conclusions

Unsupported Fe₃O₄-derived catalyst showed very promising activity toward CO formation via CO₂ hydrogenation. The high selectivity (~100% under H₂:CO₂ = 1:1) and great stability make the catalyst feasible to consider in extensive use. Only slight deactivation under conditions of excess CO₂, but can be quickly regenerated under excess H₂. Reaction rates depended more strongly on H₂ (0.8 in reaction order) compared to CO₂ (0.33 in reaction order) under near equimolar gas-phase composition. The post-reaction analyses of the catalyst indicated the catalyst was reduced to metallic iron first in the pretreatment of H₂, but the working catalyst remained partially oxidized with the composition of Fe²⁺, Fe³⁺, Fe⁰, and Fe₃C. The main active sites are believed to be the combination of the above species except Fe₃C are unlikely to directly contribute to the very steady CO formation at our reaction

conditions (1 atm, 723K-773K). Gas-switching experiments revealed that CO was formed only when switching from H₂ to CO₂, and H₂O was formed when switching from CO₂ to H₂ but not when switching from H₂ to CO₂ if purging of Helium was in between with the gas admission. Redox mechanism is identified as dominant reaction pathway for the unsupported iron catalyst.

Chapter 4

DIRECT CONVERSION OF CO₂ INTO METHANOL OVER PROMOTED INDIUM-BASED CATALYSTS

4.1 Introduction

The direct carbon dioxide (CO₂) hydrogenation to methanol is a potentially important route to decrease CO₂ emissions: methanol is a versatile compound that can be used as fuel or as a precursor to the production of many commodity chemicals such as acetic acid, formaldehyde, and dimethyl ether [33,35]. Liquid methanol is also preferable to hydrogen in terms of energy storage density and ease of transportation. If a *green* (CO₂-free) H₂ source is used, CO₂ hydrogenation to methanol is sustainable as exemplified by the George Olah CO₂ to Renewable Methanol Plant in Iceland [34]. This plant uses electricity, generated from hydro and geothermal energy, to make hydrogen. The process can be driven by a variety of renewable energy sources such as solar, wind, and waste heat from chemical or nuclear plants, making the process more sustainable. CO₂, thus, can be chemically transformed from a greenhouse gas into a valuable and renewable carbon source [35]. Although methanol synthesis from CO₂ and H₂ is exothermic ($\Delta H^\circ_{298K} = -49.5 \text{ kJ mol}^{-1}$), CO₂ conversion to methanol is kinetically limited at low temperatures and thermodynamically limited at high temperatures, resulting in a low theoretical methanol yield [103][104].

Cu/ZnO/Al₂O₃ (CZA) ternary catalysts are currently employed for industrial methanol synthesis from syngas (CO/CO₂/H₂) at elevated pressures (50-100 bar) and temperatures (473-543 K) [16][105]. However, the CZA catalysts typically have low

selectivity (around 40%), because of the competing reverse water–gas shift (RWGS) reaction, and limited stability, due to sintering of the active phase under reaction conditions [106]. Among the Cu-based materials investigated, only a few catalysts such as $\text{LaCr}_{0.5}\text{Cu}_{0.5}\text{O}_3$ [36], Cu-Ga/ZnO [37], and Cu@ZnO (core-shell) [38] exhibit high selectivity to methanol (88-100%); the long-term stability and scalability of these materials, however, have not been evaluated. Many investigations have attempted to identify new catalyst formulations (such as Cu/CeO₂ [17], Pd/Ga₂O₃ [41], Pd/CeO₂ [42], and In₂O₃ [43]) showing promising catalytic activity for CO₂ hydrogenation to methanol. Indium oxide and In-containing metal alloys, in particular, have been recognized as highly selective to CO₂ in the methanol and ethanol steam reforming reaction [107–109]; consequently, these materials also have the potential for catalyzing its reverse reaction, CO₂ hydrogenation to methanol. DFT calculations have shown that key intermediates (*HCOO) involved in CH₃OH synthesis are more stable on a defective In₂O₃ surface than those on the Cu surface, strongly suppressing the formation of CO [45] and demonstrating great potential for selective catalytic CO₂ hydrogenation. A more recent DFT and kinetic study from Frei *et al.* showed a different energetically favored path with CH₂OOH and CH₂(OH)₂ as main intermediates on the In₂O₃ (1 1 1) surface [55]. Martin *et al.* investigated ZrO₂ supported indium oxide catalysts and observed significant and stable reaction rates with high selectivity towards methanol [46]. Other studies using In₂O₃ or In-based materials [43,110,111] have not shown as high methanol selectivity (99.8%) as reported by Martin *et al.* Sun *et al.*, for example, showed 54.9 % methanol selectivity with unsupported In₂O₃ catalyst; Rui *et al.* investigated In₂O₃ and Pd/In₂O₃ catalyst,

demonstrating remarkably high methanol formation rates and ~60-72% methanol selectivity over Pd/In₂O₃ catalyst prepared with peptide templates (also see Table 4.1).

Table 4.1 Comparison of various catalysts for CO₂ hydrogenation to methanol.

Catalyst	T	P	GHSV	X _{CO2}	S _{MeOH}	r _{MeOH}	Ref.
	(K)	(bar)	(cm ³ h ⁻¹ g _{cat} ⁻¹)	(%)	(%)	(g _{MeOH} h ⁻¹ g _{cat} ⁻¹)	
In ₂ O ₃ /ZrO ₂	573	40	52000	10.5	53	0.465	this work
1.5YIn ₂ O ₃ /ZrO ₂	573	40	52000	7.6	69	0.420	this work
3La10In/ZrO ₂	573	40	52000	7.7	66	0.420	this work
	543	40	52000	2.9	91	0.241	this work
In ₂ O ₃	603	40	15000	7.1	40	0.118	[43]
In ₂ O ₃	573	50	20000	3.7	100	0.208	[46]
In ₂ O ₃ /ZrO ₂	573	50	20000	5.2	99.8	0.295	[46]
In ₂ O ₃	573	50	21000	8.2	71	0.352	[110]
Pd-P/In ₂ O ₃	573	50	21000	20.5	72	0.885	[110]
Cu-ZnO-Al ₂ O ₃	573	50	20000	2.1	11	0.122	[46]
Cu/ZnO/Al ₂ O ₃	553	46	14700	23	13	0.156	[112]
Cu/ZnO/ZrO ₂	493	80	3300 ^a	21	68	0.181	[113]
Cu-Zn-Ga/SiO ₂	543	20	18000	5.6	99.5	0.349	[114]

Cu/ZrO ₂	553	30	7200	12.1	31	0.096	[115]
Pd-ZnO/CNT	523	30	1800	6.3	99.6	0.037	[116]
Pd/Ga ₂ O ₃	523	50	18000	19.6	10.1	0.128	[41]

^a the unit is h⁻¹

Inui *et al.* have investigated the promotional effect of lanthanum oxide on Cu-Zn-Cr-Al-Oxides catalysts by increasing CO₂ adsorption and catalytic reaction rates in the CO₂ to methanol reaction [117]. Addition of Y₂O₃ into CZA catalysts also leads to higher CO₂ conversion and Cu dispersion [118]. Despite the improvements observed upon addition of La and Y to Cu catalysts, Y or La-promoted indium oxide catalysts have not been investigated for the hydrogenation of CO₂ to methanol.

Herein, Y or La-promoted In₂O₃/ZrO₂ catalysts have been prepared by wet impregnation and investigated for the CO₂ to methanol reaction. In particular, Y and La effect on selectivity and reducibility of the supported oxide have been investigated in detail. The catalysts are characterized using scanning electronic microscopy (SEM), X-ray diffraction (XRD), X-ray photoelectron spectroscopy (XPS), temperature-programmed reduction (TPR), and temperature-programmed desorption (TPD). The catalytic properties, including CO₂ conversion, methanol selectivity, and methanol or CO formation rate, were correlated to the catalysts composition and reducibility. We found that the incorporation of Y and La enhance methanol selectivity significantly by decreasing the surface reducibility and increasing the CO₂ adsorption capacity on both Y or La-containing catalyst. A mechanistic discussion comparing the initial steps of CO₂ hydrogenation over In₂O₃/ZrO₂ and Y-promoted catalysts is provided.

Furthermore, the catalytic kinetics suggests that the reaction proceeds via a formate pathway.

4.2 Experimental

4.2.1 Catalyst preparation

The ‘unpromoted’ catalyst, $\text{In}_2\text{O}_3/\text{ZrO}_2$, was prepared by wet impregnation as follows: 0.76 g $\text{In}(\text{NO}_3)_3 \cdot x\text{H}_2\text{O}$ (Alfa Aesar, 99.99%) was first dissolved in a mixture of ethanol (70 cm^3) and deionized water (24 cm^3). 2.00 g ZrO_2 (NORPRO, SZ 31164 extrudates, monoclinic phase, crushed prior to use) as the catalyst support was subsequently added to the solution and the resulting slurry was stirred for 5 h at room temperature. The solvent was removed using a rotary evaporator (Büchi Rotavap R-114) at 343 K. The sample obtained was dried in a drying oven at 353 K overnight and calcined in static air at 573 K (heating rate 2 K min^{-1} , hold for 2 h). The promoted catalysts were prepared in the similar fashion. For $1.5\text{Y}9\text{In}/\text{ZrO}_2$, $2\text{Y}8\text{In}/\text{ZrO}_2$, and $3\text{Y}8\text{In}/\text{ZrO}_2$, 0.61 g $\text{In}(\text{NO}_3)_3 \cdot x\text{H}_2\text{O}$ and 0.12 g $\text{Y}(\text{NO}_3)_3 \cdot 4\text{H}_2\text{O}$ (Sigma Aldrich, 99.99%), 0.61 g $\text{In}(\text{NO}_3)_3 \cdot x\text{H}_2\text{O}$ and 0.17 g $\text{Y}(\text{NO}_3)_3 \cdot 4\text{H}_2\text{O}$, and 0.57 g $\text{In}(\text{NO}_3)_3 \cdot x\text{H}_2\text{O}$ and 0.22 g $\text{Y}(\text{NO}_3)_3 \cdot 4\text{H}_2\text{O}$, respectively, were dissolved in a mixture of ethanol (70 cm^3) and deionized water (24 cm^3). For $3\text{La}10\text{In}/\text{ZrO}_2$, 0.61 g $\text{In}(\text{NO}_3)_3 \cdot x\text{H}_2\text{O}$ and 0.22 g $\text{La}(\text{NO}_3)_3 \cdot 6\text{H}_2\text{O}$ (Sigma Aldrich, 99.99%) were dissolved in the same solvent as above. The rest of the procedures were the same as the unpromoted $\text{In}_2\text{O}_3/\text{ZrO}_2$.

4.2.2 Catalyst Characterization

The bulk composition in catalysts was determined using a Rigaku wavelength-dispersive X-ray fluorescence (WDXRF) spectrometer. The sample names of the

catalysts are based on the metal weight percentages obtained from WDXRF. Textural characterization of the samples was carried out using N₂ adsorption at 77 K. Isotherms were collected on a Micrometrics 3Flex and analyzed using Brunauer–Emmett–Teller (BET) method to calculate surface area, and the Barrett-Joyner-Halenda (BJH) method was used to calculate pore volume and pore size distribution. X-Ray Diffraction (XRD) patterns of catalyst powders were collected at room temperature on a Bruker diffractometer using Cu K α radiation ($\lambda = 1.5418 \text{ \AA}$). Measurements were taken over the range of $20^\circ < 2\theta < 70^\circ$ with a step size of 0.02° . The phase was identified by comparing the diffraction patterns with the conventional Joint Committee on Powder Diffraction Standards (JCPDSs). Scanning electronic microscopy (SEM) analyses were carried out on a Zeiss SEM/FIB Auriga-60. X-ray photoelectron spectroscopy (XPS) measurements were performed on a K-alpha Thermo Fisher Scientific spectrometer using monochromated Al K α X-ray source. The measurements of indium oxides on supported ZrO₂ (In₂O₃/ZrO₂), and other Y or La-promoted catalysts (1.5Y9In/ZrO₂, 2Y8In/ZrO₂, 3Y8In/ZrO₂, and 3La-10In/ZrO₂) were done with a spot size of 400 μm at ambient temperature and a chamber pressure of $\sim 10^{-7}$ mbar. A flood gun was used for charge compensation. All the measured spectra were calibrated by setting the reference binding energy of adventitious carbon *1s* signal at 284.8 eV. The spectra were analyzed using Avantage[®] surface chemical analysis software (v5.986). For the spectral fitting, each component consists of a linear combination of Gaussian and Lorentzian product functions. SMART background was used over the region to define the peaks.

Temperature-programmed reduction (TPR) and temperature-programmed desorption (TPD) were carried out by using an Altamira AMI-200 catalyst

characterization flow system. Analysis of the gaseous effluent was carried out using a thermal conductivity detector (TCD) to detect the H₂ or CO₂ concentrations during the experiment. H₂-TPR was conducted via 2 steps: (i) the sample (50 mg) was dried at 398 K for 30 min in Ar (60 sccm); (ii) The TPD trace was obtained by increasing the temperature up to 973 K in a gaseous mixture of 10% H₂/Ar at the rate of 5 K min⁻¹. CO₂-TPD was conducted as the following steps: (i) 50 mg of sample was dried at 398 K for 30 min in He (40 sccm); (ii) the sample was then treated with He (40 sccm) at 573 K for 60 min and then cooled down to 313 K under the same gas stream; (iii) CO₂ adsorption was carried out at 313 K with 50% CO₂/He gaseous mixture (40sccm) for 2 h; (iv) the desorption process was programmed from 313 K to 873 K with 40 sccm He. The ramping rates in all the CO₂-TPD experiments was 5 K min⁻¹.

4.2.3 Reactor setup and catalytic activity

The reaction rates and other kinetic parameters were measured using a packed-bed microreactor operated in a down-flow mode under high pressure. 40 bar is the standard operating pressure controlled by a back pressure regulator (Swagelok[®], KPB series, 0-2000 PSIG). The setup was equipped with multiple mass flow controllers (Brooks SLA5850 and Bronkhorst EL-Flow F211CV) to feed H₂ (Keen, 99.999%), CO₂ (Keen, 99.999%), CO (Matheson, 99.99%), and He (Keen, 99.999%). A fixed-bed and down-stream reactor setup was used in this study. 0.15 g catalyst pellets (particle size: 250-420 μm) were placed between two plugs of quartz wool within a 316 SS tube (4.6 mm ID). The reactor bed temperature was monitored by the insertion of a thermocouple through the top of the reactor (Omega, K-type, 1/8 in. diameter). The thermocouples also helped maintain the position of the bed within the reactor tube. Prior to the reaction, the catalyst was activated at 573 K and 5 bar He for 1 h.

Activity tests were conducted under $P_{tot} = 40$ bar, $T = 528\text{K}$, 543K , 558K , or 573K , a total flow rate $F_{tot} = 130\text{ cm}^3\text{ STP min}^{-1}$ (sccm), and the volumetric feed composition of $\text{H}_2:\text{CO}_2:\text{He} = 80:20:30$. The standard gas hourly space velocity (GHSV) that is used was $52000\text{ cm}^3\text{ h}^{-1}\text{ g}_{cat}^{-1}$. Each condition was held for 3 h or when the effluent composition was in steady state. Helium was used as internal standard gas for concentration calibration due to the change of the total volumetric flow rate in the effluent after the CO_2 hydrogenation reaction. Gas lines after the reactor were kept at 433 K using heating tape to avoid condensation of products. The composition of the effluent stream was analyzed online by a gas chromatograph (490 MicroGC, Agilent) during continuous flow experiments. The MicroGC was equipped with a thermal conductivity detector (TCD) to quantify H_2 , He , CO_2 , CO , and CH_3OH .

Gas hourly space velocity (GHSV) in $\text{cm}^3\text{ h}^{-1}\text{ g}_{cat}^{-1}$ was calculated according to the equation below:

$$GHSV = \frac{F_{tot}}{w_{cat.}} \quad (\text{Eq. 4.1})$$

where $w_{cat.}$ is the weight of the catalyst.

The CO_2 conversion (X_{CO_2}), CH_3OH selectivity (S_{MeOH}), CO formation rate (r_{CO}), and methanol formation rate (r_{MeOH}) were calculated according to the following expressions:

$$X_{\text{CO}_2} = \frac{\dot{N}_{\text{CO}_2,in} - \dot{N}_{\text{CO}_2,out}}{\dot{N}_{\text{CO}_2,in}} \quad (\text{Eq. 4.2})$$

where \dot{N}_i stands for the molar flowrate of species i .

$$S_{MeOH} = \frac{\dot{N}_{MeOH,out}}{\dot{N}_{MeOH,out} + \dot{N}_{CO,out}} \quad (\text{Eq. 4.3})$$

$$r_i = \frac{\dot{N}_{i,in} \cdot X_{CO_2} \cdot S_i \cdot M_i}{w_{cat.}} \quad (\text{Eq. 4.4})$$

where S_i and M_i are the selectivity and the molar mass of species i , respectively.

Apparent kinetic parameters (activation energy and reaction orders) were determined near the region of $CO_2/H_2 = 4:1$ molar ratio over 0.15 g indium oxide-based catalysts. The apparent activation energy was obtained by measuring the methanol formation rate with respect to the temperature of the reaction from 573 K to 528 K in intervals of 15 K. The reaction orders of 2Y8In/ZrO₂ catalyst at 573 K were calculated from the dependence of methanol formation rate on H₂ or CO₂ partial pressure. The H₂ reaction order was obtained from the change of H₂ partial pressure, which corresponded to the change of H₂ flow rate (F_{H_2}). F_{H_2} was 60, 70, 80, 85, and 90 sccm, while F_{CO_2} was 20 sccm. F_{He} was adjusted accordingly to keep constant total flow rate. In CO₂ reaction order experiment, F_{CO_2} was 12 to 28 sccm with 4 sccm increment. F_{He} was also adjusted stepwise to keep $F_{tot} = 130$ sccm while a constant $F_{H_2} = 80$ sccm was fed into the reactor. In the CO co-feeding experiments over 2Y8In/ZrO₂ at 573K and 543K, F_{H_2} and F_{CO_2} remained constant at 80 and 20 sccm, respectively. The amount of He fed into the system, F_{He} (initially at 110 cm³ STP min⁻¹) was reduced stepwise while feeding progressively higher amounts of CO resulting in a molar carbon ratio of $R = CO/(CO_2+CO) = 0, 0.20, 0.33, 0.43, 0.50$. The conversion at $R = 0$ was acquired again after the measurement at $R = 0.50$ to control for any change of activity due to deactivation. An additional CO-TPD experiment was

conducted in the same reactor setup as measuring the catalytic reaction rates and the CO signal was monitored using a mass spectrometer (MS, Pfeiffer, GSD320). Before the TPD process, 0.1 g 2Y8In/ZrO₂ was pretreated in 100 sccm He at 458 K for 1 h to clean the sample surface, followed by 20% H₂/He (50 sccm) to partially reduce the surface. 20% CO/He (50 sccm) was then fed into the reactor at 313 K for 2h. The TPD trace was obtained by increasing the temperature from 313 K to 873 K under a constant flow of 50 sccm He.

4.3 Results and Discussion

The SEM images of In₂O₃/ZrO₂, 1.5Y9In/ZrO₂, and 3La10In/ZrO₂ show that the catalysts particles are formed of aggregates of smaller particles. The aggregates have a broad range of sizes (~100 nm to ~5μm, see Figure 4.1). The physical and textural properties of In₂O₃/ZrO₂ and the promoted catalysts were determined using N₂ adsorption, XRF, and XPS (Table 4.2). The measured surface area and the total pore volume (V_P) correspond closely to the properties of the ZrO₂ carrier (~100 m²/g) in all cases. The BET surface area (S_{BET}) of the un-promoted In₂O₃/ZrO₂ was 87 m²/g, while for the promoted catalysts the surface area ranged from 84 m²/g to 88 m²/g. Total pore volume (V_P) of the catalysts was in the narrow range of 0.21 cm³/g to 0.23 cm³/g. The incorporation of Y and La slightly decreased the relative fraction of the smaller pores and larger pores but increased the amount of medium sized pores as seen in the pore size distribution (see Figure 4.2). Clearly, the effect of yttrium and lanthanum oxides on surface area and porosity is small (vide infra). The bulk weight percentage, in metallic base, of Y, La and In of the catalyst (W_Y , W_{La} , and W_{In}) were also determined from XRF. All of observed amounts were close to the nominal weight percentages calculated from the amount of the precursors used during catalyst preparation. The

surface density of In atoms in the (1 1 1) surface of crystalline In_2O_3 was estimated to be 8.67×10^{18} In atoms/ m^2 [119,120]. Based on the BET surface area and the loading of In atoms measured from XRF, the un-promoted $\text{In}_2\text{O}_3/\text{ZrO}_2$ had approximately 6.1×10^{18} In atoms/ m^2 . Assuming a uniform distribution, the thickness of the deposited indium oxide layer can be estimated by the ratio of the measured In atom density to the theoretical In atom surface density. The coverage for $\text{In}_2\text{O}_3/\text{ZrO}_2$ was ~ 0.7 , whereas for the Y-promoted catalysts was ~ 0.6 . The amount of In_2O_3 deposited on the catalysts was slightly less than a monolayer if the distribution of In is uniform on the ZrO_2 surface.

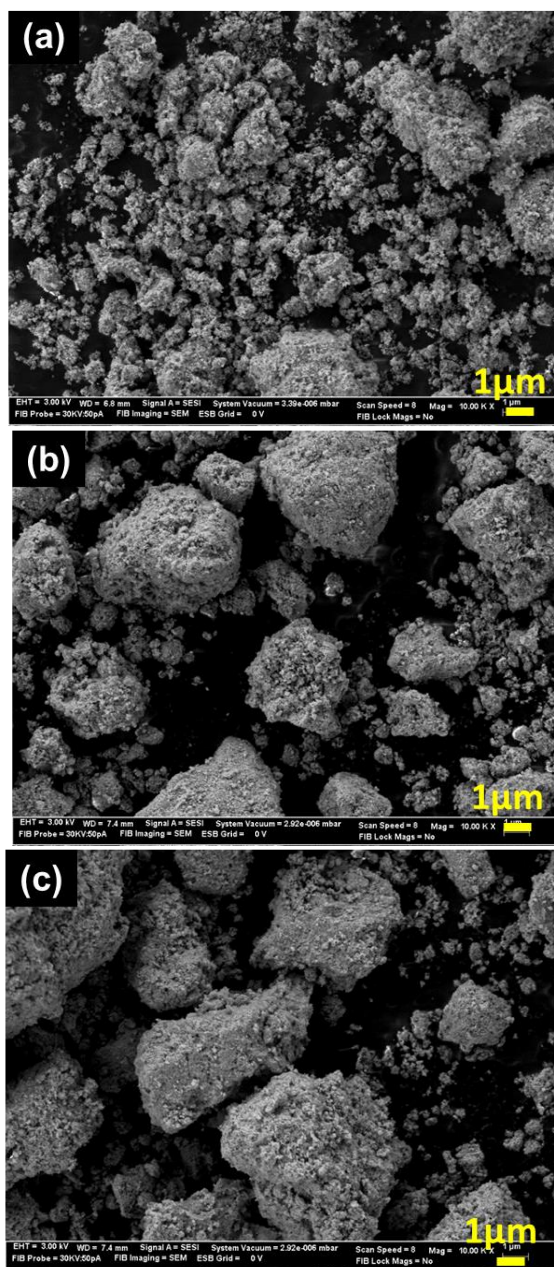


Figure 4.1 SEM images of (a) $\text{In}_2\text{O}_3/\text{ZrO}_2$, (b) $1.5\text{Y}9\text{In}/\text{ZrO}_2$, and (c) $3\text{La}10\text{In}/\text{ZrO}_2$.

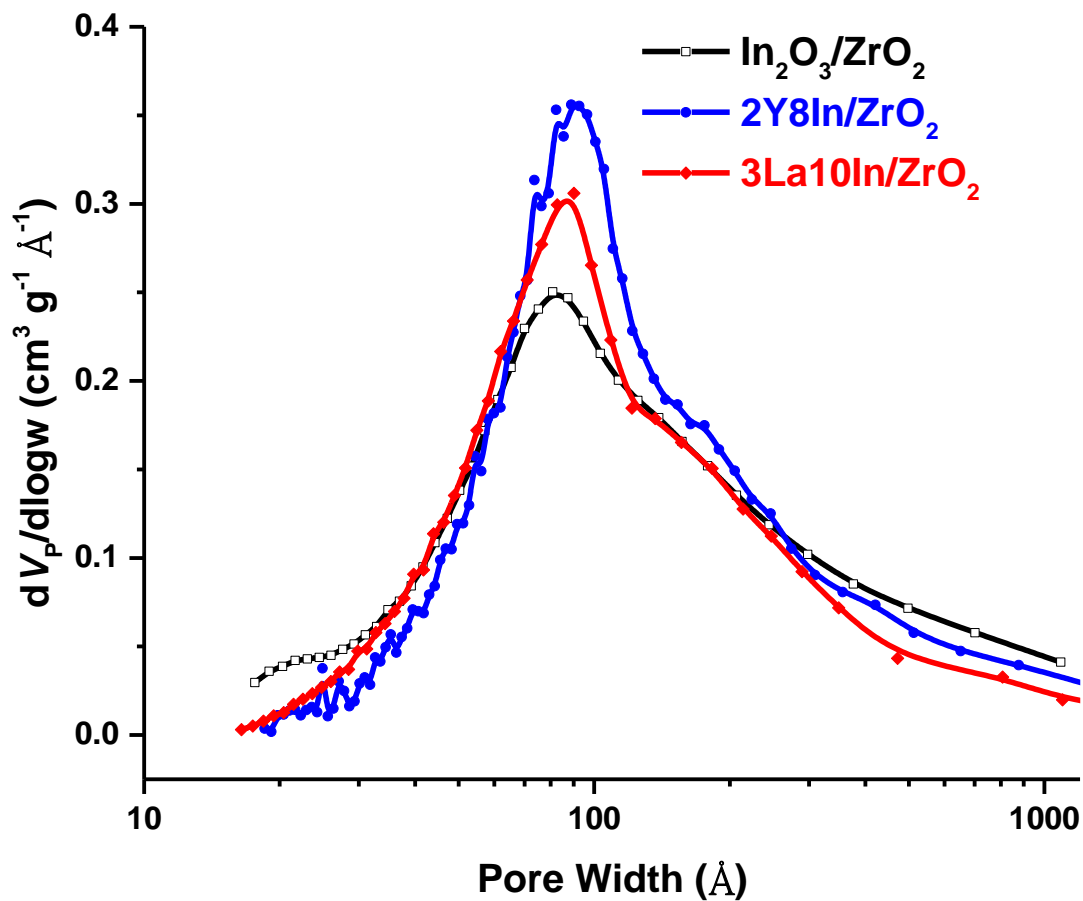


Figure 4.2 Pore size distribution of $\text{In}_2\text{O}_3/\text{ZrO}_2$, $2\text{Y}8\text{In}/\text{ZrO}_2$, and $3\text{La}10\text{In}/\text{ZrO}_2$.

In contrast to XRF, XPS is a surface sensitive technique and can reveal information about the surface composition of the promoted catalysts. W_{In} measured from XPS were also similar to the nominal concentration of the catalysts; however, W_{Y} , W_{La} on the surface were much higher than the nominal concentration. W_{Y} or W_{La} from XPS of $1.5\text{Y}9\text{In}/\text{ZrO}_2$, $2\text{Y}8\text{In}/\text{ZrO}_2$, $3\text{Y}8\text{In}/\text{ZrO}_2$, and $3\text{La}10\text{In}/\text{ZrO}_2$ were 3.1%,

4.0%, 5.3%, and 7.0%, respectively. It appears then that Y or La are preferably located on the surface of the sample after the synthesis process. Further analyses of the XPS spectra show that the atomic In/Zr ratios of $\text{In}_2\text{O}_3/\text{ZrO}_2$ and $3\text{La}10\text{In}/\text{ZrO}_2$ were both 0.17, while the In/Zr ratios of $1.5\text{Y}9\text{In}/\text{ZrO}_2$, $2\text{Y}8\text{In}/\text{ZrO}_2$, $3\text{Y}8\text{In}/\text{ZrO}_2$ were 0.11-0.12 (see Table 4.2). The In/Zr ratios of Y-modified samples decreased after the incorporation of yttrium oxide. This result implies that the surface of Y-modified samples contained less In_2O_3 that were deposited per ZrO_2 particle on the surface, resulting in lower methanol formation rate with respect to the catalyst weight. ($0.465 \text{ g}_{\text{MeOH}} \text{ g}_{\text{cat.}}^{-1} \text{ h}^{-1}$ for $\text{In}_2\text{O}_3/\text{ZrO}_2$ and $0.420 \text{ g}_{\text{MeOH}} \text{ g}_{\text{cat.}}^{-1} \text{ h}^{-1}$ for $1.5\text{Y}9\text{In}/\text{ZrO}_2$ at 573 K. See Figure 4.10 (c)). This may occur if there are In_2O_3 oxide particles (with In inaccessible to XPS) in the final form of the catalyst. On the other hand, $3\text{La}10\text{In}/\text{ZrO}_2$ had a similar In/Zr atomic ratio than $\text{In}_2\text{O}_3/\text{ZrO}_2$, which is consistent to its similar methanol formation rate compared to $\text{In}_2\text{O}_3/\text{ZrO}_2$ catalyst (see below).

Table 4.2 Physical properties of In₂O₃/ZrO₂ and promoted catalysts determined by N₂ adsorption, XRF, and XPS.

Sample	N ₂ adsorption		Nominal amount in precursors		XRF		XPS		
	S _{BET} ^a	V _P ^a	W _Y or W _{La}	W _{In}	W _Y or W _{La}	W _{In}	W _Y or W _{La}	W _{In}	In/Zr atomic ratio
	(m ² /g)	(cm ³ /g)	(%)	(%)	(%)	(%)	(%)	(%)	
In ₂ O ₃ /ZrO ₂	87	0.22	-	10.5	-	10.1	-	12.7	0.17
1.5Y9In/ZrO ₂	84	0.23	1.5	8.5	1.5	9.1	3.1	9.2	0.12
2Y8In/ZrO ₂	84	0.22	2.0	8.3	2.3	8.4	4.0	8.0	0.11
3Y8In/ZrO ₂	88	0.23	2.5	7.8	2.9	8.4	5.3	8.0	0.11
3La10In/ZrO ₂	84	0.21	3.3	8.2	3.4	9.9	7.0	11.5	0.17

^a S_{BET} and V_P represented the BET surface area and total pore volume, respectively.

The XRD patterns of ZrO₂, In₂O₃, In₂O₃/ZrO₂, 1.5Y9In/ZrO₂, and 3La10In/ZrO₂ (Figure 4.3) show that the support is monoclinic ZrO₂ (PDF#00-001-0750): the carrier structure did not change appreciably by the wet impregnation or the calcination. Peaks of pure In₂O₃ were identified at $2\theta = 21.49^\circ$, 30.58° , 35.45° , and 51.02° and were assigned to the (2 1 1), (2 2 2), (4 0 0), and (4 4 0) reflections of the cubic In₂O₃ (PDF#00-044-1087): these peaks can be found in In₂O₃/ZrO₂, 1.5Y9In/ZrO₂, and 3La10In/ZrO₂ as well, indicating that at least some of In₂O₃ in the supported materials exist in crystalline form after calcination in air. For 1.5Y9In/ZrO₂, and 3La10In/ZrO₂ catalysts, no characteristic diffraction peaks of Y or La related

compound can be observed. However, Y^{3+} or La^{3+} could still be identified on the surface by XPS (see Figure 4.4). The absence of reflections of Y and La in the XRD patterns indicates that yttrium oxide and lanthanum oxide particles are too small or the loading of these two materials is too low to be detected by XRD. XRD patterns and the XPS spectra together suggest that Y and La oxides exist in a highly dispersed form such as nano-crystallites or well-mixed with the oxide in thin layers on the surface of the material after the calcination in air. To further illustrate the intermixing of In and Y/La, SEM-EDX layered images of In_2O_3/ZrO_2 , $2Y_8In/ZrO_2$, and $3La_{10}In/ZrO_2$ are shown in Figure 4.5.

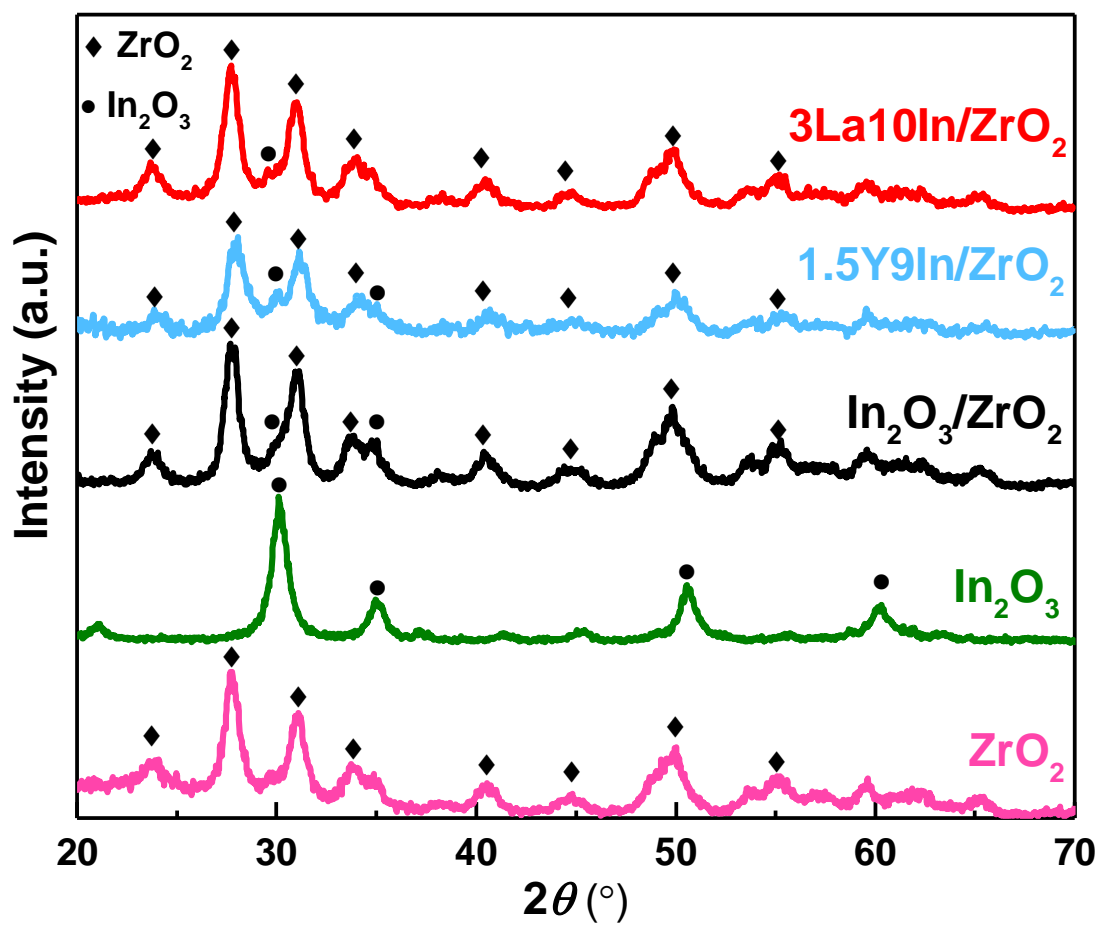


Figure 4.3 XRD patterns of ZrO₂, In₂O₃, In₂O₃/ZrO₂, 1.5Y9In/ZrO₂, and 3La10In/ZrO₂.

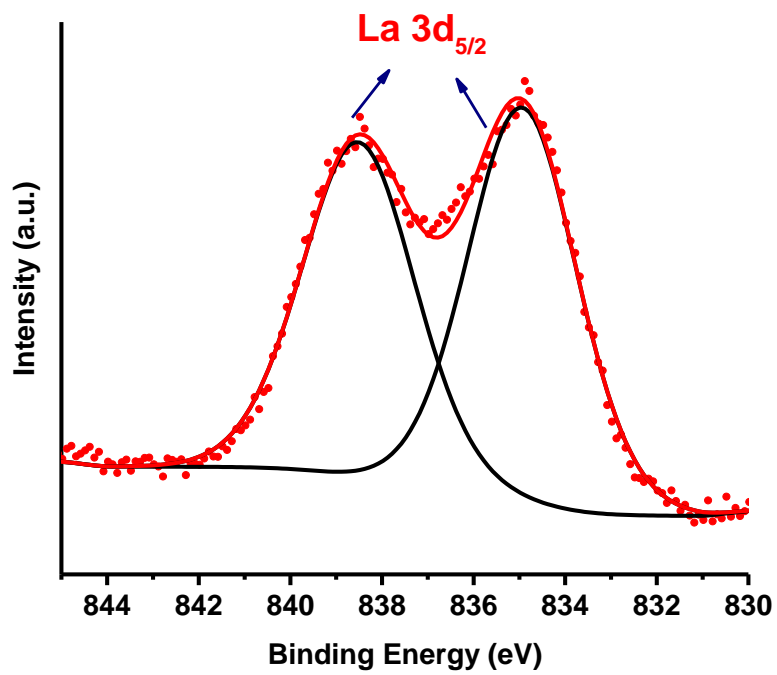
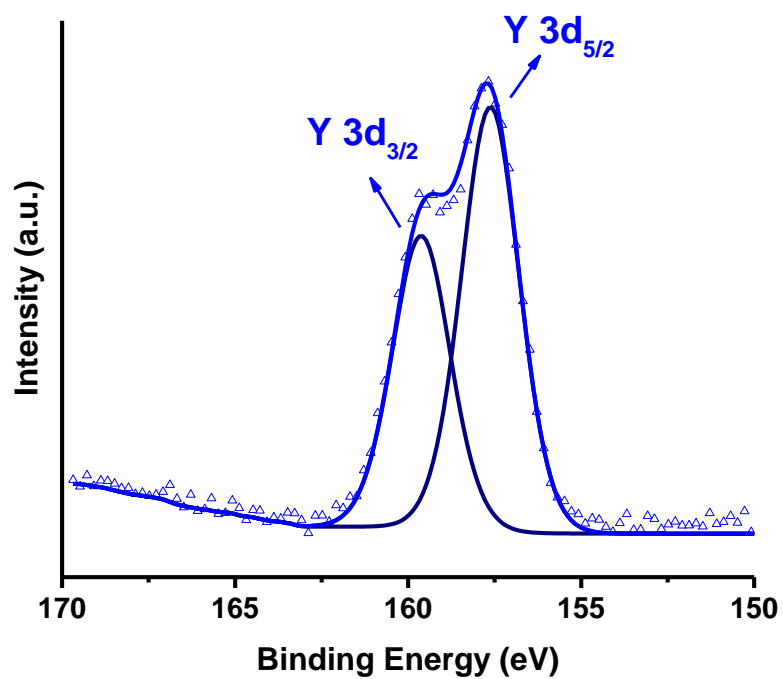


Figure 4.4 XPS spectra of Y 3d in 2Y8In/ZrO₂ and La 3d_{5/2} in 3La10In/ZrO₂ after calcined in air at 573 K for 3h.

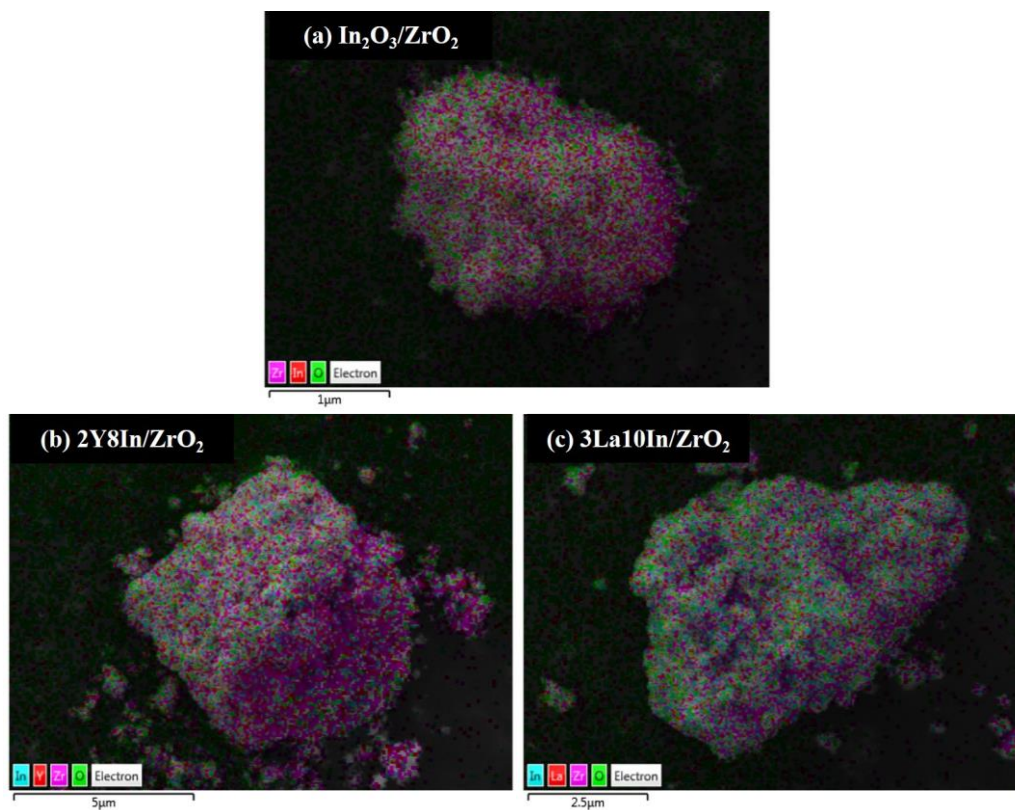


Figure 4.5 SEM-EDX layered images of (a) $\text{In}_2\text{O}_3/\text{ZrO}_2$, (b) $2\text{Y}8\text{In}/\text{ZrO}_2$, and (c) $3\text{La}10\text{In}/\text{ZrO}_2$.

The reducibility of the catalysts was examined by H_2 -TPR (Figure 4.6). For $\text{In}_2\text{O}_3/\text{ZrO}_2$, evidence for reduction starts at around 423 K, consistent with past reports [110][121]. The main peak at 470 K was assigned to the surface reduction of In_2O_3 , and the later small and broad signal near 647 K is assigned to the bulk reduction of In_2O_3 . H_2 consumption near 647 K is small due to the low loading of the In_2O_3 in $\text{In}_2\text{O}_3/\text{ZrO}_2$.

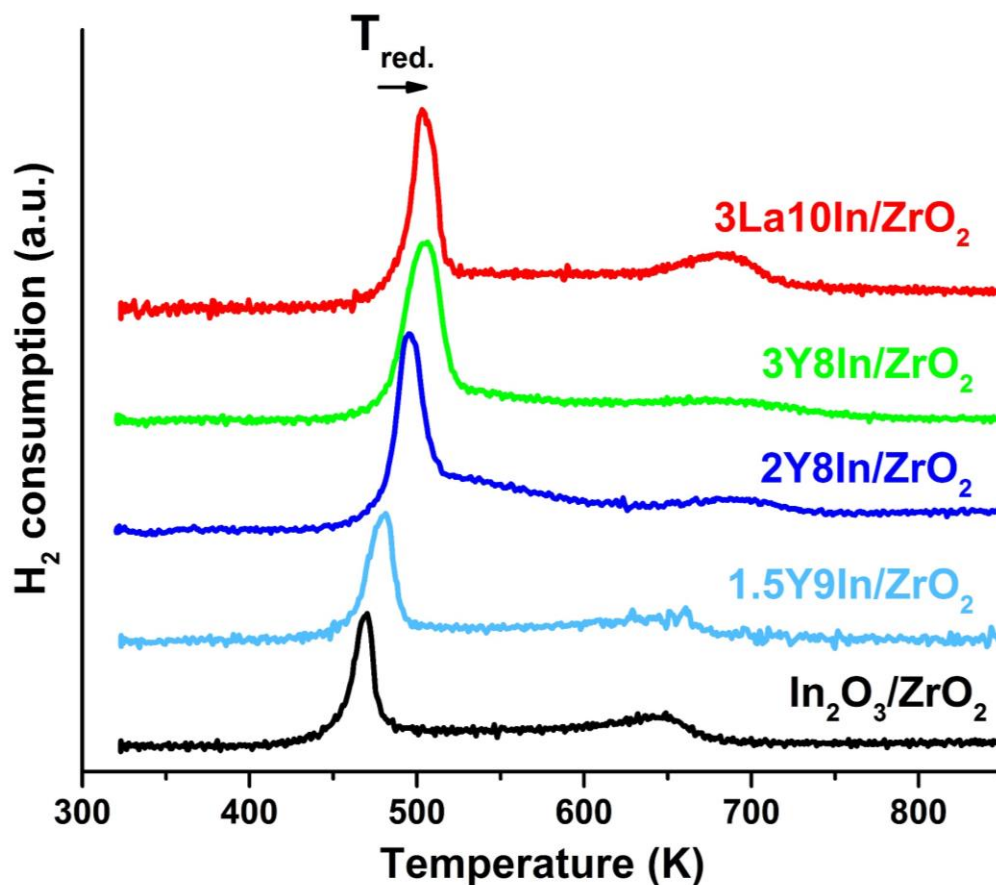


Figure 4.6 H₂-TPR profiles of In₂O₃/ZrO₂, 1.5Y9In/ZrO₂, 2Y8In/ZrO₂, 3Y8In/ZrO₂, and 3La10In/ZrO₂.

A control TPR experiment (Figure 4.7) performed on unsupported In₂O₃ showed much higher H₂ consumption in this region, as expected from bulk reduction studies described in other reports [110]. All the surface In₂O₃ reduction peaks of our samples had similar reduction temperature windows (~50 K), but the modified catalysts showed shifted TPR profiles: the reduction peaks of Y-modified samples, 1.5Y9In/ZrO₂, 2Y8In/ZrO₂, 3Y8In/ZrO₂, were at 481 K, 496 K, and 505 K, respectively. That is, higher yttrium concentration led to higher reduction

temperatures. 3La10In/ZrO₂ also showed a higher reduction temperature for surface In₂O₃ at 503 K, which is 33 K higher than the un-promoted In₂O₃/ZrO₂. These data show that, as expected, incorporation of the less reducible Y³⁺ and La³⁺ cations onto the surface of In₂O₃ decrease the reducibility of In-based catalysts.

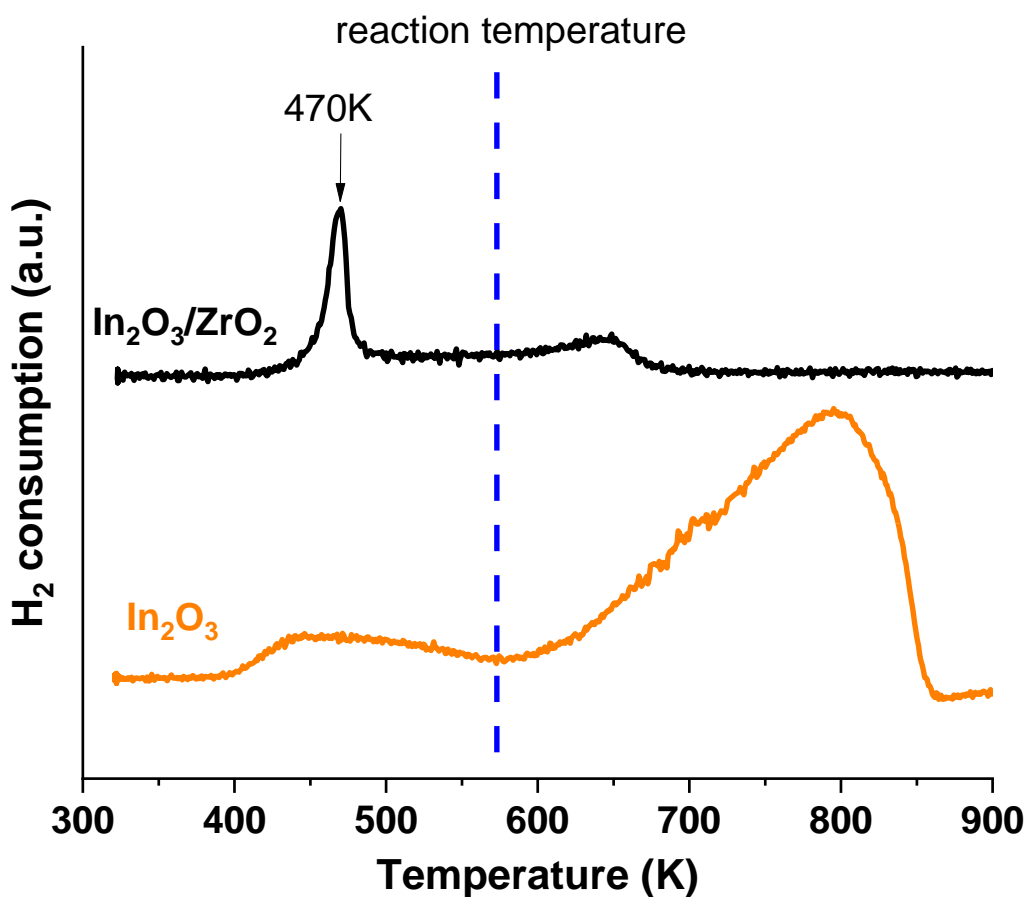


Figure 4.7 H₂-TPR profiles of unsupported In₂O₃ and In₂O₃/ZrO₂.

The CO₂-TPD profile (Figure 4.8) for samples with different compositions were recorded after heat treatment at 573 K in helium for 1 h. The CO₂ desorption

profiles of all catalysts exhibited one peak at $T < 400$ K and one broad peak in the region of $570 \text{ K} < T < 800 \text{ K}$. The first peak is assigned to the desorption of physically adsorbed CO_2 . The later peaks, which can be further deconvoluted into Gaussian peaks α and β for $2\text{Y}8\text{In}/\text{ZrO}_2$ and $3\text{La}10\text{In}/\text{ZrO}_2$, are assigned to the desorption of chemically adsorbed CO_2 . There are two common ways to create oxygen vacancies on In_2O_3 clusters for CO_2 hydrogenation [110]. One is thermal-induced oxygen vacancies (denoted here as $\text{O}_{\text{v}1}$) and the other is H_2 -induced oxygen vacancies (denoted here as $\text{O}_{\text{v}2}$). HCOO has been suggested as a key intermediate that is both thermodynamically and kinetically favorable, based on DFT investigations on In_2O_3 catalyst [44,45]. Oxygen vacancy sites on the In_2O_3 surface facilitate both CO_2 adsorption, hydrogenation, and stabilize intermediates (HCOO , H_2COO , and H_2CO) involved in methanol formation.

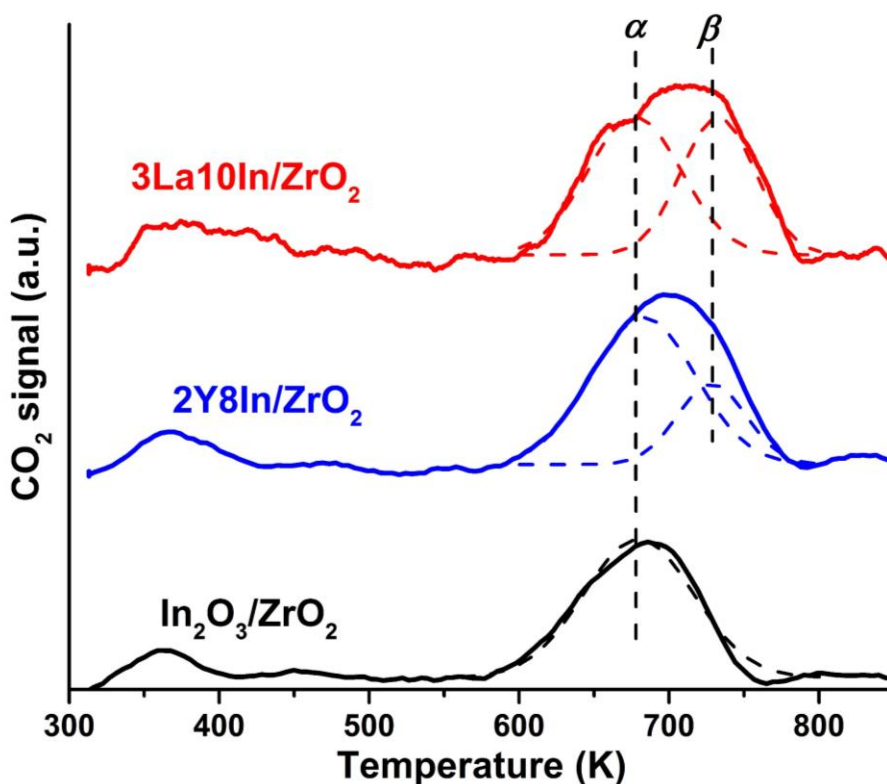


Figure 4.8 CO₂-TPD profiles of In₂O₃/ZrO₂, 2Y8In/ZrO₂, and 3La10In/ZrO₂ after He treatment at 573 K for 1 h.

Since the samples for CO₂ adsorption measurements were treated under inert gas at 573 K (without any reduction steps), the high-temperature peaks (α and β) in the CO₂-TPD profiles are assigned to O_{v1} vacancies. The β peaks are assigned to stronger basic sites induced by the incorporation of Y and La. The α peak maxima associated with O_{v1, α} were 680 K, 682 K, and 678 K for In₂O₃/ZrO₂, 2Y8In/ZrO₂, and 3La10In/ZrO₂, respectively. The β peak maxima associated with O_{v1, β} were 728 K and 732 K for 2Y8In/ZrO₂ and 3La10In/ZrO₂, respectively. The increasing CO₂ desorption temperature in the β peaks indicates an increase of the basicity for O_{v1} sites in Y or

La-promoted samples. The strength of the adsorption sites in terms of CO₂ adsorption follows the order 3La10In/ZrO₂ > 2Y8In/ZrO₂ > In₂O₃/ZrO₂. Note that 3La10In/ZrO₂ and 2Y8In/ZrO₂ desorbed more CO₂ than In₂O₃/ZrO₂ according to the integrated peak area from their TPD profiles. The total peak area associated with O_{v1} was normalized by the amount of indium loading for each catalyst, and the ratio of the area per indium loading was In₂O₃/ZrO₂:2Y8In/ZrO₂:3La10In/ZrO₂ = 1:1.6:1.7, that is, the density of surface O_{v1} sites was 60 or 70% higher for Y or La-promoted catalysts compared to In₂O₃/ZrO₂. The XPS spectra of the concentration of oxygen near defects for In₂O₃/ZrO₂, 2Y8In/ZrO₂, and 3La10In/ZrO₂ are consistent with the higher density of oxygen vacancies in the promoted samples, as shown above (see also Figure 4.9). Together, the results from H₂-TPR and CO₂-TPD indicate that Y and La promoters suppress the creation of O_{v2} by making the catalysts less reducible, strengthen the CO₂ adsorption of O_{v1}, and consequently, enhance the methanol selectivity (see below).

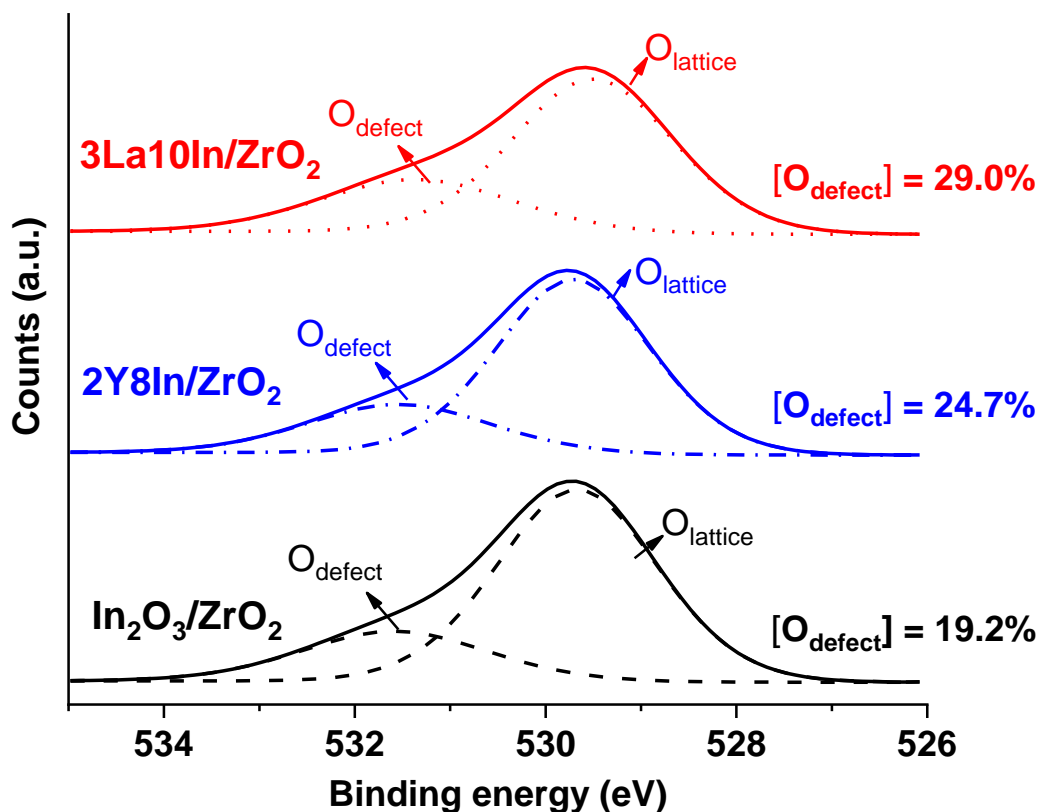


Figure 4.9 XPS spectra of O1s in $\text{In}_2\text{O}_3/\text{ZrO}_2$, $2\text{Y8In}/\text{ZrO}_2$, and $3\text{La10In}/\text{ZrO}_2$ after calcined in air at 573 K for 3h. The $[\text{O}_{\text{defect}}]$ is defined as: $[\text{O}_{\text{defect}}] = (\text{Area of } \text{O}_{\text{defect}}) / (\text{Area of } \text{O}_{\text{defect}} + \text{Area of } \text{O}_{\text{lattice}})$

The catalytic properties of $\text{In}_2\text{O}_3/\text{ZrO}_2$, $1.5\text{Y9In}/\text{ZrO}_2$, $2\text{Y8In}/\text{ZrO}_2$, $3\text{Y8In}/\text{ZrO}_2$, and $3\text{La10In}/\text{ZrO}_2$ (Figure 4.10) can be compared in terms of (a) CO_2 conversion, (b) methanol selectivity, (c) methanol formation rate, and (d) CO formation rate. The methanol selectivity versus CO_2 conversion for all catalysts is also shown in Figure 4.10 (e). For all catalysts, CO_2 conversion, methanol and CO formation rate increased with increasing reaction temperature from 528 K to 573 K. In addition, for all samples the conversion ranged between 0.9% to 10.5%: at 573 K, 558 K, and 543 K. The relative magnitude of CO_2 conversion was: $\text{In}_2\text{O}_3/\text{ZrO}_2 >$

$3\text{La}10\text{In}/\text{ZrO}_2 > 1.5\text{Y}9\text{In}/\text{ZrO}_2 > 2\text{Y}8\text{In}/\text{ZrO}_2 > 3\text{Y}8\text{In}/\text{ZrO}_2$. At 528 K, CO_2 conversion was similar for all catalysts from 0.9% to 1.3%. Methanol and CO were the only two carbon-containing products that were found in this CO_2 hydrogenation process (Figure 4.10 (b)), thus confirming that the In_2O_3 -based catalysts have high methanol selectivity. The selectivity to methanol decreased with temperature increase and CO production is more favorable at higher temperature due, in part, to the endothermicity of the RWGS reaction (Figure 4.10 (d)). This has been also found in the CO_2 hydrogenation over the classical Cu-based catalysts [122–124]. The CO_2 conversion and methanol formation rate over $\text{In}_2\text{O}_3/\text{ZrO}_2$ in this work was higher (At 573 K, 10.5% and $0.465 \text{ g}_{\text{MeOH}} \text{ g}_{\text{cat.}}^{-1} \text{ h}^{-1}$, respectively) than most other reports in the CO_2 to methanol reaction [43,46,115,125–128] (also see Table 4.1). The properties of the $\text{In}_2\text{O}_3/\text{ZrO}_2$ catalyst investigated here were highly temperature-sensitive (53-81% in methanol selectivity from 573 K to 528 K). Given the relatively low pressure (40 bar) in this investigation, the selectivity of this catalyst is expected to be lower than the values reported by Martin *et. al.*, that indicated 99.8% methanol selectivity over $\text{In}_2\text{O}_3/\text{ZrO}_2$ catalyst at 50 bar [46]. In a more recent report [55] from the same group, a methanol selectivity of 45%-65% with $\text{H}_2:\text{CO}_2$ ratios near 5 (see the supporting information of Ref. [55]) was observed under similar reaction conditions used in the previous publication [46]. Other reports have also showed moderate selectivity, between 40-70% in methanol [43] [110] (Table 4.1), suggesting that the high selectivity shown in Martin *et. al.*'s report is difficult to reproduce.

Rare earth elements, such as La, Ce, and Y were found to enhance the Cu surface area and CO_2 adsorption [40,117,129,130]. Y_2O_3 or La_2O_3 has been used in Cu-based or $\text{Fe}/\text{Al}_2\text{O}_3$ catalysts to improve the catalytic activity in CO_2 hydrogenation

reaction [117,118,124,129,131–133]. Specifically, introduction of Y_2O_3 was seen as a method to increase the Cu dispersion and surface area for $\text{Cu}/\text{Zn}/\text{ZrO}_2$ [124], while Gao *et. al.* [129] found that Mn, La, Ce, Zr and Y modifiers could increase the density of basic sites and enhanced the methanol selectivity for 5-7% compared to the un-promoted Cu-based catalysts. To further improve the selectivity, Y_2O_3 and La_2O_3 were investigated as promoters on In-based catalysts by making the $\text{In}_2\text{O}_3/\text{ZrO}_2$ catalyst less reducible and more basic. The methanol selectivity of YIn/ZrO_2 and $3\text{La}10\text{In}/\text{ZrO}_2$ catalysts remained around 70% even when the reaction temperature reached 573 K, while the un-promoted $\text{In}_2\text{O}_3/\text{ZrO}_2$ had ~53% selectivity at the same reaction conditions. The increased selectivity occurs in parallel with a reduction in catalytic rates: CO_2 conversion at 573 K decreased from 10.5 % (on $\text{In}_2\text{O}_3/\text{ZrO}_2$) to ~7.7 % (on $1.5\text{Y}9\text{In}/\text{ZrO}_2$ and $2\text{Y}9\text{In}/\text{ZrO}_2$ catalysts). The decrease of CO_2 conversion rate resulted mainly from a suppression in the CO formation rate: at 573 K, the CO formation rate of $1.5\text{Y}-9\text{In}/\text{ZrO}_2$ was $0.164 \text{ g}_{\text{CO}} \text{ g}_{\text{cat.}}^{-1} \text{ h}^{-1}$, which is only 43% of the CO formation rate over non-promoted $\text{In}_2\text{O}_3/\text{ZrO}_2$ ($0.380 \text{ g}_{\text{CO}} \text{ g}_{\text{cat.}}^{-1} \text{ h}^{-1}$).

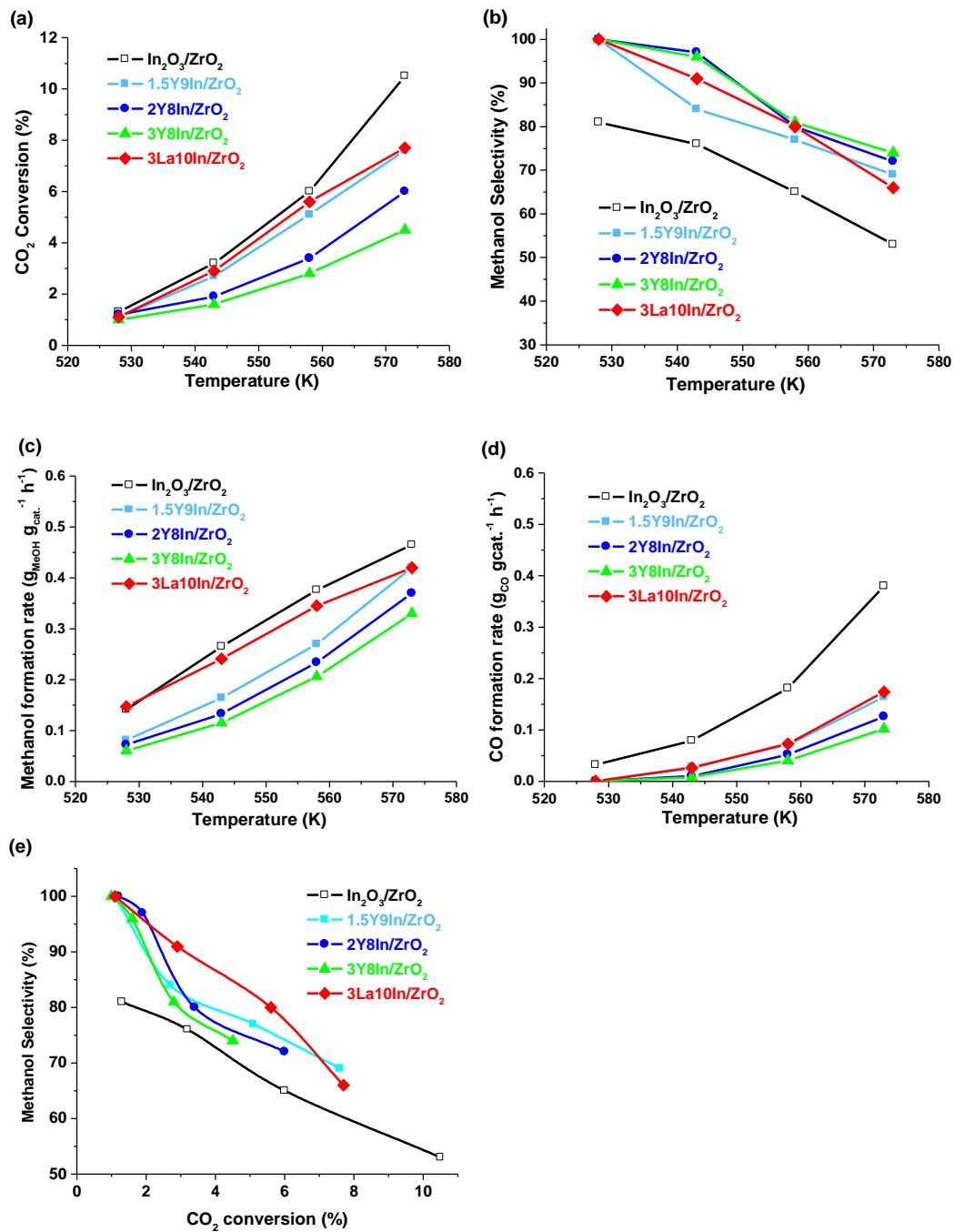


Figure 4.10 (a) CO_2 conversion, (b) selectivity to methanol, (c) methanol formation rate, and (d) CO formation rate versus temperature over $\text{In}_2\text{O}_3/\text{ZrO}_2$, $1.5\text{Y}_9\text{In}/\text{ZrO}_2$, $2\text{Y}_8\text{In}/\text{ZrO}_2$, $3\text{Y}_8\text{In}/\text{ZrO}_2$, and $3\text{La}_{10}\text{In}/\text{ZrO}_2$. (e) Methanol selectivity versus CO_2 conversion over the catalysts mentioned above.

The promotion effects of Y and La are observed under all conditions investigated. For example, an increase in methanol selectivity by about 20% is observed at all the temperatures (528 to 573 K). In fact, selectivity as high as 100% at low temperatures (528 K) could be reached for both Y and La-promoted indium oxide catalysts. Moreover, under isoconversion conditions (see Figure 4.10 (e)), e.g. 4%, methanol selectivity for the catalysts decreases in the following order: $3\text{La}10\text{In}/\text{ZrO}_2 > 1.5\text{Y}9\text{In}/\text{ZrO}_2 > 2\text{Y}8\text{In}/\text{ZrO}_2 > 3\text{Y}8\text{In}/\text{ZrO}_2 > \text{In}_2\text{O}_3/\text{ZrO}_2$, demonstrating that the modification of the catalysts is a feasible way to boost catalytic performance.

Figure 4.11 shows an Arrhenius plot of the methanol formation rate from CO_2 hydrogenation over In-based catalysts within the temperature range of 528 K and 573 K. The CO_2 conversion was less than 10% at all temperatures to ensure that the reactor operates under a differential regime. The apparent activation energy for CO_2 to methanol over $\text{In}_2\text{O}_3/\text{ZrO}_2$, $1.5\text{Y}9\text{In}/\text{ZrO}_2$, $2\text{Y}8\text{In}/\text{ZrO}_2$, $3\text{Y}8\text{In}/\text{ZrO}_2$, and $3\text{La}10\text{In}/\text{ZrO}_2$ were 66.3 kJ/mol, 91.4 kJ/mol, 92.0 kJ/mol, 95.7 kJ/mol, and 59.1 kJ/mol, respectively. The La-promoted indium oxide catalyst showed the lowest activation energy compared to the other catalysts. The activation energy of supported Cu-based catalysts is between 38 kJ/mol and 58 kJ/mol [134–138]; and the activation energy of bulk In_2O_3 was found to be 103 kJ/mol [55]. A higher activation energy (91.4–95.7 kJ/mol) was found in Y-promoted indium oxide catalysts compared to $\text{In}_2\text{O}_3/\text{ZrO}_2$. This implies that Y is directly affecting the active site of $\text{In}_2\text{O}_3/\text{ZrO}_2$ catalyst since otherwise the kinetically relevant reaction would occur on the original active sites. From the molecular stand point, the ionic radius of In^{3+} , Zr^{4+} , Y^{3+} , and La^{3+} are 92 pm, 87 pm, 106 pm, and 122 pm, respectively suggesting that the ionic

radius of the ions, with similar size with In^{3+} , is more likely to affect the reaction on $\text{In}_2\text{O}_3/\text{ZrO}_2$ catalysts, resulting in a different activation energy.

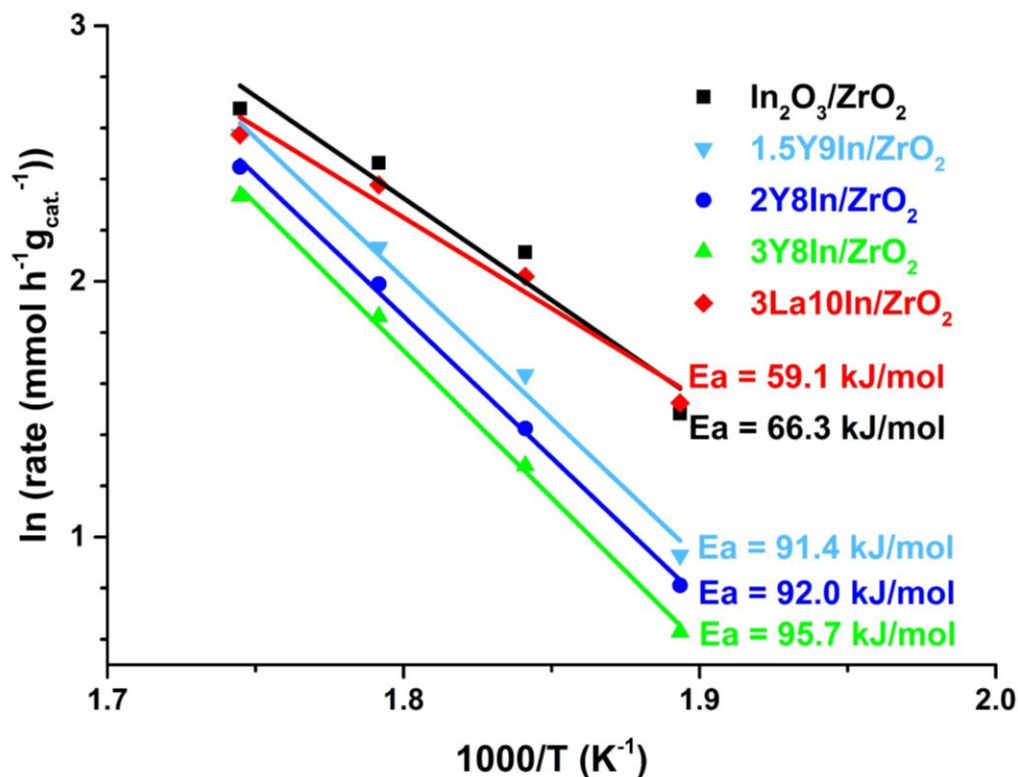


Figure 4.11 Arrhenius plot of methanol formation from CO_2 hydrogenation at 40 bar and 528 – 573 K over $\text{In}_2\text{O}_3/\text{ZrO}_2$, $1.5\text{Y}9\text{In}/\text{ZrO}_2$, $2\text{Y}8\text{In}/\text{ZrO}_2$, $3\text{Y}8\text{In}/\text{ZrO}_2$, and $3\text{La}10\text{In}/\text{ZrO}_2$.

The catalyst can also be compared with respect to methanol formation rate normalized by mole percent of surface In ($n\%_{\text{In, surface}}$) (see Figure 4.12). The normalized methanol formation rate is almost the same at every temperature for $\text{In}_2\text{O}_3/\text{ZrO}_2$ and $3\text{La}10\text{In}/\text{ZrO}_2$, but very different for the series of Y-incorporated

samples, which is consistent with the apparent activation energies in the reactions over these catalysts.

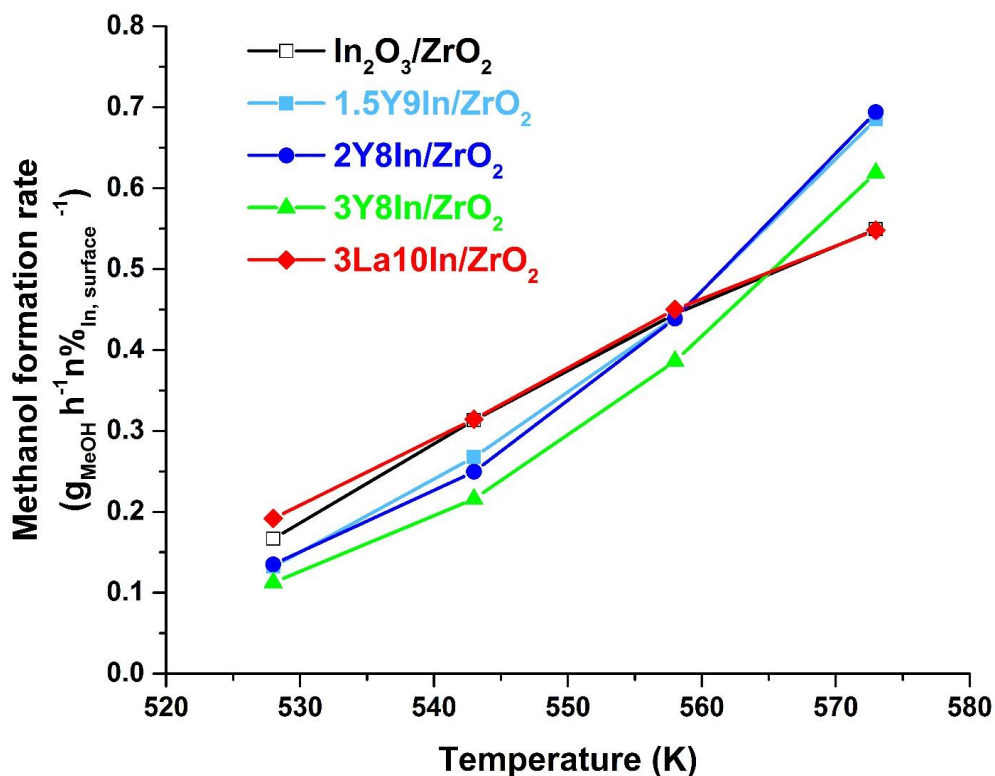


Figure 4.12 Methanol formation rate normalized by mole percent of surface In ($n\%_{\text{In, surface}}$) versus temperature over $\text{In}_2\text{O}_3/\text{ZrO}_2$, $1.5\text{Y9In}/\text{ZrO}_2$, $2\text{Y8In}/\text{ZrO}_2$, $3\text{Y8In}/\text{ZrO}_2$, and $3\text{La10In}/\text{ZrO}_2$. $n\%_{\text{In, surface}}$ was derived from XPS spectra for each sample.

The effect of reaction rates over $2\text{Y8In}/\text{ZrO}_2$ catalyst on partial pressure of the reactants was investigated at 573 K (Figure 4.13). The methanol formation rate has a high dependence on H_2 partial pressure with the apparent reaction order of 1.07. CO_2 , on the other hand, showed a negative reaction order of -0.13 near $\text{H}_2/\text{CO}_2 = 4:1$

relative composition. This result is similar to values recent reported by Frei *et. al.* [55] which showed that for bulk In_2O_3 , the reaction orders were estimate at -0.1 for CO_2 and 0.5 for H_2 above the stoichiometric ratio of $\text{H}_2/\text{CO}_2 = 3:1$. The negative reaction order of CO_2 on methanol formation rate was mainly due to the fact that higher CO_2 concentration would also favor the RWGS reaction and thus produce more CO . To reach high methanol formation rates, an excess of H_2 to CO_2 ratio is beneficial.

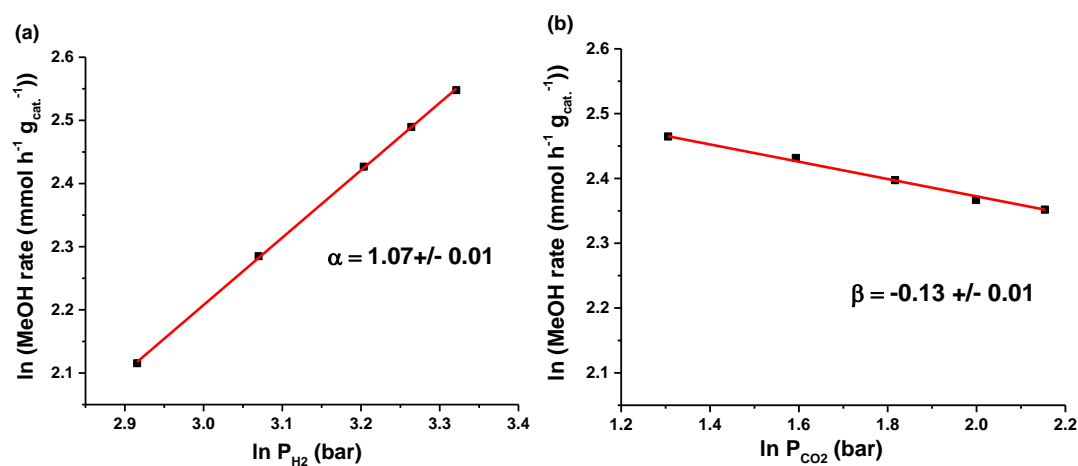


Figure 4.13 Reaction orders of (a) H_2 and (b) CO_2 for methanol synthesis at 573 K over 2Y8In/ZrO₂ catalyst.

From the above kinetic results, a power law rate expression and an Arrhenius form of the rate constant with respect to temperature can be obtained:

$$r_{\text{MeOH}} = k [\text{H}_2]^{1.07} [\text{CO}_2]^{-0.13} \quad (\text{Eq. 4.5})$$

$$k(T) = 1.66 \times 10^7 e^{\left(\frac{-96274}{RT}\right)} \quad (\text{Eq. 4.6})$$

Where r_{MeOH} is the methanol formation rate in $\text{mol s}^{-1} \text{kg}_{\text{cat.}}^{-1}$, k is the rate constant in $\text{mol s}^{-1} \text{kg}_{\text{cat.}}^{-1} (\text{mol/L})^{-0.94}$, R is the gas constant ($8.314 \text{ J mol}^{-1} \text{ K}^{-1}$).

The effect of co-feeding CO in the methanol formation rate was evaluated over 2Y8In/ZrO₂ at 543 K and 573 K (Figure 4.14) to assess the kinetic effects of CO and determine any potential recycling of the product stream, since CO is the main byproduct of the process at high temperature. CO has been used earlier as a strategy to generate more active oxygen vacancies [46]. However, a recent report showed that upon CO addition into the feed over bulk In₂O₃, a slightly higher methanol reactivity at lower pressure (3.5 MPa) could be obtained, but more than 40 % loss in methanol reactivity at higher pressure (5.5 MPa) was observed [55]. In our case, 2Y8In/ZrO₂ appears to be unaffected by CO and displays a fixed methanol formation rate within a ratio of CO/(CO+CO₂) from 0 to 0.5. This implies that CO₂ is the main carbon source of methanol synthesis over this sample. In a CO-TPD experiment over 2Y8In/ZrO₂ catalyst (Figure 4.15), we found no evidence of stable CO adsorption complexes on the surface after the catalyst was treated under reductive conditions.

The possible reaction channels for CO₂ hydrogenation to methanol have been discussed extensively [17,44,47,55,139–141]. In general, the first step of the hydrogenation of adsorbed CO₂ can lead to *HCOO (a formate intermediate, see Figure 4.16 (a)) or *HOCO (a carboxyl intermediate, see Figure 4.16 (b) and (c)). Alternatively, adsorbed CO₂ can dissociate into CO + O via the direct C–O bond cleavage pathway, and the formed *CO can desorb as a product CO in gas phase [54], but this path was not considered since CO is not easily hydrogenated to methanol on the indium catalysts. On the formate pathway, *HCOO can be hydrogenated to *HCOOH, and then to *H₂COOH, followed by bond cleavage to *H₂CO+*OH, *H₂CO+*H₂O, *H₂COH, and finally *H₃COH, sequentially. For the carboxyl pathway, HOCO was likely to go through the RWGS reaction and form *CO+ *OH.

Further hydrogenation on *CO will form *HCO, *H₂CO, *H₃CO, *H₃COH, sequentially. Frei and co-workers [55] have modeled the methanol formation mechanism over the **111** surface of In₂O₃, while Ye *et. al.* [45] have modeled the same process over **110** surface. Over these two surfaces, the preferred reaction path could involve H₂COOH* on the **111** oxide surface, but involve H₃CO* over the **110** surface. Based on our own results, we cannot clearly differentiate between these two alternatives.

Assuming bidentate CO₂ adsorption, which is likely with indium oxide and Y-modified zirconia surface according to the DFT calculations reported in [45][44] and the FTIR absorption peaks of adsorbed CO₂ [142], the first step of hydrogenation of the adsorbed CO₂ can be either to the oxygen that is bonded to In or Y or to the carbon. Since Y³⁺ is less reducible than In³⁺, the activated hydrogen will be more likely to attack the O next to In rather than the O next to Y (see Figure 4.16 (b) and (c)), leading to slower formation of *HOCO intermediate for the promoted catalysts, and therefore, a lower formation rate of unwanted CO. The trade-off is lower CO₂ consumption rates for the promoted catalysts since the CO₂ adsorbed near Y will be less likely to react. The results of the CO co-feeding experiment (Figure 4.14) and CO-TPD (Figure 4.15) also suggest that the reaction likely follows the formate pathway (*HCOO) rather than the RWGS + CO Hydro pathway (*HOCO carboxyl intermediate) or direct C-O bond cleavage pathway (*CO + *O) since CO was not a stable adsorbate to react on the surface [54][143].

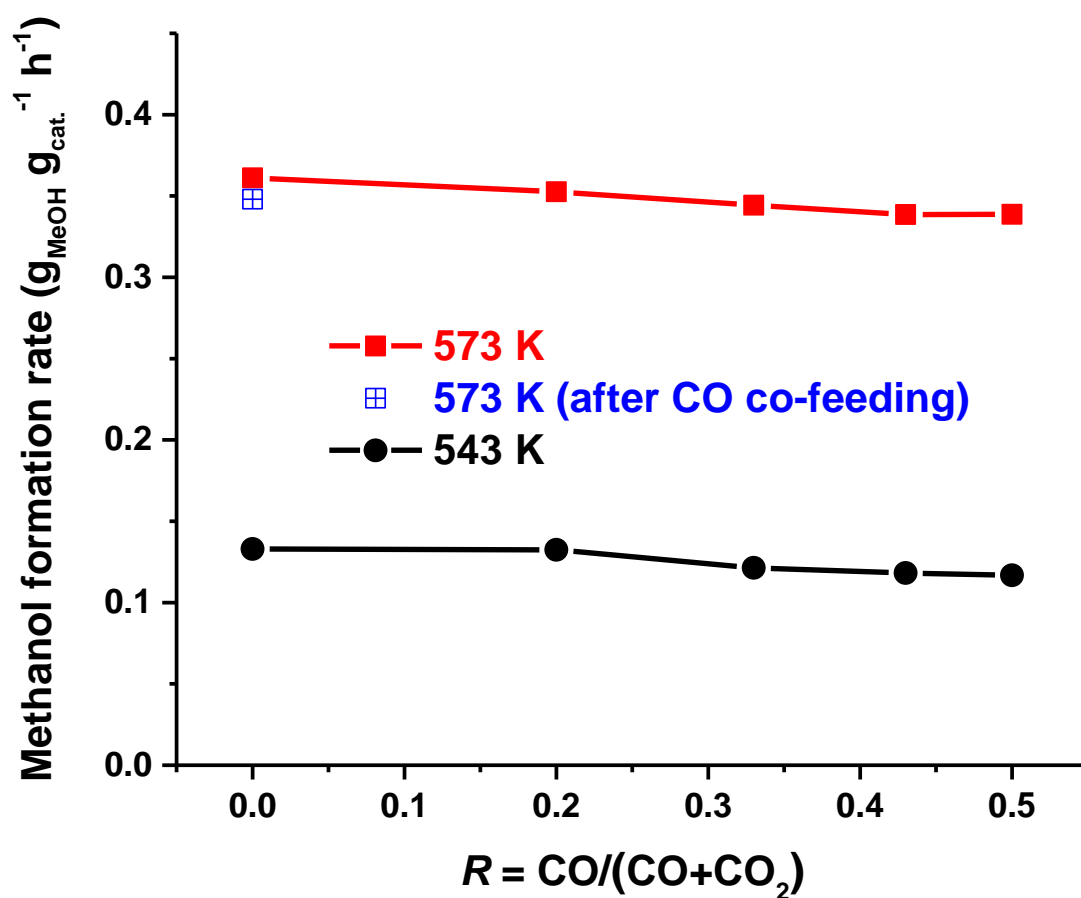


Figure 4.14 Methanol formation rate over 2Y8In/ZrO₂ as a function of CO concentration in CO and CO₂ mixture gas feed at 573 K and 543 K. Blue square with the cross indicates the methanol formation rate measured after the CO co-feeding experiment at 573 K to quantify for any change of activity due to deactivation. Reaction conditions: $P_{\text{tot.}} = 40$ bar, $SV = 52000 \text{ cm}^3 \text{ h}^{-1} \text{ g}_{\text{cat.}}^{-1}$. For $R = 0$, H₂:CO₂:He = 80:20:30 (in scm). The flow of He was stepwise reduced to admit progressively higher amounts of CO.

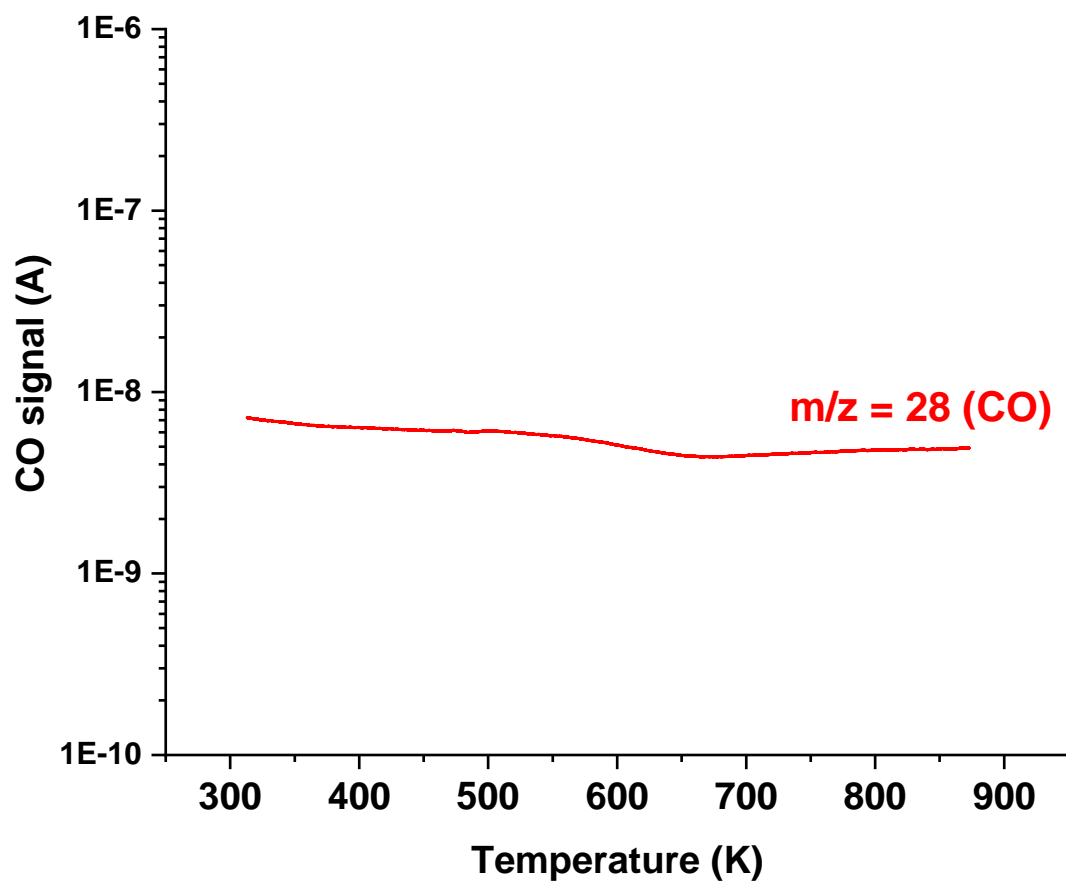


Figure 4.15 CO-TPD on partially reduced (473K, 20% H₂/He) 2Y8In/ZrO₂ catalyst. CO signal in blank test was $\sim 1.1 \times 10^{-8}$ A.

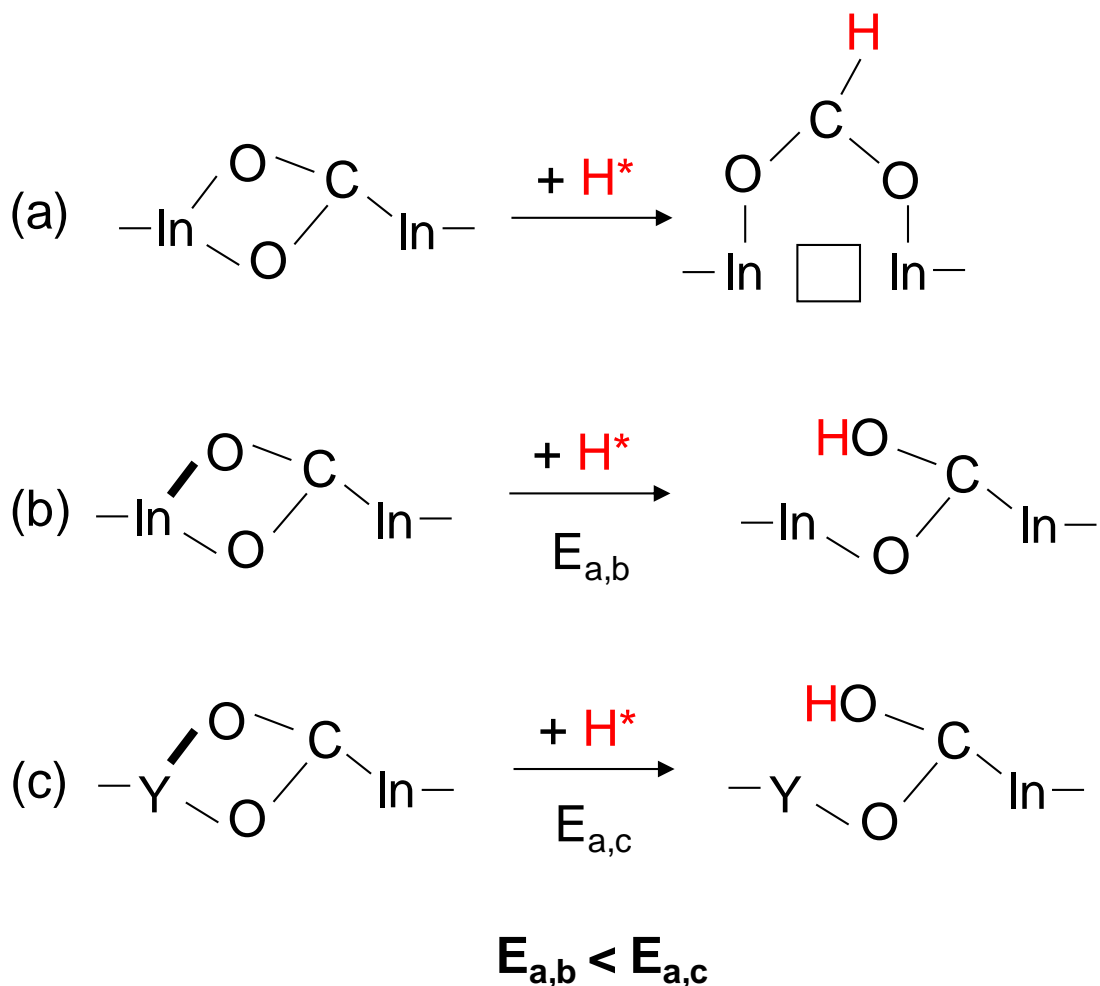


Figure 4.16 Schematic illustration of the possible initial steps of CO₂ hydrogenation on In₂O₃. (a) The formation of formate intermediate (HCOO*). The blank square is the oxygen vacancy. (b) The formation of HCOO* on In₂O₃. (c) The formation of HCOO* affected by yttrium or lanthanum oxides. E_{a,b} and E_{a,c} denote the activation energy of step (b) and (c), respectively.

4.4 Conclusions

Y and La were used to promote the catalytic properties of supported In_2O_3 ($\text{In}_2\text{O}_3/\text{ZrO}_2$) for methanol synthesis by firstly mixing yttrium nitrate and lanthanum nitrate during the wet impregnation process. Characterization studies show that the reducibility of the indium oxide catalysts in a hydrogen atmosphere is correlated to methanol production rates and selectivity. The Y and La-promoted catalysts had 11-35 K higher surface reduction temperatures compared to the supported indium oxide catalyst. Flow microreactor studies indicated that the incorporation of Y or La into the $\text{In}_2\text{O}_3/\text{ZrO}_2$ catalysts increased the number of surface CO_2 adsorption sites. The CO_2 TPD traces show 60% to 70% more heat-induced oxygen vacancies ($\text{O}_{\text{v}1}$) in $2\text{Y}8\text{In}/\text{ZrO}_2$ or $3\text{La}10\text{In}/\text{ZrO}_2$. The Y or La-promoted catalysts increased the selectivity of methanol significantly (about 20% more selective, from 528 K to 573 K). A selectivity of nearly 100% can be achieved at 528K and 40 bar, which is a mild reaction condition compared to the commercial process (513-533K, 50-100 bar). CO co-feeding experiment suggest a likely reaction route (formate pathway) for methanol formation over $2\text{Y}8\text{In}/\text{ZrO}_2$ within the reaction conditions we have examined. These results also show that the incorporation of Y and La into indium oxide catalysts is a feasible method for the design of selective catalysts for sustainable methanol economy.

Chapter 5

HIGHLY SELECTIVE CONVERSION OF CO₂ INTO METHANOL OVER COBALT-INDIUM BIMETAL OXIDES CATALYSTS

This chapter is a follow up to the investigation of In-containing catalysts for methanol synthesis from carbon dioxide presented in Chapter 4, but the central theme is new catalyst development and a novel bimetal oxide system consisting of cobalt oxide and indium oxide for selectively converting CO₂ into methanol. The Introduction of this chapter concisely describes the key catalytic uses of cobalt oxide and the subsequent sections describe the synthesis, characterization and catalytic properties of this new material. The results showed that Co-In bimetal oxide catalysts were highly selective (>99%) to methanol at temperatures between 528 K and 543 K. The evaluation of Co-In/ZrO₂ catalyst over 40 h on stream showed outstanding stability without deactivation.

5.1 Introduction

In carbon-related reaction technology, cobalt-based catalysts have been widely studied for Fischer-Tropsch (F-T) synthesis to convert synthesis gas into high molecular weight hydrocarbons, in particular, paraffinic waxes that can be hydrocracked to produce lubricants and diesel fuels [144][145]. Applications such as catalytic oxidation of volatile organic compounds (VOC) abatement over Co/ZrO₂ catalyst[146] as an inexpensive alternative to noble-metal catalysts, and doping In₂O₃ into Co₃O₄ catalysts for CO oxidation [147], demonstrate the versatility of cobalt

catalyst. In the last decade, Co-based catalysts have attracted more attention in CO₂ hydrogenation [148][149] due to the concern of anthropogenic CO₂ emission. In homogeneous catalysis, a cobalt-based organometallic complex called Co(dmpe)₂H₂ (dmpe = 1,2-bis(dimethylphosphino)ethane) was investigated as an alternative to replace precious metals such as iridium, ruthenium, and rhodium used to catalyze CO₂ hydrogenation to formate [150]. In heterogeneous catalysis, Co₃O₄ was found to be active both in CH₄/CO₂ reforming to produce H₂ and CO [151], and CO₂ methanation to CH₄ [152]. Zhou *et al.* [152] discussed the effect of Zr, Ce, and La dopants on Co₃O₄ catalysts for CO₂ methanation at 473 K and 5 bar. In their report, highest conversion of CO₂ (58%) and CH₄ selectivity (100%) was achieved by the Zr-doped catalyst (Zr-Co₃O₄) with highest promotion on the basic sites to activate CO₂ molecules. Very few reports investigated methanol synthesis from CO₂ using cobalt oxide catalysts. Defective CoO, for example, was reported to effectively accelerate the adsorption and activation for CO₂ molecules [153]. In 2015, Li *et al.* reported a hybrid oxide catalyst composed of manganese oxide nanoparticles supported on mesoporous cobalt oxide (MnO_x/m-Co₃O₄) for CO₂ conversion to methanol under mild reaction conditions (523 K, 4 bar) with high methanol formation rate (0.18 s⁻¹), however, the methanol selectivity was moderate (30%-45%).

Herein, bimetallic oxides of cobalt and indium have been prepared by wet co-impregnation and have been investigated for the direct conversion of CO₂ to methanol. The catalyst structure before and after the reaction was characterized using various techniques. The catalytic properties, in particular, methanol selectivity, methanol formation rate, and stability, were analyzed in detail. We found that the hybrid catalyst (Co-In/ZrO₂) enhanced the methanol selectivity by about 20% from the ~50-80 % to

~70-100% at the temperatures between 528 K and 573 K. High stability without deactivation over periods of hours, was achieved along with 100% methanol selectivity. The CO₂ temperature-programmed desorption (CO₂-TPD) was correlated with the catalytic performance, indicating more CO₂-adsorbing basic sites were formed over the bimetal oxides catalyst under reaction conditions. The results from CO₂-TPD and the catalytic properties of the mixed oxide show that the nature of the catalysts have been changed by the hybrid composition. This novel and interesting catalyst system could be a potential alternative for Cu-based material with its promising catalytic performance.

5.2 Materials and Methods

5.2.1 Catalyst preparation

The standard indium oxide catalyst, In₂O₃/ZrO₂, was prepared by wet impregnation as follows: 0.76 g In(NO₃)₃·xH₂O (Alfa Aesar, 99.99%) was first dissolved in a mixture of ethanol (70 cm³) and deionized water (24 cm³). 2.00 g ZrO₂ (NORPRO, SZ 31164 extrudates, monoclinic phase, crushed prior to use) as the catalyst support was subsequently added to the solution and the resulting slurry was stirred for 5 h at room temperature. The solvent was removed using a rotary evaporator (Büchi Rotavap R-114) at 343 K. The sample obtained was dried in a drying oven at 353 K overnight and calcined in static air at 573 K (heating rate 2 K min⁻¹, hold for 2 h). The bimetal oxide catalysts were prepared in the similar fashion. For 2Co-1In/ZrO₂ and 1Co-2In/ZrO₂, 0.490 g Co(NO₃)₂·6H₂O (Sigma Aldrich, >98%) and 0.253 g In(NO₃)₃·xH₂O, and 0.245 g Co(NO₃)₂·6H₂O and 0.507 g

$\text{In}(\text{NO}_3)_3 \cdot x\text{H}_2\text{O}$, respectively, were dissolved in a mixture of ethanol (70 cm^3) and deionized water (24 cm^3). The numbers before Co and In in samples' name specify the nominal molar ratio between Co and In in total metal loading. For $\text{Co}_3\text{O}_4/\text{ZrO}_2$, 0.735 g $\text{Co}(\text{NO}_3)_2 \cdot 6\text{H}_2\text{O}$ was dissolved in a mixture of ethanol (70 cm^3) and deionized water (24 cm^3). The rest of the procedures were the same as the standard $\text{In}_2\text{O}_3/\text{ZrO}_2$.

5.2.2 Catalyst Characterization

The bulk composition in catalysts was determined using a Rigaku wavelength-dispersive X-ray fluorescence (WDXRF) spectrometer. The sample names of the catalysts are based on the metal weight percentages obtained from WDXRF. Textural characterization of the samples was carried out using N_2 adsorption at 77 K. Isotherms were collected on a Micrometrics 3Flex and analyzed using Brunauer–Emmett–Teller (BET) method to calculate surface area, and the Barrett-Joyner-Halenda (BJH) method was used to calculate pore volume and pore size distribution. X-Ray Diffraction (XRD) patterns of catalyst powders were collected at room temperature on a Bruker diffractometer using $\text{Cu K}\alpha$ radiation ($\lambda = 1.5418 \text{ \AA}$). Measurements were taken over the range of $20^\circ < 2\theta < 70^\circ$ with a step size of 0.02° . The phase was identified by comparing the diffraction patterns with the conventional Joint Committee on Powder Diffraction Standards (JCPDSs). Scanning electronic microscopy (SEM) analyses were carried out on a Zeiss SEM/FIB Auriga-60. X-ray photoelectron spectroscopy (XPS) measurements were performed on a K-alpha Thermo Fisher Scientific spectrometer using monochromated $\text{Al K}\alpha$ X-ray source. The measurements of indium oxides on supported ZrO_2 ($\text{In}_2\text{O}_3/\text{ZrO}_2$), and bimetal oxide catalysts ($2\text{Co-1In}/\text{ZrO}_2$ and $1\text{Co-2In}/\text{ZrO}_2$) were done with a spot size of $400 \mu\text{m}$ at ambient temperature and a chamber pressure of $\sim 10^{-7}$ mbar. A flood gun was used for charge compensation. All

the measured spectra were calibrated by setting the reference binding energy of adventitious carbon *1s* signal at 284.8 eV. The spectra were analyzed using *Avantage*TM surface chemical analysis software (v5.986). For the spectral fitting, each component consists of a linear combination of Gaussian and Lorentzian product functions. SMART background (determined by the software) was used over the region to define the peaks.

Temperature-programmed reduction (TPR) was carried out by using an Altamira AMI-200 catalyst characterization flow system. Analysis of the gaseous effluent was carried out using a thermal conductivity detector (TCD) to detect the H₂ or CO₂ concentrations during the experiment. H₂-TPR was conducted via 2 steps: (i) the sample (50 mg) was dried at 398 K for 30 min in Ar (60 sccm); (ii) The TPR trace was obtained by increasing the temperature up to 900 K in a gaseous mixture of 10% H₂/Ar at the rate of 5 K min⁻¹.

Temperature-programmed desorption (TPD) were carried out by MicroGC 490 and the reactor used in kinetic studies and catalytic behavior. Spent catalysts (150 mg) after higher pressure CO₂ hydrogenation at the reaction conditions were used in CO₂-TPD. After the CO₂ hydrogenation reaction at 573 K -543 K for 18 h, the reactor was cooling down with 100 sccm of He to room temperature, and the pressure was reduced to 1 bar. The sample was kept in the reactor without exposure to the atmosphere. CO₂-TPD after the CO₂ hydrogenation for the spent catalysts was then conducted as follows: (i) Pure CO₂ (30 sccm) was flowed into the reactor for 1 h to to adsorb the CO₂ on the catalyst surface at room temperature; (ii) the temperature was ramped from room temperature to 353K in 1h and held for another 4h flowing 100 sccm He to remove weakly adsorbed species and flush the tubes connecting to MicroGC; (iii) the

desorption process was programmed from 353 K to 873 K with 20 sccm He. The ramping rates in all the CO₂-TPD experiments was 1 K min⁻¹. The desorbed CO₂ concentration was recorded every 4 min by the MicroGC, and was plotted versus temperature and time for the determination of the amount of desorbed CO₂ in moles.

5.2.3 Reactor setup and catalytic activity

The reactor setup is described in Chapter 2 and Chapter 4 of this thesis. For the catalytic activity, prior to the reaction, the catalyst was activated at 573 K and 5 bar He for 1 h, if not described otherwise. Activity tests were conducted under the following conditions: P_{tot} = 40 bar, T = 528K, 543K, 558K, or 573 K, a total flow rate F_{tot} = 130 cm³ STP min⁻¹ (sccm), and the volumetric feed composition of H₂:CO₂:He = 80:20:30. The standard gas hourly space velocity (GHSV) used was 52000 cm³ h⁻¹ g_{cat.}⁻¹. Each condition was held for more than 5 h or until the effluent composition achieved steady state. Helium was used as internal standard gas for concentration calibration due to the change of the total volumetric flow rate in the effluent after the CO₂ hydrogenation reaction. Gas lines after the reactor were kept at 433 K using heating tape to avoid condensation of products. The composition of the effluent stream was analyzed online by a gas chromatograph (490 MicroGC, Agilent) during continuous flow experiments. The MicroGC was equipped with a thermal conductivity detector (TCD) with three different channels to quantify H₂, He, CO₂, CO, hydrocarbons, and CH₃OH. For details on the equations and terms such as CO₂ conversion, methanol selectivity, reaction rates, and GHSV, used in evaluations of catalysts refer to Chapter 2 and Chapter 4.

5.3 Results and Discussion

Figure 5.1 presents the SEM images of 2Co-1In/ZrO₂ and 1Co-2In/ZrO₂ after the calcination in air at 573 K. The images show that the catalysts particles are formed of aggregates of smaller particles and that the aggregates have a broad range of sizes between ~100 nm to ~5 μm. The surface density of In atoms in the (1 1 1) surface of crystalline In₂O₃ was estimated to be 8.67×10^{18} In atoms/m² [119,120], and based on the BET surface area of the samples, and the loading of In atoms measured from XRF, the monolayer coverage of 2Co-In/ZrO₂ and 1Co-2In/ZrO₂ were estimated as ~0.9 and 0.52, respectively. The BJH pore volumes (V_P) of 2Co-1In/ZrO₂ and 1Co-2In/ZrO₂ catalysts obtained from N₂ adsorption were 0.238 cm³/g and 0.232 cm³/g, respectively. The majority of the sample's pore volume (>90%) for both catalysts is the result of contributions from pores with diameters between 2 nm and 50 nm, which is the regime of mesoporous material. The BET surface area (S_{BET}) of 2Co-1In/ZrO₂ and 1Co-2In/ZrO₂ were 91.3 m²/g and 88.7 m²/g, respectively. The adsorption-desorption N₂ isotherm showed Type IV mesoporous characteristics with hysteresis loops for both 2Co-1In/ZrO₂ and 1Co-2In/ZrO₂ catalysts. Type IV isotherms represent monolayer-multilayer adsorption and capillary condensation according to IUPAC classification [154]. The measured surface area and the total pore volume (V_P) correspond closely to the properties of the ZrO₂ carrier (~100 m²/g) in all Co-In bimetal oxides catalysts.

The molar percentage in total metal loading of 2Co-1In/ZrO₂ and 1Co-2In/ZrO₂ were determined using EDX, XPS, and XRF (Table 5.1). The bulk weight percentage, in total metal loading, of Y, La and In of the catalyst (W_Y , W_{La} , and W_{In}) were also determined from XRF. The nominal concentration of Co and In loading was controlled at 13.5 mol% in total metal (i.e., Co, In, and Zr, also see Table 5.2 for

comparison to $\text{In}_2\text{O}_3/\text{ZrO}_2$ and for $\text{Co}_3\text{O}_4/\text{ZrO}_2$ results). The observed amounts obtained from the XRF spectra were close to the nominal molar percentages calculated from the amount of the precursors used during catalyst preparation. The concentrations obtained from EDX, which is a semiquantitative technique, followed the same trend, though showed slightly different amounts of Co and In in concentrations (Table 5.1). In contrast to XRF, XPS is a surface sensitive technique and can reveal information about the surface composition of the bimetal oxide catalysts. The molar percentages of 1Co-2In/ ZrO_2 obtained from XPS were all similar to the amounts obtained from XRF. The only discrepancy of the molar percentage obtained from XPS compared to the nominal values was in 2Co-1In/ ZrO_2 , where the molar concentration of surface In (7.7%) was similar to the Co (7.6%). This suggests that after the co-impregnation and calcination, indium oxide distributed more on the surface, leading to a higher surface concentration than the bulk composition obtained from XRF.

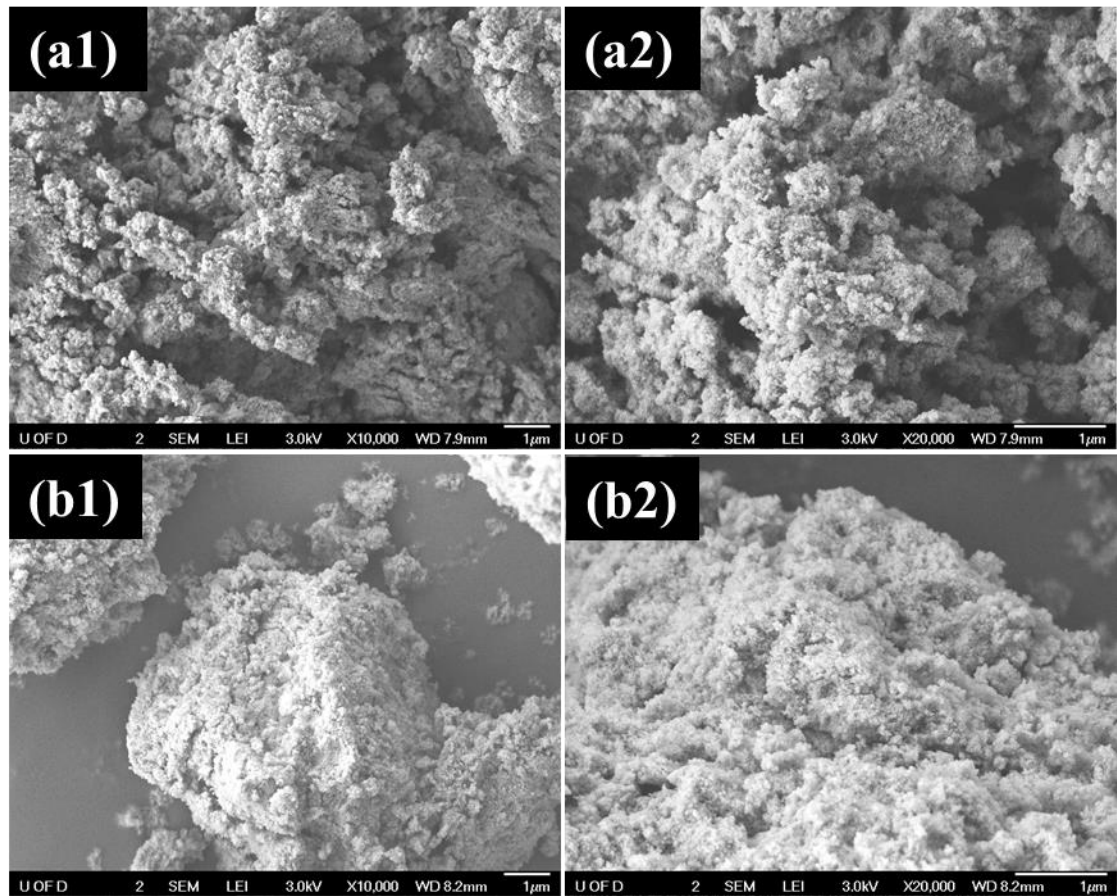


Figure 5.1 SEM images of 2Co-1In/ZrO₂ in the magnification of 10000 (a1) and 20000 (a2); 1Co-2In/ZrO₂ in the magnification of 10000 (b1) and 20000 (b2).

Table 5.1 Metallic concentrations in molar (mol) or weight (Wt) percentages of 2Co-1In/ZrO₂ and 1Co-2In/ZrO₂ determined by EDX, XPS, and XRF.

Catalyst		2Co-1In/ZrO ₂			1Co-2In/ZrO ₂			
Method	EDX	XPS	XRF		EDX	XPS	XRF	
Element	mol (%)	mol (%)	mol (%)	Wt (%)	mol (%)	mol (%)	mol (%)	Wt (%)
Co	11.7	7.6	10.4	6.9	3.2	4.2	5.3	3.4
In	3.4	7.7	5.0	6.5	5.2	9.9	8.1	10.1
Zr	84.9	84.7	84.6	86.6	91.6	85.9	86.6	86.5

Table 5.2 Metallic concentration molar (mol) or weight (Wt) percentages of In₂O₃/ZrO₂ and Co₃O₄/ZrO₂ determined by XRF.

Catalyst		In ₂ O ₃ /ZrO ₂			Co ₃ O ₄ /ZrO ₂		
Method	Nominal	XRF		Nominal	XRF		
Element	mol (%)	mol (%)	Wt (%)	mol (%)	mol (%)	Wt (%)	
Co	-	-	-	13.5	15.6	10.6	
In	13.5	10.4	12.7	-	-	-	
Zr	86.5	89.6	87.3	86.5	84.4	89.4	

The XRD patterns of $\text{Co}_3\text{O}_4/\text{ZrO}_2$, $1\text{Co-2In}/\text{ZrO}_2$, $2\text{Co-1In}/\text{ZrO}_2$, and spent $2\text{Co-1In}/\text{ZrO}_2$ are shown in Figure 5.2. The monoclinic ZrO_2 (PDF#00-001-0750) used as the catalyst support did not change significantly as a result of the wet impregnation and calcination steps with different metallic precursors; the peaks did not change either after the CO_2 hydrogenation reaction. Two peaks of Co_3O_4 at 36.73° and 38.64° assigned to the reflections with index (3 1 1) and (2 2 2) (PDF#01-073-1701), respectively, appeared in all the cobalt-contained samples except for the spent $2\text{Co-1In}/\text{ZrO}_2$. The reduction in the intensity on the Co_3O_4 peaks in spent $2\text{Co-1In}/\text{ZrO}_2$ indicate that Co_3O_4 was reduced to a lower oxidation state after the hydrogenation. The presence of CoO , as suggested in the diffraction pattern by the peak at 43.86° , is a possibility. A peak of cubic In_2O_3 at 37.53° found in $1\text{Co-2In}/\text{ZrO}_2$, $2\text{Co-1In}/\text{ZrO}_2$, and spent $2\text{Co-1In}/\text{ZrO}_2$ was assigned on the basis of the (4 1 1) reflection (PDF#01-071-2194). The existence of In_2O_3 peaks indicated that at least some isolated, crystalline In_2O_3 were formed after the catalyst was calcined in air prior to the reaction. These In_2O_3 crystallites remain in the catalyst after CO_2 hydrogenation, as suggested by the constant intensity of this peak in the pattern before and after the reaction (Figure 5.2).

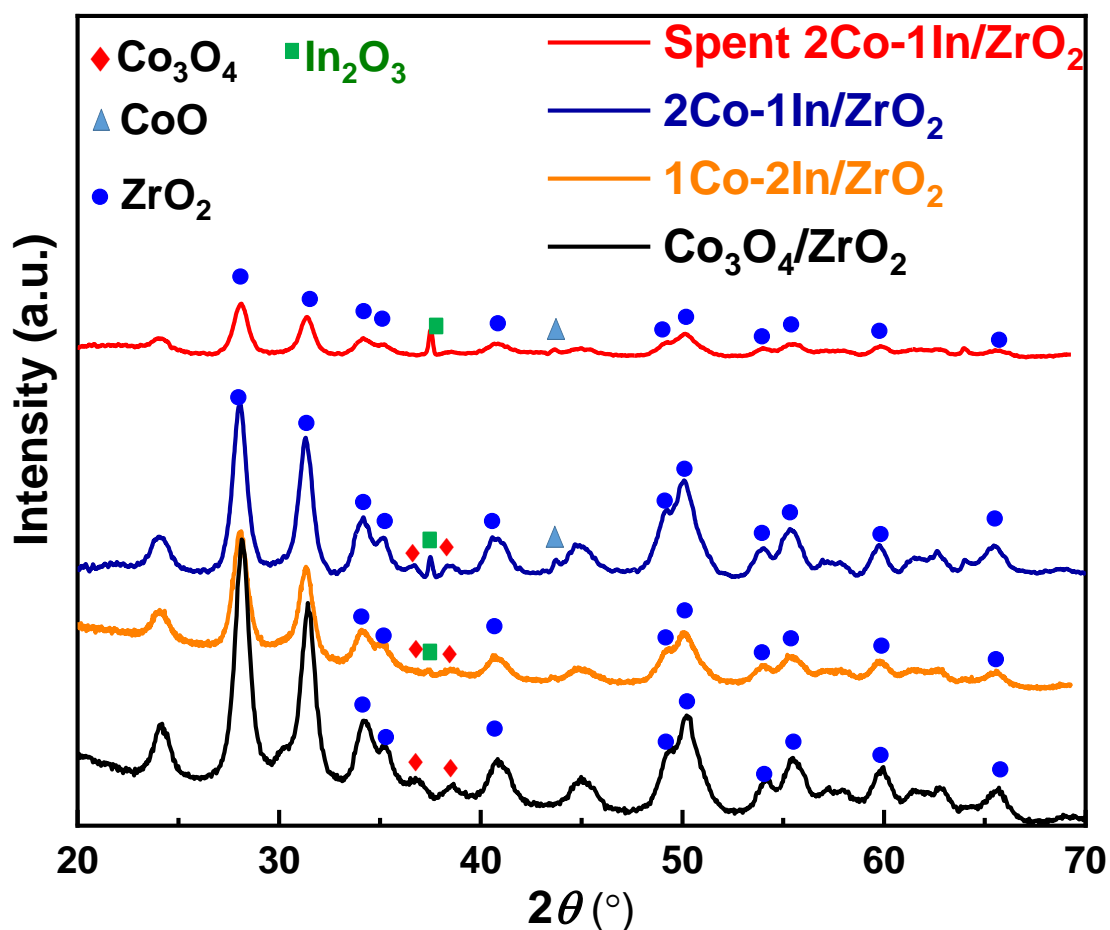


Figure 5.2 XRD patterns of $\text{Co}_3\text{O}_4/\text{ZrO}_2$, $1\text{Co}-2\text{In}/\text{ZrO}_2$, $2\text{Co}-1\text{In}/\text{ZrO}_2$, and spent $2\text{Co}-1\text{In}/\text{ZrO}_2$.

XPS analyses were conducted to characterize the surface composition of the initial fresh $2\text{Co}-1\text{In}/\text{ZrO}_2$ and the change in Co oxidation state on the catalyst after the CO_2 hydrogenation reaction (Figure 5.3). Both spectra consist of two main peaks, $\text{Co } 2p_{1/2}$ and $\text{Co } 2p_{3/2}$, both exhibiting (at higher binding energy by about 6 eV) a satellite structure arising from interaction of photo emitted electrons with core vacancy and valence electrons. The main peaks of $\text{Co}2p_{3/2}$ near 781 eV represent Co_3O_4 , which is in both fresh and spent sample as suggested by the XRD patterns in Figure 5.2. The

binding energy of Co $2p_{3/2}$ in the spectra for 2Co-1In/ZrO $_2$ and spent 2Co-1In/ZrO $_2$ were 780.8 eV and 781.7 eV, respectively. The shift to a higher binding energy by 0.9 eV indicates the presence of a more reduced cobalt oxide on the zirconia surface. The binding energy of Co $2p_{1/2}$ spectra for the catalyst before and after the reaction also showed a consistent trend; a 1.1 eV shift from 796.0 eV to 797.1 eV. This is not, of course, surprising since the reaction was conducted under a reducing environment (H $_2$:CO $_2$ = 4:1). It is well known that the XPS Co $^{2+}$ peak presents a satellite structure whereas the Co $^{3+}$ peak does not [146]. Since Co $_3$ O $_4$ has cobalt in a mixed oxidation state of Co $^{2+}$ (tetrahedral) and Co $^{3+}$ (octahedral), it is easier to use the satellite spectral features of Co $^{2+}$ to monitor the change in oxidation states. The satellite peaks near 787.4 eV and 803.6 eV for both spectra indicate the existence of Co $^{2+}$ in both samples. After the reaction, the Co $2p_{3/2}$ satellite and Co $2p_{1/2}$ satellite spectra for spent 2Co-1In/ZrO $_2$ showed 34% and 10% increase in area, respectively, compared to the satellite spectra for 2Co-1In/ZrO $_2$ before the reaction. This result indicates unambiguously an increase of Co $^{2+}$ after the CO $_2$ hydrogenation reaction. Both the main peaks of Co $_3$ O $_4$ in Co 2p spectra and Co $^{2+}$ satellite spectra suggest that part of the catalyst was reduced to a lower oxidation state for cobalt oxide after the reaction, implying that cobalt oxide was not a spectator during the hydrogenation reaction. It is possible that during the formation of Co $_3$ O $_4$ and In $_2$ O $_3$ during the calcination in air at 573 K, an intermixing between Co $_3$ O $_4$ and In $_2$ O $_3$ could happen, which was suggested by the change in binding energy of In $3d_{5/2}$ and In $3d_{3/2}$ in XPS spectra of In $_2$ O $_3$ /ZrO $_2$ and 2Co-1In/ZrO $_2$. The peaks of In $3d_{5/2}$ and In $3d_{3/2}$ were both decreased by 0.32 eV, and the FWHM of the peaks decreased 0.2 eV after cobalt oxide was added into the system (see Figure 5.3 (b)). The change of both the binding energy at In 3d and FWHM

suggest the change of chemical state of the catalyst to the more reducing side on the surface. Note that since the XPS analysis as applied here is an ex-situ technique, potential sample re-oxidation by the atmosphere could affect the measured XPS spectra. Nonetheless, obvious reduction behavior could still be found in spent 2Co-1In/ZrO₂.

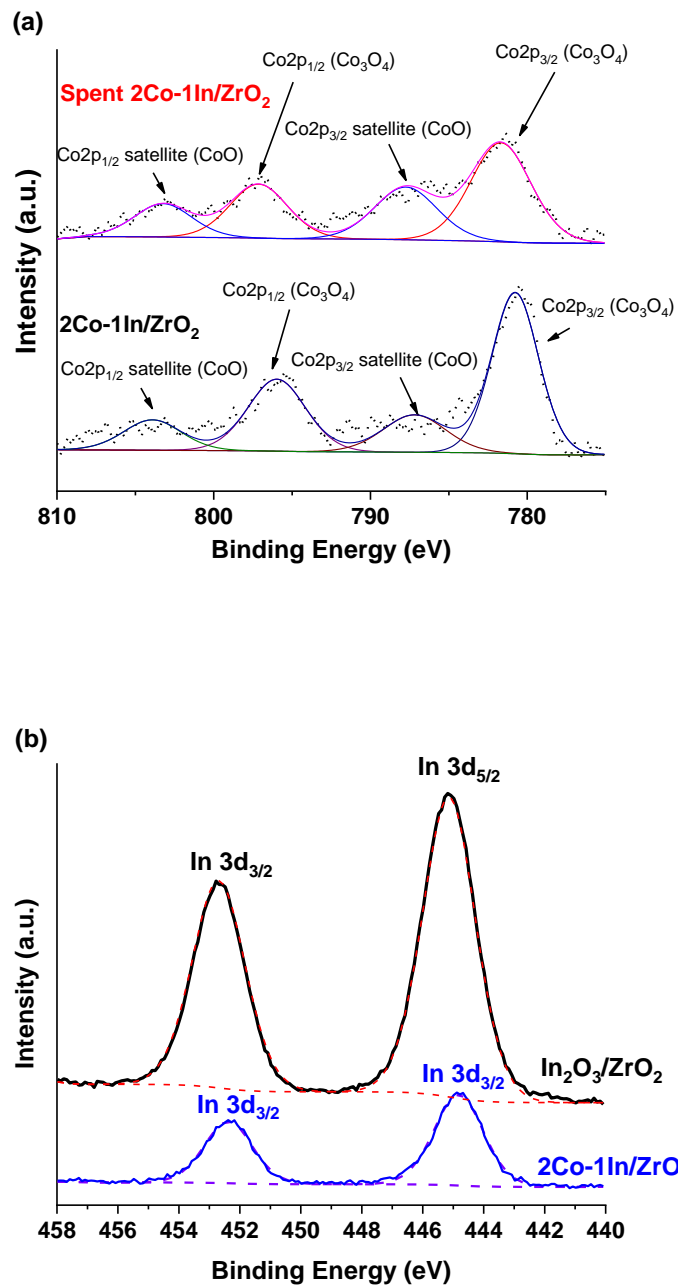


Figure 5.3 (a) XPS Co 2p spectra of 2Co-1In/ZrO₂ and spent 2Co-1In/ZrO₂. (b) XPS In 3d spectra of In₂O₃/ZrO₂ and 2Co-1In/ZrO₂ after the calcination at 573 K in air.

Figure 5.4 shows the deconvolution of the core-level O1s XPS spectra of 2Co-1In/ZrO₂ and spent 2Co-1In/ZrO₂. Using these spectra, the concentration of oxygen *near* defects ([O_{defect}]) for 2Co-1In/ZrO₂ and spent 2Co-1In/ZrO₂ can thus be characterized. [O_{defect}] can be defined as shown in Eq. 5.1.

$$[\text{O}_{\text{defect}}] = \frac{(\text{Area of } O_{\text{defect}})}{(\text{Area of } O_{\text{defect}}) + (\text{Area of } O_{\text{lattice}})} \quad (\text{Eq. 5.1})$$

Where O_{lattice} is the deconvoluted peak from O1s spectra at the binding energy of 529.8 eV, representing the lattice oxygen in metal oxides. The [O_{defect}] of spent catalyst was 70%, whereas the [O_{defect}] for fresh 2Co-1In/ZrO₂ after the calcination was 29%. The increase of [O_{defect}] after reaction indicate the formation of oxygen vacancies (i.e., reduction of the supporting metal) under the reaction conditions of high temperature and in the presence of a reducing agent (H₂).

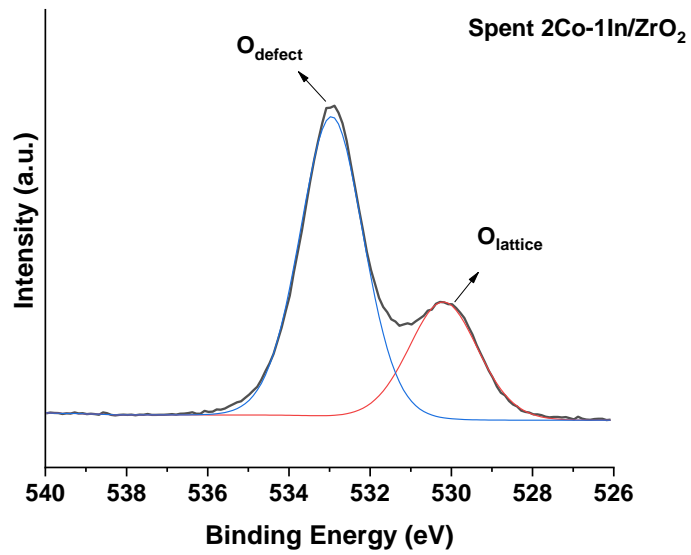
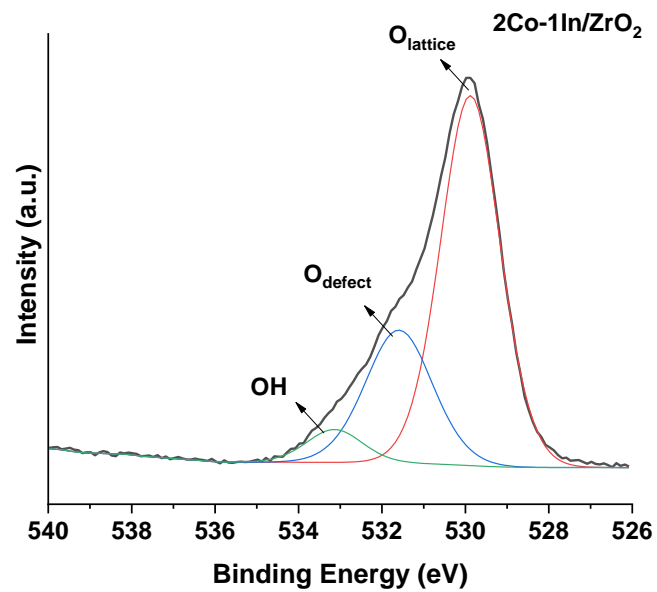


Figure 5.4 Deconvolution of the core-level O 1s XPS spectrum of 2Co-1In/ZrO₂ and spent 2Co-1In/ZrO₂.

The methanol formation rate and methanol selectivity versus time on stream over 2Co-1In/ZrO₂ and 1Co-2In/ZrO₂ bimetal oxide catalysts are shown in Figure 5.5 (a) and Figure 5.5 (b), respectively. The selectivity to methanol increases as the temperature is decreased, in other words, CO production rate is more favorable at higher temperatures due, in part, to the endothermicity of the RWGS reaction. Such phenomena has been found often in the CO₂ hydrogenation over the conventional Cu-based catalysts [122–124]. In Figure 5.5 (a), methanol formation rate over 2Co-1In/ZrO₂ decreased from 0.31 g_{MeOH} g_{cat.}⁻¹ h⁻¹ to 0.07 g_{MeOH} g_{cat.}⁻¹ h⁻¹ when the temperature was reduced from 573 K to 528 K. On the other hand, methanol selectivity increased from 68% to 82%, 99%, and 100% with decreasing temperature (573 K, 558 K, 543 K, and 528 K, respectively). It should be noted that there was also trivial amount (~10-20 ppm) of ethylene (C₂H₄) formed at the rate of 0.001 g_{C₂H₄} g_{cat.}⁻¹ h⁻¹ during the reaction at the temperatures from 573 K to 558 K. Metallic Co, as a Fischer-Tropsch material, is usually viewed as highly active in CO dissociation and is responsible for C-C chain growth [145] to produce either ethylene [155] or high alcohols [156]. In our mixed-oxide system with indium, it is likely that a small amount of metallic cobalt is form at higher temperatures, and this metallic phase is responsible for the conversion of CO into C₂H₄.

The catalytic activities of another cobalt indium oxide catalyst with different molar ratio of Co and In (Co:In = ~1:2) are shown in Figure 5.5 (b). In this case, the methanol formation rate decreased from 0.24 g_{MeOH} g_{cat.}⁻¹ h⁻¹ to 0.12 g_{MeOH} g_{cat.}⁻¹ h⁻¹ with the decreased temperatures from 573 K to 528 K. Switching the reaction temperature back from 528 K to 573 K allowed us to establish if the change of methanol formation rate was the result of catalyst deactivation, in addition to the

intrinsic effect of the activation energy. The formation rate over 1Co-2In/ZrO₂ catalyst was 0.27 g_{MeOH} g_{cat.}⁻¹ h⁻¹ at 573 K after 37 h time on stream, which was even higher than the initial formation rate at 573 K (0.24 g_{MeOH} g_{cat.}⁻¹ h⁻¹) in the first 7 h of the experiment. This result shows that the structure of the catalyst is, in fact, dynamic and that it is reconstructed into a more active phase depending on the reaction conditions. The structural transformation process into the more active catalyst, however, was slow (more than 6h). Note that the methanol selectivity over 1Co-2In/ZrO₂ increased from 51% to 69%, 87%, and 100% with the decreasing temperatures of 573 K, 558 K, 543 K, and 528 K, respectively. One possible reason for a higher methanol selectivity for the Co-In bimetallic oxide as compared to In₂O₃ alone is the ability of cobalt oxide in CO adsorption and oxidation. It has been reported that there is strong evidence of the CO adsorption on Co₃O₄, and the lattice oxygen of Co₃O₄ can oxidize CO and release CO₂ [157].

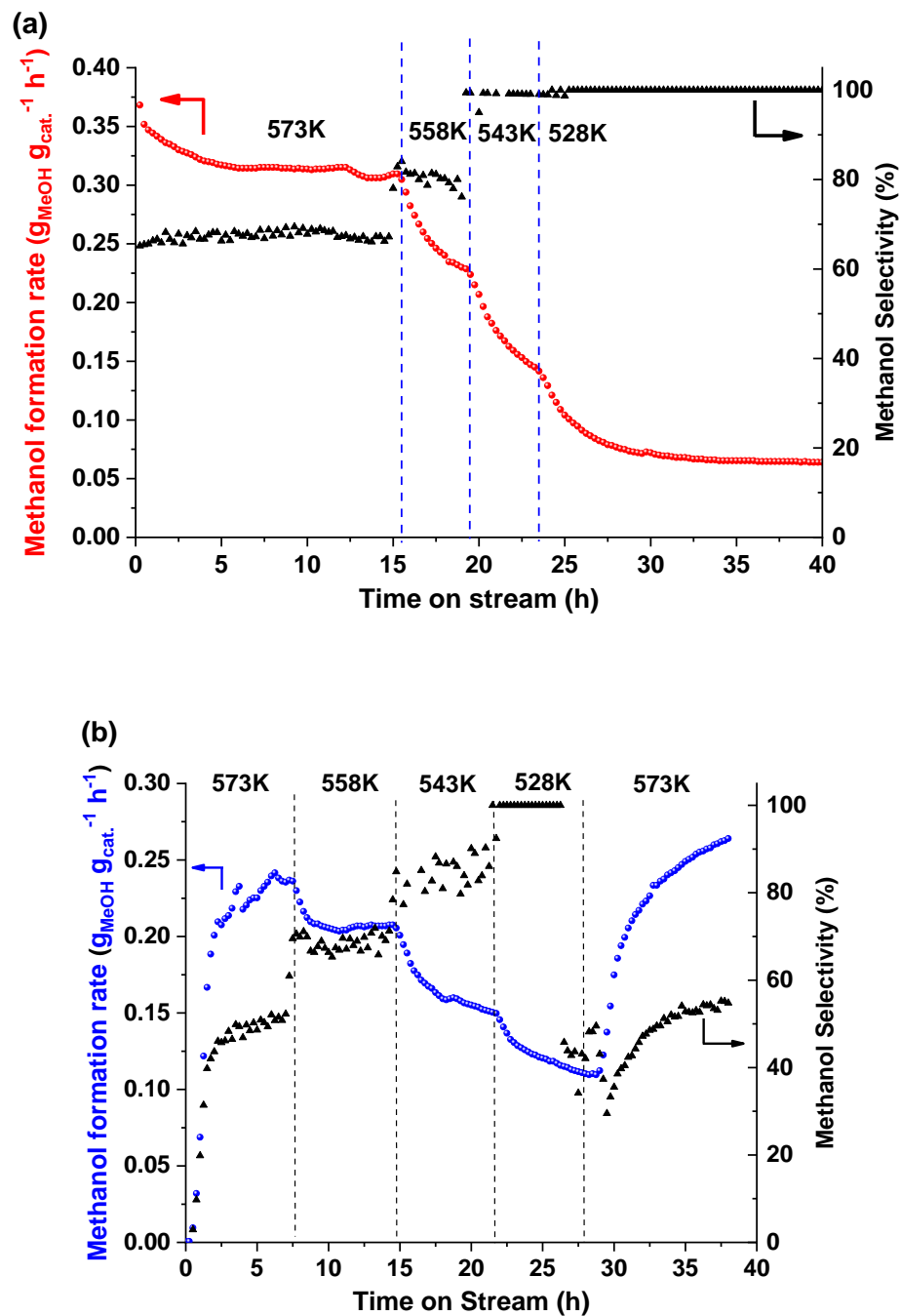


Figure 5.5 Methanol formation rate and methanol selectivity versus time on stream over (a) 2Co-1In/ZrO₂ and (b) 1Co-2In/ZrO₂ catalysts. Vertical dashed lines separate different temperature zone during the reaction.

Methanol selectivity and CO₂ conversion over 2Co-1In/ZrO₂ was compared to the standard In₂O₃/ZrO₂ catalyst (Figure 5.6). Under the same reaction conditions (GHSV = 52000 h⁻¹, P_{tot} = 40 bar, T = 573 K- 528 K), the overall CO₂ conversion for standard In₂O₃/ZrO₂ catalyst was higher than Co-In at the high temperature range partly due to the higher CO formation rates of In₂O₃/ZrO₂. The methanol selectivity over 2Co-1In/ZrO₂, however, was 20% higher than the standard In₂O₃/ZrO₂ catalyst at the similar conversion (~2%) at 528 K, indicating that the Co-In hybrid oxide catalyst is more favorable for selective methanol formation. The methanol formation rate, however, were in favor of In₂O₃/ZrO₂ with 50-70% higher rate compared to 2Co-1In/ZrO₂.

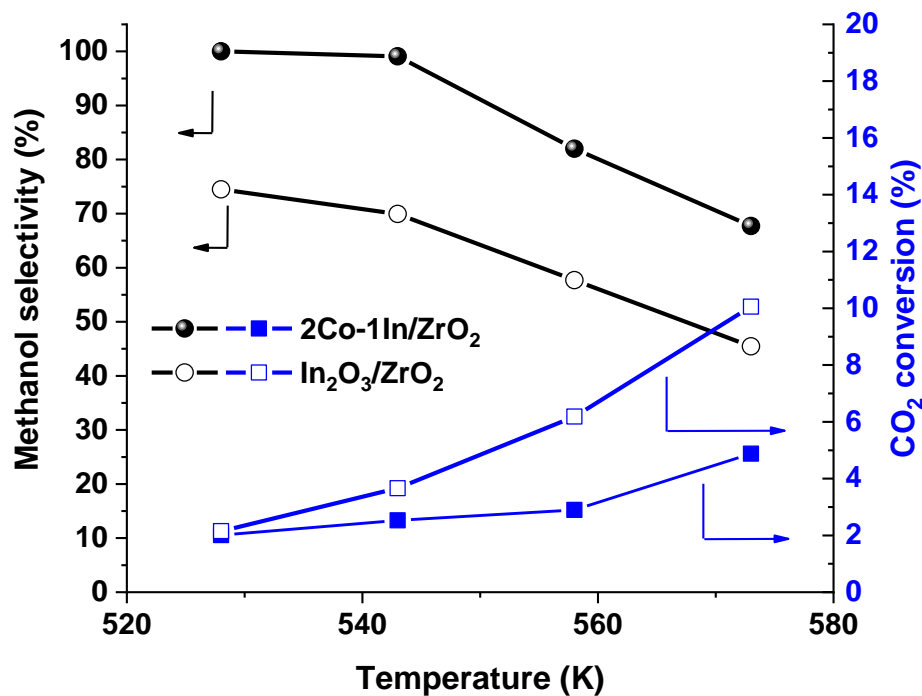


Figure 5.6 Comparison of methanol selectivity and CO₂ conversion versus temperature over 2Co-1In/ZrO₂ and In₂O₃/ZrO₂ catalysts.

The catalytic properties of $\text{Co}_3\text{O}_4/\text{ZrO}_2$ were evaluated under same reaction conditions as the hybrid oxide catalysts. The $\text{Co}_3\text{O}_4/\text{ZrO}_2$ catalyst did not produce any methanol or CO, instead, the catalyst produced mostly CH_4 with very high CO_2 conversion (80.6-88.6%) and CH_4 selectivity (>99%), with a very small amount of C_{2+} alkanes (C_2H_6 , C_3H_8 , <1%). Mesoporous Co_3O_4 (m- Co_3O_4) as support of manganese oxide ($\text{MnO}_x/\text{m-Co}_3\text{O}_4$, 2-5% Atom % Mn loading) for CO_2 hydrogenation was evaluated by Li *et.al.* at 523 K under 4 bar [155]: the cobalt oxide alone (m- Co_3O_4) produced 35% of CO, 35% of CH_4 and ~20% of methanol, with other by products such as C_2H_4 (5-7%) and CH_3OCH_3 (<5%) present in smaller quantities. MnO_x nanoparticles were primarily producing CO, but MnO_x supported by m- Co_3O_4 ($\text{MnO}_x/\text{m-Co}_3\text{O}_4$) showed better methanol selectivity (~35%) than that of pure m- Co_3O_4 (~20%). It should be noted that the m- Co_3O_4 from Li *et. al.* was pretreated in air at 623 K and then it was reduced by 20% H_2/He mixture gas treatment before the CO_2 hydrogenation; this could lead to a very different oxidation state and composition. In our case, it was unexpected and interesting that the bimetal catalyst showed very different catalytic selectivity with no CH_4 observed as compared with the monometallic $\text{Co}_3\text{O}_4/\text{ZrO}_2$. This result implies that there is a synergistic effect between the Co and In surface, which suppressed the CO formation channel observed in $\text{In}_2\text{O}_3/\text{ZrO}_2$ catalyst, and the methane formation channel observed in $\text{Co}_3\text{O}_4/\text{ZrO}_2$ catalyst.

Table 5.3 Catalytic activities of $\text{Co}_3\text{O}_4/\text{ZrO}_2$ at the temperatures between 528 K and 573 K under 40 bar.

T	CO_2 conversion (%)	CH_4 selectivity (%)	CH_4 standard time yield ($\text{g}_{\text{CH}_4} \text{g}_{\text{cat.}}^{-1} \text{h}^{-1}$)
573 K	88.6	99.8	9.78
558 K	85.2	99.7	9.21
543 K	80.6	99.5	8.18
528 K	84.1	99.7	9.17

Highly selective methanol synthesis could be achieved with feasible methanol formation rates over Co-In/ZrO_2 . The formation rates from Co-In/ZrO_2 catalysts ranged from 0.10 to $0.35 \text{ g}_{\text{MeOH}} \text{g}_{\text{cat.}}^{-1} \text{h}^{-1}$ are comparable to the rates observed in most of other reports [43,46,115,125–128] in the CO_2 to methanol reaction. $0.156 \text{ g}_{\text{MeOH}} \text{g}_{\text{cat.}}^{-1} \text{h}^{-1}$ methanol formation rate has been reported at 553K and 46 bar for $\text{Cu/Zn/Al}_2\text{O}_3$ [112] catalyst; and a rate of $0.181 \text{ g}_{\text{MeOH}} \text{g}_{\text{cat.}}^{-1} \text{h}^{-1}$ at 493 K and 80 bar over Cu/ZnO/ZrO_2 catalyst was also found in a previous report [113]. With their characteristics of highly selective and stable activities, this Co-In bimetal oxide system is promising for the advance of catalytic methanol synthesis from CO_2 .

TPR profiles of 2Co-1In/ZrO_2 , $\text{Co}_3\text{O}_4/\text{ZrO}_2$, and $\text{In}_2\text{O}_3/\text{ZrO}_2$ were used to examine the reducibility of the catalysts (Figure 5.7). For standard $\text{In}_2\text{O}_3/\text{ZrO}_2$, the reduction starts at around 423 K, which is similar data presented in other reports [110][121]. The main peak at 470 K was assigned to the surface reduction of In_2O_3 , and the later small and broad signal (peak near 647 K) is assigned to the reduction of bulk In_2O_3 particles. For $\text{Co}_3\text{O}_4/\text{ZrO}_2$, the reduction started at 400K and was

completed at 700 K. Three main signals with well-defined maxima were identified; these are qualitatively similar to the peaks observed in other reports [146,158]. The supported Co_3O_4 catalysts often show first two overlapping peaks in the temperature range of 400 K and 573 K. The peak near 463 K and 509 K were assigned to the surface reduction of Co^{3+} to Co^{2+} , and surface reduction of Co^{2+} to Co, respectively. The later broad signal between 550 K to 700 K can be traced back to the reduction of Co^{2+} with stronger interaction with the carrier (ZrO_2) to metallic Co [159]. Under normal reaction conditions (up to 573 K), they could not be reduced and therefore were probably inactive in hydrogenation reaction. The TPR profile of 2Co-In/ZrO_2 showed similar trend as Co_3O_4 , but in addition, it has the characteristic surface reduction peak of $\text{In}_2\text{O}_3/\text{ZrO}_2$ near 470 K, making the valley between two local maxima (451 K and 491 K) less pronounced. Under the reaction temperature of CO_2 hydrogenation evaluated in this report, both indium oxide and cobalt oxide should undergo a cycle of surface reduction by hydrogen and re-oxidation by concurrent CO_2 flow, and thus both the oxidation states of indium oxide and cobalt oxide were relevant in generating methanol or CO during the reaction.

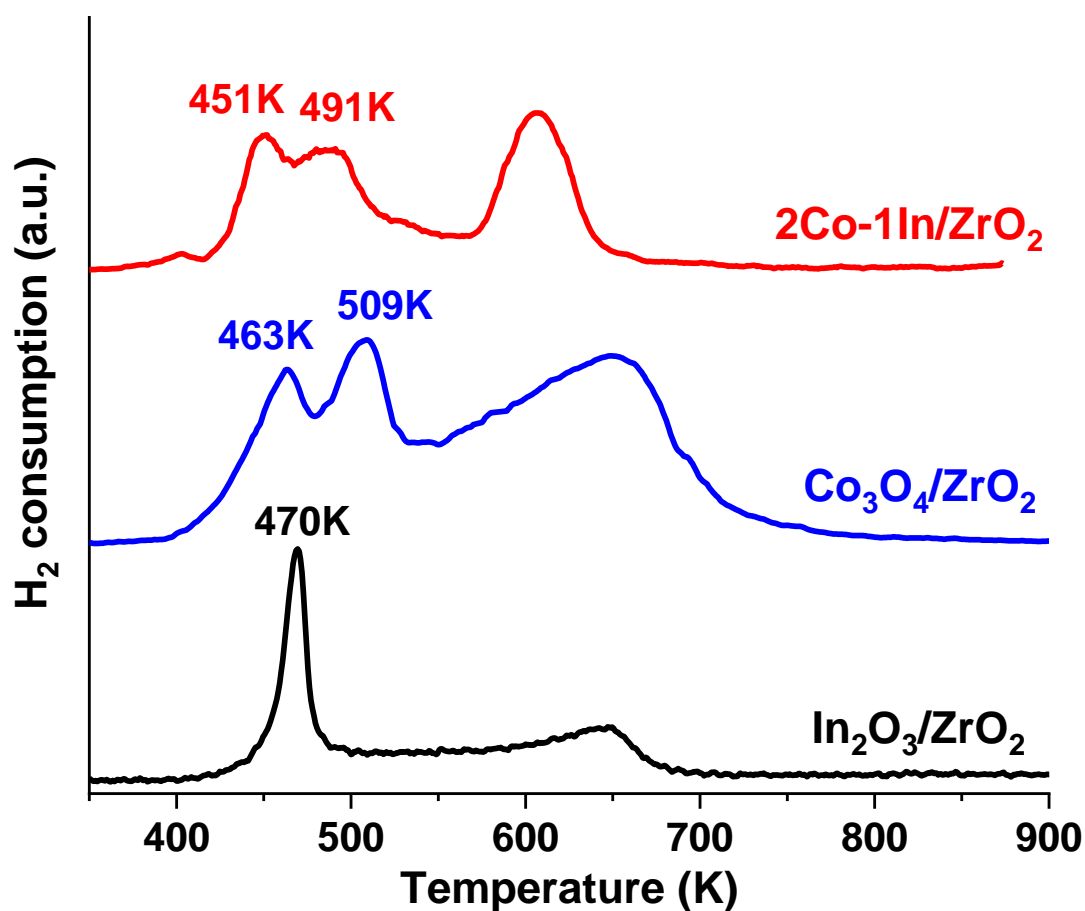


Figure 5.7 TPR profiles of 2Co-1In/ZrO₂, Co₃O₄/ZrO₂, and In₂O₃/ZrO₂.

CO₂ adsorption sites on Co-In bimetal oxides catalyst can be investigated by CO₂-TPD over spent catalyst after the reaction as shown in Figure 5.8. CO₂-TPD was conducted after the CO₂ hydrogenation reaction carried out in the temperature range of 573-543 K for 18 h over standard indium oxide catalyst (spent In₂O₃/ZrO₂) and bimetal oxides catalyst (spent 2Co-1In/ZrO₂). The catalysts were not exposed to the atmosphere after the reaction (samples were kept under He flow). The deconvolution

of TPD peaks are summarized in Table 5.4 by desorption temperature and the quantified amount of CO₂ desorption from, potentially, three different sites (α , β or γ).

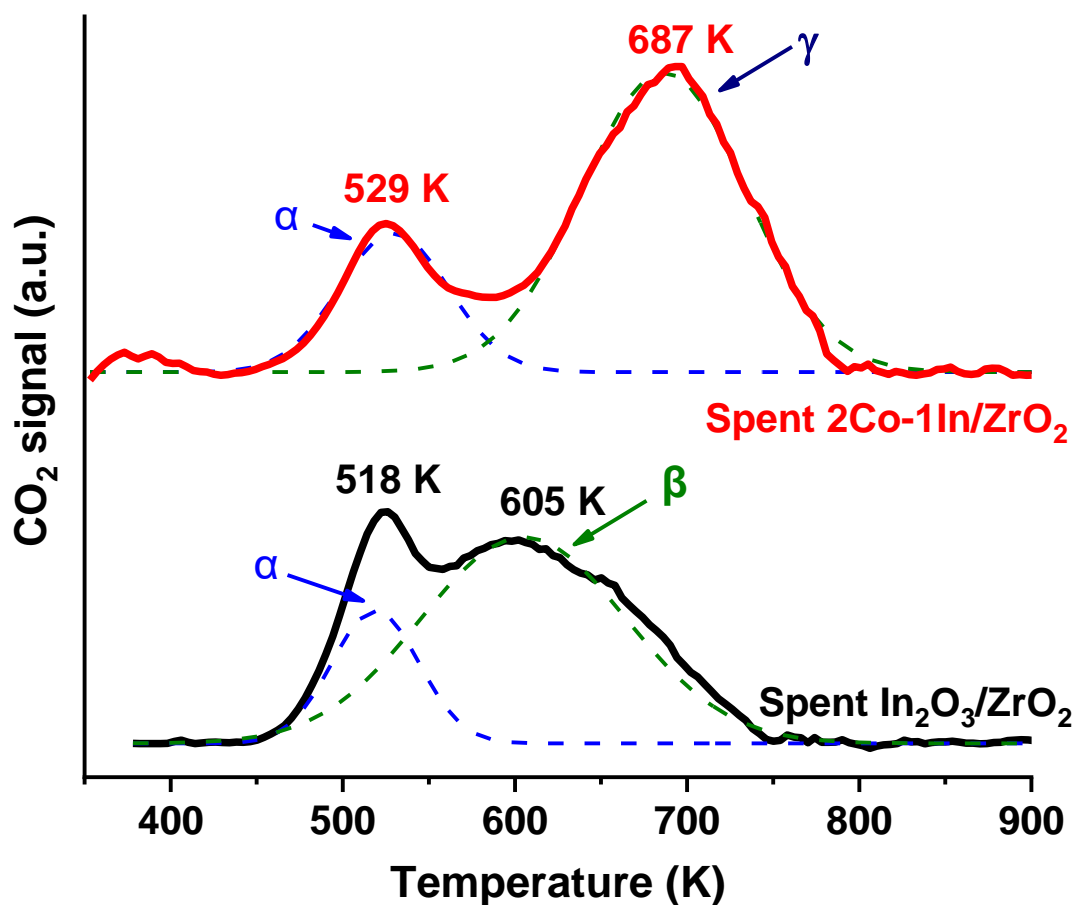


Figure 5.8 CO₂-TPD profiles of In₂O₃/ZrO₂, 2Co-1In/ZrO₂ after reaction at 573-543 K for 18 h.

The first CO₂ desorption peak for both catalysts located near 520 K (518 K for spent In₂O₃/ZrO₂ catalyst and 529 K for spent 2Co-1In/ZrO₂ catalyst, respectively) were assigned to the same CO₂ adsorption site α . The later peak for spent In₂O₃/ZrO₂ showed a broad desorption signal with maximum at 605 K, was assigned to a site β

(bottom of Figure 5.8). In contrast, the spent 2Co-1In/ZrO₂ catalyst featured a desorption peak starting near 600 K with the maximum of 687 K, which was assigned to different site γ . The amount of CO₂ desorption from both catalysts over site α was similar: 11 ± 0.5 mmol/g_{cat.} and 13 ± 0.4 mmol/g_{cat.} of CO₂ were collected during the TPD process. However, $\sim 23\%$ higher amount of CO₂ desorption (42 mmol/g_{cat.} versus 34 mmol/g_{cat.}) was obtained over spent 2Co-1In/ZrO₂ on site γ than the desorption found over spent In₂O₃/ZrO₂ on site β . Site α and site β have found in indium oxide-based catalyst in other report [46]. It has been suggested that the site α , denoted as O_{v2} in other reports, is primarily induced by hydrogen; whereas the site β , denoted as O_{v1}, is primarily induced by the heat treatment. It is believed that O_{v1} is the site responsible for the methanol production than O_{v2}, which produced more CO than methanol [46]. In the present bimetallic oxide catalyst, a stronger site than original O_{v1} an O_{v2} seemed to be formed during the reaction. This could be attributed to the interface interaction of cobalt and indium during the calcination or the reaction. Higher desorption temperature and higher adsorption of CO₂ indicate that more basic sites in bimetallic oxides Co-In catalyst were formed during the reaction, resulting in stronger and more CO₂ adsorption on this site.

Table 5.4 CO₂ desorption temperature and amount of CO₂ desorption for spent of In₂O₃/ZrO₂ and spent 2Co-1In/ZrO₂ from the deconvolution of TPD profiles as shown in Figure 5.8.

Catalysts	Spent In ₂ O ₃ /ZrO ₂	Spent 2Co-1In/ZrO ₂
Desorption temperature on site α	518 K	529 K
Desorption temperature on site β or γ	605 K	687 K
CO ₂ desorption from site α (mmol/g _{cat.})	11±0.5	13±0.4
CO ₂ desorption from site β or γ (mmol/g _{cat.})	34±0.8	42±0.5

5.4 Conclusions

In this chapter I report the discovery of a highly selective Co-In bimetallic oxide catalysts for CO₂ hydrogenation to methanol. This chapter reports key reaction result and a comprehensive characterization of the materials. Combined analyses of XRD patterns and XPS spectra of fresh and spent 2Co-1In/ZrO₂ indicated that Co₃O₄ and In₂O₃ formed after the calcination in air, but Co₃O₄ was mostly reduced to CoO after the reaction. The catalytic performance of the bimetal oxides catalyst showed good methanol formation rate (0.10 to 0.35 g_{MeOH} g_{cat.}⁻¹ h⁻¹) with very high selectivity (>99% from 528 K to 543 K) and stability (no deactivation after 40 h on stream). The slow changing methanol formation rate during the reaction, over a period of hours, implies that the working catalyst is different from the initial structure and composition, and that it self-assembles into the active phase under reaction conditions. The catalytic activity of the reference material Co₃O₄/ZrO₂ showed very high selectivity for

converting CO₂ to CH₄ with 80-88 % conversion and >99% selectivity toward CH₄. The bimetal oxide catalysts, however, only produced CO and methanol, and did not show any CH₄ production, implying the nature of the catalysts have been changed by the hybrid composition formed by the co-impregnation of Co-In. TPR profiles of the pristine 2Co-1In can be described as a linear combination of In₂O₃/ZrO₂ and Co₃O₄/ZrO₂, but TPD indicated that a more basic form of oxygen vacancy sites was formed in spent 2Co-1In/ZrO₂ catalyst. More CO₂ desorption (42 mmol/g_{cat.}) from the new site was also found compared to the CO₂ desorption from spent In₂O₃/ZrO₂ over site β. This novel and interesting catalyst system could be a potential alternative for Cu-based material with its promising catalytic behavior. Further works on surface characterization including the mechanistic studies and the discussion of the catalyst structure are needed to fully understand the mechanistic details of this catalyst.

Chapter 6

COMPARISON OF DIFFERENT CATALYSTS BY SIMULATION OF CO₂ TO METHANOL PRODUCTION PROCESS VIA ASPEN PLUS

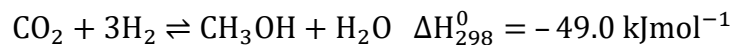
6.1 Introduction

Chapter 4 and Chapter 5 discussed the development of highly selective catalysts in CO₂ hydrogenation to methanol and showed their potential in industrial use. The aim of this chapter is to compare the difference between selective methanol synthesis *process* to the conventional *process*. This chapter investigates the results of two scenarios. The first scenario (section 6.3.1) shows the process under equilibrium condition, which one of the process produces only methanol from CO₂ and H₂, and the other process produces both CO and methanol from CO₂ and H₂. The second scenario (section 6.3.2) discusses the difference between conventional Cu/Zn/Al₂O₃ (CZA) catalyst, the promoted Indium-based catalyst (3La10In/ZrO₂), and the bimetal oxides catalyst (1Co-2In/ZrO₂) in terms of key parameters such as methanol productivity and net energy consumption in the methanol synthesis process. A chemical process optimization tool developed from Aspen Tech, Aspen Plus, is employed since it is widely used in industries for developing new processes or improving existing processes. Here Aspen Plus is used to understand the impact of catalyst selectivity and rate on process operation and cost. From the simulations of both scenarios, it is shown that a highly selective reaction toward methanol is beneficial in the synthesis process. It is shown that with higher methanol selectivity, methanol productivity is increased while the operating cost and net energy consumption are decreased.

6.2 Methods

The software used in this chapter is Aspen Plus V10 for the simulation of methanol synthesis process. A Gibbs reactor (RGibbs) was employed in the flowsheet of Aspen Plus in the first scenario (section 6.3.1) of the simulation. The reactor is used for modeling the reaction under specified conditions at equilibrium. The temperature and pressure used in this scenario were 543 K and 60 bar, which are the industrially relevant conditions for methanol synthesis. The designed process in this work was simplified from a former report in designing methanol reactor/column process [160].

A stoichiometric reactor (RStoic) was employed in the flowsheet in Aspen Plus during the discussion of second scenario (section 6.3.2). It is known as a type of reactors where the extent of reaction, conversion, and selectivity can be assigned a priori (that is, it is not determined based on a rate expression). The reaction heat can also be calculated from the stoichiometric reactor. The temperature and pressure of reaction were assigned at 543 K and 40 bar during the simulation as the same reaction conditions investigated in Chapter 4 and Chapter 5. The reactions included in the simulation were:



The occurring reactions, CO₂ to CO and CO₂ to methanol, were filled in with their known CO₂ conversion and methanol selectivity obtained from the experimental data of 3La10In/ZrO₂ (CO₂ conversion = 5%, methanol selectivity = 90%) in Chapter 4, and 1Co-2In/ZrO₂ (CO₂ conversion = 3%, methanol selectivity = ~90%) in Chapter 5, under the given reaction conditions. Conventional CZA catalyst (CO₂ conversion = 12%, methanol selectivity = 35%) was also implemented as the benchmark of the

above catalysts. Peng-Robinson equation of state was applied for the interaction parameters in whole simulation processes.

Several indices used in evaluating the performance of the simulated processes are defined below.

The methanol productivity used for comparing the performance of the catalysts in producing methanol in the process is defined in Eq. 6.1

$$\text{Productivity} = \frac{\text{moles of methanol (out)}}{\text{moles of CO}_2 \text{ (in)}} \times 100\% \quad (\text{Eq. 6.1})$$

The net energy consumption was the thermal consumption of the heat duties generated from the compressors, cooler, and the reactor. A heat exchanger efficiency of 50% was assumed for exchanging the heat from hot streams to the reaction purpose. Energy consumption is defined in Eq. 6.2

$$\text{Net energy consumption} = \frac{\text{net heat duties from all the units}}{\text{amount of methanol (out)}} \quad (\text{Eq. 6.2})$$

CO₂ consumption and H₂ efficiency are used to evaluate the efficiency of consuming CO₂ and utilizing H₂ in the simulated processes and are defined in Eq. 6.3 and Eq. 6.4, respectively.

$$\text{CO}_2 \text{ consumption (\%)} = \frac{\text{moles of CO}_{2,in} - \text{moles of CO}_{2,out}}{\text{moles of CO}_{2,in}} \times 100\% \quad (\text{Eq. 6.3})$$

$$\text{H}_2 \text{ Efficiency (\%)} = \frac{\text{moles of H}_{2,in} - \text{moles of H}_{2,out}}{\text{moles of H}_{2,in}} \times 100\% \quad (\text{Eq. 6.4})$$

6.3 Results and Discussion

6.3.1 Methanol synthesis process under equilibrium condition

The flowsheet of CO₂ hydrogenation to methanol process under equilibrium condition is illustrated in Figure 6.1. The process starts with 100 kmol h⁻¹ pure CO₂ (stream CO₂, 1 bar) and 300 kmol h⁻¹ pure pressurized H₂ (stream H₂, 60 bar) in the vapor phase. After the pressure is adjusted by the first compressor (COMP1), two streams were mixed (stream MIXTURE1), and the mixed stream was combined with the recycled stream (RECYCLE2) and formed the stream MIXTURE2. This gas mixture was then fed into a Gibbs reactor at 543 K and 60 bar. After the CO₂ hydrogenation reaction, the product was first passed to a cooler and partial condenser and was then separated into two phases: stream SEP-VAP (gas phase) and SEP-LIQ3 (liquid phase). This was done by two consecutive flash separators. The SEP-VAP stream was then split to two streams under a split ratio of 0.99, which PURGE1 was purged away and RECYCLE1 stream was then pressurized again (RECOUT). Note that RECOUT and RECYCLE1 or RECYCLE2 are identical streams. The reason to break the RECOUT and RECYCLE2 streams was to obtain easier convergence in Aspen under high split ratio at the splitter. The high split ratio usually causes mass balance error, with minor discrepancy. Breaking the streams and using the “design spec” function can help to prevent the unbalance problems. The RECYCLE2 stream was then fed back and mixed with the main stream to form MIXTURE2 and finish the cycle. The final product was obtained by distilling stream SEP-LIQ3 into CH₃OH and H₂O by a distillation column. The purity of methanol in METHANOL stream was assigned to be at least 98%.

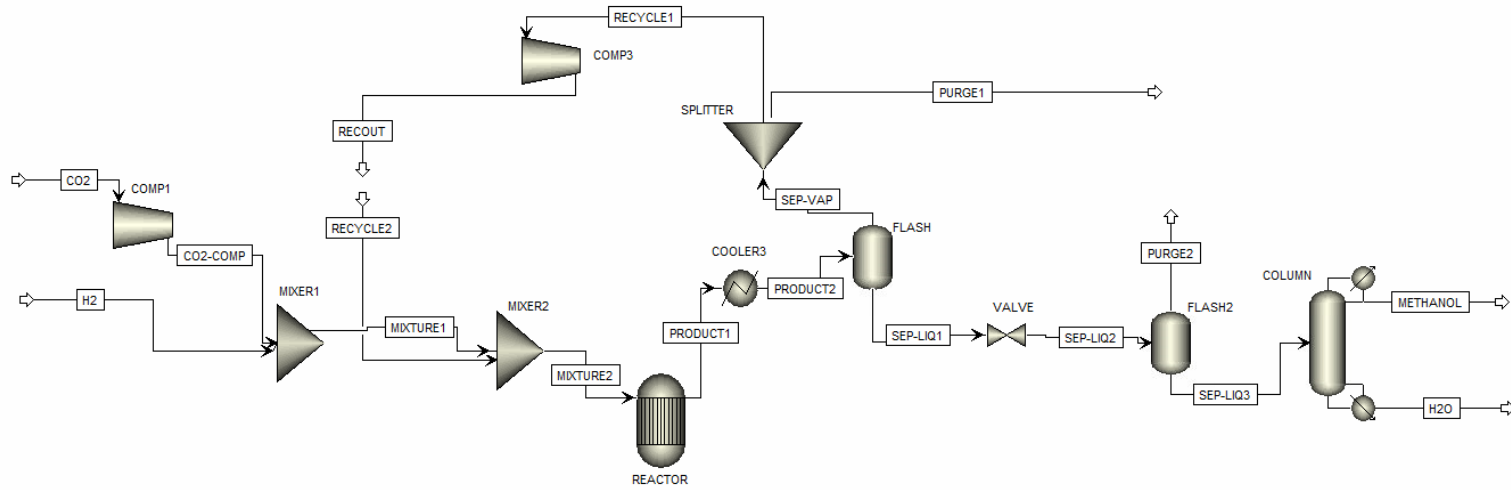


Figure 6.1 Flowsheet of CO₂ hydrogenation to methanol process using RGibbs reactor at equilibrium ($T = 543 \text{ K}$, $P = 60 \text{ bar}$).

Under equilibrium conditions, two cases were simulated. The first case considers all the major products including CO, methanol, and water in a reactor under equilibrium. The second case assumes an *ideal* reaction which only methanol and water are the products from CO₂ and H₂ and no CO is produced. The stream results for the first and second case described in this section are presented in Table A1 and Table A2, respectively, in Appendix A.

Table 6.1 summarizes CO₂ consumption, H₂ efficiency, single-pass methanol yield, and methanol productivity for case (i) Equilibrium and (ii) Equilibrium without CO production in the reactor. The CO₂ consumption for case (i) is 95.9%, which is 1.7% higher than 94.2% in case (ii). This is predictable with CO production in the reactor at equilibrium, the overall consumption of CO₂ in case (i) should be slightly higher than that in case (ii). H₂ efficiency was very high and similar in case (i) (96.4%) and case (ii) (96.6%), suggesting an efficient process was proposed in this simulation. The single-pass methanol yield was obtained from the change of molar fraction before and after the reactor. At equilibrium, a 5.1% yield was found with CO as byproduct, while a much higher yield of 7.8% was obtained from case (ii) without any formation of CO. The overall methanol productivity further suggests that case (ii) is a more efficient process. A 95.0% methanol productivity was obtained in case (ii) compared to 61.9% methanol productivity shown in case (i). The process simulation in equilibrium condition with RGibbs reactor illustrates how important a selective process (case (ii)) can make the process more efficient in producing desired product.

Table 6.1 Simulation results for the methanol process under (i) Equilibrium condition and (ii) Equilibrium without CO as product at 543 K, 60 bar with RGibbs reactor in Aspen Plus.

	(i) with CO production	(ii) without CO production
CO ₂ consumption (%)	95.9	94.2
H ₂ efficiency (%)	96.4	96.6
Single-pass methanol yield (%)	5.1	7.8
Methanol productivity (%)	61.9	95.0

To evaluate the impact of the selectivity on cost structure of the process, the cost analysis of the above two cases are shown in Table 6.2. The cost estimation source used in this table was directly calculated based on the data bank of Aspen Plus V10. It should be noted that the raw material cost and total product sales were not included in this table because the raw material is the same in feed streams (CO₂, H₂) and productivity has been described in Table 6.1. For the cost in unit operations in the simulated process, compressors (COMP1 and COMP3) and cooler (COOLER3) are the most energy-intensive units. COMP1 in both case (i) and case (ii) are the same since it compressed the same feed stream to 60 bar. The most significant difference is shown in COMP3, which compresses the recycle stream. The utility cost of COMP3 in case (i) and case (ii) are 101.2 USD/h and 86.7 USD/h, respectively. Without CO production in the reactor, the utility cost in pressurizing the recycle stream can be decreased by ~14.4%. This is mainly due to a smaller recycle stream RECYCLE1 in case (ii) with a molar flow rate of 0.374 kmol/s compared to the RECYCLE1 stream with a molar flow rate of 0.398 kmol/s in case (i). The higher molar flow rate in case (i) therefore increased the utility cost in compressor. Lower operating cost in COMP3 lowers the total utility cost in case (ii). The total utility cost of case (ii) is 1382010

USD, which is 9% lower than the utility cost of case (i) (1512920 USD). The equipment cost for both cases were 2,857200 USD and 2,854500 USD for case (i) and case (ii), respectively. The equipment cost for case (ii) is slightly lower was attributed by a smaller and lighter compressor (COMP3) installed in the process for a smaller recycle stream. Based on this simplified process under equilibrium condition, a higher selectivity of reaction in case (ii) benefits the productivity of methanol significantly and reduces the operating cost of the process. Thus, a highly selective catalyst used in methanol synthesis is recommended for a more productive and cost-efficient process.

Table 6.2 Cost analysis for case (i): equilibrium reaction in RGibbs reactor and case (ii): equilibrium reaction without CO production in RGibbs reactor.

		(i) with CO production	(ii) without CO production	
Unit Operation	COMP1	52.0	52.0	USD/h
	COMP3	101.2	86.7	USD/h
	COOLER3	12.7	12.8	USD/h
Utilities	Electricity	159.9	144.8	USD/h
	Cooling Water	12.7	12.8	USD/h
Total Utility cost		1512920	1382010	USD
Equipment cost		2857200	2854500	USD

6.3.2 Methanol synthesis process over conventional catalyst and selective catalysts using RStoic reactor

The flowsheet of CO₂ hydrogenation to methanol process for RStoic reactor is illustrated in Figure 6.2. The process is similar to Figure 6.1. The main difference is the reactor used here is RStoic reactor for assigning conversion and selectivity of the products. Also, the split ratio of the splitter is 0.95, which is lower than 0.99 in the previous equilibrium reactor in Figure 6.1. Thus, the recycle stream did not break to

RECOUT and RECYCLE2 as shown in Figure 6.1. The process is described briefly below. Initially, 100 kmol h^{-1} pure CO_2 (stream CO_2) and 300 kmol h^{-1} pure H_2 (stream H_2) were fed into the system in the vapor phase. After the two streams were mixed (stream MIXTURE1), the mixed stream was combined with the recycled stream and formed the stream MIXTURE2. This gas mixture was then fed into a stoichiometric reactor at 543 K and 40 bar. After the CO_2 hydrogenation reaction, the product was first passed to a cooler and partial condenser and was then separated into two phases: stream SEP-VAP (gas phase) and SEP-LIQ3 (liquid phase). This was done by two consecutive flash separators. The final product was obtained by distilling stream SEP-LIQ3 into CH_3OH and H_2O , while the other gas stream SEP-VAP was recycled back into stream MIXTURE1. The simulated stream results are listed in Appendix A.

Figure 6.3 presents the calculated methanol productivity for $\text{Cu/Zn/Al}_2\text{O}_3$, $3\text{La}10\text{In/ZrO}_2$, and 1Co-2In/ZrO_2 catalysts, which were 23%, 42%, and 37%, respectively. An almost 2-fold increase was obtained from switching the catalyst from conventional CZA catalyst to La-promoted indium oxide catalyst. Co-In bimetal oxides catalyst also increased the productivity by 61% compared to the original 23% productivity. It is noticed that the methanol productivity of the process is lower than previous scenario presented in section 6.3.1. This is due to the heavy loss of the carbon and hydrogen in the vented stream (PURGE1). For example, the PURGE1 stream of the processes using $\text{Cu/Zn/Al}_2\text{O}_3$, $3\text{La}10\text{In/ZrO}_2$, and 1Co-2In/ZrO_2 catalysts were 0.070, 0.059, and 0.073 kmol/sec, respectively. The molar ratios of $\text{H}_2:\text{CO}_2:\text{CO}$ in above streams were 0.69:0.11:0.19, 0.74:0.23:0.02, and 0.74:0.23:0.01, respectively. Comparing these molar flows to the molar flow rate of 0.111 kmol/sec in

MIXTURE1 stream, the vented stream showed a significant loss in carbon and hydrogen. This suggests that large amounts of reactants were not recycled back to the reactor due to the lower split ratio in the splitter used in these processes for an easier mass-balance convergence. Nonetheless, the result still shows the same conclusion that a highly selective catalyst is beneficial for an efficient production of methanol for every mole of CO₂ flowing into the process.

The next question needed to be answered is the impact of catalyst selectivity over energy consumption. Figure 6.4 shows the net energy consumption of Cu/Zn/Al₂O₃, 3La10In/ZrO₂, and 1Co-2In/ZrO₂ catalysts, which were 23862 KJ/Kg, 9622 KJ/Kg, and 18125 KJ/Kg, respectively. Although CZA catalyst had the highest conversion (12%), the low selectivity (35%) apparently brought about the difficulties in separation process and increased the energy consumption. Only 40% of the energy consumed by the CZA process is required by a process using 3La10In/ZrO₂ catalyst compared to the original CZA catalyst. This result clearly demonstrates the advantage of the highly selective catalyst in the process.

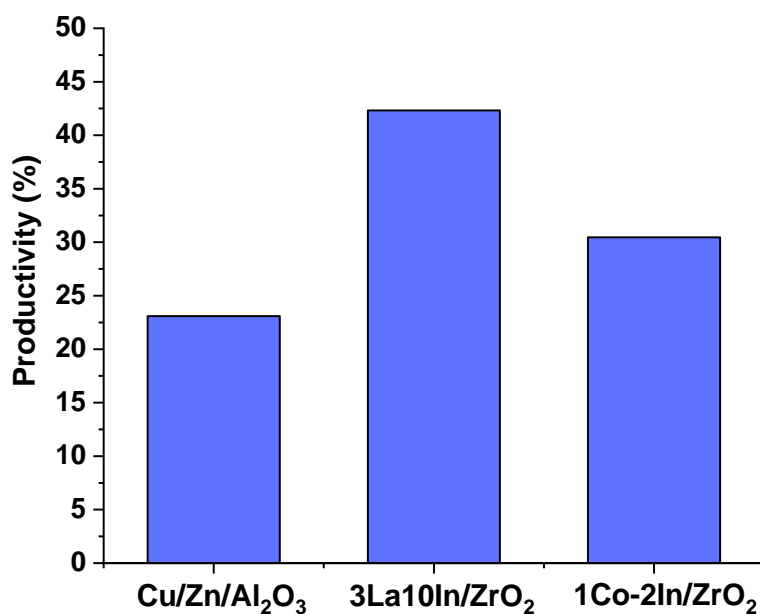


Figure 6.3 Methanol productivity (%) simulated from Aspen Plus over Cu/Zn/Al₂O₃, 3La10In/ZrO₂, and 1Co-2In/ZrO₂ catalysts at 543 K and 40 bar.

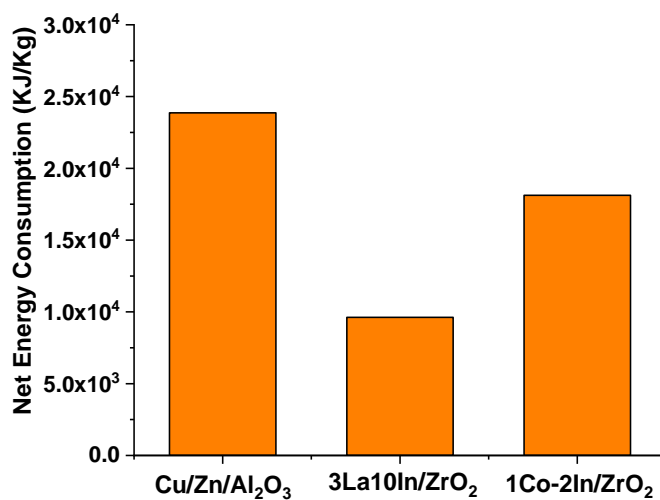


Figure 6.4 Net energy consumption (KJ/Kg) simulated from Aspen Plus over Cu/Zn/Al₂O₃, 3La10In/ZrO₂, and 1Co-2In/ZrO₂ catalysts at 543 K and 40 bar.

The productivity and net energy consumption versus different CO₂ conversion for selective CO₂ hydrogenation to methanol catalysts (methanol selectivity = 90%) were simulated and shown in Figure 6.5. The productivity increased monotonically from 11% to 42% when CO₂ conversion was increased from 1% to 5% under the same selectivity of 90%. On the other hand, the net energy consumption dropped dramatically from 71165 KJ/Kg to 18125 KJ/Kg as the CO₂ conversion increased from 1% to 3%. Further increasing CO₂ conversion from 3% to 5% decreased the energy consumption to 9622 KJ/Kg. Comparing to the CZA catalyst, the conversion of the new catalyst should be always higher than 2.4% at 90% methanol selectivity to match the performance of the conventional catalyst in terms of the productivity and energy consumption. This result sheds light on the target to aim for in the catalyst development in the future.

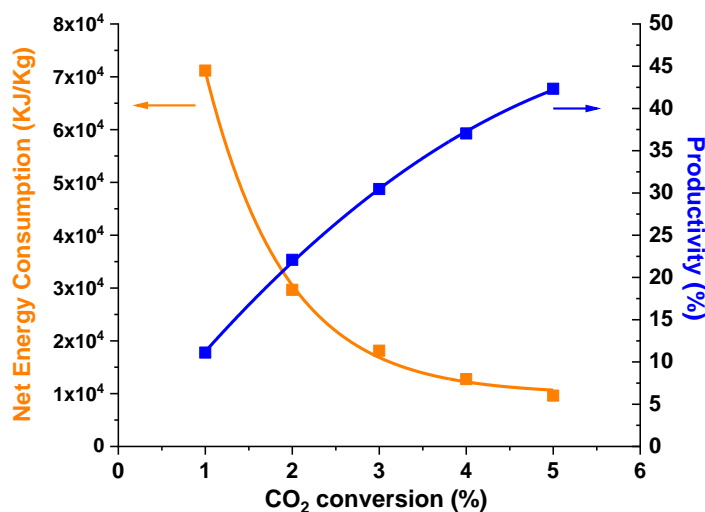


Figure 6.5 Methanol productivity (%) and net energy consumption versus CO₂ conversion at the methanol selectivity of 90% at 543 K and 40 bar simulated from Aspen Plus.

6.4 Conclusions

Reactions under equilibrium (543 K, 60 bar) with or without CO production were first evaluated in methanol synthesis process in this chapter. Under ideal condition, when there is no CO produced in the reactor, the methanol productivity increased 33.1% from the process with CO production at equilibrium. The utility costs can be further lowered by 14.4% primarily attributed to the less energy-intensive compressor. Cu/Zn/Al₂O₃ (CZA) catalyst, the promoted Indium-based catalyst (3La10In/ZrO₂), and the bimetal oxides catalyst (1Co-2In/ZrO₂) were implemented into a simulated process calculated using Aspen Plus. Under 543 K and 40 bar, both of the newly developed catalysts showed impressive performance in the aspects of methanol productivity and net energy consumption. 3La10In/ZrO₂ and 1Co-2In/ZrO₂ showed 83% and 61% higher methanol productivity than the CZA catalyst, respectively. The net energy consumption dropped 60% for 3La10In/ZrO₂ catalyst and dropped 24% for 1Co-2In/ZrO₂ catalyst. At least a CO₂ conversion of 2.4% is needed with 90% of methanol selectivity for matching the performance of the CZA catalyst. The above simulation elucidates the advantages of using highly selective catalysts and demonstrates the future targets in developing new catalyst for a more efficient process.

In the next chapter, the accomplishments and conclusions of this dissertation are summarized and a few recommendations for future directions in catalytic CO₂ hydrogenation are proposed.

Chapter 7

CONCLUSIONS AND RECOMMENDATIONS

7.1 Dissertation Summary

This thesis discusses the heterogeneous catalysis for the synthesis of value-added chemicals such as carbon monoxide and methanol from CO₂ and H₂. Several catalysts for CO₂ hydrogenation reaction have been studied and developed.

In Chapter 3, unsupported catalyst derived from magnetite was found to be highly active and stable in RWGS reaction. In addition, the catalyst is selective toward CO (>99%) with H₂:CO₂ = 1:1 at temperatures between 723 K and 773 K under 1 atm. The working catalyst was initially metallic iron after the activation in hydrogen and turned into a combination of metallic Fe, Fe²⁺, Fe³⁺, and Fe₃C under the H₂/CO₂ flow during the reaction. The main active sites are believed to be the combination of the above species except Fe₃C are unlikely to directly contribute to the very steady CO formation at our reaction conditions (1 atm, 723K-773K). Mechanism of RWGS reaction over this catalyst have been discussed. From gas-switching experiment and isotopic experiment, we have observed that CO was formed only when switching from H₂ to CO₂, and H₂O was formed when switching from CO₂ to H₂ but not when switching from H₂ to CO₂ if purging of Helium was in between with the gas admission. Redox mechanism is identified as dominant reaction pathway for CO₂ hydrogenation to CO over this unsupported iron catalyst. This chapter contributes more understandings of RWGS as an essential intermediate reaction in turning the problem of CO₂ emission into value-added products.

In Chapter 4, direct conversion of CO₂ to methanol was investigated over indium oxide-based catalysts supported on ZrO₂. Specifically, Y and La were used to promote the catalytic properties of supported In₂O₃ (In₂O₃/ZrO₂) for methanol synthesis by firstly mixing yttrium nitrate and lanthanum nitrate during the wet impregnation process. Characterization studies show that the reducibility of the indium oxide catalysts in a hydrogen atmosphere is correlated to methanol production rates and selectivity. The Y and La-promoted catalysts (1.5Y9In/ZrO₂, 2Y8In/ZrO₂, 3Y8In/ZrO₂, and 3La10In/ZrO₂) had 11-35 K higher surface reduction temperatures compared to the standard indium catalyst (In₂O₃/ZrO₂). Packed-bed microreactor studies indicated that the incorporation of Y or La into the In₂O₃/ZrO₂ catalysts increased the number of surface CO₂ adsorption sites. The CO₂ TPD traces show 60% to 70% more heat-induced oxygen vacancies (O_{v1}) in 2Y8In/ZrO₂ or 3La10In/ZrO₂. The Y or La-promoted catalysts increased the selectivity of methanol significantly (about 20% more selective, from 528 K to 573 K). A selectivity of nearly 100% can be achieved at 528K and 40 bar, which is a mild reaction condition compared to the commercial process (513-533K, 50-100 bar). CO co-feeding experiment suggest a likely reaction route (formate pathway) for methanol formation over 2Y8In/ZrO₂ within the reaction conditions we have examined. This study demonstrates that the incorporation of Y and La into indium oxide catalysts is a feasible method for the design of selective catalysts for a more sustainable methanol economy in the future.

Chapter 5 describes the study on developing a novel bimetal oxide system consisting of cobalt oxide and indium oxide for selectively converting CO₂ into methanol. Key catalytic behaviors and a comprehensive characterization of the materials are included. Combined analyses of XRD patterns and XPS spectra of fresh

and spent 2Co-1In/ZrO₂ indicated that Co₃O₄ and In₂O₃ formed after the calcination in air, but Co₃O₄ was mostly reduced to CoO after the reaction. The catalytic performance of the bimetal oxides catalyst showed good methanol formation rate (0.10 to 0.35 g_{MeOH}/g_{cat.} h⁻¹) with very high selectivity (>99% from 528 K to 543 K) and stability (no deactivation after 40 h on stream) was obtained. The slow changing methanol formation rate during the reaction, over a period of hours, implies that the working catalyst is different from the initial structure and composition, and that it self-assembles into the active phase under reaction conditions. The catalytic activity of the reference material Co₃O₄/ZrO₂ showed very high selectivity for converting CO₂ to CH₄ with 80-88 % conversion and >99% selectivity toward CH₄. The bimetal oxide catalysts, however, only produced CO and methanol, and did not show any CH₄ production, implying the nature of the catalysts have been changed by the hybrid composition formed by the co-impregnation of Co-In. TPR profiles of the pristine 2Co-1In can be described as a linear combination of In₂O₃/ZrO₂ and Co₃O₄/ZrO₂, but TPD indicated that a more basic form of oxygen vacancy sites was formed in spent 2Co-1In/ZrO₂ catalyst. More CO₂ desorption (42 mmol/g_{cat.}) from the new site was also found compared to the CO₂ desorption from spent In₂O₃/ZrO₂ over site β (34 mmol/g_{cat.}). This novel and interesting catalyst system, with its promising catalytic behavior, could be a potential alternative for Cu-based material. Further works (suggested in next section) on surface characterization including the mechanistic studies and the discussion of the catalyst structure are needed to fully understand the mechanistic details of this new catalyst.

In Chapter 6, a methanol synthesis process from CO₂ and H₂ was simulated via Aspen Plus. Three catalysts Cu/Zn/Al₂O₃ (CZA) catalyst, the promoted Indium-based

catalyst ($3\text{La}10\text{In}/\text{ZrO}_2$), and the bimetal oxides catalyst ($1\text{Co}-2\text{In}/\text{ZrO}_2$) were implemented into a simulated process. $3\text{La}10\text{In}/\text{ZrO}_2$ and $1\text{Co}-2\text{In}/\text{ZrO}_2$ showed 83% and 61% higher methanol productivity than the CZA catalyst, respectively. The net energy consumption dropped 60% for $3\text{La}10\text{In}/\text{ZrO}_2$ catalyst and dropped 24% for $1\text{Co}-2\text{In}/\text{ZrO}_2$ catalyst. At least a CO_2 conversion of 2.4% is needed with 90% of methanol selectivity for matching the performance of the conventional CZA catalyst. These results not only demonstrate the advantage of the highly selective catalyst but also the future targets in developing new catalyst for a more efficient process.

7.2 Recommendations for future work

The studies presented in the preceding chapters have made progress towards identifying effective catalysts and understanding many of the important details regarding the reaction mechanisms for the RWGS and the CO_2 hydrogenation to methanol reactions. However, the scope of the reactions is huge, and therefore many questions still need to be addressed. The following sections in this chapter describes several possible directions for future work based on the findings in this dissertation.

7.2.1 Further improvements on In_2O_3 catalyst for methanol synthesis

The catalytic performance of highly selective In_2O_3 -based catalyst is promising. However, the high selectivity usually comes with lower conversion (3-5%). Increasing the catalyst mass to increase the conversion usually comes with lower methanol formation rate due to the limit of external mass transfer. More investigations on kinetics regarding internal and external mass transfer limits, particle sizes, morphology are crucial to improve the catalytic performance in this regard. Other means of improving the activity or stability of the catalyst could be investigated by

further exploring the catalyst composition. In Chapter 4, the composition of the promoters and the indium oxide catalysts were determined based on the total moles of metal loading. It was found that the reactivity increased with higher loading of In but the selectivity could drop, and higher loading of promoters could potentially block both the active sites to form CO and methanol. Further studies on both composition and loadings of the promoter and indium oxide and their effects on reactivity could be important.

Using In_2O_3 as catalyst in CO_2 hydrogenation is relatively new to the research community. Thus, despite the promising performance and some information about the reaction pathway as addressed in the previous chapter, a lot of mechanistic questions still needed to be answered. A combination of X-ray absorption (XAS), operando infrared and Raman spectroscopy, and density functional theory calculations is crucial to identify the surface structure and oxidation state of the intermediates during the hydrogenation reaction.

7.2.2 Further improvements on bimetal oxide catalysts for methanol synthesis

An interesting and novel system composed of supported cobalt oxide and indium oxide catalysts for methanol synthesis deserves more attention in research community in the future. Therefore, a few directions are suggested below.

Based on our results in Chapter 5, the interface of Co and In is crucial for such a special activity, which turned cobalt oxide from CO_2 methanation catalyst into methanol producer. A few new structures of catalysts should be studied. For example, indium oxide supported on high surface area Co_3O_4 ($\text{In}_2\text{O}_3/\text{Co}_3\text{O}_4$) and an inverse structure, *i.e.*, cobalt oxide supported on high surface area In_2O_3 ($\text{Co}_3\text{O}_4/\text{In}_2\text{O}_3$) should be further investigated to explore the synergistic effect between the surface. From

molecular point of view, the structure of the material should be highly linked to the selectivity and activity of the catalyst. Several tools are proved to be informative[161]. Electron energy-loss spectroscopy (EELS) in the scanning transmission electron microscopy (TEM) mode, which indicates the predominant phase of the composition, can give bulk information of the catalyst. Synchrotron-based, surface-sensitive X-ray absorption (XAS) performed on beamlines can generate the information of oxidation state on cobalt or indium oxide during the reaction. Eventually an elemental fractions of different oxidation states of materials used in the reaction can be discovered with different reaction conditions including the change of temperature or reactant concentration.

For experimental process and operation, effect of calcination temperatures and the pretreatment conditions before the reaction for the catalyst activation should be investigated. It was reported that the pretreatment temperature can change the surface area and the composition of the initial catalyst [46]. Besides Co-In shown in this thesis, Pd-In [111,162] and Pd-Cu [163] have recently drawn a lot of attention. Pd-In bimetallic catalyst has reported to be active in CO₂ conversion to methanol at the rate of 5.1 $\mu\text{mol}_{\text{MeOH}} \text{g}_{\text{InPd}}^{-1} \text{s}^{-1}$ and selectivity of 61% toward methanol [162]. The catalyst contained both In–Pd intermetallic compounds and an indium oxide phase, resulted in promotion of the catalytic activity. Another report using In-Pd showed >80% methanol selectivity and high stability [111]. Support effect such as using Al₂O instead of ZrO₂ is also worth studying to obtain insight on the interaction in the interface between the support and the bimetal oxide catalyst.

The investigation of different composition and the elemental phases of the catalysts could benefit not only to the performance, but also more understandings from the molecular point of view.

7.2.3 Conversion of methanol to other value-added products

The progress of CO₂ to methanol conversion can further lead us to other catalytic conversion from methanol to hydrocarbons. There are several classes of methanol transformations to hydrocarbons: methanol-to-olefins (MTO) [164], methanol-to-gasoline (MTG) [10,11] and methanol homologation to mixtures of alkanes and alkenes (C₄-C₇). In these applications, different zeolites were combined with methanol-producing catalyst. Gao *et.al.* [13] proposed a bifunctional catalyst composed of indium-zirconium composite oxide and SAPO-34 zeolite, which is responsible for CO₂ activation and selective C-C coupling, respectively, to generate light olefins from CO₂ directly. Another bifunctional catalyst composed of reducible indium oxides (In₂O₃) and HZSM-5 zeolites, was reported to yield a high selectivity to gasoline-range hydrocarbons (78.6%) with a very low methane selectivity (1%) [11].

REFERENCES

- [1] Gaseous Carbon Waste Streams Utilization: Status and Research Needs, Natl. Acad. Press. (2019). doi:10.17226/25232.
- [2] B. Kahn, Earth's CO₂ Passes the 400 PPM Threshold—Maybe Permanently, *Clim. Cent.* (2016).
- [3] National Oceanic & Atmospheric Administration, Full Mauna Loa CO₂ record, <https://www.esrl.noaa.gov/gmd/ccgg/trends/full.html>. (2019).
- [4] S. Perathoner, G. Centi, CO₂ recycling: A key strategy to introduce green energy in the chemical production chain, *ChemSusChem.* 7 (2014) 1274–1282. doi:10.1002/cssc.201300926.
- [5] W. Wang, S. Wang, X. Ma, J. Gong, Recent advances in catalytic hydrogenation of carbon dioxide, *Chem Soc Rev.* 40 (2011) 3703–3727. doi:10.1039/c1cs15008a.
- [6] Y.A. Daza, J.N. Kuhn, CO₂ conversion by reverse water gas shift catalysis: Comparison of catalysts, mechanisms and their consequences for CO₂ conversion to liquid fuels, *RSC Adv.* 6 (2016) 49675–49691. doi:10.1039/c6ra05414e.
- [7] I. Ro, R. Carrasquillo-Flores, J.A. Dumesic, G.W. Huber, Intrinsic kinetics of plasmon-enhanced reverse water gas shift on Au and Au–Mo interfacial sites supported on silica, *Appl. Catal. A Gen.* (2015) 6–13. doi:10.1016/j.apcata.2015.11.021.
- [8] F.M. Sun, C.F. Yan, Z. Da Wang, C.Q. Guo, S.L. Huang, Ni/Ce-Zr-O catalyst for high CO₂ conversion during reverse water gas shift reaction (RWGS), *Int. J. Hydrogen Energy.* 40 (2015) 15985–15993. doi:10.1016/j.ijhydene.2015.10.004.
- [9] B. Mutz, H.W.P. Carvalho, S. Mangold, W. Kleist, J.D. Grunwaldt, Methanation of CO₂: Structural response of a Ni-based catalyst under fluctuating reaction conditions unraveled by operando spectroscopy, *J. Catal.* 327 (2015) 48–53. doi:10.1016/j.jcat.2015.04.006.

- [10] J. Wei, Q. Ge, R. Yao, Z. Wen, C. Fang, L. Guo, H. Xu, J. Sun, Directly converting CO₂ into a gasoline fuel, *Nat. Commun.* 8 (2017) 1–8. doi:10.1038/ncomms15174.
- [11] P. Gao, S. Li, X. Bu, S. Dang, Z. Liu, H. Wang, L. Zhong, M. Qiu, C. Yang, J. Cai, W. Wei, Y. Sun, Direct conversion of CO₂ into liquid fuels with high selectivity over a bifunctional catalyst, *Nat. Chem.* 9 (2017) 1019–1024. doi:10.1038/nchem.2794.
- [12] J. Su, D. Wang, Y. Wang, H. Zhou, C. Liu, S. Liu, C. Wang, W. Yang, Z. Xie, M. He, Direct Conversion of Syngas into Light Olefins over Zirconium-Doped Indium(III) Oxide and SAPO-34 Bifunctional Catalysts: Design of Oxide Component and Construction of Reaction Network, *ChemCatChem.* 10 (2018) 1536–1541. doi:10.1002/cctc.201702054.
- [13] P. Gao, S. Dang, S. Li, X. Bu, Z. Liu, M. Qiu, C. Yang, H. Wang, L. Zhong, Y. Han, Q. Liu, W. Wei, Y. Sun, Direct Production of Lower Olefins from CO₂ Conversion via Bifunctional Catalysis, *ACS Catal.* 8 (2018) 571–578. doi:10.1021/acscatal.7b02649.
- [14] T. Inui, T. Takeguchi, A. Kohama, K. Tanida, Effective conversion of carbon dioxide to gasoline, *Energy Convers. Manag.* 33 (1992) 513–520. doi:10.1016/0196-8904(92)90050-7.
- [15] F. Studt, I. Sharafutdinov, F. Abild-Pedersen, C.F. Elkjær, J.S. Hummelshøj, S. Dahl, I. Chorkendorff, J.K. Nørskov, Discovery of a Ni-Ga catalyst for carbon dioxide reduction to methanol., *Nat. Chem.* 6 (2014) 320–4. doi:10.1038/nchem.1873.
- [16] M. Behrens, F. Studt, I. Kasatkin, S. Kühn, M. Hävecker, F. Abild-Pedersen, S. Zander, F. Girgsdies, P. Kurr, B.-L. Knief, M. Tovar, R.W. Fischer, J.K. Nørskov, R. Schlögl, The active site of methanol synthesis over Cu/ZnO/Al₂O₃ industrial catalysts., *Science (80-.)*. 336 (2012) 893–7. doi:10.1126/science.1219831.
- [17] J. Graciani, K. Mudiyanse, F. Xu, a. E. Baber, J. Evans, S.D. Senanayake, D.J. Stacchiola, P. Liu, J. Hrbek, J.F. Sanz, J. a. Rodriguez, Highly active copper-ceria and copper-ceria-titania catalysts for methanol synthesis from CO₂, *Science (80-.)*. 345 (2014) 546–550. <http://www.sciencemag.org/cgi/doi/10.1126/science.1253057>.
- [18] J. Nakamura, T. Fujitani, S. Kuld, S. Helveg, I. Chorkendorff, J. Sehested, Comment on “Active sites for CO₂ hydrogenation to methanol on Cu/ZnO catalysts”, *Science (80-.)*. 357 (2017) eaan8074.

doi:10.1126/science.aan8074.

- [19] T. Inui, T. Yamamoto, M. Inoue, H. Hara, T. Takeguchi, J.B. Kim, Highly effective synthesis of ethanol by CO₂-hydrogenation on well balanced multi-functional FT-type composite catalysts, *Appl. Catal. A Gen.* 186 (1999) 395–406. doi:10.1016/S0926-860X(99)00157-X.
- [20] T. Numpilai, K. Faungnawakij, Y. Suwannapichat, J. Limtrakul, T. Witoon, M. Chareonpanich, N. Chanlek, Direct synthesis of dimethyl ether from CO₂ hydrogenation over novel hybrid catalysts containing a Cu ZnO ZrO₂ catalyst admixed with WO_x/Al₂O₃ catalysts: Effects of pore size of Al₂O₃ support and W loading content, *Energy Convers. Manag.* 159 (2018) 20–29. doi:10.1016/j.enconman.2018.01.016.
- [21] D.W. Lee, M.S. Lee, J.Y. Lee, S. Kim, H.J. Eom, D.J. Moon, K.Y. Lee, The review of Cr-free Fe-based catalysts for high-temperature water-gas shift reactions, *Catal. Today.* 210 (2013) 2–9. doi:10.1016/j.cattod.2012.12.012.
- [22] C. Ratnasamy, J.P. Wagner, Water Gas Shift Catalysis, *Catal. Rev.* 51 (2009) 325–440. doi:10.1080/01614940903048661.
- [23] M. Zhu, I.E. Wachs, Iron-Based Catalysts for the High-Temperature Water–Gas Shift (HT-WGS) Reaction: A Review, *ACS Catal.* 6 (2016) 722–732. doi:10.1021/acscatal.5b02594.
- [24] S.-W. Park, O.-S. Joo, K.-D. Jung, H. Kim, S.-H. Han, Development of ZnO/Al₂O₃ catalyst for reverse-water-gas-shift reaction of CAMERE (carbon dioxide hydrogenation to form methanol via a reverse-water-gas-shift reaction) process, *Appl. Catal. A Gen.* 211 (2001) 81–90. doi:10.1016/S0926-860X(00)00840-1.
- [25] O.S. Joo, K.D. Jung, I. Moon, A.Y. Rozovskii, G.I. Lin, S.H. Han, S.J. Uhm, Carbon dioxide hydrogenation to form methanol via a reverse-water-gas- shift reaction (the CAMERE process), *Ind. Eng. Chem. Res.* 38 (1999) 1808–1812. doi:10.1021/ie9806848.
- [26] Y.A. Daza, D. Maiti, B.J. Hare, V.R. Bhethanabotla, J.N. Kuhn, More Cu, more problems: Decreased CO₂ conversion ability by Cu-doped La_{0.75}Sr_{0.25}FeO₃ perovskite oxides, *Surf. Sci.* 648 (2016) 92–99. doi:10.1016/j.susc.2015.11.017.
- [27] Y.A. Daza, R.A. Kent, M.M. Yung, J.N. Kuhn, Carbon dioxide conversion by reverse water-gas shift chemical looping on perovskite-type oxides, *Ind. Eng. Chem. Res.* 53 (2014) 5828–5837. doi:10.1021/ie5002185.

- [28] Martin Bertau, H. Offermanns, L. Plass, F. Schmidt, H.-J. Wernicke, *Methanol The Basic Chemical and Energy Feedstock of the Future*, Springer, Berlin Heidelberg, 2014.
- [29] D. Sheldon, *Methanol Production – A Technical History*, *Johnson Matthey Technol. Rev.* 61 (2017) 172–182.
- [30] <https://igpenergy.com/methanol-overview/>, <https://www.methanol.org/the-methanol-industry/>, <https://Igpenergy.Com/Methanol-Overview/>, <https://Www.Methanol.Org/the-Methanol-Industry/>. (n.d.).
- [31] A. Álvarez, A. Bansode, A. Urakawa, A. V. Bavykina, T.A. Wezendonk, M. Makkee, J. Gascon, F. Kapteijn, Challenges in the Greener Production of Formates/Formic Acid, Methanol, and DME by Heterogeneously Catalyzed CO₂ Hydrogenation Processes, *Chem. Rev.* 117 (2017) 9804–9838. doi:10.1021/acs.chemrev.6b00816.
- [32] M. de Falco, G. Iaquaniello, G. Centi, CO₂: A valuable source of carbon, 2013. doi:10.1007/978-1-4471-5119-7.
- [33] A. Goepfert, M. Czaun, J.P. Jones, G.K. Surya Prakash, G.A. Olah, Recycling of carbon dioxide to methanol and derived products-closing the loop, *Chem. Soc. Rev.* 43 (2014) 7995–8048. doi:10.1039/c4cs00122b.
- [34] G.A. Olah, Towards oil independence through renewable methanol chemistry, *Angew. Chemie - Int. Ed.* 52 (2013) 104–107. doi:10.1002/anie.201204995.
- [35] G.A. Olah, A. Goepfert, G.K.S. Prakash, Chemical recycling of carbon dioxide to methanol and dimethyl ether: From greenhouse gas to renewable, environmentally carbon neutral fuels and synthetic hydrocarbons, *J. Org. Chem.* 74 (2009) 487–498. doi:10.1021/jo801260f.
- [36] L. Jia, J. Gao, W. Fang, Q. Li, Carbon dioxide hydrogenation to methanol over the pre-reduced LaCr_{0.5}Cu_{0.5}O₃ catalyst, *Catal. Commun.* 10 (2009) 2000–2003. doi:10.1016/J.CATCOM.2009.07.017.
- [37] J. Toyir, P.R. de la Piscina, J.L.G. Fierro, N. Homs, Highly effective conversion of CO₂ to methanol over supported and promoted copper-based catalysts: influence of support and promoter, *Appl. Catal. B Environ.* 29 (2001) 207–215. doi:10.1016/S0926-3373(00)00205-8.
- [38] A. Le Valant, C. Comminges, C. Tisseraud, C. Canaff, L. Pinard, Y. Pouilloux, The Cu–ZnO synergy in methanol synthesis from CO₂, Part 1: Origin of active site explained by experimental studies and a sphere contact quantification

model on Cu + ZnO mechanical mixtures, *J. Catal.* 324 (2015) 41–49.
doi:10.1016/J.JCAT.2015.01.021.

- [39] A. Bansode, B. Tidona, P.R. Von Rohr, A. Urakawa, Impact of K and Ba promoters on CO₂ hydrogenation over Cu/Al₂O₃ catalysts at high pressure, *Catal. Sci. Technol.* 3 (2013) 767–778. doi:10.1039/c2cy20604h.
- [40] X. Guo, D. Mao, G. Lu, S. Wang, G. Wu, The influence of La doping on the catalytic behavior of Cu/ZrO₂ for methanol synthesis from CO₂ hydrogenation, *J. Mol. Catal. A Chem.* 345 (2011) 60–68.
doi:10.1016/J.MOLCATA.2011.05.019.
- [41] T. Fujitani, M. Saito, Y. Kanai, T. Watanabe, J. Nakamura, T. Uchijima, Development of an active Ga₂O₃ supported palladium catalyst for the synthesis of methanol from carbon dioxide and hydrogen, *Appl. Catal. A Gen.* 125 (1995) 199–202. doi:10.1016/0926-860X(95)00049-6.
- [42] L. Fan, K. Fujimoto, Development of an active and stable ceria-supported palladium catalyst for hydrogenation of carbon dioxide to methanol, *Appl. Catal. A Gen.* 106 (1993) L1–L7. doi:10.1016/0926-860X(93)80152-G.
- [43] K. Sun, Z. Fan, J. Ye, J. Yan, Q. Ge, Y. Li, W. He, W. Yang, C.J. Liu, Hydrogenation of CO₂ to methanol over In₂O₃ catalyst, *J. CO₂ Util.* 12 (2015) 1–6. doi:10.1016/j.jcou.2015.09.002.
- [44] J. Ye, C. Liu, Q. Ge, DFT Study of CO₂ Adsorption and Hydrogenation on the In₂O₃ Surface, *J. Phys. Chem. C.* 116 (2012) 7817–7825.
doi:10.1021/jp3004773.
- [45] J. Ye, C. Liu, D. Mei, Q. Ge, Active oxygen vacancy site for methanol synthesis from CO₂ hydrogenation on In₂O₃(110): A DFT study, *ACS Catal.* 3 (2013) 1296–1306. doi:10.1021/cs400132a.
- [46] O. Martin, A.J. Martín, C. Mondelli, S. Mitchell, T.F. Segawa, R. Hauert, C. Drouilly, D. Curulla-Ferré, J. Pérez-Ramírez, Indium Oxide as a Superior Catalyst for Methanol Synthesis by CO₂ Hydrogenation, *Angew. Chemie Int. Ed.* 55 (2016) 1–6. doi:10.1002/anie.201600943.
- [47] E.L. Kunkes, F. Studt, F. Abild-Pedersen, R. Schlögl, M. Behrens, Hydrogenation of CO₂ to methanol and CO on Cu/ZnO/Al₂O₃: Is there a common intermediate or not?, *J. Catal.* 328 (2015) 43–48.
doi:10.1016/j.jcat.2014.12.016.
- [48] F. Arena, G. Mezzatesta, G. Zafarana, G. Trunfio, F. Frusteri, L. Spadaro,

- Effects of oxide carriers on surface functionality and process performance of the Cu-ZnO system in the synthesis of methanol via CO₂ hydrogenation, *J. Catal.* 300 (2013) 141–151. doi:10.1016/j.jcat.2012.12.019.
- [49] K.C. Waugh, Methanol synthesis, *Catal. Letters.* 142 (2012) 1153–1166. doi:10.1007/s10562-012-0905-2.
- [50] A. Bansode, A. Urakawa, Towards full one-pass conversion of carbon dioxide to methanol and methanol-derived products, *J. Catal.* 309 (2014) 66–70. doi:10.1016/j.jcat.2013.09.005.
- [51] O. Martin, J. Pérez-Ramírez, New and revisited insights into the promotion of methanol synthesis catalysts by CO₂, *Catal. Sci. Technol.* 3 (2013) 3343–3352. doi:10.1039/c3cy00573a.
- [52] Y. Yang, C.A. Mims, D.H.H. Mei, C.H.F.H.F. Peden, C.T.T. Campbell, Mechanistic studies of methanol synthesis over Cu from CO/CO₂/H₂/H₂O mixtures: The source of C in methanol and the role of water, *J. Catal.* 298 (2013) 10–17. doi:10.1016/j.jcat.2012.10.028.
- [53] Y. Yang, C.A. Mims, R.S. Disselkamp, J.H. Kwak, C.H.F. Peden, C.T. Campbell, (Non)formation of methanol by direct hydrogenation of formate on copper catalysts, *J. Phys. Chem. C.* 114 (2010) 17205–17211. doi:10.1021/jp104068k.
- [54] S. Kattel, P. Liu, J.G. Chen, Tuning Selectivity of CO₂ Hydrogenation Reactions at the Metal/Oxide Interface, *J. Am. Chem. Soc.* 139 (2017) 9739–9754. doi:10.1021/jacs.7b05362.
- [55] M.S. Frei, M. Capdevila-Cortada, R. García-Muelas, C. Mondelli, N. López, J.A. Stewart, D. Curulla Ferré, J. Pérez-Ramírez, Mechanism and microkinetics of methanol synthesis via CO₂ hydrogenation on indium oxide, *J. Catal.* 361 (2018) 313–321. doi:10.1016/j.jcat.2018.03.014.
- [56] B.D.D. J. Haber, J. H. Block, Manual of methods and procedures for catalyst characterization (Technical Report), *Pure Appl. Chem.* 67 (1995) 1257–1306.
- [57] K. Siegbahn, K. Edvarson, β -Ray spectroscopy in the precision range of 1 : 10⁵, *Nucl. Phys.* 1 (1956) 137–159.
- [58] H. Konno, Chapter 8 - X-ray Photoelectron Spectroscopy, in: M. Inagaki, F.B.T.-M.S. and E. of C. Kang (Eds.), *Mater. Sci. Eng. Carbon Charact.*, Butterworth-Heinemann, 2016: pp. 153–171. doi:https://doi.org/10.1016/B978-0-12-805256-3.00008-8.

- [59] G.S. Sewell, E. Van Steen, C.T. O'Connor, Use of TPR/TPO for characterization of supported cobalt catalysts, *Catal. Letters*. 37 (1996) 255–260. doi:10.1007/BF00807763.
- [60] W.K. Jozwiak, E. Kaczmarek, T.P. Maniecki, W. Ignaczak, W. Maniukiewicz, Reduction behavior of iron oxides in hydrogen and carbon monoxide atmospheres, *Appl. Catal. A Gen.* 326 (2007) 17–27. doi:10.1016/j.apcata.2007.03.021.
- [61] M. Fadoni, L. Lucarelli, Homogeneous catalysis with transition metal complexes, *Stud. Surf. Sci. Catal.* 79 (1993) 199–248. doi:10.1016/S0167-2991(08)63810-0.
- [62] G. Attard, C. Barnes, *Surfaces*, Oxford University Press, 1998.
- [63] S.S. Kim, H.H. Lee, S.C. Hong, A study on the effect of support's reducibility on the reverse water-gas shift reaction over Pt catalysts, *Appl. Catal. A Gen.* 423–424 (2012) 100–107. doi:10.1016/j.apcata.2012.02.021.
- [64] S.S. Kim, H.H. Lee, S.C. Hong, The effect of the morphological characteristics of TiO₂ supports on the reverse water-gas shift reaction over Pt/TiO₂ catalysts, *Appl. Catal. B Environ.* 119–120 (2012) 100–108. doi:10.1016/j.apcatb.2012.02.023.
- [65] A. Goguet, S.O. Shekhtman, R. Burch, C. Hardacre, F.C. Meunier, G.S. Yablonsky, Pulse-response TAP studies of the reverse water-gas shift reaction over a Pt/CeO₂ catalyst, *J. Catal.* 237 (2006) 102–110. doi:10.1016/j.jcat.2005.10.020.
- [66] D.J. Pettigrew, N.W. Cant, The effects of rare earth oxides on the reverse water-gas shift reaction on palladium/alumina, *Catal Lett.* 28 (1994) 313–319.
- [67] J.N. Park, E.W. McFarland, A highly dispersed Pd-Mg/SiO₂ catalyst active for methanation of CO₂, *J. Catal.* 266 (2009) 92–97. doi:10.1016/j.jcat.2009.05.018.
- [68] G.C. Wang, J. Nakamura, Structure sensitivity for forward and reverse water-gas shift reactions on copper surfaces: A DFT study, *J. Phys. Chem. Lett.* 1 (2010) 3053–3057. doi:10.1021/jz101150w.
- [69] G.-C. Wang, L. Jiang, X.-Y. Pang, Z.-S. Cai, Y.-M. Pan, X.-Z. Zhao, Y. Morikawa, J. Nakamura, A theoretical study of surface-structural sensitivity of the reverse water-gas shift reaction over Cu(hkl) surfaces, *Surf. Sci.* 543 (2003) 118–130. doi:10.1016/S0039-6028(03)00876-8.

- [70] C.S. Chen, W.H. Cheng, S.S. Lin, Enhanced activity and stability of a Cu/SiO₂ catalyst for the reverse water gas shift reaction by an iron promoter, *Chem. Commun.* 1 (2001) 1770–1771. doi:10.1039/b104279n.
- [71] J.N. T. Fujitani, The effect of ZnO in methanol synthesis catalysts on Cu dispersion and the specific activity, *Catal. Lett.* 56 (1998) 119–124. doi:10.1023/A:1019000927366.
- [72] A. Wolf, A. Jess, C. Kern, Syngas Production via Reverse Water-Gas Shift Reaction over a Ni-Al₂O₃ Catalyst: Catalyst Stability, Reaction Kinetics, and Modeling, *Chem. Eng. Technol.* 39 (2016) 1040–1048. doi:10.1002/ceat.201500548.
- [73] J.A. Loiland, M.J. Wulfers, N.S. Marinkovic, R.F. Lobo, Fe/ γ -Al₂O₃ and Fe-K/ γ -Al₂O₃ as reverse water-gas shift catalysts, *Catal. Sci. Technol.* (2016). doi:10.1039/C5CY02111A.
- [74] Y. Liu, D. Liu, Study of bimetallic Cu–Ni/ γ -Al₂O₃ catalysts for carbon dioxide hydrogenation, *Int. J. Hydrogen Energy.* 24 (1999) 351–354. doi:10.1016/S0360-3199(98)00038-X.
- [75] F.S. Stone, D. Waller, Cu – ZnO and Cu – ZnO / Al₂O₃ catalysts for the reverse water-gas shift reaction . The effect of the Cu / Zn ratio on precursor characteristics and on the activity of the derived catalysts, *Top. Catal.* 22 (2003).
- [76] C.S. Chen, W.H. Cheng, S.S. Lin, Study of reverse water gas shift reaction by TPD, TPR and CO₂ hydrogenation over potassium-promoted Cu/SiO₂ catalyst, *Appl. Catal. A Gen.* 238 (2002) 55–67. doi:10.1016/S0926-860X(02)00221-1.
- [77] H. Schulz, Short history and present trends of Fischer-Tropsch synthesis, *Appl. Catal. A Gen.* 186 (1999) 3–12. doi:10.1016/j.chembiol.2003.09.004.
- [78] G.P. Van Der Laan, A.A.C.M. Beenackers, Kinetics and Selectivity of the Fischer-Tropsch Synthesis: A Literature Review, *Catal. Rev. - Sci. Eng.* 41 (1999) 255–318. doi:10.1081/CR-100101170.
- [79] D.S. Newsome, The Water-Gas Shift Reaction, *Catal. Rev.* 21 (1980) 275–318. doi:10.1080/03602458008067535.
- [80] G.K. Reddy, K. Gunasekara, P. Boolchand, P.G. Smirniotis, Cr- and Ce-doped ferrite catalysts for the high temperature water-gas shift reaction: TPR and mossbauer spectroscopic study, *J. Phys. Chem. C.* 115 (2011) 920–930. doi:10.1021/jp102959p.

- [81] H. Schulz, T. Riedel, G. Schaub, Fischer-Tropsch principles of co-hydrogenation on iron catalysts, *Top. Catal.* 32 (2005) 117–124. doi:10.1007/s11244-005-2883-8.
- [82] T. Riedel, H. Schulz, G. Schaub, K.W. Jun, J.S. Hwang, K.W. Lee, Fischer-Tropsch on iron with H₂/CO and H₂/CO₂ as synthesis gases: The episodes of formation of the Fischer-Tropsch regime and construction of the catalyst, *Top. Catal.* 26 (2003) 41–54. doi:10.1023/B:TOCA.0000012986.46680.28.
- [83] C.G. Visconti, M. Martinelli, L. Falbo, A. Infantes-Molina, L. Lietti, P. Forzatti, G. Iaquaniello, E. Palo, B. Picutti, F. Brignoli, CO₂ hydrogenation to lower olefins on a high surface area K-promoted bulk Fe-catalyst, *Appl. Catal. B Environ.* 200 (2017) 530–542. doi:10.1016/j.apcatb.2016.07.047.
- [84] Z.S. Fishman, Y. He, K.R. Yang, A.W. Lounsbury, J. Zhu, T.M. Tran, J.B. Zimmerman, V.S. Batista, L.D. Pfefferle, Hard templating ultrathin polycrystalline hematite nanosheets: Effect of nano-dimension on CO₂ to CO conversion: Via the reverse water-gas shift reaction, *Nanoscale.* 9 (2017) 12984–12995. doi:10.1039/c7nr03522e.
- [85] D.H. Kim, S.W. Han, H.S. Yoon, Y.D. Kim, Reverse water gas shift reaction catalyzed by Fe nanoparticles with high catalytic activity and stability, *J. Ind. Eng. Chem.* 23 (2014) 67–71. doi:10.1016/j.jiec.2014.07.043.
- [86] C.M. Kalamaras, S. Americanou, A.M. Efstathiou, “Redox” vs “associative formate with -OH group regeneration” WGS reaction mechanism on Pt/CeO₂: Effect of platinum particle size, *J. Catal.* 279 (2011) 287–300. doi:10.1016/j.jcat.2011.01.024.
- [87] M.I. Temkin, The Kinetics of Some Industrial Heterogeneous Catalytic Reactions, *Adv. Catal.* 28 (1979) 173–291. doi:10.1016/S0360-0564(08)60135-2.
- [88] C. Rhodes, G.J. Hutchings, A.M. Ward, Water-gas shift reaction: finding the mechanistic boundary, *Catal. Today.* 23 (1995) 43–58.
- [89] J.A. Loiland, M.J. Wulfers, N.S. Marinkovic, R.F. Lobo, Supporting Information Fe/γ-Al₂O₃ and Fe-K/γ-Al₂O₃ as reverse water-gas shift catalysts, *Catal. Sci. Technol.* (2016).
- [90] M.J.L. Ginés, a. J. Marchi, C.R. Apesteguía, Kinetic study of the reverse water-gas shift reaction over CuO/ZnO/Al₂O₃ catalysts, *Appl. Catal. A Gen.* 154 (1997) 155–171. doi:10.1016/S0926-860X(96)00369-9.

- [91] a. Pineau, N. Kanari, I. Gaballah, Kinetics of reduction of iron oxides by H₂. Part II. Low temperature reduction of magnetite, *Thermochim. Acta.* 456 (2007) 75–88. doi:10.1016/j.tca.2007.01.014.
- [92] C.L. Zhang, S. Li, L.J. Wang, T.H. Wu, S.Y. Peng, Studies on the decomposing carbon dioxide into carbon with oxygen-deficient magnetite. II. The effects of properties of magnetite on activity of decomposition CO₂ and mechanism of the reaction, *Mater. Chem. Phys.* 62 (2000) 52–61. doi:10.1016/S0254-0584(99)00168-6.
- [93] F. Bonnet, F. Ropital, P. Lecour, D. Espinat, Y. Huiban, L. Gengembre, Y. Berthier, P. Marcus, Study of the oxide/carbide transition on iron surfaces during catalytic coke formation, *Surf. Interface Anal.* 34 (2002) 418–422. doi:10.1002/sia.1330.
- [94] K. Mondal, H. Lorethova, E. Hippo, T. Wiltowski, S.B. Lalvani, Reduction of iron oxide in carbon monoxide atmosphere - Reaction controlled kinetics, *Fuel Process. Technol.* 86 (2004) 33–47. doi:10.1016/j.fuproc.2003.12.009.
- [95] T. Yamashita, P. Hayes, Analysis of XPS spectra of Fe²⁺ and Fe³⁺ ions in oxide materials, *Appl. Surf. Sci.* 254 (2008) 2441–2449. doi:10.1016/j.apsusc.2007.09.063.
- [96] M.C. Biesinger, B.P. Payne, A.P. Grosvenor, L.W.M. Lau, A.R. Gerson, R.S.C. Smart, Resolving surface chemical states in XPS analysis of first row transition metals, oxides and hydroxides: Cr, Mn, Fe, Co and Ni, *Appl. Surf. Sci.* 257 (2011) 2717–2730. doi:10.1016/j.apsusc.2010.10.051.
- [97] N.S. McIntyre, D.G. Zetaruk, X-ray photoelectron spectroscopic studies of iron oxides - *Analytical Chemistry* (ACS Publications), *Anal. Chem.* 49 (1977) 1521–1529. doi:10.1021/ac50019a016.
- [98] M.D. Shroff, D.S. Kalakkad, K.E. Coulter, S.D. Kohler, M.S. Harrington, N.B. Jackson, A.G. Sault, A.K. Datye, Activation of Precipitated Iron Fischer-Tropsch Synthesis Catalysts, *J. Catal.* 156 (1995) 185–207. doi:10.1006/jcat.1995.1247.
- [99] E. De Smit, F. Cinquini, A.M. Beale, O. V Safonova, W. Van Beek, P. Sautet, B.M. Weckhuysen, N. Supe, R.J. Horowitz, F.-G. Cedex, Stability and Reactivity of E-X-θ Iron Carbide Catalyst Phases in Fischer - Tropsch Synthesis : Controlling μC, *J. Am. Chem. Soc.* (2010) 14928–14941.
- [100] B.H. Davis, Fischer-Tropsch Synthesis: Reaction mechanisms for iron catalysts, *Catal. Today.* 141 (2009) 25–33. doi:10.1016/j.cattod.2008.03.005.

- [101] S.I. Fujita, M. Usui, N. Takezawa, Mechanism of the reverse water gas shift reaction over Cu/ZnO catalyst, *J. Catal.* 134 (1992) 220–225. doi:10.1016/0021-9517(92)90223-5.
- [102] G.C. Wang, J. Nakamura, Structure sensitivity for forward and reverse water-gas shift reactions on copper surfaces: A DFT study, *J. Phys. Chem. Lett.* 1 (2010) 3053–3057. doi:10.1021/jz101150w.
- [103] M.D. Porosoff, B. Yan, J.G. Chen, Catalytic reduction of CO₂ by H₂ for synthesis of CO, methanol and hydrocarbons: challenges and opportunities, *Energy Environ. Sci.* 9 (2016) 62–73. doi:10.1039/C5EE02657A.
- [104] A. Goeppert, M. Czaun, J.-P. Jones, G.K. Surya Prakash, G.A. Olah, Recycling of carbon dioxide to methanol and derived products – closing the loop, *Chem. Soc. Rev.* 43 (2014) 7995–8048. doi:10.1039/C4CS00122B.
- [105] G.C. Chinen, P.J. Denny, D.G. Parker, M.S. Spencer, D.A. Whan, Mechanism of methanol synthesis from CO₂/CO/H₂ mixtures over copper/zinc oxide/alumina catalysts: use of ¹⁴C-labelled reactants, *Appl. Catal.* 30 (1987) 333–338. doi:10.1016/S0166-9834(00)84123-8.
- [106] M.B. Fichtl, D. Schlereth, N. Jacobsen, I. Kasatkin, J. Schumann, M. Behrens, R. Schlögl, O. Hinrichsen, Kinetics of deactivation on Cu/ZnO/Al₂O₃ methanol synthesis catalysts, *Appl. Catal. A Gen.* 502 (2015) 262–270. doi:10.1016/J.APCATA.2015.06.014.
- [107] H. Lorenz, W. Jochum, B. Klötzer, M. Stöger-Pollach, S. Schwarz, K. Pfaller, S. Penner, Novel methanol steam reforming activity and selectivity of pure In₂O₃, *Appl. Catal. A Gen.* 347 (2008) 34–42. doi:10.1016/j.apcata.2008.05.028.
- [108] N. Iwasa, T. Mayanagi, N. Ogawa, K. Sakata, N. Takezawa, New catalytic functions of Pd–Zn, Pd–Ga, Pd–In, Pt–Zn, Pt–Ga and Pt–In alloys in the conversions of methanol, *Catal. Letters.* 54 (1998) 119–123. doi:10.1023/A:1019056728333.
- [109] T. Umegaki, K. Kuratani, Y. Yamada, A. Ueda, N. Kuriyama, T. Kobayashi, Q. Xu, Hydrogen production via steam reforming of ethyl alcohol over nano-structured indium oxide catalysts, *J. Power Sources.* 179 (2008) 566–570. doi:10.1016/J.JPOWSOUR.2008.01.010.
- [110] N. Rui, Z. Wang, K. Sun, J. Ye, Q. Ge, C. jun Liu, CO₂ hydrogenation to methanol over Pd/In₂O₃: effects of Pd and oxygen vacancy, *Appl. Catal. B Environ.* 218 (2017) 488–497. doi:10.1016/j.apcatb.2017.06.069.

- [111] A. García-Trenco, A. Regoutz, E.R. White, D.J. Payne, M.S.P. Shaffer, C.K. Williams, PdIn intermetallic nanoparticles for the Hydrogenation of CO₂ to Methanol, *Appl. Catal. B Environ.* 220 (2018) 9–18.
doi:10.1016/J.APCATB.2017.07.069.
- [112] R. Gaikwad, A. Bansode, A. Urakawa, High-pressure advantages in stoichiometric hydrogenation of carbon dioxide to methanol, *J. Catal.* 343 (2016) 127–132. doi:10.1016/J.JCAT.2016.02.005.
- [113] J. Słoczyński, R. Grabowski, A. Kozłowska, P. Olszewski, J. Stoch, J. Skrzypek, M. Madej-Lachowska, Catalytic activity of the M/(3ZnO·ZrO₂) system (M=Cu, Ag, Au) in the hydrogenation of CO₂ to methanol, 2004. doi:10.1016/j.apcata.2004.09.014.
- [114] J. Toyir, P. Ramírez De La Piscina, J.L.G. Fierro, N. Homs, Highly effective conversion of CO₂ to methanol over supported and promoted copper-based catalysts: Influence of support and promoter, *Appl. Catal. B Environ.* 29 (2001) 207–215. doi:10.1016/S0926-3373(00)00205-8.
- [115] T. Witton, J. Chalorntham, P. Dumrongbunditkul, M. Chareonpanich, J. Limtrakul, CO₂ hydrogenation to methanol over Cu/ZrO₂ catalysts: Effects of zirconia phases, *Chem. Eng. J.* 293 (2016) 327–336.
doi:10.1016/j.cej.2016.02.069.
- [116] X.L. Liang, X. Dong, G.D. Lin, H. Bin Zhang, Carbon nanotube-supported Pd-ZnO catalyst for hydrogenation of CO₂ to methanol, *Appl. Catal. B Environ.* 88 (2009) 315–322. doi:10.1016/j.apcatb.2008.11.018.
- [117] T. Inui, T. Takeguchi, A. Kohama, K. Tanida, Effective conversion of carbon dioxide to gasoline, *Energy Convers. Manag.* 33 (1992) 513–520.
doi:10.1016/0196-8904(92)90050-7.
- [118] P. Gao, L. Zhong, L. Zhang, H. Wang, N. Zhao, W. Wei, Y. Sun, Yttrium oxide modified Cu/ZnO/Al₂O₃ catalysts via hydrotalcite-like precursors for CO₂ hydrogenation to methanol, *Catal. Sci. Technol.* 5 (2015) 4365–4377.
doi:10.1039/C5CY00372E.
- [119] M. Wagner, P. Lackner, S. Seiler, A. Brunsch, R. Bliem, S. Gerhold, Z. Wang, J. Osiecki, K. Schulte, L.A. Boatner, M. Schmid, B. Meyer, U. Diebold, Resolving the Structure of a Well-Ordered Hydroxyl Overlayer on In₂O₃(111): Nanomanipulation and Theory, *ACS Nano.* 11 (2017) 11531–11541.
doi:10.1021/acsnano.7b06387.
- [120] M. Wagner, S. Seiler, B. Meyer, L.A. Boatner, M. Schmid, U. Diebold,

Reducing the In₂O₃(111) Surface Results in Ordered Indium Adatoms, *Adv. Mater. Interfaces*. 1 (2014) 1–6.
doi:10.1002/admi.201400289.

- [121] T. Bielz, H. Lorenz, W. Jochum, R. Kaindl, F. Klauser, B. Klötzer, S. Penner, Hydrogen on in₂O₃: Reducibility, bonding, defect formation, and reactivity, *J. Phys. Chem. C*. 114 (2010) 9022–9029. doi:10.1021/jp1017423.
- [122] K. Kobl, S. Thomas, Y. Zimmermann, K. Parkhomenko, A.C. Roger, Power-law kinetics of methanol synthesis from carbon dioxide and hydrogen on copper-zinc oxide catalysts with alumina or zirconia supports, *Catal. Today*. 270 (2016) 31–42. doi:10.1016/j.cattod.2015.11.020.
- [123] J.F. Portha, K. Parkhomenko, K. Kobl, A.C. Roger, S. Arab, J.M. Commenge, L. Falk, Kinetics of Methanol Synthesis from Carbon Dioxide Hydrogenation over Copper-Zinc Oxide Catalysts, *Ind. Eng. Chem. Res.* 56 (2017) 13133–13145. doi:10.1021/acs.iecr.7b01323.
- [124] J. Słoczyński, R. Grabowski, P. Olszewski, A. Kozłowska, J. Stoch, M. Lachowska, J. Skrzypek, Effect of metal oxide additives on the activity and stability of Cu/ZnO/ZrO₂ catalysts in the synthesis of methanol from CO₂ and H₂, *Appl. Catal. A Gen.* 310 (2006) 127–137.
doi:10.1016/j.apcata.2006.05.035.
- [125] X.M. Liu, G.Q. Lu, Z.F. Yan, Nanocrystalline zirconia as catalyst support in methanol synthesis, *Appl. Catal. A Gen.* 279 (2005) 241–245.
doi:10.1016/j.apcata.2004.10.040.
- [126] J. Toyir, P.R. De la Piscina, J.L.G. Fierro, N. Homs, Catalytic performance for CO₂ conversion to methanol of gallium-promoted copper-based catalysts: Influence of metallic precursors, *Appl. Catal. B Environ.* 34 (2001) 255–266.
doi:10.1016/S0926-3373(01)00203-X.
- [127] A. Ota, E.L. Kunkes, I. Kasatkin, E. Groppo, D. Ferri, B. Poceiro, R.M. Navarro Yerga, M. Behrens, Comparative study of hydrotalcite-derived supported Pd₂Ga and PdZn intermetallic nanoparticles as methanol synthesis and methanol steam reforming catalysts, *J. Catal.* 293 (2012) 27–38.
doi:10.1016/j.jcat.2012.05.020.
- [128] Y. Hartadi, D. Widmann, R.J. Behm, Methanol formation by CO₂ hydrogenation on Au/ZnO catalysts - Effect of total pressure and influence of CO on the reaction characteristics, *J. Catal.* 333 (2016) 238–250.
doi:10.1016/j.jcat.2015.11.002.

- [129] P. Gao, F. Li, N. Zhao, F. Xiao, W. Wei, L. Zhong, Y. Sun, Influence of modifier (Mn, La, Ce, Zr and Y) on the performance of Cu/Zn/Al catalysts via hydrotalcite-like precursors for CO₂ hydrogenation to methanol, *Appl. Catal. A Gen.* 468 (2013) 442–452. doi:10.1016/j.apcata.2013.09.026.
- [130] G. Avgouropoulos, T. Ioannides, H. Matralis, Influence of the preparation method on the performance of CuO–CeO₂ catalysts for the selective oxidation of CO, *Appl. Catal. B Environ.* 56 (2005) 87–93. doi:10.1016/J.APCATB.2004.07.017.
- [131] S.-S. Nam, G. Kishan, M.-W. Lee, M.-J. Choi, K.-W. Lee, Effect of lanthanum loading in Fe-K/La-Al₂O₃ catalysts for CO₂ hydrogenation to hydrocarbons, *Appl. Organomet. Chem.* 14 (2000) 794–798. doi:10.1002/1099-0739(200012)14:12<794::AID-AOC81>3.0.CO;2-G.
- [132] S. Natesakhawat, J.W. Lekse, J.P. Baltrus, P.R. Ohodnicki, B.H. Howard, X. Deng, C. Matranga, Active sites and structure-activity relationships of copper-based catalysts for carbon dioxide hydrogenation to methanol, *ACS Catal.* 2 (2012) 1667–1676. doi:10.1021/cs300008g.
- [133] L. Znak, K. Stołeczki, J. Zieliński, The effect of cerium, lanthanum and zirconium on nickel/alumina catalysts for the hydrogenation of carbon oxides, *Catal. Today.* 101 (2005) 65–71. doi:10.1016/j.cattod.2005.01.003.
- [134] J. Graciani, K. Mudiyansele, F. Xu, A.E. Baber, J. Evans, S.D. Senanayake, D.J. Stacchiola, P. Liu, J. Hrbek, J. Fernández Sanz, J.A. Rodríguez, Highly active copper-ceria and copper-ceria-titania catalysts for methanol synthesis from CO₂ (SI), *Science* (80-.). 345 (2014) 546–550. doi:10.1126/science.1253057.
- [135] Y. Yang, J. Evans, J.A. Rodríguez, M.G. White, P. Liu, Fundamental studies of methanol synthesis from CO₂ hydrogenation on Cu(111), Cu clusters, and Cu/ZnO(0001), *Phys. Chem. Chem. Phys.* 12 (2010) 9909. doi:10.1039/c001484b.
- [136] S. Du, W. Tang, X. Lu, S. Wang, Y. Guo, P. Gao, Cu-Decorated ZnO Nanorod Array Integrated Structured Catalysts for Low-Pressure CO₂ Hydrogenation to Methanol Cu-Decorated ZnO Nanorod Array Integrated Structured Catalysts for Low-Pressure CO₂ Hydrogenation to Methanol, *Adv. Mater. Interfaces.* 5 (2018) 1700730. doi:10.1002/admi.201700730.
- [137] K. Chang, T. Wang, J.G. Chen, Hydrogenation of CO₂ to methanol over CuCeTiO_x catalysts, *Appl. Catal. B Environ.* 206 (2017) 704–711. doi:10.1016/j.apcatb.2017.01.076.

- [138] A. Karelavic, P. Ruiz, The role of copper particle size in low pressure methanol synthesis via CO₂ hydrogenation over Cu/ZnO catalysts, *Catal. Sci. Technol.* 5 (2015) 869–881. doi:10.1039/C4CY00848K.
- [139] L.C. Grabow, M. Mavrikakis, Mechanism of methanol synthesis on Cu through CO₂ and CO hydrogenation, *ACS Catal.* 1 (2011) 365–384. doi:10.1021/cs200055d.
- [140] M. Behrens, Heterogeneous Catalysis of CO₂ Conversion to Methanol on Copper Surfaces, *Angew. Chemie Int. Ed.* (2014) 12022–12024. doi:10.1002/anie.201409282.
- [141] K. Larmier, W.-C. Liao, S. Tada, E. Lam, R. Verel, A. Bansode, A. Urakawa, A. Comas-Vives, C. Copéret, CO₂-to-Methanol Hydrogenation on Zirconia-Supported Copper Nanoparticles: Reaction Intermediates and the Role of the Metal-Support Interface, *Angew. Chemie Int. Ed.* (2017) 2358–2363. doi:10.1002/anie.201610166.
- [142] E.-M. Köck, M. Kogler, T. Bielz, B. Klötzer, S. Penner, In Situ FT-IR Spectroscopic Study of CO₂ and CO Adsorption on Y₂O₃, ZrO₂, and Yttria-Stabilized ZrO₂ (SI), *J. Phys. Chem. C.* 117 (2013) 17666–17673. doi:10.1021/jp405625x.
- [143] S. Kattel, B. Yan, Y. Yang, J.G. Chen, P. Liu, Optimizing Binding Energies of Key Intermediates for CO₂ Hydrogenation to Methanol over Oxide-Supported Copper, *J. Am. Chem. Soc.* 138 (2016) 12440–12450. doi:10.1021/jacs.6b05791.
- [144] G. Jacobs, T.K. Das, Y. Zhang, J. Li, G. Racoillet, B.H. Davis, Fischer-Tropsch synthesis: Support, loading, and promoter effects on the reducibility of cobalt catalysts, *Appl. Catal. A Gen.* 233 (2002) 263–281. doi:10.1016/S0926-860X(02)00195-3.
- [145] G. Melaet, W.T. Ralston, C.S. Li, S. Alayoglu, K. An, N. Musselwhite, B. Kalkan, G.A. Somorjai, Evidence of highly active cobalt oxide catalyst for the Fischer-Tropsch synthesis and CO₂ hydrogenation, *J. Am. Chem. Soc.* 136 (2014) 2260–2263. doi:10.1021/ja412447q.
- [146] F. Wyrwalski, J.F. Lamonier, S. Siffert, L. Gengembre, A. Aboukaïs, Modified Co₃O₄/ZrO₂ catalysts for VOC emissions abatement, *Catal. Today.* 119 (2007) 332–337. doi:10.1016/j.cattod.2006.08.025.
- [147] Z. Zhao, P. Hu, Y. Cai, X. Cao, J. Ma, W. Zhan, Y. Guo, Y. Lou, G. Lu, Y. Guo, Q. Dai, L. Wang, Promoting Effects of In₂O₃ on Co₃O₄ for CO

Oxidation: Tuning O₂ Activation and CO Adsorption Strength Simultaneously, *ACS Catal.* 4 (2014) 4143–4152. doi:10.1021/cs501049r.

- [148] W. Wei, L. Zhong, H. Liu, H. Yang, H. Wang, Y. Sun, X. Li, P. Gao, Z. Shi, Direct conversion of CO₂ to long-chain hydrocarbon fuels over K-promoted CoCu/TiO₂ catalysts, *Catal. Today*. 311 (2017) 65–73. doi:10.1016/j.cattod.2017.09.053.
- [149] P. Yang, Y. Yu, G.A. Somorjai, C. Xie, J. Su, C. Chen, Y. Li, Tandem Catalysis for CO₂ Hydrogenation to C₂–C₄ Hydrocarbons, *Nano Lett.* 17 (2017) 3798–3802. doi:10.1021/acs.nanolett.7b01139.
- [150] M.S. Jeletic, M.T. Mock, A.M. Appel, J.C. Linehan, A cobalt-based catalyst for the hydrogenation of CO₂ under ambient conditions, *J. Am. Chem. Soc.* 135 (2013) 11533–11536. doi:10.1021/ja406601v.
- [151] X. Zhang, R. Hu, Y. Liu, J. Zhao, L. Hou, D. Yang, Z. Hao, H. Su, The performance of Co/ZrO₂-Al₂O₃ composite oxide catalyst for CH₄/CO₂ reforming reaction, *Int. J. Hydrogen Energy*. 40 (2015) 10026–10032. doi:10.1016/j.ijhydene.2015.06.076.
- [152] Y. Zhou, Y. Jiang, Z. Qin, Q. Xie, H. Ji, Influence of Zr, Ce, and La on Co₃O₄ catalyst for CO₂ methanation at low temperature, *Chinese J. Chem. Eng.* 26 (2018) 768–774. doi:10.1016/j.cjche.2017.10.014.
- [153] G. Yin, X. Yuan, X. Du, W. Zhao, Q. Bi, F. Huang, Efficient Reduction of CO₂ to CO Using Cobalt–Cobalt Oxide Core–Shell Catalysts, *Chem. - A Eur. J.* 24 (2018) 2157–2163. doi:10.1002/chem.201704596.
- [154] K.S.W.S.D.H.E.M.R.A.P.; J.R.T.S. R.A.W.Haul;, INTERNATIONAL UNION OF PURE COMMISSION ON COLLOID AND SURFACE CHEMISTRY INCLUDING CATALYSIS * REPORTING PHYSISORPTION DATA FOR GAS / SOLID SYSTEMS with Special Reference to the Determination of Surface Area and Porosity, *Pure Appl. Chem.* 57 (1985) 603–619.
- [155] C.S. Li, G. Melaet, W.T. Ralston, K. An, C. Brooks, Y. Ye, Y.S. Liu, J. Zhu, J. Guo, S. Alayoglu, G.A. Somorjai, High-performance hybrid oxide catalyst of manganese and cobalt for low-pressure methanol synthesis, *Nat. Commun.* 6 (2015) 1–5. doi:10.1038/ncomms7538.
- [156] Y.-P. Pei, J.-X. Liu, Y.-H. Zhao, Y.-J. Ding, T. Liu, W.-D. Dong, H.-J. Zhu, H.-Y. Su, L. Yan, J.-L. Li, W.-X. Li, High Alcohols Synthesis via Fischer–Tropsch Reaction at Cobalt Metal/Carbide Interface, *ACS Catal.* 5 (2015) 3620–3624.

doi:10.1021/acscatal.5b00791.

- [157] D.S. Kim, Y.H. Kim, J.E. Yie, E.D. Park, NO oxidation over supported cobalt oxide catalysts, *Korean J. Chem. Eng.* 27 (2010) 49–54. doi:10.1007/s11814-009-0290-8.
- [158] P.A. Chernavskii, A.S. Lermontov, G. V. Pankina, S.N. Torbin, V. V. Lunin, Effect of the ZrO₂ pore structure on the reduction of a supported cobalt oxide in catalysts for Fischer-Tropsch synthesis, *Kinet. Catal.* 43 (2002) 268–274. doi:10.1023/A:1015332930882.
- [159] E. van Steen, G.S. Sewell, R.A. Makhothe, C. Micklethwaite, H. Manstein, M. de Lange, C.T. O'Connor, TPR Study on the Preparation of Impregnated Co/SiO₂Catalysts, *J. Catal.* 162 (1996) 220–229. doi:10.1006/jcat.1996.0279.
- [160] W.L. Luyben, Design and control of a methanol reactor/column process, *Ind. Eng. Chem. Res.* 49 (2010) 6150–6163. doi:10.1021/ie100323d.
- [161] O. Martin, C. Mondelli, A. Cervellino, D. Ferri, D. Curulla-Ferré, J. Pérez-Ramírez, Operando Synchrotron X-ray Powder Diffraction and Modulated-Excitation Infrared Spectroscopy Elucidate the CO₂ Promotion on a Commercial Methanol Synthesis Catalyst, *Angew. Chemie Int. Ed.* (2016) 1–7. doi:10.1002/anie.201603204.
- [162] J.L. Snider, V. Streibel, M.A. Hubert, T.S. Choksi, E. Valle, D.C. Upham, J. Schumann, M.S. Duyar, A. Gallo, F. Abild-Pedersen, T.F. Jaramillo, Revealing the Synergy between Oxide and Alloy Phases on the Performance of Bimetallic In–Pd Catalysts for CO₂ Hydrogenation to Methanol, *ACS Catal.* (2019) 3399–3412. doi:10.1021/acscatal.8b04848.
- [163] X. Jiang, X. Nie, X. Wang, H. Wang, N. Koizumi, Y. Chen, X. Guo, C. Song, Origin of Pd-Cu bimetallic effect for synergetic promotion of methanol formation from CO₂ hydrogenation, *J. Catal.* 369 (2019) 21–32. doi:10.1016/j.jcat.2018.10.001.
- [164] J. Su, D. Wang, Y. Wang, H. Zhou, C. Liu, S. Liu, Direct Conversion of Syngas into Light Olefins over Zirconium-Doped Indium (III) Oxide and SAPO-34 Bifunctional Catalysts : Design of Oxide Component and Construction of Reaction Network (SI), *ChemCatChem.* (2018).

Appendix A

STREAM RESULTS FROM ASPEN PLUS SIMULATION

Table A1 Stream results in section 6.3.1 using RGibbs reactor with CO as byproduct at 543 K and 60 bar.

	Units	CO2	CO2-COMP	H2	H2O	METHANOL	MIXTURE1	MIXTURE2	PRODUCT1	PRODUCT2
Temperature	K	298.00	700.50	298.00	370.01	330.08	437.03	373.79	543.00	323.00
Pressure	N/sqm	1.0E+05	6.0E+06	6.0E+06	1.0E+05	1.0E+05	6.0E+06	6.0E+06	6.0E+06	3.0E+06
Molar Vapor Fraction		1.00	1.00	1.00	0.00	0.00	1.00	1.00	1.00	0.90
Molar Liquid Fraction		0.00	0.00	0.00	1.00	1.00	0.00	0.00	0.00	0.10
Molar Enthalpy	J/kmol	-3.9E+08	-3.8E+08	3.2E+04	-2.8E+08	-2.4E+08	-9.4E+07	-8.8E+07	-9.4E+07	-1.1E+08
Mass Enthalpy	J/kg	-8.9E+06	-8.5E+06	1.6E+04	-1.5E+07	-7.5E+06	-7.5E+06	-7.2E+06	-7.0E+06	-7.9E+06
Molar Entropy	J/kmol-K	2.9E+03	5.4E+03	-3.4E+04	-1.5E+05	-2.4E+05	-1.7E+04	-1.9E+04	-1.2E+04	-3.5E+04
Mass Entropy	J/kg-K	6.5E+01	1.2E+02	-1.7E+04	-8.3E+03	-7.4E+03	-1.3E+03	-1.6E+03	-9.1E+02	-2.6E+03
Molar Density	kmol/cum	4.1E-02	1.0E+00	2.4E+00	5.0E+01	2.4E+01	1.6E+00	1.9E+00	1.3E+00	1.2E+00
Mass Density	kg/cum	1.8E+00	4.5E+01	4.7E+00	9.1E+02	7.6E+02	2.0E+01	2.3E+01	1.8E+01	1.7E+01
Enthalpy Flow	Watt	-1.1E+07	-1.0E+07	2.7E+03	-6.5E+06	-5.3E+06	-1.0E+07	-4.4E+07	-4.2E+07	-4.7E+07
Average MW		4.4E+01	4.4E+01	2.0E+00	1.8E+01	3.2E+01	1.3E+01	1.2E+01	1.3E+01	1.3E+01
Mole Flows	kmol/sec	2.78E-02	2.78E-02	8.33E-02	2.33E-02	2.22E-02	1.11E-01	4.93E-01	4.48E-01	4.48E-01
CO2	kmol/sec	2.78E-02	2.78E-02	0.00E+00	2.75E-20	3.00E-05	2.78E-02	1.06E-01	8.28E-02	8.28E-02
H2	kmol/sec	0.00E+00	0.00E+00	8.33E-02	2.13E-31	1.69E-08	8.33E-02	3.66E-01	2.98E-01	2.98E-01
H2O	kmol/sec	0.00E+00	0.00E+00	0.00E+00	2.28E-02	4.66E-04	0.00E+00	1.03E-03	2.44E-02	2.44E-02
Methanol	kmol/sec	0.00E+00	0.00E+00	0.00E+00	4.43E-04	2.17E-02	0.00E+00	4.54E-03	2.71E-02	2.71E-02
CO	kmol/sec	0.00E+00	0.00E+00	0.00E+00	2.01E-31	2.86E-09	0.00E+00	1.56E-02	1.64E-02	1.64E-02
Mole Fractions										
CO2		1.00	1.00	0.00	0.00	0.00	0.25	0.22	0.18	0.18
H2		0.00	0.00	1.00	0.00	0.00	0.75	0.74	0.66	0.66
H2O		0.00	0.00	0.00	0.98	0.02	0.00	0.00	0.05	0.05
Methanol		0.00	0.00	0.00	0.02	0.98	0.00	0.01	0.06	0.06
CO		0.00	0.00	0.00	0.00	0.00	0.00	0.03	0.04	0.04
Mass Flows	kg/sec	1.22	1.22	0.17	0.43	0.71	1.39	6.01	6.01	6.01

Table A1 (continued) Stream results in section 6.3.1 using RGibbs reactor with CO as byproduct at 543 K and 60 bar.

	Units	PURGE1	PURGE2	RECYCLE1	RECYCLE2	SEP-LIQ1	SEP-LIQ2	SEP-LIQ3	SEP-VAP	RECOUNT
Temperature	K	323.00	322.22	323.00	355.16	323.00	322.22	322.22	323.00	404.12
Pressure	N/sqm	3.0E+06	1.0E+05	3.0E+06	6.0E+06	3.0E+06	1.0E+05	1.0E+05	3.0E+06	6.0E+06
Molar Vapor Fraction		1.00	1.00	1.00	1.00	0.00	0.01	0.00	1.00	1.00
Molar Liquid Fraction		0.00	0.00	0.00	0.00	1.00	0.99	1.00	0.00	0.00
Molar Enthalpy	J/kmol	-8.8E+07	-3.1E+08	-8.8E+07	-8.7E+07	-2.6E+08	-2.6E+08	-2.6E+08	-8.8E+07	-8.5E+07
Mass Enthalpy	J/kg	-7.2E+06	-8.4E+06	-7.2E+06	-7.2E+06	-1.1E+07	-1.1E+07	-1.1E+07	-7.2E+06	-7.0E+06
Molar Entropy	J/kmol-K	-1.7E+04	-2.8E+04	-1.7E+04	-2.0E+04	-1.9E+05	-1.9E+05	-1.9E+05	-1.7E+04	-1.6E+04
Mass Entropy	J/kg-K	-1.4E+03	-7.5E+02	-1.4E+03	-1.7E+03	-7.7E+03	-7.7E+03	-7.8E+03	-1.4E+03	-1.3E+03
Molar Density	kmol/cum	1.1E+00	3.8E-02	1.1E+00	2.0E+00	3.3E+01	3.6E+00	3.3E+01	1.1E+00	1.8E+00
Mass Density	kg/cum	1.3E+01	1.4E+00	1.3E+01	2.4E+01	8.2E+02	8.9E+01	8.2E+02	1.3E+01	2.1E+01
Enthalpy Flow	Watt	-3.5E+05	-1.3E+05	-3.5E+07	-3.3E+07	-1.2E+07	-1.2E+07	-1.2E+07	-3.5E+07	-3.4E+07
Average MW		1.2E+01	3.7E+01	1.2E+01	1.2E+01	2.5E+01	2.5E+01	2.5E+01	1.2E+01	1.2E+01
Mole Flows	kmol/sec	4.02E-03	4.32E-04	3.98E-01	3.82E-01	4.59E-02	4.59E-02	4.55E-02	4.02E-01	3.98E-01
CO2	kmol/sec	8.25E-04	2.60E-04	8.16E-02	7.83E-02	2.90E-04	2.90E-04	3.00E-05	8.25E-02	8.16E-02
H2	kmol/sec	2.98E-03	1.30E-05	2.95E-01	2.83E-01	1.30E-05	1.30E-05	1.69E-08	2.98E-01	2.95E-01
H2O	kmol/sec	1.09E-05	2.96E-05	1.08E-03	1.03E-03	2.33E-02	2.33E-02	2.33E-02	1.09E-03	1.08E-03
Methanol	kmol/sec	4.78E-05	1.27E-04	4.73E-03	4.54E-03	2.23E-02	2.23E-02	2.22E-02	4.78E-03	4.73E-03
CO	kmol/sec	1.64E-04	1.24E-06	1.62E-02	1.56E-02	1.24E-06	1.24E-06	2.86E-09	1.64E-02	1.62E-02
Mole Fractions										
CO2		0.20	0.60	0.20	0.20	0.01	0.01	0.00	0.20	0.20
H2		0.74	0.03	0.74	0.74	0.00	0.00	0.00	0.74	0.74
H2O		0.00	0.07	0.00	0.00	0.51	0.51	0.51	0.00	0.00
Methanol		0.01	0.30	0.01	0.01	0.49	0.49	0.49	0.01	0.01
CO		0.04	0.00	0.04	0.04	0.00	0.00	0.00	0.04	0.04
Mass Flows	kg/sec	0.05	0.02	4.81	4.62	1.15	1.15	1.13	4.86	4.81

Table A2 Stream results in section 6.3.1 using RGibbs reactor without CO as byproduct at 543 K and 60 bar

	Units	CO2	CO2-COMP	H2	H2O	METHANOL	MIXTURE1	MIXTURE2	PRODUCT1	PRODUCT2
Temperature	K	298.00	700.50	298.00	366.96	326.36	437.03	373.79	543.00	323.00
Pressure	N/sqm	1.0E+05	6.0E+06	6.0E+06	1.0E+05	1.0E+05	6.0E+06	6.0E+06	6.0E+06	3.0E+06
Molar Vapor Fraction		1.00	1.00	1.00	0.00	0.00	1.00	1.00	1.00	0.88
Molar Liquid Fraction		0.00	0.00	0.00	1.00	1.00	0.00	0.00	0.00	0.12
Molar Enthalpy	J/kmol	-3.9E+08	-3.8E+08	3.2E+04	-2.8E+08	-2.4E+08	-9.4E+07	-8.8E+07	-1.0E+08	-1.1E+08
Mass Enthalpy	J/kg	-8.9E+06	-8.5E+06	1.6E+04	-1.5E+07	-7.5E+06	-7.5E+06	-7.2E+06	-7.2E+06	-8.1E+06
Molar Entropy	J/kmol-K	2.9E+03	5.4E+03	-3.4E+04	-1.5E+05	-2.4E+05	-1.7E+04	-1.9E+04	-1.9E+04	-4.3E+04
Mass Entropy	J/kg-K	6.5E+01	1.2E+02	-1.7E+04	-8.2E+03	-7.4E+03	-1.3E+03	-1.6E+03	-1.3E+03	-3.1E+03
Molar Density	kmol/cum	4.1E-02	1.0E+00	2.4E+00	4.9E+01	2.4E+01	1.6E+00	1.9E+00	1.3E+00	1.3E+00
Mass Density	kg/cum	1.8E+00	4.5E+01	4.7E+00	9.1E+02	7.6E+02	2.0E+01	2.3E+01	1.8E+01	1.8E+01
Enthalpy Flow	Watt	-1.1E+07	-1.0E+07	2.7E+03	-5.0E+06	-7.5E+06	-1.0E+07	-4.4E+07	-4.3E+07	-4.9E+07
Average MW		4.4E+01	4.4E+01	2.0E+00	1.9E+01	3.2E+01	1.3E+01	1.2E+01	1.4E+01	1.4E+01
Mole Flows	kmol/sec	2.78E-02	2.78E-02	8.33E-02	1.77E-02	3.13E-02	1.11E-01	4.93E-01	4.28E-01	4.28E-01
CO ₂	kmol/sec	2.78E-02	2.78E-02	0.00E+00	3.89E-20	6.43E-05	2.78E-02	1.06E-01	8.89E-02	8.89E-02
H ₂	kmol/sec	0.00E+00	0.00E+00	8.33E-02	1.71E-31	2.79E-08	8.33E-02	3.66E-01	2.83E-01	2.83E-01
H ₂ O	kmol/sec	0.00E+00	0.00E+00	0.00E+00	1.71E-02	3.49E-04	0.00E+00	1.03E-03	1.83E-02	1.83E-02
Methanol	kmol/sec	0.00E+00	0.00E+00	0.00E+00	6.31E-04	3.09E-02	0.00E+00	4.54E-03	3.74E-02	3.74E-02
CO	kmol/sec	0.00E+00	0.00E+00	0.00E+00	0.00E+00	0.00E+00	0.00E+00	1.56E-02	0.00E+00	0.00E+00
Mole Fractions										
CO ₂		1.00	1.00	0.00	0.00	0.00	0.25	0.22	0.21	0.21
H ₂		0.00	0.00	1.00	0.00	0.00	0.75	0.74	0.66	0.66
H ₂ O		0.00	0.00	0.00	0.96	0.01	0.00	0.00	0.04	0.04
Methanol		0.00	0.00	0.00	0.04	0.99	0.00	0.01	0.09	0.09
CO		0.00	0.00	0.00	0.00	0.00	0.00	0.03	0.00	0.00
Mass Flows	kg/sec	1.22	1.22	0.17	0.33	1.00	1.39	6.01	6.01	6.01

Table A2 (continued) Stream results in section 6.3.1 using RGibbs reactor without CO as byproduct at 543 K and 60 bar

	Units	PURGE1	PURGE2	RECYCLE1	RECYCLE2	SEP-LIQ1	SEP-LIQ2	SEP-LIQ3	SEP-VAP	RECOU
Temperature	K	323.00	320.02	323.00	355.16	323.00	320.02	320.02	323.00	403.18
Pressure	N/sqm	3.0E+06	1.0E+05	3.0E+06	6.0E+06	3.0E+06	1.0E+05	1.0E+05	3.0E+06	6.0E+06
Molar Vapor Fraction		1.00	1.00	1.00	1.00	0.00	0.02	0.00	1.00	1.00
Molar Liquid Fraction		0.00	0.00	0.00	0.00	1.00	0.98	1.00	0.00	0.00
Molar Enthalpy	J/kmol	-9.5E+07	-3.1E+08	-9.5E+07	-8.7E+07	-2.6E+08	-2.6E+08	-2.6E+08	-9.5E+07	-9.2E+07
Mass Enthalpy	J/kg	-7.7E+06	-8.3E+06	-7.7E+06	-7.2E+06	-9.4E+06	-9.4E+06	-9.4E+06	-7.7E+06	-7.5E+06
Molar Entropy	J/kmol-K	-2.2E+04	-3.2E+04	-2.2E+04	-2.0E+04	-2.0E+05	-2.0E+05	-2.1E+05	-2.2E+04	-2.1E+04
Mass Entropy	J/kg-K	-1.8E+03	-8.6E+02	-1.8E+03	-1.7E+03	-7.5E+03	-7.5E+03	-7.7E+03	-1.8E+03	-1.7E+03
Molar Density	kmol/cum	1.1E+00	3.8E-02	1.1E+00	2.0E+00	2.9E+01	1.7E+00	3.0E+01	1.1E+00	1.8E+00
Mass Density	kg/cum	1.4E+01	1.4E+00	1.4E+01	2.4E+01	8.0E+02	4.5E+01	8.0E+02	1.4E+01	2.2E+01
Enthalpy Flow	Watt	-3.6E+05	-3.4E+05	-3.5E+07	-3.3E+07	-1.3E+07	-1.3E+07	-1.3E+07	-3.6E+07	-3.4E+07
Average MW		1.2E+01	3.8E+01	1.2E+01	1.2E+01	2.7E+01	2.7E+01	2.7E+01	1.2E+01	1.2E+01
Mole Flows	kmol/sec	3.78E-03	1.09E-03	3.74E-01	3.82E-01	5.02E-02	5.02E-02	4.91E-02	3.78E-01	3.74E-01
CO ₂	kmol/sec	8.81E-04	6.53E-04	8.73E-02	7.83E-02	7.18E-04	7.18E-04	6.43E-05	8.81E-02	8.73E-02
H ₂	kmol/sec	2.83E-03	2.76E-05	2.80E-01	2.83E-01	2.76E-05	2.76E-05	2.79E-08	2.83E-01	2.80E-01
H ₂ O	kmol/sec	7.91E-06	5.11E-05	7.84E-04	1.03E-03	1.75E-02	1.75E-02	1.75E-02	7.91E-04	7.84E-04
Methanol	kmol/sec	5.47E-05	3.56E-04	5.42E-03	4.54E-03	3.19E-02	3.19E-02	3.16E-02	5.47E-03	5.42E-03
CO	kmol/sec	0.00E+00	0.00E+00	0.00E+00	1.56E-02	0.00E+00	0.00E+00	0.00E+00	0.00E+00	0.00E+00
Mole Fractions										
CO ₂		0.23	0.60	0.23	0.20	0.01	0.01	0.00	0.23	0.23
H ₂		0.75	0.03	0.75	0.74	0.00	0.00	0.00	0.75	0.75
H ₂ O		0.00	0.05	0.00	0.00	0.35	0.35	0.36	0.00	0.00
Methanol		0.01	0.33	0.01	0.01	0.64	0.64	0.64	0.01	0.01
CO		0.00	0.00	0.00	0.04	0.00	0.00	0.00	0.00	0.00
Mass Flows	kg/sec	0.05	0.04	4.59	4.62	1.37	1.37	1.33	4.64	4.59

Table A3 Stream results in section 6.3.2 using RStoic reactor over CZA catalyst at 543 K and 40 bar.

	Units	CO2	CO2-COMP	H2	H2O	METHANOL	MIXTURE1	MIXTURE2	PRODUCT1	PRODUCT2
Temperature	K	298.00	649.98	298.00	372.90	328.26	418.21	361.20	543.00	323.00
Pressure	N/SQM	1.0E+05	4.0E+06	4.5E+06	1.0E+05	8.0E+04	4.0E+06	4.0E+06	4.0E+06	3.0E+06
Vapor Fraction		1.00	1.00	1.00	0.00	0.00	1.00	1.00	1.00	0.98
Liquid Fraction		0.00	0.00	0.00	1.00	1.00	0.00	0.00	0.00	0.02
Molar Enthalpy	J/KMOL	-3.9E+08	-3.8E+08	2.2E+04	-2.8E+08	-2.4E+08	-9.5E+07	-6.6E+07	-6.0E+07	-6.8E+07
Mass Enthalpy	J/KG	-8.9E+06	-8.6E+06	1.1E+04	-1.6E+07	-7.7E+06	-7.6E+06	-5.6E+06	-5.1E+06	-5.8E+06
Enthalpy Flow	WATT	-1.1E+07	-1.1E+07	1.9E+03	-5.6E+06	-1.6E+06	-1.1E+07	-9.5E+07	-8.6E+07	-9.7E+07
Molar Entropy	J/KMOL-K	2.9E+03	5.3E+03	-3.2E+04	-1.5E+05	-2.3E+05	-1.5E+04	-3.1E+03	1.0E+04	-6.2E+03
Mass Entropy	J/KG-K	6.5E+01	1.2E+02	-1.6E+04	-8.3E+03	-7.4E+03	-1.2E+03	-2.7E+02	8.5E+02	-5.2E+02
Molar Density	KMOL/CUM	4.1E-02	7.4E-01	1.8E+00	5.1E+01	2.4E+01	1.1E+00	1.3E+00	8.7E-01	1.1E+00
Mass Density	KG/CUM	1.8E+00	3.3E+01	3.6E+00	9.2E+02	7.6E+02	1.4E+01	1.5E+01	1.0E+01	1.3E+01
Average MW		4.4E+01	4.4E+01	2.0E+00	1.8E+01	3.1E+01	1.3E+01	1.2E+01	1.2E+01	1.2E+01
Mole Flows	KMOL/SEC	2.78E-02	2.78E-02	8.33E-02	1.98E-02	6.82E-03	1.11E-01	1.45E+00	1.43E+00	1.43E+00
CO ₂	KMOL/SEC	2.78E-02	2.78E-02	0.00E+00	9.76E-21	3.94E-06	2.78E-02	1.69E-01	1.49E-01	1.49E-01
H ₂	KMOL/SEC	0.00E+00	0.00E+00	8.33E-02	8.85E-31	6.31E-09	8.33E-02	1.01E+00	9.76E-01	9.76E-01
H ₂ O	KMOL/SEC	0.00E+00	0.00E+00	0.00E+00	1.97E-02	4.02E-04	0.00E+00	4.44E-03	2.48E-02	2.48E-02
Methanol	KMOL/SEC	0.00E+00	0.00E+00	0.00E+00	1.31E-04	6.41E-03	0.00E+00	1.06E-02	1.77E-02	1.77E-02
CO	KMOL/SEC	0.00E+00	0.00E+00	0.00E+00	1.09E-30	2.35E-09	0.00E+00	2.51E-01	2.64E-01	2.64E-01
Mole Fractions										
CO ₂		1.00	1.00	0.00	0.00	0.00	0.25	0.12	0.10	0.10
H ₂		0.00	0.00	1.00	0.00	0.00	0.75	0.70	0.68	0.68
H ₂ O		0.00	0.00	0.00	0.99	0.06	0.00	0.00	0.02	0.02
Methanol		0.00	0.00	0.00	0.01	0.94	0.00	0.01	0.01	0.01
CO		0.00	0.00	0.00	0.00	0.00	0.00	0.17	0.18	0.18
Mass Flow	KG/SEC	1.22	1.22	0.17	0.36	0.21	1.39	16.93	16.93	16.93

Table A3 (continued) Stream results in section 6.3.2 using RStoic reactor over CZA catalyst at 543 K and 40 bar.

	Units	PURGE1	PURGE2	RECYCLE1	RECYCLE2	SEP-LIQ1	SEP-LIQ2	SEP-LIQ3	SEP-VAP
Temperature	K	323.00	323.56	323.00	356.28	323.00	323.56	323.56	323.00
Pressure	N/SQM	3.0E+06	1.0E+05	3.0E+06	4.0E+06	3.0E+06	1.0E+05	1.0E+05	3.0E+06
Vapor Fraction		1.00	1.00	1.00	1.00	0.00	0.00	0.00	1.00
Liquid Fraction		0.00	0.00	0.00	0.00	1.00	1.00	1.00	0.00
Molar Enthalpy	J/KMOL	-6.4E+07	-3.0E+08	-6.4E+07	-6.3E+07	-2.7E+08	-2.7E+08	-2.7E+08	-6.4E+07
Mass Enthalpy	J/KG	-5.5E+06	-8.5E+06	-5.5E+06	-5.4E+06	-1.3E+07	-1.3E+07	-1.3E+07	-5.5E+06
Enthalpy Flow	WATT	-4.5E+06	-7.7E+03	-8.6E+07	-8.4E+07	-7.3E+06	-7.3E+06	-7.3E+06	-9.0E+07
Molar Entropy	J/KMOL-K	-2.9E+03	-1.5E+04	-2.9E+03	-2.4E+03	-1.8E+05	-1.8E+05	-1.8E+05	-2.9E+03
Mass Entropy	J/KG-K	-2.5E+02	-4.3E+02	-2.5E+02	-2.0E+02	-8.2E+03	-8.2E+03	-8.2E+03	-2.5E+02
Molar Density	KMOL/CUM	1.1E+00	3.7E-02	1.1E+00	1.3E+00	4.1E+01	2.0E+01	4.1E+01	1.1E+00
Mass Density	KG/CUM	1.3E+01	1.3E+00	1.3E+01	1.6E+01	8.8E+02	4.3E+02	8.8E+02	1.3E+01
Average MW		1.2E+01	3.6E+01	1.2E+01	1.2E+01	2.1E+01	2.1E+01	2.1E+01	1.2E+01
Mole Flows	KMOL/SEC	7.02E-02	2.54E-05	1.33E+00	1.33E+00	2.66E-02	2.66E-02	2.66E-02	1.40E+00
CO ₂	KMOL/SEC	7.45E-03	1.53E-05	1.41E-01	1.41E-01	1.93E-05	1.93E-05	3.94E-06	1.49E-01
H ₂	KMOL/SEC	4.88E-02	1.81E-06	9.27E-01	9.27E-01	1.81E-06	1.81E-06	6.31E-09	9.76E-01
H ₂ O	KMOL/SEC	2.34E-04	2.34E-06	4.44E-03	4.44E-03	2.01E-02	2.01E-02	2.01E-02	4.68E-03
Methanol	KMOL/SEC	5.59E-04	5.36E-06	1.06E-02	1.06E-02	6.55E-03	6.55E-03	6.54E-03	1.12E-02
CO	KMOL/SEC	1.32E-02	5.66E-07	2.51E-01	2.51E-01	5.68E-07	5.68E-07	2.35E-09	2.64E-01
Mole Fractions									
CO ₂		0.11	0.60	0.11	0.11	0.00	0.00	0.00	0.11
H ₂		0.69	0.07	0.69	0.69	0.00	0.00	0.00	0.69
H ₂ O		0.00	0.09	0.00	0.00	0.75	0.75	0.75	0.00
Methanol		0.01	0.21	0.01	0.01	0.25	0.25	0.25	0.01
CO		0.19	0.02	0.19	0.19	0.00	0.00	0.00	0.19
Mass Flow	KG/SEC	0.82	0.00	15.54	15.54	0.57	0.57	0.57	16.36

Table A4 Stream results in section 6.3.2 using RStoic reactor over 3La10In/ZrO₂ catalyst at 543 K and 40 bar.

	Units	CO2	CO2-COMP	H2	H2O	METHANOL	MIXTURE1	MIXTURE2	PRODUCT1	PRODUCT2
Temperature	K	298.00	649.98	298.00	370.41	330.56	418.21	360.61	543.00	323.00
Pressure	N/SQM	1.0E+05	4.0E+06	4.5E+06	1.0E+05	1.0E+05	4.0E+06	4.0E+06	4.0E+06	3.0E+06
Vapor Fraction		1.00	1.00	1.00	0.00	0.00	1.00	1.00	1.00	0.98
Liquid Fraction		0.00	0.00	0.00	1.00	1.00	0.00	0.00	0.00	0.02
Molar Enthalpy	J/KMOL	-3.9E+08	-3.8E+08	2.2E+04	-2.8E+08	-2.4E+08	-9.5E+07	-9.3E+07	-9.0E+07	-9.8E+07
Mass Enthalpy	J/KG	-8.9E+06	-8.6E+06	1.1E+04	-1.5E+07	-7.5E+06	-7.6E+06	-7.4E+06	-7.0E+06	-7.6E+06
Enthalpy Flow	WATT	-1.1E+07	-1.1E+07	1.9E+03	-3.9E+06	-2.9E+06	-1.1E+07	-1.2E+07	-1.1E+08	-1.2E+08
Molar Entropy	J/KMOL-K	2.9E+03	5.3E+03	-3.2E+04	-1.5E+05	-2.3E+05	-1.5E+04	-1.8E+04	-5.2E+03	-2.3E+04
Mass Entropy	J/KG-K	6.5E+01	1.2E+02	-1.6E+04	-8.3E+03	-7.4E+03	-1.2E+03	-1.4E+03	-4.1E+02	-1.8E+03
Molar Density	KMOL/CUM	4.1E-02	7.4E-01	1.8E+00	5.0E+01	2.4E+01	1.1E+00	1.3E+00	8.8E-01	1.1E+00
Mass Density	KG/CUM	1.8E+00	3.3E+01	3.6E+00	9.1E+02	7.6E+02	1.4E+01	1.7E+01	1.1E+01	1.5E+01
Average MW		4.4E+01	4.4E+01	2.0E+00	1.8E+01	3.2E+01	1.3E+01	1.3E+01	1.3E+01	1.3E+01
Mole Flows	KMOL/SEC	2.78E-02	2.78E-02	8.33E-02	1.39E-02	1.21E-02	1.11E-01	1.24E+00	1.21E+00	1.21E+00
CO ₂	KMOL/SEC	2.78E-02	2.78E-02	0.00E+00	1.52E-20	1.53E-05	2.78E-02	2.83E-01	2.69E-01	2.69E-01
H ₂	KMOL/SEC	0.00E+00	0.00E+00	8.33E-02	1.18E-31	7.89E-09	8.33E-02	9.13E-01	8.73E-01	8.73E-01
H ₂ O	KMOL/SEC	0.00E+00	0.00E+00	0.00E+00	1.37E-02	2.80E-04	0.00E+00	3.16E-03	1.73E-02	1.73E-02
Methanol	KMOL/SEC	0.00E+00	0.00E+00	0.00E+00	2.40E-04	1.18E-02	0.00E+00	1.30E-02	2.58E-02	2.58E-02
CO	KMOL/SEC	0.00E+00	0.00E+00	0.00E+00	5.96E-32	7.35E-10	0.00E+00	2.69E-02	2.83E-02	2.83E-02
Mole Fractions										
CO ₂		1.00	1.00	0.00	0.00	0.00	0.25	0.23	0.22	0.22
H ₂		0.00	0.00	1.00	0.00	0.00	0.75	0.74	0.72	0.72
H ₂ O		0.00	0.00	0.00	0.98	0.02	0.00	0.00	0.01	0.01
Methanol		0.00	0.00	0.00	0.02	0.98	0.00	0.01	0.02	0.02
CO		0.00	0.00	0.00	0.00	0.00	0.00	0.02	0.02	0.02
Mass Flow	KG/SEC	1.22	1.22	0.17	0.25	0.38	1.39	15.54	15.54	15.54

Table A4 (continued) Stream results in section 6.3.2 using RStoic reactor over 3La10In/ZrO₂ catalyst at 543 K and 40 bar.

	Units	PURGE1	PURGE2	RECYCLE1	RECYCLE2	SEP-LIQ1	SEP-LIQ2	SEP-LIQ3	SEP-VAP
Temperature	K	323.00	322.31	323.00	354.95	323.00	322.31	322.31	323.00
Pressure	N/SQM	3.0E+06	1.0E+05	3.0E+06	4.0E+06	3.0E+06	1.0E+05	1.0E+05	3.0E+06
Vapor Fraction		1.00	1.00	1.00	1.00	0.00	0.01	0.00	1.00
Liquid Fraction		0.00	0.00	0.00	0.00	1.00	0.99	1.00	0.00
Molar Enthalpy	J/KMOL	-9.4E+07	-3.2E+08	-9.4E+07	-9.3E+07	-2.6E+08	-2.6E+08	-2.6E+08	-9.4E+07
Mass Enthalpy	J/KG	-7.5E+06	-8.4E+06	-7.5E+06	-7.4E+06	-1.1E+07	-1.1E+07	-1.1E+07	-7.5E+06
Enthalpy Flow	WATT	-5.6E+06	-7.5E+04	-1.1E+08	-1.1E+08	-6.9E+06	-6.9E+06	-6.9E+06	-1.1E+08
Molar Entropy	J/KMOL-K	-1.9E+04	-2.7E+04	-1.9E+04	-1.8E+04	-1.9E+05	-1.9E+05	-1.9E+05	-1.9E+04
Mass Entropy	J/KG-K	-1.5E+03	-7.3E+02	-1.5E+03	-1.5E+03	-7.8E+03	-7.8E+03	-7.9E+03	-1.5E+03
Molar Density	KMOL/CUM	1.1E+00	3.8E-02	1.1E+00	1.3E+00	3.4E+01	3.7E+00	3.4E+01	1.1E+00
Mass Density	KG/CUM	1.4E+01	1.4E+00	1.4E+01	1.7E+01	8.3E+02	9.1E+01	8.3E+02	1.4E+01
Average MW		1.3E+01	3.8E+01	1.3E+01	1.3E+01	2.5E+01	2.5E+01	2.5E+01	1.3E+01
Mole Flows	KMOL/SEC	5.94E-02	2.37E-04	1.13E+00	1.13E+00	2.62E-02	2.62E-02	2.60E-02	1.19E+00
CO ₂	KMOL/SEC	1.35E-02	1.45E-04	2.56E-01	2.56E-01	1.61E-04	1.61E-04	1.53E-05	2.69E-01
H ₂	KMOL/SEC	4.37E-02	6.56E-06	8.30E-01	8.30E-01	6.57E-06	6.57E-06	7.89E-09	8.73E-01
H ₂ O	KMOL/SEC	1.66E-04	1.69E-05	3.16E-03	3.16E-03	1.40E-02	1.40E-02	1.40E-02	3.32E-03
Methanol	KMOL/SEC	6.84E-04	6.78E-05	1.30E-02	1.30E-02	1.21E-02	1.21E-02	1.20E-02	1.37E-02
CO	KMOL/SEC	1.41E-03	3.56E-07	2.69E-02	2.69E-02	3.57E-07	3.57E-07	7.35E-10	2.83E-02
Mole Fractions									
CO ₂		0.23	0.61	0.23	0.23	0.01	0.01	0.00	0.23
H ₂		0.74	0.03	0.74	0.74	0.00	0.00	0.00	0.74
H ₂ O		0.00	0.07	0.00	0.00	0.53	0.53	0.54	0.00
Methanol		0.01	0.29	0.01	0.01	0.46	0.46	0.46	0.01
CO		0.02	0.00	0.02	0.02	0.00	0.00	0.00	0.02
Mass Flow	KG/SEC	0.74	0.01	14.15	14.15	0.65	0.65	0.64	14.89

Table A5 Stream results in section 6.3.2 using RStoic reactor over 1Co-2In/ZrO₂ catalyst at 543 K and 40 bar.

	Units	CO2	CO2-COMP	H2	H2O	METHANOL	MIXTURE1	MIXTURE2	PRODUCT1	PRODUCT2
Temperature	K	298.00	649.98	298.00	370.51	330.68	418.21	359.57	543.00	323.00
Pressure	N/SQM	1.0E+05	4.0E+06	4.5E+06	1.0E+05	1.0E+05	4.0E+06	4.0E+06	4.0E+06	3.0E+06
Vapor Fraction		1.00	1.00	1.00	0.00	0.00	1.00	1.00	1.00	0.99
Liquid Fraction		0.00	0.00	0.00	1.00	1.00	0.00	0.00	0.00	0.01
Molar Enthalpy	J/KMOL	-3.9E+08	-3.8E+08	2.2E+04	-2.8E+08	-2.4E+08	-9.5E+07	-9.5E+07	-9.0E+07	-9.8E+07
Mass Enthalpy	J/KG	-8.9E+06	-8.6E+06	1.1E+04	-1.5E+07	-7.5E+06	-7.6E+06	-7.5E+06	-7.1E+06	-7.7E+06
Enthalpy Flow	WATT	-1.1E+07	-1.1E+07	1.9E+03	-2.9E+06	-2.1E+06	-1.1E+07	-1.4E+08	-1.3E+08	-1.5E+08
Molar Entropy	J/KMOL-K	2.9E+03	5.3E+03	-3.2E+04	-1.5E+05	-2.3E+05	-1.5E+04	-1.9E+04	-5.7E+03	-2.2E+04
Mass Entropy	J/KG-K	6.5E+01	1.2E+02	-1.6E+04	-8.3E+03	-7.4E+03	-1.2E+03	-1.5E+03	-4.5E+02	-1.7E+03
Molar Density	KMOL/CUM	4.1E-02	7.4E-01	1.8E+00	5.0E+01	2.4E+01	1.1E+00	1.3E+00	8.8E-01	1.1E+00
Mass Density	KG/CUM	1.8E+00	3.3E+01	3.6E+00	9.1E+02	7.6E+02	1.4E+01	1.7E+01	1.1E+01	1.4E+01
Average MW		4.4E+01	4.4E+01	2.0E+00	1.8E+01	3.2E+01	1.3E+01	1.3E+01	1.3E+01	1.3E+01
Mole Flows	KMOL/SEC	2.78E-02	2.78E-02	8.33E-02	1.03E-02	8.68E-03	1.11E-01	1.50E+00	1.48E+00	1.48E+00
CO ₂	KMOL/SEC	2.78E-02	2.78E-02	0.00E+00	1.10E-20	1.08E-05	2.78E-02	3.52E-01	3.42E-01	3.42E-01
H ₂	KMOL/SEC	0.00E+00	0.00E+00	8.33E-02	8.56E-32	5.43E-09	8.33E-02	1.10E+00	1.07E+00	1.07E+00
H ₂ O	KMOL/SEC	0.00E+00	0.00E+00	0.00E+00	1.01E-02	2.07E-04	0.00E+00	3.91E-03	1.45E-02	1.45E-02
Methanol	KMOL/SEC	0.00E+00	0.00E+00	0.00E+00	1.73E-04	8.46E-03	0.00E+00	1.58E-02	2.53E-02	2.53E-02
CO	KMOL/SEC	0.00E+00	0.00E+00	0.00E+00	2.54E-32	3.01E-10	0.00E+00	2.01E-02	2.11E-02	2.11E-02
Mole Fractions										
CO ₂		1.00	1.00	0.00	0.00	0.00	0.25	0.24	0.23	0.23
H ₂		0.00	0.00	1.00	0.00	0.00	0.75	0.74	0.73	0.73
H ₂ O		0.00	0.00	0.00	0.98	0.02	0.00	0.00	0.01	0.01
Methanol		0.00	0.00	0.00	0.02	0.97	0.00	0.01	0.02	0.02
CO		0.00	0.00	0.00	0.00	0.00	0.00	0.01	0.01	0.01
Mass Flow	KG/SEC	1.22	1.22	0.17	0.19	0.28	1.39	18.88	18.88	18.88

Table A5 (continued) Stream results in section 6.3.2 using RStoic reactor over 1Co-2In/ZrO₂ catalyst at 543 K and 40 bar.

	Units	PURGE1	PURGE2	RECYCLE1	RECYCLE2	SEP-LIQ1	SEP-LIQ2	SEP-LIQ3	SEP-VAP
Temperature	K	323.00	322.32	323.00	354.87	323.00	322.32	322.32	323.00
Pressure	N/SQM	3.0E+06	1.0E+05	3.0E+06	4.0E+06	3.0E+06	1.0E+05	1.0E+05	3.0E+06
Vapor Fraction		1.00	1.00	1.00	1.00	0.00	0.01	0.00	1.00
Liquid Fraction		0.00	0.00	0.00	0.00	1.00	0.99	1.00	0.00
Molar Enthalpy	J/KMOL	-9.6E+07	-3.2E+08	-9.6E+07	-9.5E+07	-2.6E+08	-2.6E+08	-2.6E+08	-9.6E+07
Mass Enthalpy	J/KG	-7.6E+06	-8.4E+06	-7.6E+06	-7.5E+06	-1.1E+07	-1.1E+07	-1.1E+07	-7.6E+06
Enthalpy Flow	WATT	-7.0E+06	-5.5E+04	-1.3E+08	-1.3E+08	-5.1E+06	-5.1E+06	-5.0E+06	-1.4E+08
Molar Flow	J/KMOL-K	-2.0E+04	-2.7E+04	-2.0E+04	-1.9E+04	-1.9E+05	-1.9E+05	-1.9E+05	-2.0E+04
Mass Entropy	J/KG-K	-1.6E+03	-7.2E+02	-1.6E+03	-1.5E+03	-7.8E+03	-7.8E+03	-7.9E+03	-1.6E+03
Molar Density	KMOL/CUM	1.1E+00	3.8E-02	1.1E+00	1.3E+00	3.4E+01	3.7E+00	3.4E+01	1.1E+00
Mass Density	KG/CUM	1.4E+01	1.4E+00	1.4E+01	1.7E+01	8.3E+02	9.1E+01	8.3E+02	1.4E+01
Average MW		1.3E+01	3.8E+01	1.3E+01	1.3E+01	2.5E+01	2.5E+01	2.4E+01	1.3E+01
Mole Flows	KMOL/SEC	7.29E-02	1.72E-04	1.39E+00	1.39E+00	1.92E-02	1.92E-02	1.90E-02	1.46E+00
CO ₂	KMOL/SEC	1.71E-02	1.06E-04	3.25E-01	3.25E-01	1.17E-04	1.17E-04	1.08E-05	3.42E-01
H ₂	KMOL/SEC	5.37E-02	4.65E-06	1.02E+00	1.02E+00	4.65E-06	4.65E-06	5.43E-09	1.07E+00
H ₂ O	KMOL/SEC	2.06E-04	1.24E-05	3.91E-03	3.91E-03	1.04E-02	1.04E-02	1.04E-02	4.12E-03
Methanol	KMOL/SEC	8.33E-04	4.88E-05	1.58E-02	1.58E-02	8.68E-03	8.68E-03	8.63E-03	1.67E-02
CO	KMOL/SEC	1.06E-03	1.52E-07	2.01E-02	2.01E-02	1.52E-07	1.52E-07	3.01E-10	2.11E-02
Mole Fractions									
CO ₂		0.23	0.62	0.23	0.23	0.01	0.01	0.00	0.23
H ₂		0.74	0.03	0.74	0.74	0.00	0.00	0.00	0.74
H ₂ O		0.00	0.07	0.00	0.00	0.54	0.54	0.55	0.00
Methanol		0.01	0.28	0.01	0.01	0.45	0.45	0.45	0.01
CO		0.01	0.00	0.01	0.01	0.00	0.00	0.00	0.01
Mass Flow	KG/SEC	0.92	0.01	17.49	17.49	0.47	0.47	0.46	18.41

Appendix B

REPRINT PERMISSION LETTERS

Reprint Permission for Figure 1.3

4/22/2019

Rightslink® by Copyright Clearance Center



RightsLink®

Home

Account Info

Help



ACS Publications
Most Trusted. Most Cited. Most Read.

Title:

Carbon Dioxide Conversion by Reverse Water–Gas Shift Chemical Looping on Perovskite-Type Oxides

Logged in as:

Chen-Yu Chou
University of Delaware

LOGOUT

Author:

Yolanda A. Daza, Ryan A. Kent, Matthew M. Yung, et al

Publication:

Industrial & Engineering Chemistry Research

Publisher:

American Chemical Society

Date: Apr 1, 2014

Copyright © 2014, American Chemical Society

PERMISSION/LICENSE IS GRANTED FOR YOUR ORDER AT NO CHARGE

This type of permission/license, instead of the standard Terms & Conditions, is sent to you because no fee is being charged for your order. Please note the following:

- Permission is granted for your request in both print and electronic formats, and translations.
- If figures and/or tables were requested, they may be adapted or used in part.
- Please print this page for your records and send a copy of it to your publisher/graduate school.
- Appropriate credit for the requested material should be given as follows: "Reprinted (adapted) with permission from (COMPLETE REFERENCE CITATION). Copyright (YEAR) American Chemical Society." Insert appropriate information in place of the capitalized words.
- One-time permission is granted only for the use specified in your request. No additional uses are granted (such as derivative works or other editions). For any other uses, please submit a new request.

If credit is given to another source for the material you requested, permission must be obtained from that source.

BACK

CLOSE WINDOW

Copyright © 2019 Copyright Clearance Center, Inc. All Rights Reserved. [Privacy statement](#). [Terms and Conditions](#).
Comments? We would like to hear from you. E-mail us at customercare@copyright.com

Reprint Permission for Figure 1.4



Dear Chou Chen-Yu,

Your permission requested is granted and there is no fee for this reuse. In your planned reuse, you must cite the ACS article as the source, add this direct link <https://pubs.acs.org/doi/abs/10.1021/acs.chemrev.6b00816>, and include a notice to readers that further permissions related to the material excerpted should be directed to the ACS.

If you need further assistance, please let me know.

Sincerely,

Raquel Picar-Simpson
ACS Publications Support
Customer Services & Information
Website: <https://help.acs.org/>

Incident Information:

Incident #: 2701782
Date Created: 2019-04-22T15:00:34
Priority: 3
Customer: Chou Chen-Yu
Title: Reuse of content (figure) in thesis

Reprint Permission for Figure 1.5

4/22/2019

Rightslink® by Copyright Clearance Center



RightsLink®

Home

Account
Info

Help



Title: Tuning Selectivity of CO₂ Hydrogenation Reactions at the Metal/Oxide Interface

Logged in as:
Chen-Yu Chou
University of Delaware

Author: Shyam Kattel, Ping Liu, Jinguang G. Chen

LOGOUT

Publication: Journal of the American Chemical Society

Publisher: American Chemical Society

Date: Jul 1, 2017

Copyright © 2017, American Chemical Society

PERMISSION/LICENSE IS GRANTED FOR YOUR ORDER AT NO CHARGE

This type of permission/license, instead of the standard Terms & Conditions, is sent to you because no fee is being charged for your order. Please note the following:

- Permission is granted for your request in both print and electronic formats, and translations.
- If figures and/or tables were requested, they may be adapted or used in part.
- Please print this page for your records and send a copy of it to your publisher/graduate school.
- Appropriate credit for the requested material should be given as follows: "Reprinted (adapted) with permission from (COMPLETE REFERENCE CITATION). Copyright (YEAR) American Chemical Society." Insert appropriate information in place of the capitalized words.
- One-time permission is granted only for the use specified in your request. No additional uses are granted (such as derivative works or other editions). For any other uses, please submit a new request.

If credit is given to another source for the material you requested, permission must be obtained from that source.

BACK

CLOSE WINDOW

Copyright © 2019 [Copyright Clearance Center, Inc.](#) All Rights Reserved. [Privacy statement](#). [Terms and Conditions](#).
Comments? We would like to hear from you. E-mail us at customercare@copyright.com

Reprint Permission for Figure 2.3

4/22/2019

RightsLink Printable License

ELSEVIER LICENSE TERMS AND CONDITIONS

Apr 22, 2019

This Agreement between University of Delaware -- Chen-Yu Chou ("You") and Elsevier ("Elsevier") consists of your license details and the terms and conditions provided by Elsevier and Copyright Clearance Center.

License Number	4574360401921
License date	Apr 22, 2019
Licensed Content Publisher	Elsevier
Licensed Content Publication	Applied Catalysis A: General
Licensed Content Title	Reduction behavior of iron oxides in hydrogen and carbon monoxide atmospheres
Licensed Content Author	W.K. Jozwiak, E. Kaczmarek, T.P. Maniecki, W. Ignaczak, W. Maniukiewicz
Licensed Content Date	Jun 30, 2007
Licensed Content Volume	326
Licensed Content Issue	1
Licensed Content Pages	11
Start Page	17
End Page	27
Type of Use	reuse in a thesis/dissertation
Portion	figures/tables/illustrations
Number of figures/tables/illustrations	1
Format	both print and electronic
Are you the author of this Elsevier article?	No
Will you be translating?	No
Original figure numbers	Figure 1
Title of your thesis/dissertation	Catalytic CO ₂ hydrogenation to CO and Methanol
Expected completion date	May 2019
Estimated size (number of pages)	200
Requestor Location	University of Delaware 150 Academy Street NEWARK, DE 19716 United States Attn: University of Delaware
Publisher Tax ID	98-0397604
Total	0.00 USD
Terms and Conditions	